Dry Friction between Rough Surfaces of Silicon and Functionalized Gear Microelectromechanical Systems

by

Nabeel Shallal Thamer Almuramady

Thesis submitted in candidature for the degree of

Doctor of Philosophy at Cardiff University

Tribology and Contact Mechanics Research Group

Institute of Mechanics and Advanced Materials

School of Engineering

Cardiff University

2017

Declaration

This work has not been submitted in substance for any other degree or award at this or any other university or place of learning, nor is being submitted concurrently in candidature for any degree or another award.

Signed …………………… (Nabeel Almuramady) Date ……………………………

STATEMENT 1

This thesis is being submitted in partial fulfilment of the requirements for the degree of PhD.

Signed …………………… (Nabeel Almuramady) Date ……………………………

STATEMENT 2

This thesis is the result of my own independent work/investigation, except where otherwise stated, and the thesis has not been edited by a third party beyond what is permitted by Cardiff University Policy on the Use of Third Party Editors by Research Degree Student. Other sources are acknowledged by explicit references. The views expressed are my own.

Signed ……………………. (Nabeel Almuramady) Date ……………………………

STATEMENT 3

I hereby give consent for my thesis, if accepted, to be available online in the University's Open Access repository and for inter-library loan, and for the title and summary to be made available to outside organisations.

Signed …………………… (Nabeel Almuramady) Date ……………………………

Abstract

Microelectromechanical systems (MEMS or micro-electro-mechanical systems) is a branch of nanotechnology studying microscopic devices, especially those with moving parts. Microgear MEMS is probably the most common type of MEMS that involves transmission of rotational motion between a gear pair. Understanding of physical and chemical mechanisms related to friction between components of microgear MEMS is important for their design and accurate prediction of their tribological properties. In this thesis, various problems related to modelling of tribological performance of silicon microgear MEMS are under investigation. The microgear MEMS teeth have been simulated in the vacuum environment and, therefore, the energy dissipation mechanisms may be reduced the dissociation of chemical and van der Waals interactions as well as the elastic interlocking between counterparts subscale asperities. The models developed have been used to simulate various tribological phenomena, including adhesion, friction, wear and the elastic interlocking of the tooth surfaces.

The MEMS tooth roughness is described using statistical approach in accordance with the experimental data obtained by AFM (Atomic Force Microscopy). It has been shown that the microgear MEMS tooth surface roughness does not have any microscale roughness and hence, there is no plastic deformation of the atomic and adhesive subscale asperity due to the Polonsky-Keer effect. The tooth asperity of microgear MEMS is modelled as a nanoblock obtained by superposition of two hierarchical subscales that are specified by the character of interactions at the subscale: an atomic subscale, where chemical interactions are likely to occur, adhesive subscale, where molecular adhesion (van der Waals interaction) is significant and bulk elastic material. The tooth surface is covered by the nanoasperity blocks.

According to the roughness studies, a real silicon rough surface has been described at different scales: nanoscale that include atomic subscale of active chemical interactions and molecular subscale of active van der Waals interactions, and bulk elastic scale. The Borodich-Savencu (B-S) one level model that have been developed before for tribology of nominally flat surfaces has been developed. In order to mirror the specific features of interactions between MEMS teeth, the B-S model assumed the gap between the surfaces is constant, while the gap in a gear MEMS pair is changing during the mesh cycle. This was taken into account by the iterative solutions of two-dimensional frictional Hertz-type problems using the Cardiff numerical solver. The new model allows us to model tribology of curved teeth using nanoblocks consisting of atomic and molecular subscales located at varying levels. The apparent friction force and coefficient of friction μ have been calculated by estimations of the total energy per unit length dissipated through the above-mentioned physical and chemical mechanisms. It has been shown that there is a high possibility of stiction (cohesion or the so-called cold welding) between pure silicon MEMS teeth. To improve the system performance and to find ways for controlling

friction effects and reducing stiction possibility, it is suggested to functionalise the MEMS microgear tooth surfaces by self-assembled monomolecular (SAM) layers.

A damage model has been developed to study the damage accumulation and wear of these carbon-based functionalised monomolecular layers. The model is based on the Goryacheva-Torskaya model for damage accumulation in fatigue elements. The maximum damage occurs under action of the maximum load, hence the dry friction contact of a single tooth contact is considered. To use the damage model, the surface stresses are calculated. Numerical simulations for silicon-based MEMS micro-tooth surfaces functionalised by monomolecular layer carbon-based coatings show that initially the surfaces do not stick to each other. However, the stiction occur after some number of cycles because the functionalised monomolecular is gradually worn away due to damage accumulation in the layer.

Acknowledgements

During the last three years, I have been fortunate enough to meet some truly unique characters without them I would have been unable to submit my thesis.

I would firstly like to express my appreciation, gratitude and thank my supervisors: Prof F.M. Borodich and Prof H.P. Evans. Each of whom has shown dedication and patience in mentoring me throughout my study of Tribology.

I would also like to express my sensing and deep appreciation for the Iraqi Ministry of Higher Education and Scientific Research and the University of Al-Qadisiyah for supporting me financially during the period of my study and many thanks for staff of Iraqi Cultural Attaché in London for their support

Thank is also due to my good friends for their good friendship and also It has also been a pleasure to share the office with my colleagues Maasi Al-Mayali, Dr Sergey Khaustov, Dr Ovidiu Savencu to work alongside and interact with on a daily basis.

I also would like to thank Prof. I. G. Goryacheva and Prof. E. V. Torskaya for their advice in modelling of accumulative damage in the functionalised monomolecular OTS layers.

My parents are also due gratitude for their love and support that have given to me over the years, without them; I would not be in the privileged position I am today.

Finally, I would also like to express the gratitude and thank my wife, and my kids– despite living with me in Wales for the last three years, they have played a crucial role in dispersing some of the clouds that have hung over me.

Contents

Declaration I

Abstract II

Acknowledgements IV

Contents V

Chapter 1 Background and Literature Review 1

1.1 Introduction to Dry Contact Tribology 1

1.2 Tribology Science in the History 2

1.3 Micro-Electro-Mechanical-Systems: Classification and Properties 7

1.4 MEMS and Surface Topography Effects 12

1.5 Non-Optical Surface Topography Measurements Tools 13

1.5.1 Atomic Force Microscopy 14

1.6 Main Problems and Challenges in MEMS Microgear 16

1.6.1 Adhesion and Stiction 17

1.6.2 Contact, Friction and Stiction at the Small-scale 22

1.6.3 Multi-asperity Contact 25

1.6.4 The Greenwood-Williamson Models 27

1.7 Multiscale Properties of Surfaces and Fractal Models 28

1.7.1 Archard’s Model 29

1.7.2 Fractal Models 31

1.8 Anti-stiction Models for Surface Coating 35

1.9 Classical Models of Adhesive Contact 38

1.10 Thesis Layout 43

Chapter 2 Modelling of Multiscale Structure of a Single MEMS Asperity 44

2.1 Introduction 44

2.2 Basic Definitions: Multiscale, Hierarchical and Multi-level Models 44

2.3 The Polonsky-Keer Effect and its Influence on Characteristics of MEMS 46

2.4 Contact and Adhesion between MEMS Elements 48

2.5 MEMS Materials, Properties, and Techniques 49

2.5.1 Surface Micromachining 49

2.5.2 Bulk Micromachining 50

2.6 Multiscale Structure of a Single MEMS Asperity 52

2.6.1 The Borodich-Savencu (B-S) Model 52

2.6.2 An Extended Borodich-Savencu (B-S) Model for MEMS Surface 53

2.7 Conclusions to Chapter 2 58

Chapter 3 Modelling of the Frictional Work of a Multi-Asperity Surface 60

3.1 Introduction 60

3.2 Modelling of Surface Roughness by a General Multi-scale Hierarchical Model of a Nominally Flat Slider 60

3.3 Mechanical and Chemical Mechanisms of Energy Dissipation and Models of Friction 61

3.3.1 Simulations of Energy Dissociation in the Chemical Bonds 65

3.3.2 Simulations of Energy Dissociation in the VdW Bonds 67

3.3.3 Simulation of Adhesion Layer on the MEMS Tooth Surface 69

3.3.4 Molecular Mechanics Approach to Model Chemical Interactions using Lennard-Jones Potentials 73

3.3.5 Modelling vdW Interactions using Lennard-Jones Potentials 77

3.3.6 Energy Dissipation by Mechanical Interlocking of Asperities 81

3.4 Simulations of Friction between Two Nominally Flat Surfaces 82

3.4.1 The Fixed Gap Model 83

3.4.2 Simulations for the Multi-scale Hierarchical Structure with a Vertical Degree of Freedom 91

3.5 Estimation of the COF Taking into Account the Dissociation of the Chemical and vdW Bonds for Silicon 92

3.6 Results of Numerical Simulations Using Various Parameters of Contact 99

3.6.1 Non-functionalised Silicon Microgear MEMS Tooth 99

3.7 Discussion of the Influence of Environmental Conditions on Dry Friction and Extensions of Models to Non-crystalline Coatings 103

3.8 Conclusions to Chapter 3 104

Chapter 4 Modelling of the Frictional Work of a MEMS Gear 105

4.1 Introduction 105

4.2 Microgear MEMS Surface Topography 105

4.2.1 Experimental Study of MEMS Teeth Roughness Modelling 106

4.2.2 Modifications and Manufacturing Techniques of MEMS Microgears 107

4.2.3 Statistical Analysis of the MEMS Gear Surface 108

4.2.4 Specific Features of MEMS Surface Scales 111

4.3 Contact Geometry of Microgears in MEMS. 112

4.3.1 Load Distribution over the Meshing Gear Contact Cycle 120

4.4 Hertz Line Contact of MEMS Microgears 122

4.5 Modelling of a Frictionless Gear MEMS Contact 124

4.6 The Algorithm for Searching of True Gaps 129

4.7 Effect of Normal and Tangential Force on the Interaction between Particles in Microgears 133

4.8 Friction, Adhesion, Stiction and Wear in Silicon Microgears MEMS 135

4.9 Numerical Simulations of the Frictional Work of Gear MEMS 136

4.9.1 Simulations for the Multi-scale Hierarchical Structure with a Vertical Degree of Freedom 136

4.9.2 Numerical Simulation Results Using Various Parameters of Contact 139

4.9.3 Dependence of COF on External Load 140

4.9.4 Dependence of the COF on nominal contact area 154

4.10 Conclusion to Chapter 4 156

Chapter 5 Functionalised Silicon MEMS Microgear Tooth Surfaces, Damage Accumulation and Wear of the Functionalised Layer 157

5.1 Introduction 157

5.2 Functionalised Surfaces 157

5.3 Materials for Functionalised Layers 159

5.4 Simulations of the Frictional Work of a Functionalised Gear MEMS 162

5.4.1 Frictional Force between Interacting Functionalised Surfaces 162

5.4.2 Tangential Force between Interacting Molecules 164

5.4.3 Microgear MEMS Stiction, Formulation and Solutions 168

5.5 Damage Accumulation Models 171

5.5.1 The Extension of Goryacheva-Torskaya Model 171

5.5.2 The Contact Problem Solution 173

5.5.3 Coefficient of Friction for OTS-SAM layer 187

5.6 Conclusion to Chapter 5 192

Chapter 6 Conclusions and Future Work 194

6.1 Conclusion 194

6.2 Future Work 195

References 197

Chapter 1 Background and Literature Review

This chapter aims to give an overview of some areas of modern nanotechnology that are related to tribological effects, such as friction, contact as well as the production of Micro-Electro-Mechanical Systems (MEMS). In particular, it will briefly overview the main physical and chemical processes that are important for nanotechnology MEMS, it will also describe the models of contact and dry friction, as well as the methods of testing the surface topography. This description will help to justify the choice made in this work, which aims to study microgear silicon based-MEMS and it will formulate the main changes of their production and work.

1.1 Introduction to Dry Contact Tribology

Friction, adhesion and stiction can all play an important role in the different aspects of mechanical and physical phenomena, which are related to the contact and sliding motion of surfaces (Tanner, 2009, Maboudian et al., 2002, Carpick et al., 1997 and 2002, Berger, 2002 and Popov, 2010). Consequently, these issues have attracted a large number of researchers to carry out a broad range of studies (Hardy, 1936, Bowden and Tabor, 1956, 1973, Deryagin et al., 1978, Kragelsky et al., 1982 and Galin, 2008). As part of these studies, the target of the current research aims to develop and modify a dry frictional adhesive model to explain the effect of friction and contact interactions between microgear silicon-based MEMS teeth working in a clean and vacuum environment.

This chapter will start with a historical review of the tribology features and it includes a brief description of the classic laws of friction, wear, and stiction. In addition, the friction of solid materials is described by using the Amontons-Kotelnikov law, which is quite

often confused with Coulomb's law. The rest of this chapter aims to trace the development of the classic laws of friction. The necessary mechanisms of friction, stiction and adhesion will then be discussed.

1.2 Tribology Science in the History

Department of Education and Science report that was published in 1966 defines tribology as a science or technology that deals with the interaction of surfaces and the relative motion between them, as well as the particles related that interact. The word 'tribology' comes originally from the Greek word '*Tribos*', which means 'rubbing'. Historically, people started to think about the surface of the material and its effect a very long time ago. This is very clear when you look at the picture, scripts, and the symbols that are found on ancient clay tablets or in cave paintings. Dowson in his book "History of Tribology" (1979) mentioned that the Sumerian people in Mesopotamia (3200 BC) and the ancient Egyptians had produced the greatest significant features of the tribological record. For example, people in these civilisations used drills to produce rotary motion to make fire as well as drilling holes. Figure (1-1) (a) shows an ancient Egyptian bow structure and (b) shows an Egyptian using a bow to drill a hole in a wooden piece.

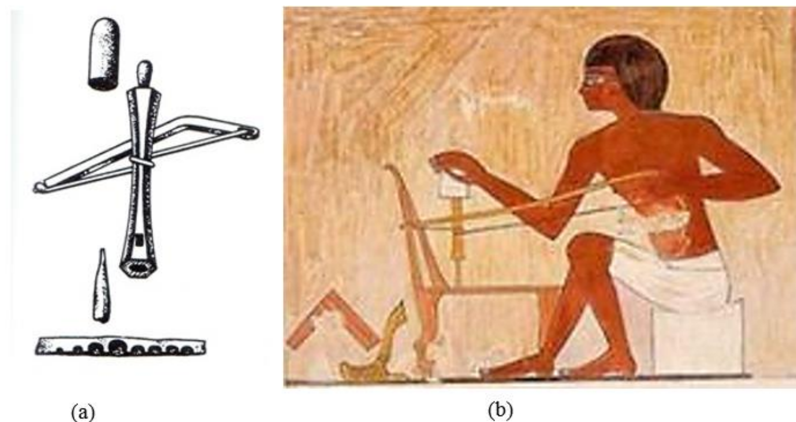

Figure 1-1 (a) Egyptian bow structure (b) Egyptian using a bow to drill a hole or make fire (Dowson, 1979)

Other examples of the tribological influence in ancient civilisations include a potter's wheel that has been found in Ur (present day Iraq), which dated to 3250BC (±250). Another example can be seen in the use of welding on vehicles in Mesopotamia, as represented in a copper model of a Mesopotamian welded vehicle that dates to 2800BC and which was found in the Tell Agrab region in the middle of Iraq , as shown in Figure (1-2).

Figure 1-2 Copper model of a Mesopotamian welded vehicle, Tell Agrab, Iraq (2800 BC) (Frankfort, 1943 and Dowson, 1979)

Friction and lubrication have also been mentioned in ancient Egypt. Evidence has been found that the ancient Egyptians were able to move massive stone blocks across the desert by wetting the sand in front of them to pull these heavy objects and, finally, build their famous pyramids or make their huge statues such as Abu al-Hol. Figure (1-3), shows how ancient Egyptians in 1880 BC transported a giant statue by using manpower and some forms of lubricant to reduce the friction of the statue's base with the ground.

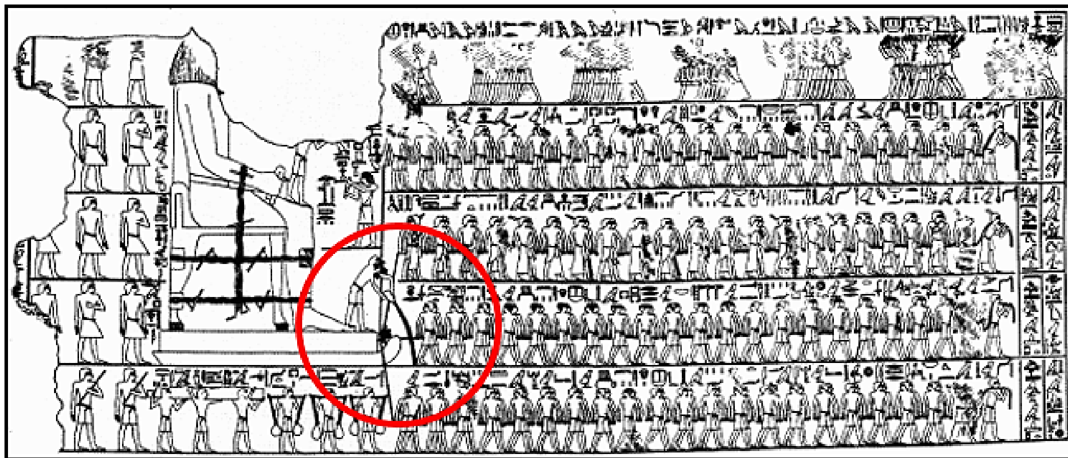

Figure 1-3 Transporting an Egyptian statue from the tomb of Tehuti-Hetep, El-Bersheh (1880 BC) (Popov, 2010 and Dowson, 1979)

From the ancient to the modern world, the science of tribology has rapidly developed, especially in the last two centuries. The influence of friction, wear, adhesion, stiction and the effects of relative motion of surfaces have started to attract the attention of researcher's who wish to fill the gaps of information in this field of knowledge (see e.g. Mate, 2008). Consequently, a wide variety of tribological phenomena have been studied to produce theories to describe these effects.

Leonardo da Vinci (1452–1519) was one of the first to mention many different tribological phenomena in his manuscripts and he described many problems related to tribology, such as wear, friction, gears and rolling (Kragelsky et al., 1982 and Hutchings, 2016). Consequently, researchers in tribology field represented him as a father of modern tribology. Da Vinci wrote his description for friction between surfaces about 150 years before Amonton (1699) put his friction laws. He was also the first to introduce the concept of friction coefficient as a ratio equal to 1/4 between friction force and normal pressure, and it is independent of the area of the contact between the counterpart's surfaces (Dowson, 1979 and Zhuravlev, 2013).

The basic principles of sliding friction, which is known these days as Coulomb's laws of friction, have been formulated first by the French physicist Guillaume Amontons (1663-1705). According to Amontons, friction is proportional to the weight of the slider and it is independent of the contact area between the contacting surfaces. However, the French engineer, Charles Augustin Coulomb (1736-1806) regarded Amontons law of friction as just an approximation, and scientists have accepted his point of view of friction phenomena since that time (see, for example, Hardy, 1936). However, Hardy himself has explained his point of view and mentioned in his book that he made a large number of measurements to verify the friction law and all of his measurement results have led to one fact that it is not an approximation law but an absolutely exact law (Hardy, 1936, p.647).

A mathematical model of tribology has been assumed by Leonhard Euler (1707-1783) to explain a geometrical resistance theory of dry friction. Euler believed that friction initiates from the interlocking of triangular irregularities. He was also the first to identify the difference between static and kinetic friction. Euler and his student Kotelnikov also introduced the symbol μ for the friction coefficient. He illustrated terms for both static and dynamic friction. The tangent of the asperity angle provides the static friction coefficient and the dynamic friction coefficient has been reduced by the kinetic term (Popov, 2010).

Osborne Reynolds (1842–1912) developed his theory at the end of the nineteenth century. He has the first scientist to experimentally examine the actions that happen in the contact area between surfaces during lubricated contact. He showed that there are always areas in which the two contacting surfaces are in no-slip contact and areas where slipping is taking place (Dowson, 1979).

The revolution of modern tribology started when Heinrich Hertz published his theory on contact in 1882 when he tried to solve the contact problem for elastic bodies with curved surfaces, which is represented as key in the tribology disciplines. Hertz's contact theory opened the door for researchers to produce a significant number of studies and models in different fields of tribology (see, for example, Johnson, 1985, Mate, 2008). Early in the last century, Sir William Hardy published a book which contained a number of different scientific studies regarding friction, wear and adhesion, and which attempted to give their explanations and discussions (see Hardy, 1936).

Nanotribology is a branch of tribology that involves the interactions of two relative moving surfaces in contact on the atomic and nanometre scale. One of the most famous examples of nano tribological aspects is MEMS (Sinha, et al., 2013) because it has a significant number of nano elements. Hence, the study of nanotribology has been stimulated by the use of micro-electro-mechanical systems (MEMS). The innovative strategies of the nano-tribological systems began to be developed after scanning probe microscopy (SPM) started to be used in the second half of the twentieth century.

As has mentioned previously, tribology is a surface contact phenomenon. Therefore, it can be significantly affected by a large surface to volume ratio, especially when it is in a micro or nanostructure (see, for example, Moore, 1975, Dowson, 1979). The small size of MEMS, their adhesion, friction, wear when a small load is applied and their elastic interaction are typical of nanotribology. Also there are several tribological conditions that should be taken into account; for example, pressure, velocity, temperature, surface free energy, surface topography and the environment, which play significant roles in the field of nanotribology.

1.3 Micro-Electro-Mechanical-Systems: Classification and Properties

MEMS merge the technology of micromachining and silicon-based microelectronics, therefore, they offer a lot of promise for use in industrial and consumer products. MEMS have been developed using different integration and miniaturisation techniques and they have the ability to achieve different mechanical, electrical and thermal tasks (see, for example, Beeby, 2004, Setter, 2005, Banks, 2006). These techniques and microsystem-based devices have the potential to dramatically affect people lives. Therefore, while semiconductor microfabrication was the first micro manufacturing revolution in the last century, MEMS is the second revolution in this century (Leondes, 2006, Ghodssi and Lin, 2011).

To understand the classifications, terminology and specific applications related to microsystems and MEMS technology, it is important to understand the particular features of these tiny systems. The general features of MEMS and the developed technology that are used to create these micromachined systems are presented in Figure (1-4). Although MEMS are a subcategory of microsystems, there is a difference between MEMS and microsystems. For example, MEMS use semiconductor technology to produce a mechanical part. In contrast, the deposition of a material on silicon does not create MEMS but is an application of microsystems. MEMS are microdevices that have been developed by using different integration and miniaturisation techniques. In addition, MEMS can do multi-functions, including mechanical, electrical and thermal. Their tiny size enables them to be used in many different applications that are inaccessible to conventional devices, while suitable scaling for MEMS and their elements leads to enhanced performance advantages (Maboudian, 1998, Madou, 2002, Gad-El-Hak, 2002 and Fischer et al., 2015).

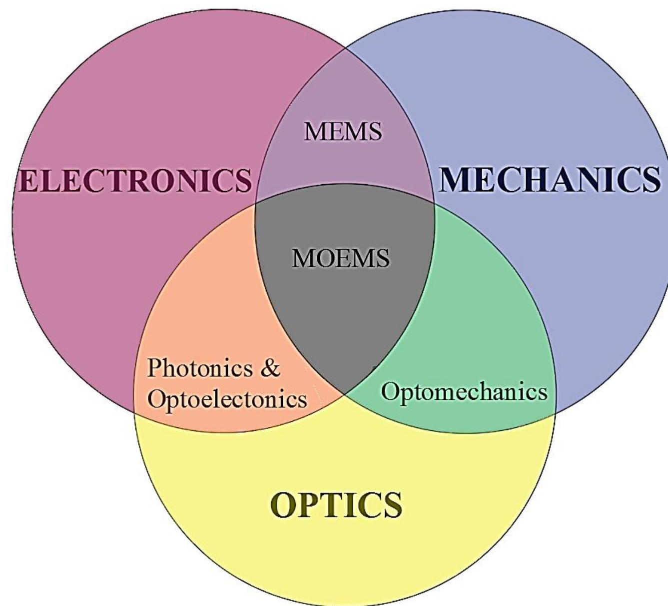

Figure 1-4 Classifications of MEMS and other microsystems technology (adopted from PRIME Faraday Partnership, 2002)

In recent years, a high number of MEMS devices may be found in a broad range of applications. In particular, the automobile industry has been the biggest user of MEMS technology; for example, in the accelerometers used in airbag deployment in vehicles. Significant numbers of MEMS accelerometers have been sold and used over the past years. Analog devices produced the first accelerometer sensor that was employed in an airbag in the 1990s, as shown in Figure (1-5a). In another example, HP Company has used MEMS in its ink jet print heads. The pressure sensors shown in Figure (1-5b) are widely used to monitor blood pressure in medical organisations (their size is 0.15 mm x 0.40 mm x 0.90 mm). These tiny pressure sensors are popular in medical applications (Madou, 2002). These pressure sensors are small and easy to use, and are inexpensive. They can be used to replace large, difficult and costly external sensors. They have also changed how the industry views the future of MEMS technology in medicine. The digital micromirror device (DMD), shown in Figure (1-5c), has more than a million tiny pixel-

mirrors that can rotate 108° and more than 1000 times/second. This MEMS technique is widely used for displays in PC projectors and high definition televisions (HDTV). The optical MEMS switch is another type of applications of MEMS, which can be used to control and switch optical signals directly. An optical MEMS switch has many advantages because it avoids the difficulty of changing electrical signals to optical signals, and vice versa, when transferring or receiving data (Papadimitriou et al., 2003). The DMD that are manufactured by Agere Systems are a good example of Optical MEMS that consists of a vast number of microscopic mirrors, as shown in Figure (1-5d).

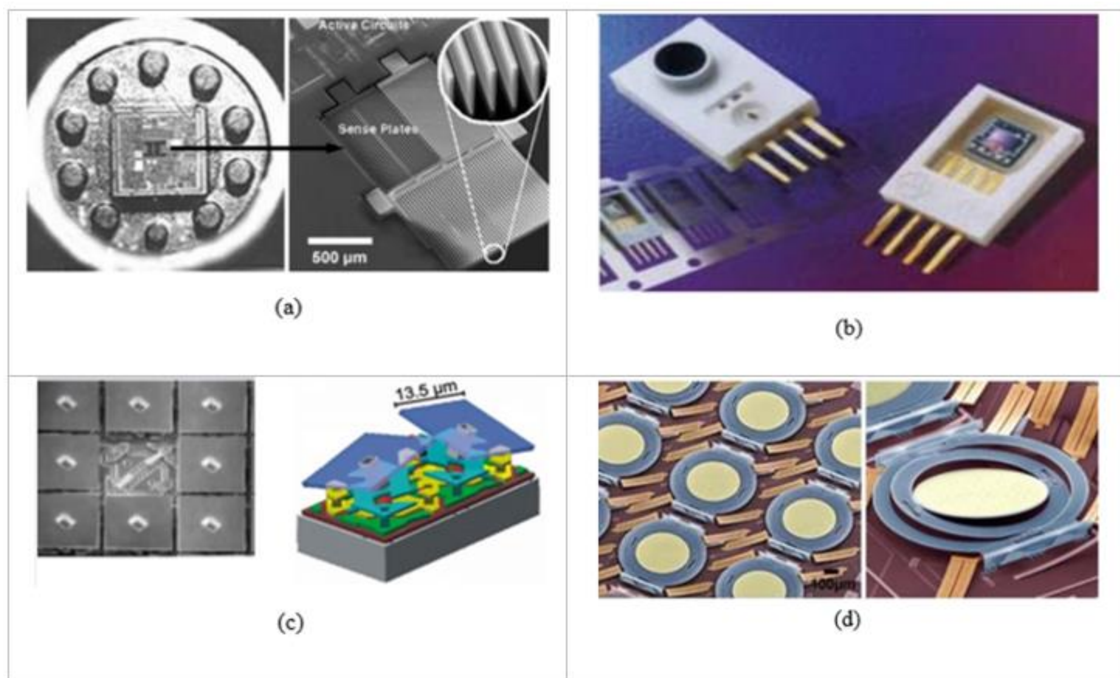

Figure 1-5 Examples of Si-based MEMS applications. (a) The first accelerometer used for air bag deployment, (b) Disposable blood pressure sensor, (c) Schematic of a DMD, and (d) an optical MEMS switch that consists of a microscopic mirror (Madou,2002)

Many other MEMS applications have recently been introduced, including a pressure sensor, inertia sensor, microfluidics/bio-MEMS, optical MEMS, RF MEMS and others (Maboudian, 1998, Leang and Taylor, 2008, Madou, 2002).

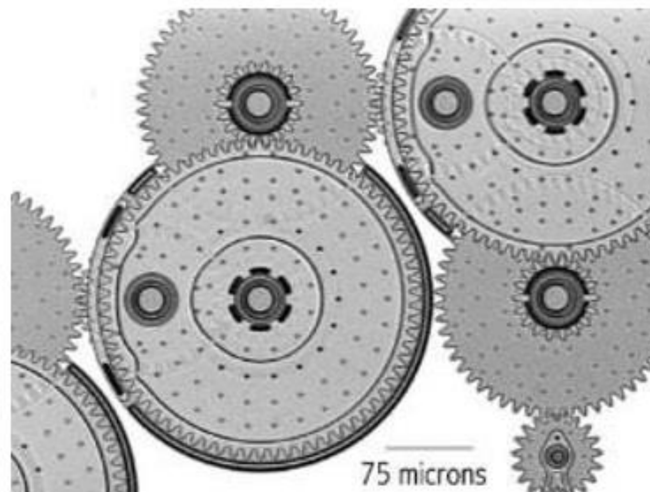

Figure 1-6 Complex micro system with a large number of sliding contacts between the gear teeth (Maboudian 2002)

MEMS typically contain different types of micro and nanoelements, such as microgears, cantilevers, and drive combs, and these elements are responsible for torque and load transmission. In this research, the main focus will be on the microgear elements in MEMS. Figures (1-6) and (1-7) show a number of microgear MEMS that have been produced by Sandia National laboratory.

There are various kinds of MEMS and nanoelectromechanical systems (NEMS), and different measurement tools used in the fabrication of micro/nanoassembly of micro or nanosystems (Leang and Taylor, 2008). Microfabrication technology can be used to manufacture micro/nano tools for the production of integrated MEMS systems. Because of their low cost and small size, as well as their fast response and flexibility in the integrated systems, they are widely used in nano and micro applications (Liu et al., 2007, Dong and Nelson, 2007).

Figure 1-7 MEMS gears sliding interfaces. (Carpick et al., 2002)

The key aspect of MEMS is miniaturisation. Since the second half of the twentieth century, minuturisation has played a vital role in engineering, which is expected to become even more important in future MEMS applications (Zesch et al., 1997). MEMS has been considered not only for the scientific and industrial products but also for some commercial products, including MEMS accelerometers (see, for example, Chau and Sulouff, 1998, Zhou et al., 2012), gyroscopic MEMS (Bernstein et al., 1993), micromachined optical MEMS switches (Yeow, 2001), and other different medical micromachined devices (Cao, 2001). MEMS are also very useful in the assembly of micromachines.

Serious challenges have been faced by MEMS and NEMS applications in different fields. One of the significant issues faced by such a tiny system is adhesion. At the nanoscale, the effects of surface roughness and the underlying physical phenomena, such as adhesion, can be such strong factors that they will not allow microdevices to work at all or maybe greatly limit the reliability of MEMS devices (see, for example, Maboudian, 1997 and 2002). Researchers have worked on a large number of models to describe the contact issues, with or without adhesion effect. The classical contact theories such as

Johnson, Kendall and Roberts (JKR) or Derjaguin, Muller and Toporov (DMT) were implemented in these models in different ways (see Borodich, 2014 for references and a discussion about the models). The inspiration to produce some of these models came from animals or insects such as the gecko, flies, and beetles (see, for example, Scherge and Gorb, 2001, Borodich and Savencu, 2017).

1.4 MEMS and Surface Topography Effects

Topography, or surface roughness, is one of the most crucial matters not only in the working and manufacturing fields related to silicon based-MEMS but also in all fields of mechanical contact. Bowden and Tabor (1956) discussed the surface topography in dry contact between two solid surfaces. They said that all surfaces are rough, even in the atomic scale, and that contact only occurs between the tips of the asperities when they have been placed in contact and, therefore, the real contact area is smaller than the nominal area.

Until the 1990s, the surface roughness measurements of the surfaces were tested with a contact stylus profilometer (Whitehouse et al., 1974). This method of testing had a number of limitations, such as the size of the tip, the high load applied and the low magnification in the plane. In addition, it may cause scratching or damage the real surface topography because of the finite dimension of the stylus tip (Vorburger and Raja, 1990). The measurement results of the stylus profilometer are complex and need to be clarified. Therefore, a new technique of filtering the surface was implemented by Raja et al. (2002) to remove the different wavelength components and then to produce a clear 2D roughness profile, as illustrated in Figure (1-8).

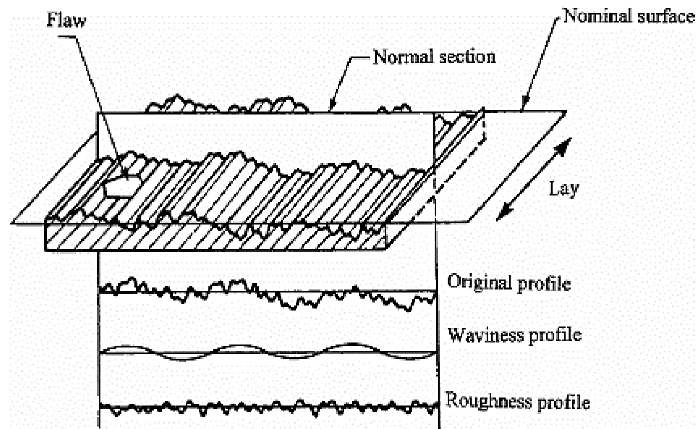

Figure 1-8 Filtering of roughness and waviness in a surface (Raja et al., 2002)

In MEMS and the micromachined devices, the effect of the surface roughness could significantly reduce the reliability, durability and repeatability of micro/nano elements in MEMS, which finally leads to structure collapse or mechanism failure (Maboudian, 2002). Therefore, to ensure measurements that are more accurate on such a small scale, atomic force microscopy (AFM) has been developed to obtain a 3D image of the tested material surface at the molecular scale.

1.5 Non-Optical Surface Topography Measurements Tools

The tools and the methods of surface topography measurements change depending on the size of the specimen and the purpose of the measurement. Each device has some limitations and the assumptions made when it works make this device suitable for some case and not for others, mainly and according to how precise a measurement is required. There are two types of non-optical instruments for such measurements, AFM and the stylus profilometer. Stylus profilometers are more appropriate for manufacturing settings where disturbances exist on the tested surface. Both AFM and stylus profilometers, can be used to measure surface topography. The AFM provides a better resolution than the

stylus profilometer especially when surfaces are well-characterised and no high irregularities, such as particles, pits, scratches, and contamination layers on the surface (see, for example, Poon and Bhushan, 1995). Stylus profilometers do not need any requirements or assumption be made about the sample. A probe is used which is in direct contact with the surface and follows height variations as a sample is moved. The height variations are then converted into electrical signals to produce the profile. In this study the AFM has been used to test the silicon surface roughness.

1.5.1 Atomic Force Microscopy

AFM has typically been used to test the topography structure of surfaces by measuring the force between a sharp tip and the surface of interest (Binnig et al., 1986). AFM is used to provide information about a surface by interpreting the light reflected off the cantilever surface. It can provide a better resolution than the stylus profilometer. The AFM device has a microscale cantilever manufactured by particular micromachining techniques. It is contained in a very sharp pyramid/cone-shaped tip that exists at the end of this cantilever (see Figure 1-9b). Many studies have been conducted in this field to explain the measurement process of ultra-small forces between particles.

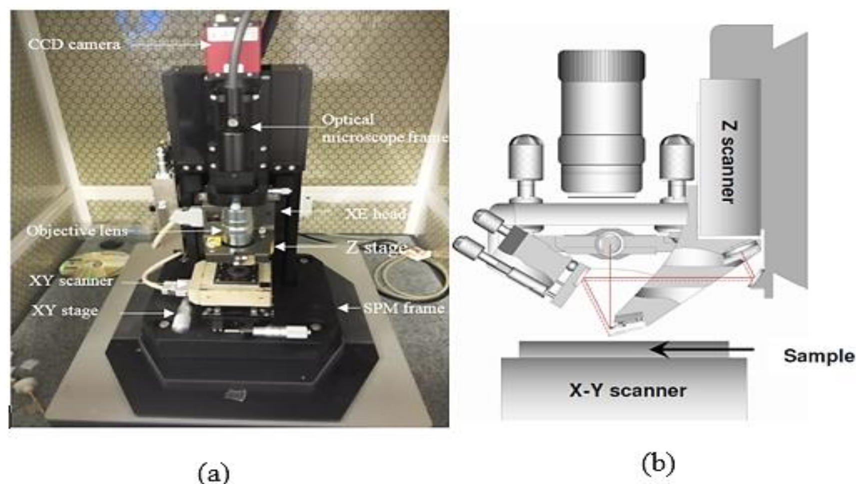

Figure 1-9 (a) Park XE-100 AFM device, (b) cantilever and Z-scanner of AFM (XE-100 standard)

AFM images can be obtained by measurement of the force on a sharp tip at the end of the cantilever (insulating or not) produced by the proximity to the sample surface. This force is kept small and at a constant level with a feedback mechanism. If this tip is moved sideways it will follow the surface contours as the trace *B* contour in Figure (1-10), therefore, the roughness profile for specimen can be obtained.

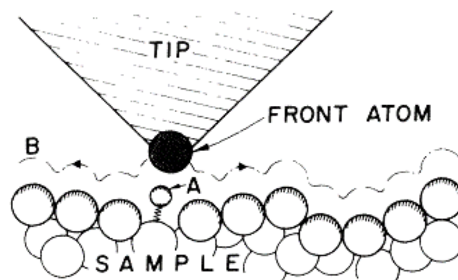

Figure 1-10 Illustration of the principle of an AFM (Binnig et al., 1986)

In addition to that, as shown in Figure (1-11), the AFM cantilever probe can be used for nanomachining, but in this case, the force applied by the tip must be large enough to produce a plastic deformation on the surface of the specimen (see e.g. Brousseau, et al., 2015, Al-Musawi et al., 2016).

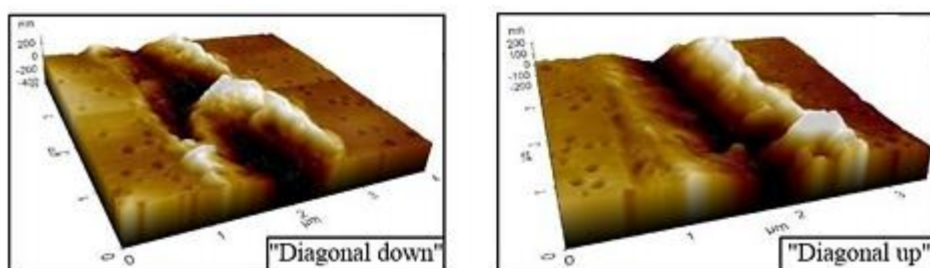

Figure 1-11 Nanomachining of grooves using AFM (Brousseau et al., 2015)

In the current study, the AFM Park systems XE-100 device (as shown in Figure 1-9a) has been used to obtain the silicon roughness profile. This technique provide us the nanoscale roughness of the silicon sample (more details in section 4.2.1).

1.6 Main Problems and Challenges in MEMS Microgear

Silicon based-MEMS structures in manufacturing and applications should be considered to be as important as the performance of the device. Theoretically, the structure of MEMS devices has to be designed to be as sensitive as desired and manufactured in a robust way. Otherwise, these MEMS will be classified as useless devices (see Sitte, 2016). Challenges such as stiction, friction, reliability, packaging, stability of device structure, and the characteristics of the MEMS material, are very important issues that should be studied and understood carefully. In addition, high aspect ratio technologies have created new challenges in manufacturing and controlling processes (Gad-El-Hak, 2002 and 2006). Reducing the size of MEMS elements has forced us to deal with the surface topography and the roughness of these elements. There is a strong relation between MEMS performance and surface roughness, especially when the elements are in contact. Reducing the contact area between MEMS elements by surface nanostructuring can lead to a reduction in the vdW forces, which means that there is a decrease of adhesion forces. Carpick et al. (2002) found that surface imaging at the nanoscale should be integrated with contact asperity modelling to get the best expectations of surface topography, which make parameters such as adhesion, friction and wear at their minimum values when the surfaces of MEMS are designed. Shukla (2002) referred to humidity as one of the most important issues on the performance of nano/micro scale devices because of the stiction caused by creating meniscus hence, he suggests these devices should work in a dry environment to avoid capillary force and reduce stiction phenomenon.

1.6.1 Adhesion and Stiction

As it has been noted by Borodich et al. (2014), the term "adhesion" may have rather different meanings, including occurrence of the strong chemical bonds between surfaces (this is cohesion if materials are the same) and weak connections due to vdW forces. In addition, contact problems with non-slipping boundary conditions are often called adhesive contact problems. Typically, it is accepted that adhesion is caused by molecular vdW forces; electrostatic forces and direct metallic contact (see Komvopoulos, 1996, Serry et al., 1998, Zhao et al., 2003).

It is known that when object sizes decrease to the micro/nanoscale, some physical phenomena such as inter-molecular adhesion and many other surface effects become significant (see Komvopoulos, 1996, Li, 2010, Dejeu etal., 2011, Ramakrishna etal., 2013). Although MEMS devices face many challenges, stiction is one of the most harmful effects in MEMS. According to Gad-El-Hak (2002 and 2006), stiction refers to two different situations: releasing and in-use stiction. He defined *the release stiction* as the irreversible stick of some elements of the construction of moveable microdevices; while, *in-use stiction* is defined as the permanent adhesion of elements of a moveable structure during the operation of microdevices. Here we study only in-use stiction and, therefore, we refer to it further as stiction.

Stiction could extremely restrict the movement of microdevices or it could greatly limit the reliability of the MEMS devices (see, for example, Maboudian et al., 2002). The effects of stiction, adhesion and surface topography at such tiny scales can be significant and can become the greatest barrier to obtaining sufficient reliability for commercial MEMS applications in many different fields (Kim, et al., 2010). Thus, it has been stated by many researchers that stiction represents one of the greatest challenges and it is a

serious problem of micromachined systems, especially at the micro/nanoscale (Tanner, 2009, Tiwari and Raj, 2015). Stiction causes a restriction or highly limited reliability of microdevice equipment (see, for example, Tas, et al., 1996, Mastrangelo and Hsu, 1993). The stiction phenomena in micromachined devices due to the capillary forces have been described by Komvopoulos (1996), as shown in Figure (1-12); however, this is not related to the current work due to vacuum environment and hence, we focus on the chemical interaction between the counterpart surfaces. This phenomenon was also studied by Goryacheva and Makhovskaya (2001 and 2008) see also Myshkin et al, (1998).

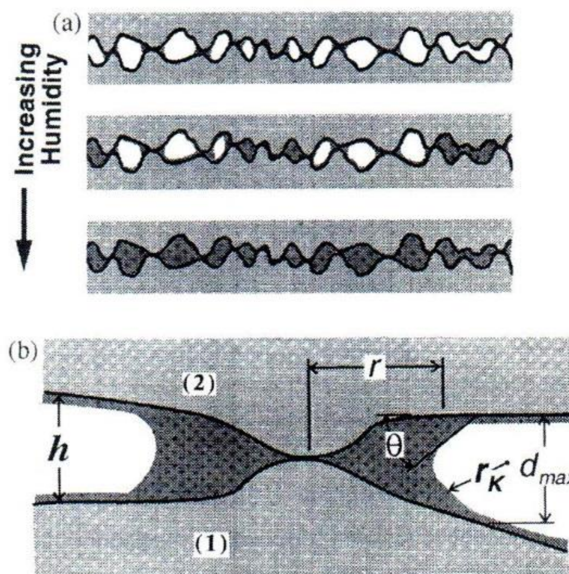

Figure 1-12 Stiction between two rough surfaces due to capillary phenomena (Komvopoulos, 1996)

Several studies have revealed the difference between the nominal area and the actual area of contact, and their influence on the behaviour of friction and adhesion (see Komvopoulos, 1996, Karpenko and Akay, 2001). For example, Komvopoulos (1996) has explained that adhesion occurs when two surfaces come into contact; therefore, the counterpart micro and nano-asperities on the surfaces touch each other in many small

spots, but there are still gaps between the surfaces where they do not touch each other. Figure (1-13), which is modified from (Johnson, 1985 and Goryacheva, 1998) shows the difference between the real contact areas between the two surfaces.

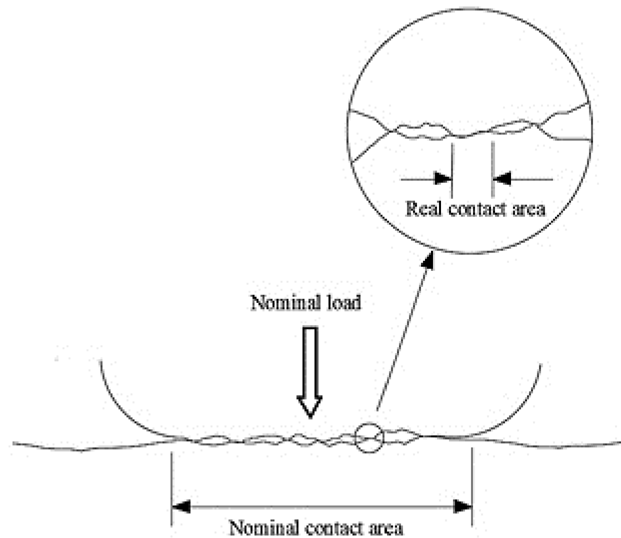

Figure 1-13 Schematic of two rough surfaces in contact and corresponding contact areas (modified from Johnson, 1985 and Goryacheva, 1998)

Studying the relative motion between the two contact surfaces, Savencu and Borodich (2014), Savencu (2016), and Borodich and Savencu (2017) developed a model assuming that both the adhesion force and deformation of asperities in the contact area contribute to the resulting friction force. Figure (1-14) shows the friction force between two surfaces with respect to tangential force and time, then it shows the magnitude of tangential force required to start the motion, which is larger than the force needed to keep the motion. The high tangential force, which is required to initiate sliding to beat the high static friction or stiction, represents the threshold of sliding motion between the surfaces.

Kuhlmann-Wilsdorf (1996) found that when the contacting surfaces have a large number of contact spots per unit area, these tiny contacts would undergo only elastic deformation

without any plastic yielding (Kuhlmann-Wilsdorf 1996). Studying the behaviour of the contact surfaces with multi spots contact, Polonsky and Keer (1996a and 1996b) argued that in the case of a very small micro contact, the behaviour of contact spots becomes purely elastic. Due to their statement, it will be assumed that asperities at the atomic and adhesive subscales deform only elastically, i.e. there is no plastic deformation at the scales. This assumption was also accepted by Savencu (2016).

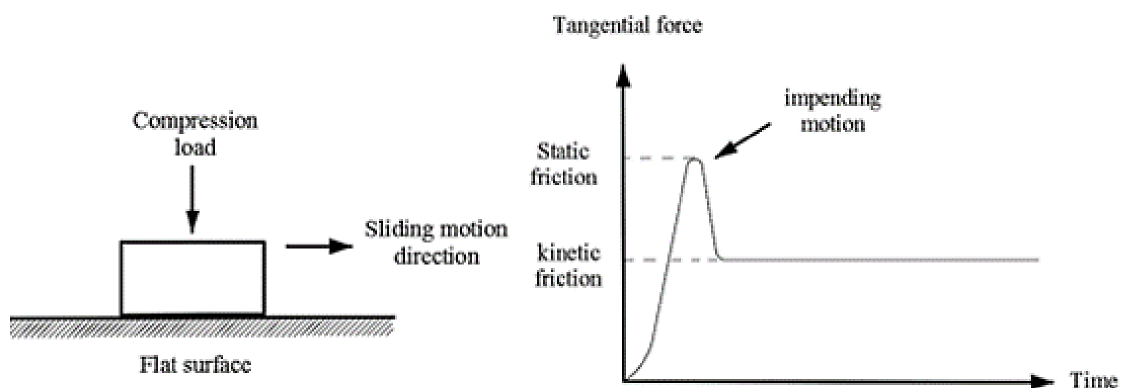

Figure 1-14 (a) Slider on a flat surface under action of a normal compression and (b) the corresponding tangential force vs time (adapted from Kragelsky et al., 1982).

If humidity is considered then stiction can occur due to meniscus and capillary effects. These effects are out the scope of the thesis because only friction in the vacuum enviroment is considered. Therefore, it is assumed that stiction may occur only due to cohesion or so-called cold welding, and when it happens the surface appears as a welded or strong joint.

The failure in MEMS due to adhesion arises when at least one element or more is very sensitive to surface forces, such as capillary and vdW forces because this element is weak and very close to the substrate, and so sticks to the substrate. A failure like this effects the production and reliability of MEMS according to Mastrangelo (1997).

Adhesion occurs between two dry solid surfaces when they come into contact or even when there is a thin layer of liquid between them during the contact. However, stiction occurs when the surfaces are clean and smooth, all the chemical films and adsorbents should be removed. Many types of measurements, techniques and methods are used to decrease or eliminate the stiction in NEMS, MEMS and other nano/microscale devices. Bhushan (2008) said that stiction might be reduced by controlling some parameters such as water adsorption and meniscus formation during sliding and that its changes, viscosity, and also he shows that surface roughness properties have a significant effect on the stiction and adhesion. At the micro/nanoscale, adhesion forces have an important impact and this makes the quick, accurate release of tiny objects difficult, and pick and place manipulation challenging. Zhang et al. (2010) developed an efficient pick-and-place technique using a new MEMS microgripper that combines both gripping and release mechanisms. This technique was used to manipulate a particle with the diameter of 7.5–10.9µm. A plunger was used to give the particle sufficient momentum to overcome the adhesion force. However, Zhang et al. (2010) completely ignored the effects of the chemical bonds and they gave all of their attention to the adhesion forces.

Roughening, coating the surface and using new materials in the manufacturing of microdevices are also used to reduce the effects of adhesion and friction, depending on the deposition of monolayers produced to avoid stiction between surfaces (Ashurst et al., 2003). In MEMS devices, there is a range of surface roughness varying from an atomically smooth surface, as in a polished silicon wafer, to the rough surface of deposited polysilicon. From stiction and wafer bonding experiments, it is known that the attractive adhesive forces between contacting surfaces can be decreased by increasing the surface roughness (Tas, et al., 2000). Several scales of surface roughness are investigated

representing polished and deposited polysilicon films are found in MEMS. The sub-boundary lubrication adhesion model reveals the significance of the surface roughness on the adhesion and pull-off forces as the surfaces become smoother (Suh, 2003).

1.6.2 Contact, Friction and Stiction at the Small-scale

When two surfaces come into contact, they will both experience some distortion. Deformations may be purely elastic or it may contain some additional plastic deformations and changes in shape. At the microscale there is no real surface which can be correctly smooth, such as either a roller or race. It follows that when these two solid bodies contact each other, they will initially touch at some distinct points or asperities. Deformation in a surface occurs in or near the areas of actual contact.

Tribology has been an interesting subject of scientific and engineering studies since ancient times. The basic law of friction in mechanics is empirical formulae that inexplicitly established by da Vinci in 1508. In 1699, by using an extremely primitive polishing element in which the pressure of the lens on a plate has established by means of a curved flexible element, the French physicist Amontons presented three friction laws. The formulations of the Amontons laws were also presented by Kragelsky et al. (1982) as:

- The polishing force is independent of the dimensions of the lens.
- The polishing force is proportional to the applied force.
- The ratio of these forces is independent of the combination of tool and component material and under boundary lubrication conditions is 0.3.

Thus, according to Amontons, friction is proportional to the weight of the slider and it is independent of the contact area between the contacting surfaces. The third 'law' is in fact

not correct. Indeed, Kotelnikov (1774), who was one of the eight former students of L. Euler, introduced the notion of coefficient of friction μ, and presented the law as a formula. This is the so-called Amontons-Kotelnikov law

$$F = \mu P \tag{1-1}$$

"*If the friction content F to the mentioned force P one puts as unknown that is equal to μ: 1 then the friction will be $F = \mu P$*" (Kotelnikov 1774).

Here and henceforth we say the Amontons laws for descriptive formulations of the friction laws, while we say the Amontons-Kotelnikov law for the formula (1-1). This formula simply states that the resistance to relative displacement is proportional to the normal force between the two surfaces in contact and is not related to the visible area of contact. Often this law is wrongly attributed to Coulomb (1778). In fact, Coulomb proposed the two-term formula

$$F = A + \mu P \tag{1-2}$$

where A is a constant. Hence, he generalised Amontons law by introducing a constant term A, that was later connected with the adhesion effects on the surface.

Coulomb regarded the Amontons law of friction as just an approximation and researchers have accepted his view of the law since that time. In 1785, Coulomb set out to investigate the effects of the load on both the area and the time of contact on the dry frictional resistance of a broad range of material combinations.

By the influence of Tomlinson model (1929), Derjaguin (1934a, c) has developed a molecular theory of friction and this theory led to the binomial friction law, which gave molecular meaning to Coulomb's term A. He wrote his formula as follows:

$$F_f = \mu(P + P_o) \tag{1-3}$$

where μ is the friction coefficient according to Derjaguin and P is the external normal load, and P_o is the normal load due to adhesion. This equation also can written as

$$F_f = \mu(P + Sp_o) \tag{1-4}$$

where S is the true contact area of the interacting surfaces and p_o is the specific molecular attractive force. Hence, the term $A = \mu Sp_o$ represents the tangential component of the force of molecular interactions. According to his law of friction (1-4), Derjaguin (1934a, c) suggested distinguishing between the true friction coefficient μ_t and the apparent friction coefficient μ_a , where:

$$\mu_a = \frac{F_f}{P} \tag{1-5}$$

Currently, it is common to present the total friction force F_f as the sum of the mechanical or deformational $F_{f,mech}$ and molecular friction forces $F_{f,mol}$.

$$F_f = F_{f,mech} + F_{f,mol} \tag{1-6}$$

Let us discuss now the physical sources of the Amontons law. Motivated by the Tomlinson model, Davidenkov suggested to Zhuravlev that he perform research to explain the Amontons-Kotelnikov law of friction. In 1940, Zhuravlev presented a statistical model to justify Amontons law. This model will be discussed in the next section.

A sufficient knowledge in the field of contact and friction behaviour at multi-scales is required to be able to design high-reliability MEMS components, especially with sliding contact surfaces. In macroscale devices, friction force F_f could be modelled according to

Amontons friction law (1-1). Actually this law stops to describe the experiments as the dimensions go to the micro and nano scales. The effect of the surface topography and the surface forces, such as stiction and adhesion, will be significant at micro and nanoscale. This effect changes the frictional behaviour of the MEMS surfaces. It also reduces the reliability of MEMS, or entirely or partially restrict the element's movement (Tanner, 2009, Maboudian et al., 2002, Carpick et al., 2002 and 1997, Li 2010, Jackson, 2011, Ramakrishna et al., 2013).

1.6.3 Multi-asperity Contact

A large number of researchers have studied the topography of surface roughness and its effects on the single and multi-asperity contact using different techniques and simplifications.

Prandtl (1928) and Tomlinson (1929) argued on importance of adhesion for understanding friction phenomenon (Popov and Gray, 2012). In 1940, Zhuravlev was the first researcher to produce the statistical structure of the contact between rough surfaces.

Zhuravlev's model is the first multi-scale model to have been produced in the field of statistical contact between rough surfaces. Zhuravlev (1940) published his results in the Russian language, his paper was translated and published in English by Borodich only in 2007. However, Zhuravlev's model was discussed by (Johnson, 1975, Greenwood, 1990, Adams and Nosonovsky, 2000). It is also described in an English version of a book that was published by Kragelsky et al. (1982). Zhuravlev assumed that contact occurred between spherical protuberances with the same radius and different heights. He also assumed that the protuberances at a particular level increases as the level become smaller and smaller (see Figure 1-15).

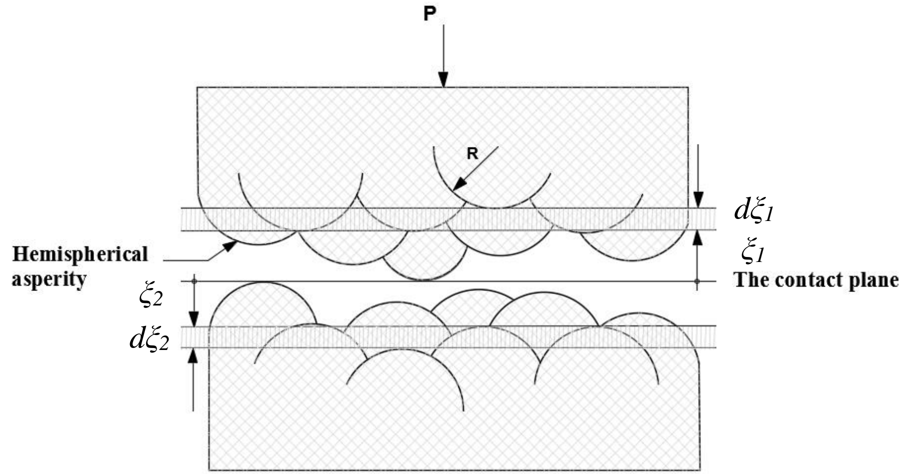

Figure 1-15 Zhuravlev's model (1940), showing the contact between spherical protuberances of the same radius and with different heights

Zhuravlev denoted the distribution of the protuberance summits at various levels for an element of a rough surface as

$$n = n(\xi) \tag{1-7}$$

Then $dn = n(\xi)d\xi$ is the number of summits situated in the layer $d\xi$ at depth ξ. The total number of protuberance summits situated at various levels of the surface element from the highest summit to the level of depth x, is

$$N = \int_0^x n(\xi)d\xi \tag{1-8}$$

Within the framework of his model, Zhuravlev obtained the following general expression for the compressing force P

$$P = \frac{\sqrt{2R}}{\pi}\int_0^{x/2}\int_0^{x/2}[x-(\xi_1+\xi_2)]^{3/2}\,\frac{n(\xi_1)n(\xi_2)d\xi_1 d\xi_2}{3kN} \tag{1-9}$$

where $k = (1-\nu^2)/\pi E$, ν is the Poisson's ratio and E is the Young's elastic modulus of the material. Therefore the actual contact area S is

$$S = \pi R \int_0^{\frac{x}{2}} \int_0^{\frac{x}{2}} [x - (\xi_1 + \xi_2)] \frac{n(\xi_1) n(\xi_2) d\xi_1 d\xi_2}{2N} \tag{1-10}$$

Zhuravlev (1940) assumed that the total number of molecular contacts between both contacting surfaces was proportional to the actual contact area and therefore, there is a proportional relationship between friction force and the actual contact area

$$F_f = \alpha S \tag{1-11}$$

where α is a coefficient depending on the cohesive forces. In the above equation, Zhuravlev gives a mathematical expression to illustrate the proportional relationship between the frictional force and the actual contact area. Hence, the friction force F_f is

$$F_f = \alpha \pi R \int_0^{\frac{x}{2}} \int_0^{\frac{x}{2}} [x - (\xi_1 + \xi_2)] \frac{n(\xi_1) n(\xi_2) d\xi_1 d\xi_2}{2N} \tag{1-12}$$

For receiving a simple analytical expression, Zhuravlev suggested in the first instance to approximate the height distribution as a linear function, i.e.

$$n(\xi) = \beta \xi, \tag{1-13}$$

where β is a proportionality coefficient. Then he showed that

$$F_f \sim P^{10/11} \tag{1-14}$$

That is very close to the linear law, and, therefore, he provided a simple explanation of the Amontons law.

1.6.4 The Greenwood-Williamson Models

In 1966, Greenwood and Williamson published a similar statistical model. They assumed in this model that the rough surfaces are represented as collections of spherical elastic

asperities and that all contacts occurred in the peaks of the asperities in the same geometry shape and with the same average radius of curvature (see Figure 1-16).

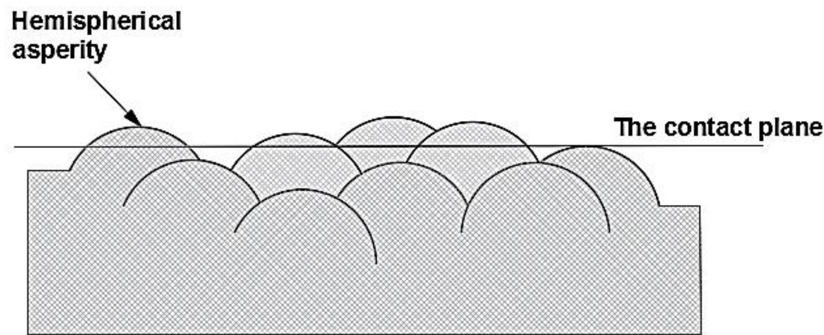

Figure 1-16 Greenwood and Williamson's model

Although, this model has the same main assumptions as the Zhuravlev model, they considered other laws for summits distributions. Zhuravlev considered the linear distribution of the summit of the asperities in the contact region, while in Greenwood and Williamson's model assumes an exponential distribution of the summits of the asperities.

In addition, they considered the elastoplastic transition of protuberances (Greenwood and Williamson 1966). Other researchers have tried to modify the GW model by applying a different radius of curvatures, such as Bush et al. (1979) and McCool (1986).

1.7 Multiscale Properties of Surfaces and Fractal Models

A number of models have also described roughness at the small scales to determine the real contact area. They tried to show that roughness at the small-scale is geometrically similar to roughness at the large-scale, of course taking into account the difference in dimensions of length and height. The best example of this is Archard's model (1957).

1.7.1 Archard's Model

Archard (1957) introduced a model similar to Zhuravlev's model but included a multilayer of protuberances. In other words, a hierarchical surface model of contact consists of multiple asperity layers of protuberances or asperities (see Figure 1-17). Asperities of roughness were given in different scales to give separate radii values. The single contact between the contacting surfaces has been described by the classical Hertz theory of contact. The relation between the friction force F and normal force N has been calculated using varying parameters to model the surface. Archard's model did not show the variety of scale roughness and, therefore, it is not a multiscale structure. This was clear when it used the elastic deformation of asperity as the only physical contact mechanism.

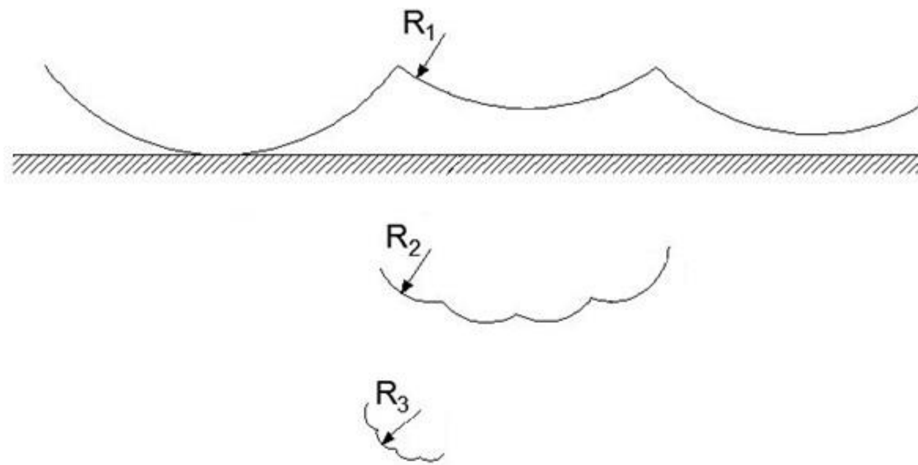

Figure 1-17 Archard model of contact (Archard, 1957)

Archard (1957) developed his model to study the contact of rough surfaces by using hemispherical asperities layers that are arranged as arrays. In this model, each layer of hemispherical asperities has been covered with a set of asperities that are similar in shape and smaller than the previous set, as illustrated in Figure (1-18). Archard (1957) explained that there is a proportional relationship between the real area of contact and the

normal compressive force. In this model, Archard showed that adhesion is the main parameter that causes friction between sliding surfaces. Adhesion occurs between the summits of the asperities in the counterpart. When the tips of the surfaces are in contact and they form junctions, the actual area of contact, as opposed to the apparent contact area, consists of the junctions and the region in-between them. In the area where there is a real contact between surfaces, the interatomic forces work to weld the summits of the asperities together. The welded asperities are sheared due to the sliding motion; therefore, the weld points will break and the tips of the asperities start a new contact with a different point.

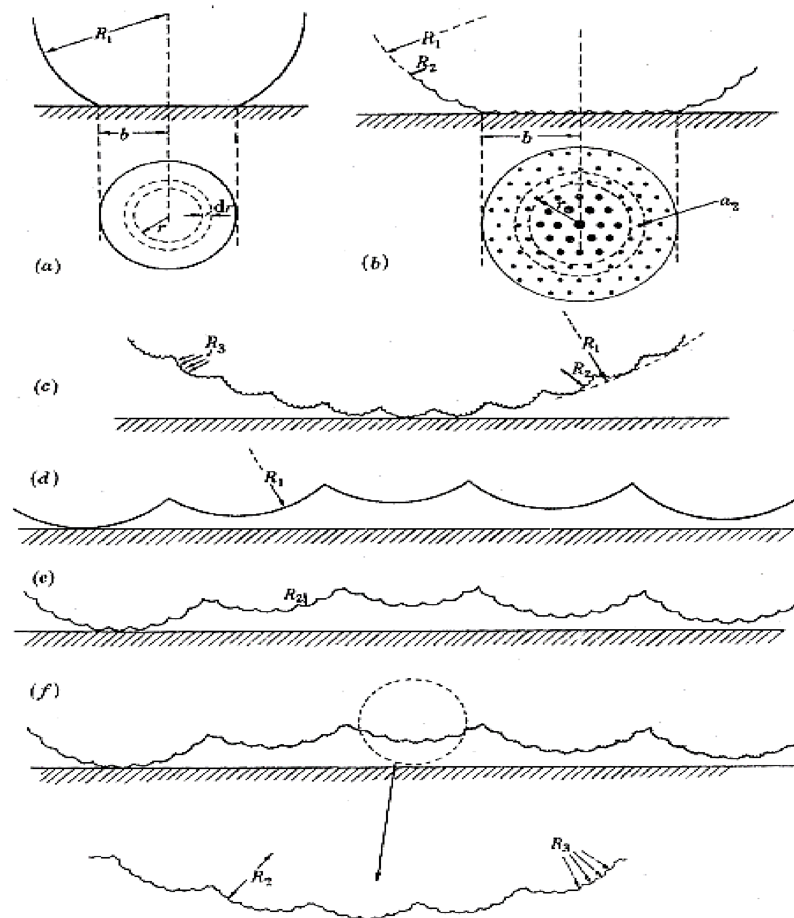

Figure 1-18 Archard approximation model (a-b) contact surface under load and in (c-f) without any load (Archard, 1957).

The proportionality between the total real area of contact and the load behaviour is asymptotically linear as the number of layers is increased, even if the fundamental of contact at a single real contact problem is non-linear. In 1992, Borodich and Mosolov found that Archard's model is not a self-similar fractal construction due to the number of overlapping regions. However, the hierarchy of protuberances is a very good addition and it could be employed in the description of the surface roughness. Borodich and Galanov (2002) also concluded that the assumptions used in Archard's model are not accurate in their numerical simulations of smooth PH-punch contact problems.

1.7.2 Fractal Models

In 1990, Majumdar and Bhushan claimed that physical rough surfaces may be characterised by the fractal Weierstrass–Mandelbrot (WM) function:

$$z(x) = G^{(D-1)} \sum_{n=n_1}^{\infty} \frac{\cos 2\pi\, \gamma^n x}{\gamma^{(2-D)n}} \quad ; 1 < D < 2\, ; \;\; \gamma > 1 \tag{1-15}$$

where G is representing the scaling constant, D is the fractal dimension (FD), n is the number of added waves, n_1 is the cut-off frequency got by $log\, \gamma\, (1/L)$ and γ is the scaling ratio determining the spectral density. The roughness parameter D can be obtained from the power spectrum of the surface, and G is taken according to the amplitude of the surface roughness. They claimed that this formula represents all main features of the actual contacting rough surfaces.

Based on the above description, Majumdar and Bhushan (1991) produced the M-B model of elastic–plastic contact of rough surfaces. They argued that contact problems for a real surface are equivalent to the contact problems for the profile of the WM function having

the same power spectrum as the surface or having the same FD. However, the model was criticized by Borodich (2005). The criticism was based on the results of the following papers: Borodich (1993) and Borodich and Onishchenko (1993), where detailed analyses of two different fractal contact models were presented. In the former paper an analysis of a problem of contact between a fractal parametric homogeneous (PH) punch and a non-linear elastic half-space was presented (see also Borodich 1998a, b, Borodich and Galanov 2002). In the later paper, the Cantor-Borodich contact models were considered. It followed from the results of the above papers that FD alone cannot characterise the behaviour of contacting solids. After a careful analysis of the M-B model assumptions, Borodich (2005) concludes that the M-B model is not consistent. It does not give a procedure to solve the problem of contact either for a general fractal surface or for the fractal WM profile.

In 1991 Borodich introduced the so-called Cantor-Borodich profile (see in Figure 1-19) and suggested to use it for analytical studies of fractal contact models (see, e.g. Borodich and Mosolov 1991 and 1992). The Cantor-Borodich profile width is denoted as L_o, and then it is divided into three parts and the middle part of the model is removed. The main parameter that defines how the length after a division is related to the previous width is a ratio f_x and the heights have been scaled with a similar ratio f_z. Hence, the initial protrusion height is h_o and the other two have been left as protrusions on the sides (see Figure 1-19).

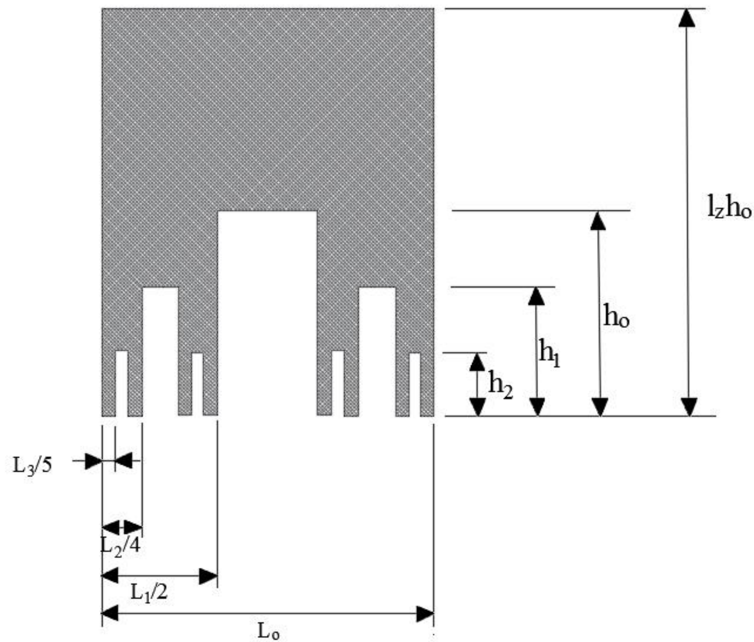

Figure 1-19 Fractal Cantor-Borodich profile (x-z plane) constructed from the Cantor set (Warren and Krajcinovic, 1995)

Warren and Krajcinovic (1995 and 1996) and Plesha and Ni (2001) used Cantor-Borodich profile as a basis for their fractal contact models (see in Figure 1-20). These protrusions have been divided into s segments and the middle part has been cut. Hence, s refers to the number of protrusions left on a section of a division. The fractal dimension D for a surface has the following formulae:

$$D = 1 + \frac{ln(s)}{ln(sf_x)} - \frac{ln(f_z)}{ln(sf_x)} \quad (1\text{-}16)$$

The second term on the right-hand side of formulae, $ln(s)/ln\,(sf_x)$, defines the fractal dimension D_c of the Cantor set.

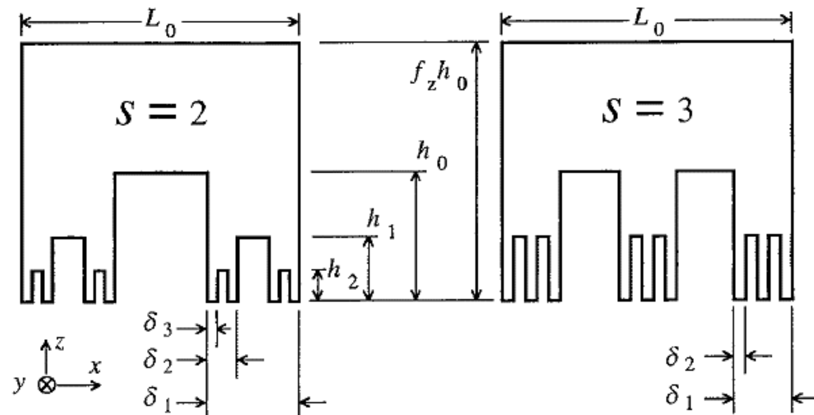

Figure 1-20 Fractal Cantor-Borodich profile (s=2) and its generalization by Warren and Krajcinovic (1995) according to Plesha and Ni (2001).

Borodich and Onishchenko (1993) used a fractal Cantor-Borodich model to illustrate their contact model, as shown in Figure (1-21).

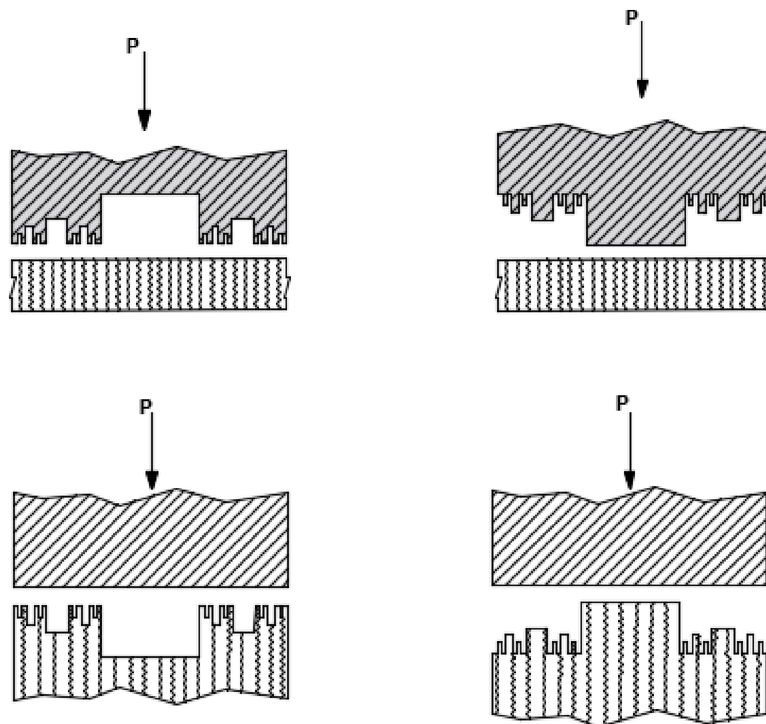

Figure 1-21 Borodich and Onishchenko (1993) hierarchical multilevel profiles contacting a Winkler elastic foundation

Based on the results obtained by Borodich and Onishchenko (1993, 1999) and Borodich (1993), Borodich (2002) wrote: "*the fractal dimension alone cannot characterise the features of contact*" and he then added, "*The problems for elastic rough surfaces cannot be solved using just geometrical arguments and equations of elasticity should be involved*".

Jackson and Streator (2006) agreed with the above arguments by Borodich (2002). They added that these models have assumed that the asperity is entirely flat. Hence, nothing is referring to the gradual increase in the deformation of the radius of curvature for asperities. A review of fractal contact models was given by Borodich (2013). A review of statistical, fractal and other methods for description of surface roughness was given by Borodich et al. (2016).

1.8 Anti-stiction Models for Surface Coating

Modelling of the coating, contact, wear and the damage due to fatigue in the elastic objects is needed to determine the stress distribution in these bodies. In the coated elastic bodies, the multilayer model of elastic half-space is usually used to calculate the contact features, such as the area of the contact and the pressure distribution over it, as well as the sub-stresses in the coating and substrate. The contact of an object with a multilayer elastic half-space surface has been explained by using the integral transforms, mainly the Fourier transform for the two-dimensional problems and Hankel transforms axisymmetric problems (see Goryacheva, 1998, Jackson and Streator, 2006). Other researchers have used the Finite Element Method (FEM) to solve the contact and wear problems, and they have also calculated the stresses for an elastic half-space layer in contact with a rough surface (Mesarovic and Fleck, 1999). On the other hand,

Komvopoulos and Gong (2007) have used FEM to solve two-dimensional plane-strain problem of a rigid and rough surface, which is sliding against an elastic coated surface, as shown in Figure (1-22). They assumed Coulomb law of friction between the rough surface and the coated surface. The contacting sliding surfaces are subjected to distributed normal pressure and tangential tractions, producing a total normal load P and a tangential, which is represented by friction force $F = \mu P$, where μ is the coefficient of friction.

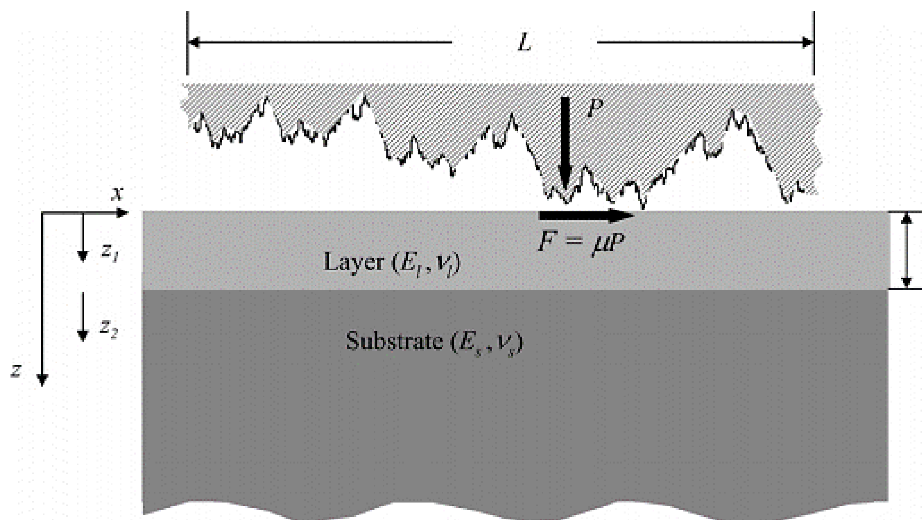

Figure 1-22 Schematic representation of an elastic coated surface in contact with a rigid rough surface (Komvopoulos and Gong, 2007)

Komvopoulos and Gong (2007) used FEM simulations to analyse the quasi-static indentation of a coated surface by a rigid cylindrical asperity, as shown in Figure (1-23). The meshes and nodes that are used in the simulations have accurately been described in this study, which consists of 19,232 nodes.

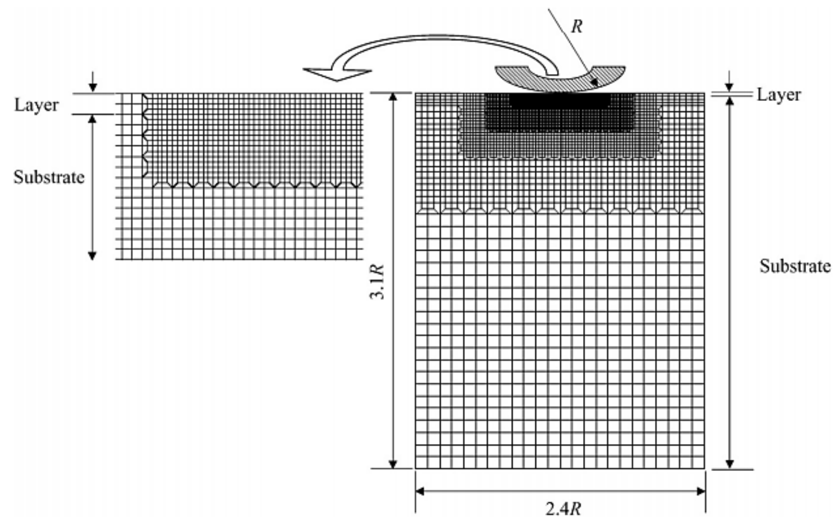

Figure 1-23 Finite element discretisation of an elastic coated surface. The refinement of the mesh at the surface is shown on the left-hand side (Komvopoulos and Gong, 2007)

These techniques use the analytical solution and assume some parameters in the calculations due to the complexity of the inverse integral transforms. The simplicity and the accuracy of the results make this method suitable for axisymmetric and two-dimensional problems. However, many researchers have preferred to use numerical analysis for complicated three-dimensional contact problems. The effect of the surface geometry parameters in the microscale on the performance of the contact pressure and sub-stresses in the coating layer joined to an elastic surface has been explained and analysed by Goryacheva and Torskaya (2003). In their investigation, these researchers studied contact in coated axisymmetric dies by using Hankel transform, and the localisation and superposition methods. They modelled surface roughness on a periodic system of indenters, as shown in Figure (1-24).

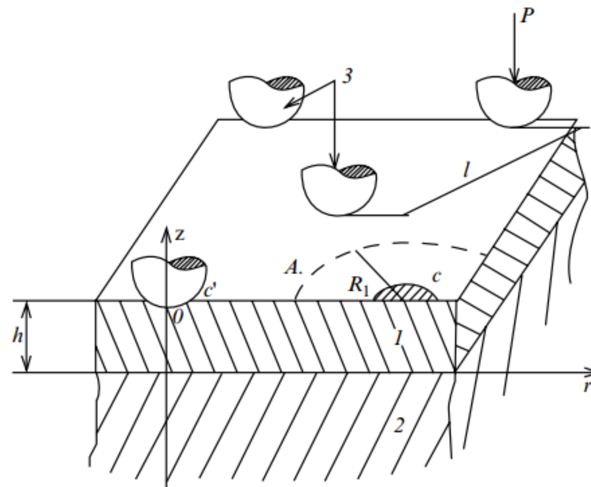

Figure 1-24 Contact of the periodic system of axisymmetric dies and an elastic layer adhered to an elastic substrate (Goryacheva and Torskaya, 2003)

The contact of real rough surface and coated bodies is numerically considered in Sainsot et al., (1990) Cai and Bhushan, (2007). The effect of friction on the distribution of internal stresses inside layered elastic half-space was studied in Torskaya and Goryacheva, (2003).

1.9 Classical Models of Adhesive Contact

The classic contact mechanics begins with Heinrich Hertz, who solved the contact problem between two elastic bodies with curved surfaces in 1880 (Johnson 1985) and his study has been published two years later (Hertz 1882a). Hertz contact model does not take into account the force of adhesion and it builds on the following assumptions: (i) the curvature radii of the contacting bodies and their dimensions are large compared to the radius of the contact area; (ii) small strains are assumed; (iii) the bodies are involved in frictionless contact; (iv) the surfaces of the bodies in contact are continuous and

nonconforming. The full description of assumptions and the mathematical formulation of the Hertz contact problem has been given by Borodich (2014).

Johnson-Kendall-Roberts (JKR) and Derjaguin-Muller-Toporov (DMT) have proposed famous theories, which describe the adhesive contact between surfaces. The JKR theory is applied with materials that have high surface energy and subjected to important elastic deformations when in contact. The JKR theory assumes strong, short-range adhesion forces that dominate the surface interactions. The effect of these interactions are included within the contact region. On the other hand, the DMT theory is applicable for materials with low surface energy, which resist deformation in contact. Therefore, adhesion forces are caused by weak, long-range attractive forces felt outside the contact area. The behavior of materials between the JKR and DMT extremes can be described by parameters such as Tabor's dimensionless parameter or the Maugis transition parameter (Shi and Zhao, 2004, Ramakrishna et al., 2013) . Figure (1-25) shows the interaction forces acting at different regions of the gradient substrate.

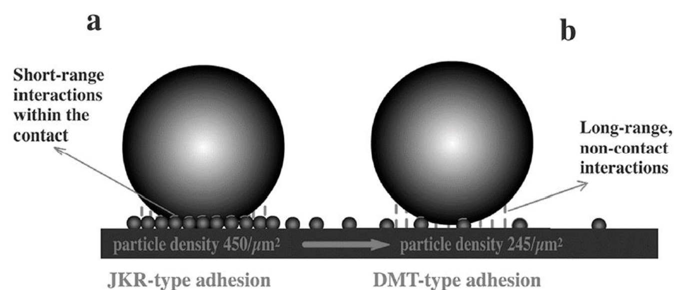

Figure 1-26 The interaction forces in the JKR and DMT theories (Ramakrishna 2013)

Figure (1-26) gives a description of surface forces in the Hertz, JKR, DMT and Maugis theories. It starts with the Hertz theory, which does not consider the adhesion in contact while the JKR model includes only the short-range adhesion in the contact zone. The

DMT theory shows longer-range forces which act outside the area of contact. Then the Maugis model assumes that adhesive interactions can be averaged over a square well potential (Carpick 2002 , Shi and Zhao, 2004).

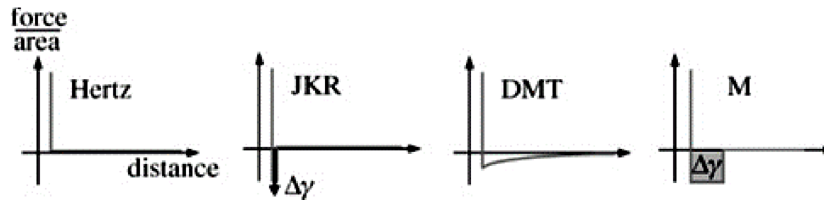

Figure 1-27 Description of surface forces in the Hertz, JKR, DMT and M theories. (Shi and Zhao, 2004)

The approach followed in this Thesis for the numerical calculations is to consider the pull-off force as the force of adhesion. Many studies have also employed the pull-off force in their calculations as adhesion force (see e.g. Gent and Kaang, 1986, Butt, 2005, Moore and Houston, 2010, Adams, 2014). Another clear example of using pull-off forces as adhesion forces has been studied experimentally between pharmaceutical particles with irregular geometry and rough polymeric surfaces using the atomic force microscope (Beach et al., 2002) see Figure (1-27). They have applied their model successfully to calculate pull-off forces (adhesion forces) depending on the model that was suggested by Rabinovich et al. (2000a, 2000b).

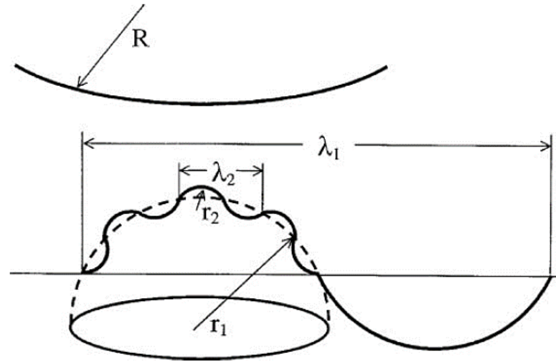

Figure.1-28 Multiscale model of roughness (Beach et al., 2002)

$$F_{pull-off} = \frac{AR}{h_o^2}\left[\frac{1}{1 + R/(1.48 \times RMS)} + \frac{1}{(1 + 1.48 \times RMS/h_o)^2}\right] \quad (1\text{-}17)$$

Rabinovich model has been originally developed from a simple theoretical model introduced by Rumpf (see Rumpf and Bull, 1990) to describe the effect of surface roughness on adhesion. Rumpf model shows the force between a spherical particle and a surface with a small hemispherical asperity centred below the particle. The interaction force in the Rumpf model is given by

$$F_{ad} = \frac{A_H R}{6D_o}\left[\frac{r}{r + R} + \frac{1}{(1 + r/D_o)^2}\right] \quad (1\text{-}18)$$

Here R represents the particle radius, r is the asperity radius, A_H is the Hamaker constant and D_o is the interatomic spacing (short distance between sphere and asperity). The equation is based on the use of the Derjaguin (1934b) approximation (see Borodich, 2014, for the details of the approximation) and it consists of two parts in the brackets: (i) term that describes the vdW interaction between the asperity and the particle; while (ii) term that describes the vdW force between the particle and planar surface. The presence of an asperity of radius r results in reducing the contact area and increasing the gap between

the particle and planar surface. Therefore, the total adhesion force is smaller than the force for a smooth particle of the same nominal radius R.

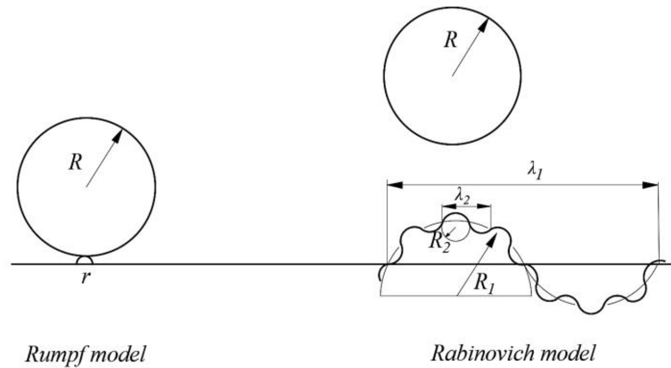

Figure 1-29 Schematics of models considering the influence of roughness on adhesion-modified from Rumpf (1999) and Rabinovich et al. (2000).

A modification of the Rumpf model (Figure 1-28a) by Rabinovich et al. (2000a, 2000b) is more suitable for description of the adhesive forces (Figure 1-28b) between rough surfaces because they have introduced the second order of roughness, with a smaller radius or peak-to-peak distance, superimposed on the first order of roughness asperities. Note that the surface roughness is typically specified by the root mean square (RMS) value not by a mean asperity radius. Rabinovich et al. (2000a, 2000b) have derived a relationship between RMS of the roughness and r based on a surface model of close-packed hemispherical peaks and valleys and obtained the modified equation with respect to the RMS

$$F_{ad} = \frac{A_H R}{6D_o} \left[\frac{1}{1+(R/1.48 \times RMS)} + \frac{1}{(1+1.48 \times RMS/D_o)^2}\right] \tag{1-19}$$

As Rabinovich et al. (2000b) noted themselves, the Rumpf model underestimated adhesion by 10-50 times, while their model gave correct predictions within 50% of experimental values. However, disagreements with experiments were rather large for the other 50% of tests. Thus, the studies of adhesion are still far from completion.

1.10 Thesis Layout

In chapter 2 the specific details of silicon MEMS asperities are discussed. Using a single multi-scale but non-hierarchical model of an asperity, a justification is given for the choice of the used scales (bulk, nano and atomic) employed in modelling of dry contact in microgear silicon MEMS teeth. In chapter 3, the results of the numerical simulations of friction between two nominally flat surfaces covered by hierarchical multiscale nanoblocks are presented. Two approaches: a fixed gap model and a model with the vertical degree of freedom are discussed. The models are not multilevel because all elements of the same scale have the same height. In chapter 4, the results of numerical simulations and modelling of frictional work of a silicon microgear MEMS are described. The nanoblocks representing the asperities are located on the curved surfaces of the MEMS teeth and, hence, the model is multilevel. It is shown that the friction between pure silicon surfaces, which are working in vacuum environment, is very high and, therefore, the stiction between microgear teeth is likely to occur. Finally, in chapter 5, the results of numerical simulations and modelling of frictional work of a microgear MEMS coated by molecular thin functionalised layers are described. It is assumed that wear of the functionalised layer occur due to damage accumulation. The Goryacheva-Torskaya model of the damage accumulation is modified. It is shown that the stiction possibility is initially very low but it increases with accumulation of damage in the layer. The final chapter will conclude this study and will make a number of recommendations for future work.

Chapter 2 Modelling of Multiscale Structure of a Single MEMS Asperity

2.1 Introduction

This chapter will start with the specific details of silicon MEMS asperities and the techniques used in their manufacturing. Then, the Borodich-Savencu (B-S) multiscale, single-level and non-hierarchical model will be discussed. Here, an extension has been carried out to develop the B-S model and the results have been illustrated and discussed.

2.2 Basic Definitions: Multiscale, Hierarchical and Multi-level Models

Using a single multi-scale but non-hierarchical model of an asperity, a justification is given for the choice of the used scales (bulk, nano and atomic) employed in modelling of dry contact in microgear silicon MEMS teeth. The study of rough surfaces often detects multi-level and multi-scale or hierarchical properties of these surfaces. The small scales of roughness can be seen when we magnify a section of a rough surface (Archard, 1957, Greenwood and Wu, 2001). In this chapter, a number of models will discuss to determine whether they are multi-scale, multi-level or hierarchical. However, it is first appropriate to define the meaning of these terms.

Measurements of surface roughness scale are connected to physical-chemical properties, mechanism of interactions and deformations. In this study, chemical interactions are related to the first scale of nanoasperities. This nanoasperities scale is related to chemical interactions, while the second round of nanoasperities scale is primarily responsible for modelling the vdW interaction of asperities in friction. This is in addition to the

mechanical interlocking between the counterparts of asperities. The considered scale is found by changing the characteristic length of the processes involved in friction. Figure (2-1) shows the length scale of some natural and manmade items.

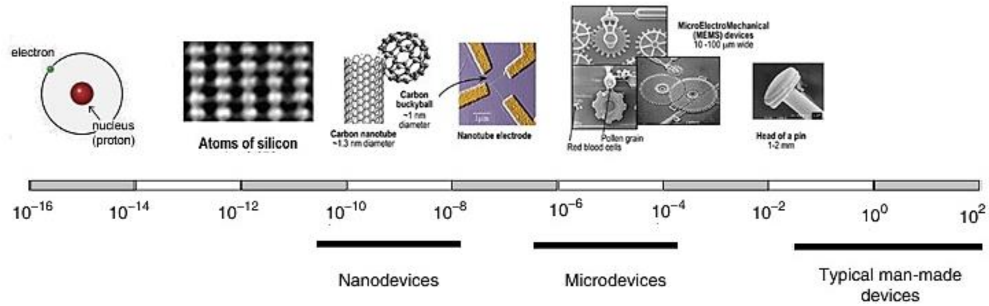

Figure 2-1 Length scale of natural and manmade items (Gad-el-Hak, 2006)

The following assumptions will be used: The atomic scale has a length l << 2nm and it reflects the characteristics of the surface roughness, at this scale chemical interactions are involved between surfaces. The nano scale has a feature length 2nm << l<<1μm and vdW bonds are involved in the interaction between surfaces. The micro scale has a length between 1μm and 1mm and it is responsible for the mechanical interlocking between the asperities. Finally, the macro scale has a length scale over 1mm and it includes the behaviour of the bulk of the body, which connects the microscale asperities together.

The meaning of the *multilevel* model is related to the question of whether or not asperities of the same scale are at the same height. If they are at the same height, then the model is single-level, even if it is multi-scale. If the asperities of the nth scale are at different heights, then the model is multi-level. On the other hand, we can call the model hierarchical if the nth generation of asperities consists of more than just one asperity. It is not enough for the asperities to exist over each other to have a hierarchy; they should have at least one subdivision in the asperity generation to be hierarchical.

2.3 The Polonsky-Keer Effect and its Influence on Characteristics of MEMS

Previous studies in the field of mechanics have proven that the traditional laws of plasticity that were developed for material at the macroscale, are not applicable for microscale and nanoscale structures (see Polonsky and Keer, 1996a and 1996b). They found that when the contact size is comparable to the dimensions of the microstructure length of the material (distance between dislocations), no plastic deformations occur. This is also true in atomic subscale contact. Experiments and simulations have shown that the behaviour of the particles in a material at the atomic scale is different to that at the macro-structure (see Kallman et al., 1993 and Mordehai et al., 2011).

Polonsky and Keer (1996a and 1996b) explained the effects of scale in the ploughing of a flat elastic-plastic surface by a hard asperity and developed a new micro-contact numerical approach. In their simulations, they used discrete crystal dislocations to represent plasticity. They established that "*plastic deformation at the micro-asperity during contact becomes increasingly difficult and even impossible if the asperity size decreases below a certain threshold value compared to the microstructural length*". This happens because the resistance to plastic deformation will increase when the asperity size is decreased to a comparable level with the characteristic microstructure length of the material (i.e. the distance between dislocation sources). In other words, when the contact is below the scale of the microstructural length, the dislocated volume is insufficient to cause plastic flow.

One could attribute this effect to Kuhlmann-Wilsdorf (1996). However, speaking about surface effects and the role of dislocations, Kuhlmann-Wilsdorf (1996) wrote: "*Naturally, extraordinarily unexpected facts may be encountered in terra incognita, viz.*

quantum mechanics and relativity theory, but as a rule it is better to expect that the normal laws of nature and logic continue to operate also where there are still gaps in our knowledge. Figuratively speaking, therefore, it is best to assume that there are no mermaids unless proven otherwise. In regard to the behaviors at contact spots ... the same mechanisms of plastic and elastic deformation apply as are known from bulk metals." Hence, she stated clearly that her experiments show only elastic deformation because the load is distributed to a large number of contact spots and the stress per contact spot is kept below Meyer impression hardness, and is not caused by any physical particularity that the nano-contacts may have. Indeed, one of her conclusions was that "*there is every indication that dislocations in tribology behave the same way as in bulk material*" or one could use her words, '*there are no mermaids*.' (Kuhlmann-Wilsdorf, 1996). Therefore, Polonsky and Keer's (1996a and 1996b) results show that there may be 'mermaids' after all, this effect will be referred to as the Polonsky-Keer effect. That they formulated in the following words: "*when asperity size decreases and becomes comparable to the characteristic microstructural length, contact plastic deformation becomes increasingly difficult, and finally impossible*" (Polonsky and Keer's, 1996a).

Deshpande et al. (2003) conducted discrete plasticity modelling of cracks in single crystals and considered dislocation nucleation from Frank–Read sources distributed randomly in the material. Some researchers have taken into account that the pre-existing sources of dislocations are believed to be a more realistic reason for increasing number of dislocations during loading, rather than completely new nucleated dislocations (Hull and Bacon, 2011).

2.4 Contact and Adhesion between MEMS Elements

MEMS contain a significant number of micro/nanoscale elements. Many of these components work as load bearing and torque transmitting elements and usually at very high speeds. One of most important torque transmitting components is the micro gear pair (Takeuchi, et al., 2000, Yang and Liao, 2007). The majority of adhesion modelling and surface interaction energy in all complexity scales have brought us close to a better understanding of adhesion and stiction in MEMS and micromachined devices. Komvopoulos (1996) has briefly showed the specific tribological difficulties and challenges that occur in MEMS and micromachined devices, as shown in Figure (2-2). He has showed that (a) stiction may occur during the release-etch process; (b) stiction arises between overdriven suspended mass accelerometer and limit stop in MEMS; and (c) a small clearance interface that causes intermittent contact leads to wear in the counterpart's surfaces.

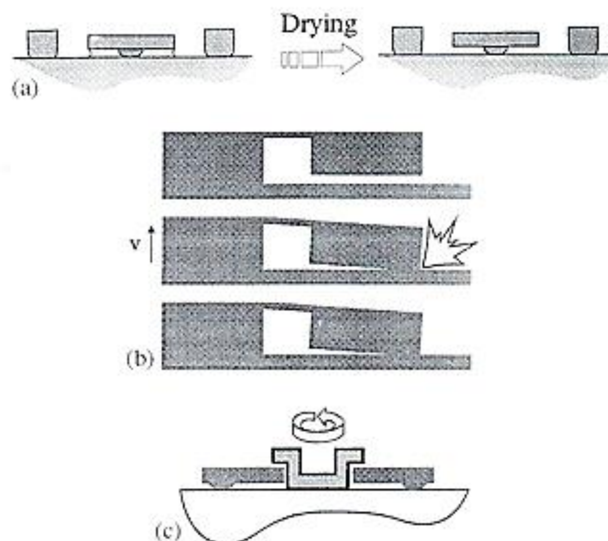

Figure 2-2 Tribological problem in MEMS (a) stiction during release-etch process, (b) stiction between overdriven suspended mass, (c) a small clearance interface where intermittent contact causes wear (Komvopoulos, 1996)

The important thing here is calculating the magnitude of adhesion and it is effect on the performance of the MEMS and the surface roughness of the contacting bodies.

2.5 MEMS Materials, Properties, and Techniques

MEMS consist of a significant number of mechanical parts that act as torque or load transmission elements, such as gears, cantilevers, actuators, sensors and others electronic elements. MEMS are normally based on a silicon substrate and their production widely use lithography technologies such as moulding/LIGA processing (Mastrangelo, 1997, Anis, et al., 2006, Tanner, 2000, Tanner, 2009). MEMS have many advantages and their technologies suggest the possibility to improve the performance of many devices in different fields because they are small, light and consume a small amount of power, which can have a significant number of advantages in certain product specifications (Liu et al., 2007, Tanner, 2009). There are three general methods of MEMS fabrication methods: surface micromachining, bulk micromachining, and moulding/LIGA processing.

2.5.1 Surface Micromachining

Surface micromachining is used to build the main structure of micromachining tools. In the beginning, (a) to protect it during the later etching stags, the substrate is covered with an isolation layer. (b) Then adding thin sacrificial layer and (c) structural layers by deposition. These layers are patterned on a substrate, usually silicon wafer, to create the structure of the MEMS device. Finally, (d) etching process is then used to remove the sacrificial layers to get the required shape for the MEMS element. The scheme in Figure

(2-3) illustrates the general steps of this procedure with a simple example of a freestanding polysilicon bridge (Maboudian, 1998).

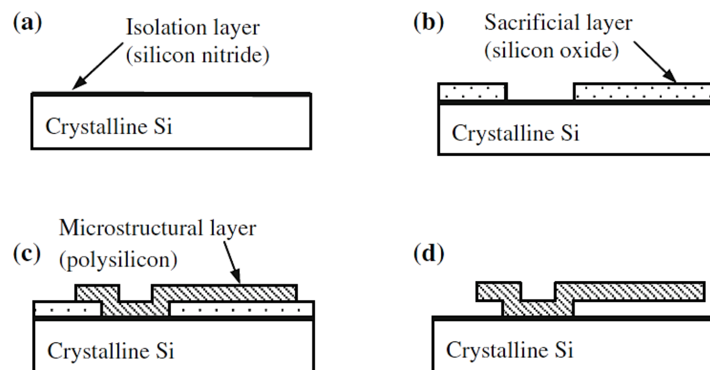

Figure 2-3 the basic steps of surface micromachining (Maboudian, 1998 and Madou, 2002)

2.5.2 Bulk Micromachining

In this method, some parts of the substrate are removed. This is achieved by wet isotropic or anisotropic etching, or by dry etching method or dry reactive ion etching (DRIE), which is used to create large cavities, grooves, and channels. Figure (2-4) shows a simple scheme of the steps of bulk micromachining. Wet etching is used with materials such as silicon and quartz while dry etching is used with silicon, metals, plastics and ceramics. The results of both procedures are two-dimensional structures. Complex multi-layer MEMS structures can be created by adding more layers of thin film to the main structures.

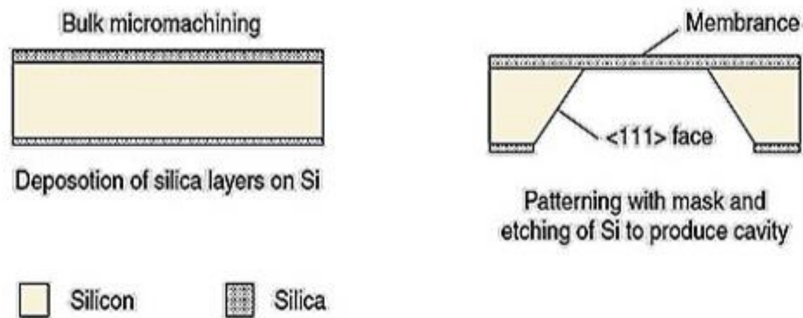

Figure 2-4 Demonstration of the steps used in bulk micromachining (Madou, 2002)

Madou (2002) and Rosen (2012) have shown that bulk micromachining is one of the earliest micromachining technologies. This method can be summarised as removing parts of the substrate material to create miniaturised mechanical components. Bulk micromachining can use chemical etchants, and these are widely used in the MEMS industry in both wet and dry form. Wet etching immerses the substrate in a liquid bath of a chemical etchant. These etchants can be isotropic or anisotropic. Stiction can happen between the MEMS elements when the rinsing liquid is evaporated during the etching process. A very high attractive capillary force can be developed by stiction between surfaces, which may cause structure collapse (Mastrangelo, 1999). Modern processes prefer anisotropic etching because it produces sharp, well-controlled features. The etchants will remove the exposed regions of the substrate. In MEMS, this technique is very useful due to the high rate of etching and high selectivity. The etching rate and the selectivity could be controlled by changing the etchant type or modifying its temperature, for which crystallographic planes of the substrate are exposed to the etchant solution.

Crystallographic orientation is not that important in isotropic wet etching because the etching proceeds in all directions at equal rates and the etching under the masking layer etches at the same speed as the etching rate in the normal direction. Practically lateral

etching with stirring is much faster than without stirring. This may happen because stirring makes the etchant reach the substrate material under the mask layer near the surface and etches it, so isotropic wet etching is almost performed with strong stirring of the etchant solution.

2.6 Multiscale Structure of a Single MEMS Asperity

2.6.1 The Borodich-Savencu (B-S) Model

B-S model was multiscale, but it is not multilevel, as the asperities of the same generation are on the same level (being only one). In addition, it was not hierarchical model because hierarchical model needs more than one micro-asperity or more than one nano-asperity. It was a simple model, which is containing a single rod with multiscale (micro, nano scales) and having the same width but no subdivision from scale to scale as shown in Figure (2-5).

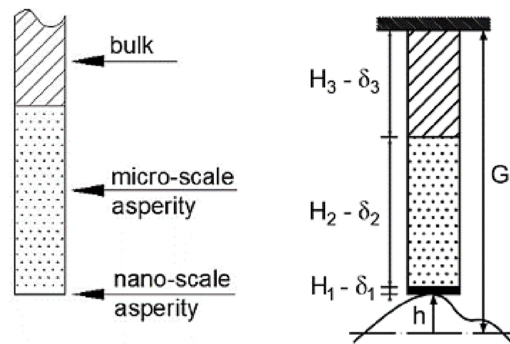

Figure 2-5 Multiscale, single-level, non-hierarchical model example

B-S model can be a model of single asperity friction against a contacting surface. Hooke's law has been used to formulate this model. This model was formulated for both fixed gap and also fixed load. The heights and the Young's modulus of the nano-asperity,

micro-asperity and the considered bulk section of the slider are represented in Figure (2-5). A is the cross-sectional area of the three sections of the slider while *h* is the height of the asperity of the counter-surface.

From the deformed geometry, it can be written:

$$\mathrm{h} + (\mathrm{H}_1 - \delta_1) + (H_2 - \delta_2) + (H_3 - \delta_3) = G \tag{2-1}$$

The force equilibrium equation can be written as:

$$\delta_1 \frac{E_1 A}{H_1} = \delta_2 \frac{E_2 A}{H_2} = \delta_3 \frac{E_3 A}{H_3} \tag{2-2}$$

From equation (2-2) δ_2 and δ_3 can be expressed in terms of δ_1 and substituted in equation (2-1) and obtain:

$$\delta_1 = \frac{h + H_1 + H_2 + H_3 - G}{1 + \frac{E_1 H_2}{E_2 H_1} + \frac{E_1 H_3}{E_3 H_1}} \tag{2-3}$$

If δ_1 is known, δ_2 and δ_3 can be found by:

$$\delta_2 = \delta_1 \frac{E_1 H_2}{E_2 H_1} \text{ and } \delta_3 = \delta_1 \frac{E_1 H_3}{E_3 H_1} \tag{2-4}$$

In this single asperity model, the cross sectional area of the different scale was constant, while in the extended (B-S) model the cross sectional area is different at each subscale of the nanoblock asperity as we will see in the next section.

2.6.2 An Extended Borodich-Savencu (B-S) Model for MEMS Surface

A key discussion of a single MEMS nanoblock dry friction model shows the scale, level and hierarchy concepts by the explanations of a single nanoblock model, which is characterised by a rod consisting of different scales and cross-sections. This model is an

extension to B-S model, represents multiscale and non-hierarchical at the same time. It is a single nanoblock rubbing against a counter-surface that can be simply formulated for elastic deformation using Hooke's law. The current model is expressed as a fixed-gap model as shown in Figure (2-6).

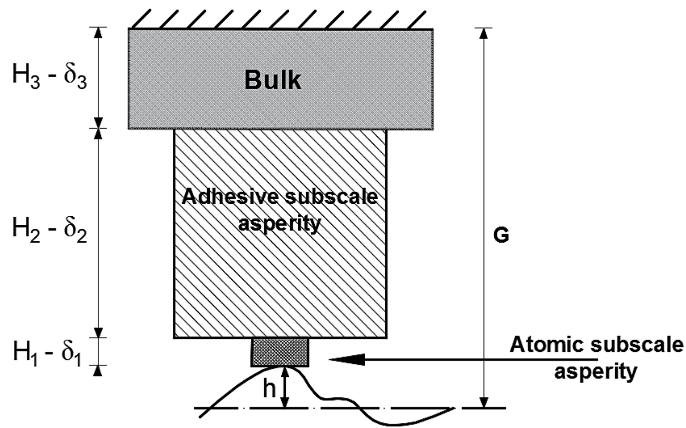

Figure 2-6 Single nanoblock MEMS dry friction model

Where H_1, H_2, H_3 are the heights of the atomic subscale block, adhesive subscale block and the considered bulk section of the model and E_1, E_2, E_3 are the values of Young's modulus of the atomic subscale, adhesive subscale and the considered bulk of the model. While A_1, A_2, A_3 are the cross-sectional area of the atomic subscale, adhesive subscale and the considered bulk of the model. The distance or the gap between the top of the nanoblock slider and the mean-line of the counter surface is G and the height of the asperity of the counter-surface is h.

From deformed nanoblock shown in the Figure (2-6), and as in (2-1), the force equilibrium equation can be written as:

$$\delta_1 \frac{E_1 A_1}{H_1} = \delta_2 \frac{E_2 A_2}{H_2} = \delta_3 \frac{E_3 A_3}{H_3} \tag{2-5}$$

Then, δ_2 and δ_3 can be expressed regarding δ_1, substituted in gap equation. Therefore it can be obtained:

$$\delta_1 = \frac{h + H_1 + H_2 + H_3 - G}{1 + \frac{E_1 A_1 H_2}{E_2 A_2 H_1} + \frac{E_1 A_1 H_3}{E_3 A_3 H_1}} \tag{2-6}$$

If δ_1 is known, then δ_2 and δ_3 can be found by:

$$\delta_2 = \delta_1 \frac{E_1 A_1 H_2}{E_2 A_2 H_1} \tag{2-7}$$

and

$$\delta_3 = \delta_1 \frac{E_1 A_1 H_3}{E_3 A_3 H_1} \tag{2-8}$$

Also the model can be developed by including the Polonsky and Keer effect, the influence of the force of adhesion and the energy dissipated by breaking the chemical and vdW bonds,

Also, it can be modified to a single nanoblock model against a surface under a fixed load (Figure 2-7). The material for the rubbing surfaces is silicon. A force has been applied at the top of the slider, compressing the nanoblock. To remain in the elastic domain with the deformation at all the scales, the magnitude of the load has been chosen as $P = 25\mu N$. Young's modulus for the bulk has considered equal to silicon's Young's modulus, while at the adhesive subscale and the atomic subscale has been considered to be a contact modulus.

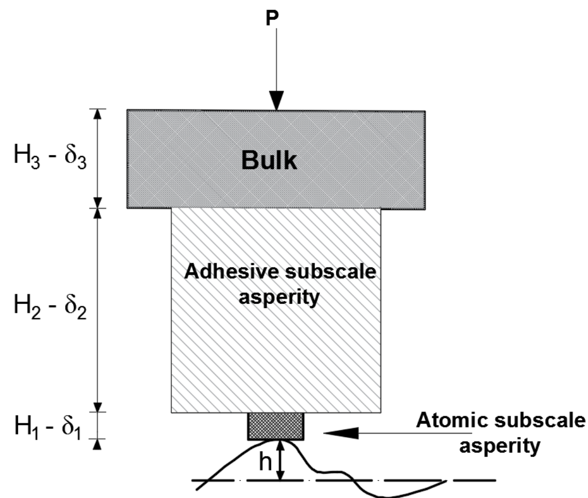

Figure 2-7 Single- nanoblock model against a surface under a fixed load

The resulting coefficient of friction has a value of 0.389 and is constant for all the simulation time (see Figure 2-8). First of all, the magnitude of the coefficient of friction may seem acceptable. However, such a constant value is to be expected, as all the atoms on the tip of the atomic subscale are considered to be engaged in chemical bonds; when these chemical bonds are broken, amount of energy are dissipated. In real life, surfaces are contaminated with oxides, water vapours or other particles, so surfaces will not be perfectly clean to allow all atoms to establish chemical bonds. Furthermore, 0.389 is the value of the actual coefficient of friction, rather than the apparent coefficient of friction, as there is the difference between the nominal and the real contact area. The atomic subscale of the model, which is only one, is engaged in contact with the counter-surface at all times.

Secondly, it is reasonable to expect a constant coefficient of friction because all the components of the dissipated energy remain constant during friction of this single asperity (single nanoblock) model.

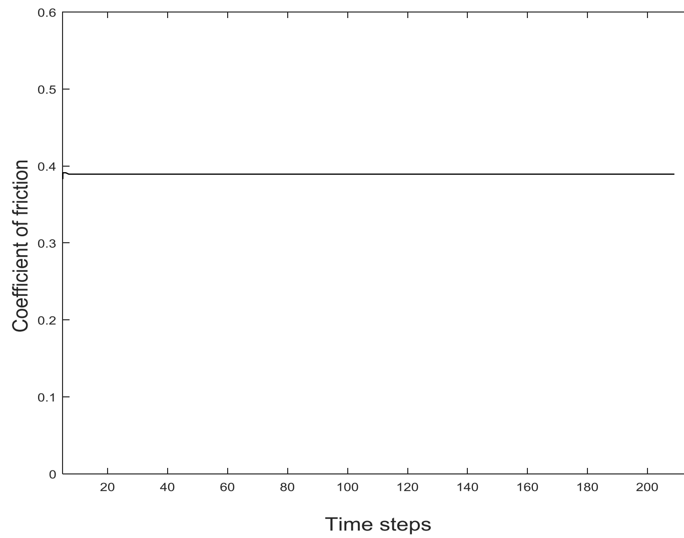

Figure 2-8 coefficient of friction for single nanoblock contact model

There is no variation in the state of deformation of the nanoblock, as it is subject to the same compressing force through all the simulation, and there are no other asperities to which to shift the load due to different heights of asperities on the counter-surface. The energy dissipated by dissociation of chemical interactions and molecular attraction does not introduce any variation in the loss energy either, as the same areas are always engaged in chemical (atomic subscale) and vdW interactions (the second nano subscale). Figure (2-9) shows that the loss energy is constant for all mechanisms taken into account.

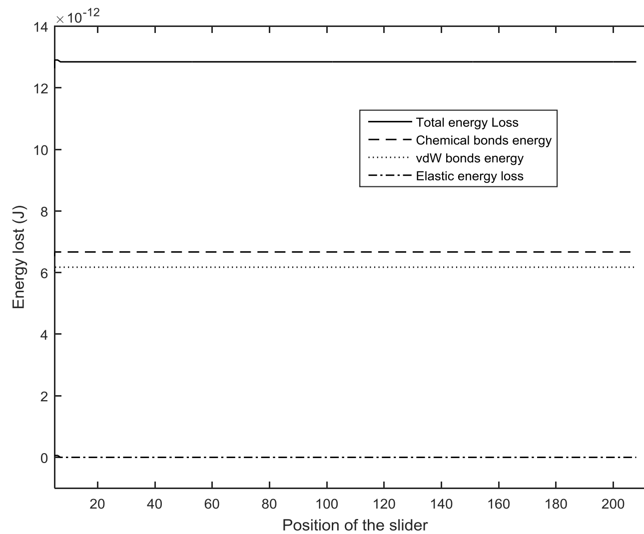

Figure 2-9 Influence of different energy dissipation mechanisms on single nanoblock model

It can also be seen that there is no energy dissipation through the mechanical interlocking of nanoblock, as there is no change in the elastic deformation state of the nanoblock model since the external load is constant. The highest contribution to friction is the energy lost by breaking of the chemical bonds. While, the breaking of the vdW bonds is approximately 7% less than of the chemical energy loss. That occurs even with the difference in the cross-sectional area between the adhesive subscale where the vdW interaction are likely to occur and the atomic subscale because of the chemical bonds much stronger than vdW bonds.

2.7 Conclusions to Chapter 2

A specific silicon MEMS features and technologies are discussed. Using a single multi-scale nanoblock but non hierarchical model of an asperity, a justification is given for the choice of the used scales (bulk, nano and atomic) employed in modelling of dry contact in microgear silicon MEMS teeth.

This is a rather simple model, but it can be beneficial to describe the single nanoblock contact with different cross-sectional areas sliding over a silicon surface. The modelling of the single nanoblock asperity can be considered as a good guide to describe the multi-asperity hierarchical structures as will described in the following chapter. To the best of our knowledge and according to the above analysis of literature (see Chapter 1), the first hierarchical model of rough surface was introduced by Archard (1957). However, nobody developed this idea of hierarchical structure of roughness, until Borodich and Mosolov (1991) suggested to use the hierarchical one-level model (the Cantor-Borodich profile) and then Borodich and Onishchenko (1993) introduced a multilevel hierarchical model of rough surfaces. These ideas will be developed in the next chapter.

Chapter 3 Modelling of the Frictional Work of a Multi-Asperity Surface

3.1 Introduction

This chapter will describe a new approach to compute the friction force between the silicon MEMS surfaces by using the energy dissipated through different physical and chemical mechanisms along the contact sliding distance. The physical mechanisms in the current model have used some procedures that are specific to the length scales most relevant to dry contact friction (the multi-scale approach). These procedures have taken into account the chemical interactions between silicon MEMS surfaces at the atomic subscale and the adhesive subscale, where the vdW interactions are significant at the nanoscale, and the elastic interlocking of the nanoblock asperities and their coupling at the atomic and adhesive subscales. One of the most important assumptions is that the nanoblock asperities on the surfaces do not deform plastically due to the Polonsky-Keer effect.

3.2 Modelling of Surface Roughness by a General Multi-scale Hierarchical Model of a Nominally Flat Slider

A silicon MEMS multi-scale hierarchical model has been simulated to work in a vacuum environment. The structure of the multiscale block has mainly been characterised depending on the roughness parameters, which have been calculated in the specific subscales. This design consists of a hierarchical multiscale asperity structure and a supporting rigid surface that are meshed with each other, in addition to the sliding relative motion. Nanoblock asperities of the surface are presented as a block consisting of several

scales: an atomic scale where chemical interactions are likely to occur, an adhesive nano-subscale where molecular adhesion is significant, and bulk elastic material. Many blocks cover the tooth surface. The gaps between the surfaces of the meshing teeth are found using the Hertz line contact theory (see e.g. Johnson, 1985, Davies, 2005 and Khaustov, 2016). The experimental analysis of the surface roughness data showed that the MEMS surface does not have any microscale roughness as we will see in the next chapter and, hence, there is no plastic deformation. The apparent friction is calculated using the total energy dissipated via different physical/chemical mechanisms.

3.3 Mechanical and Chemical Mechanisms of Energy Dissipation and Models of Friction

A multiscale hierarchical structure model was developed and modified to reflect specific features of silicon MEMS structures. This model takes into the account the basic principles of Savencu and Borodich (2014) model (see also Savencu, 2016, Savencu and Borodich, 2017). In this chapter, new and different perspectives are considered that instead focuses on three main disciplines in the modelling. The first main development in this model can be briefly described in the silicon MEMS devices that are working in a vacuum environment, such as in space (see e.g. Almuramady et al., 2016).

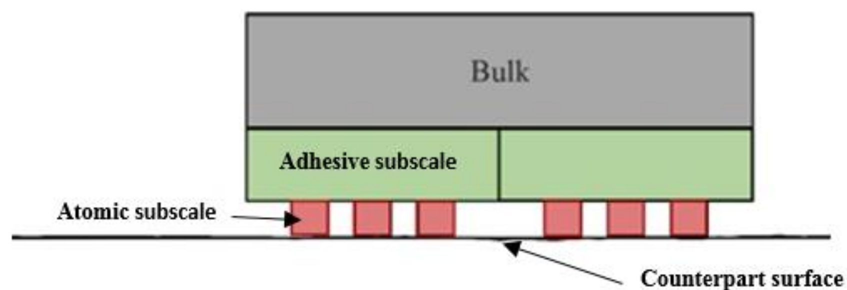

Figure 3-1 Multiscale hierarchical model

The second contribution in this study is that the microgear MEMS tooth surface has been modelled by multiscale hierarchical structures (see Figure 3-1) of multiple blocks located at different subscales. The subscales of each block (adhesive subscale asperities) have been defined by the gap between the contacting teeth surfaces at each particular instance, as will be shown in the next chapters of this thesis.

In this approach, the dry friction force F_f has been calculated through the energy dissipated U_{diss} during relative sliding distance x between two meshed micro-tooth elastic rough surfaces according to the following equation:

$$F_f = \frac{U_{diss}}{x} \tag{3-1}$$

Energy is lost due to the dissociation of chemical and vdW bonds, and energy is also lost through elastic deformation of nanoasperity over the sliding contact distance. The total energy $U_{Totalchem}$ dissipated by chemical bonds at the moment t is:

$$U_{Totalchem}(t) = N_{chem}(t)\, U_{chem} \tag{3-2}$$

where U_{chem} is the energy of the dissociation of one chemical bond and $N_{chem}$is the current number of the chemical bonds between counterpart's surfaces. Using (3-3), one can find the total energy $U_{TotalvdW}$ dissipated by vdW bonds:

$$U_{TotalvdW} = N_{vdW}\, U_{vdW} \tag{3-3}$$

where U_{vdW} is the energy of the dissociation of a vdW bond, N_{vdW} is the current number of the vdW bonds within the adhesive scale of contact. This energy is different at each time moment along the sliding distance due to the variability of the number of nanoasperities in touch at that point. The energy spent for elastic deformation $U_{elastic}$ of

a nanoasperity or the elastic interlocking between the counterpart's surfaces of the silicon microgears teeth is also taken into account. Hence, the total energy loss is:

$$U_{diss=} U_{Totalchem} + U_{TotalvdW} + U_{elastic} \quad (3\text{-}4)$$

It follows from Equations (3-1) and (3-4) that the friction force because of dissipation of energy has been obtained through different types of mechanisms, the equation can then be written in the following form with respect to the mechanism of dissipated energy.

$$F_f = \frac{U_{Totalchem} + U_{TotalvdW} + U_{elastic} + U_{capillary} + \cdots}{x} \quad (3\text{-}5)$$

Due to the vacuum environment in the current case, the energy dissipated will be reduced to $U_{Totalchem}$, $U_{TotalvdW}$ and $U_{elastic}$ only. Two types of force have been considered as parameter effects in the friction force, which are the normal force F_N and the adhesion force F_{adh}. Therefore, the coefficient of friction can then be calculated according to an equation that is similar to Coulomb-Derjaguin approach (see section 1.6.2 for more details):

$$\mu = F_f/(F_N + F_{adh}) \quad (3\text{-}6)$$

According to Equations (3-1) and (3-6), we can use the dissipated energy approach to define the coefficient of friction:

$$\mu = U_{diss}/(F_N + F_{adh})\, x \quad (3\text{-}7)$$

where U_{diss} is the dissipated energy by various mechanisms, F_f is the friction force and x is the sliding distance. Therefore, we can write the friction coefficient as:

$$\mu = \frac{U_{Totalchem}}{(F_N + F_{adh})\ x} + \frac{U_{TotalvdW}}{(F_N + F_{adh})\ x} + \frac{U_{elastic}}{(F_N + F_{adh})\ x} + \cdots \tag{3-8}$$

Finally, the friction coefficient can be expressed as:

$$\mu = \mu_{chem} + \mu_{vdW} + \mu_{elastic} + \cdots \tag{3-9}$$

The energy dissipation in this study comes from the dissociation of chemical bonds at the atomic subscale of the asperities (where chemical bonds are possible). The dissociation of vdW bonds occur in the adhesive subscale of the nanoasperities (adhesive subscale where vdW bonds are likely to occur). Mechanical interlocking happens between the first and second nanoscale of the asperities.

In the multiscale hierarchical model that has been shown in Figure (3-1), the dissociation of energy occurs when the chemical and the vdW bonds break through the sliding motion during the contact distance of the microgear teeth. In this motion, there is a high possibility for stiction or getting a cold welding between the counterpart summits of the asperities. This happens because the area of contact is very small. Bowden and Leben (1938) and Derjaguin (1934a, c) explained and defined the concept of ‘cold welding’ term for the first time. They explained that the contact occurred locally in the summits of the asperities where the area of the contact is very small. So, there is enough load to generate a sufficient local pressure to weld these asperities together.

Bowden and Tabor (1943) also referred to this concept and they found that cold welding occurs between the counterpart’s asperities in the contact surfaces when they are under high pressure, so that the high asperities will be joined together. At the atomic subscale, a pressure increase will lead to elastic deformation. The actual area of contact and the vdW force will increase, which means that adhesion will also increase. This will make

the atoms in the opposite asperities on the surfaces connected with each other by chemical bonds, which is called cold welding.

The tangential force F_t is necessary to keep the microgear MEMS system working and it is responsible for the sliding motion between the contact-meshing surfaces of the microgear MEMS teeth. F_t should be larger than the friction force F_f to overcome this interaction forces. The friction force F_f should not exceed the value of tangential force to enable sliding motion of the surfaces on each other.

3.3.1 Simulations of Energy Dissociation in the Chemical Bonds

The dissociation of the chemical bonds corresponds to the atomic subscale of asperities (where the chemical bonds are possible to occur) in the model. In silicon MEMS, when the microgear teeth surface come into the contact, the atoms in the meshing teeth surfaces will approach each other and engage in a chemical interaction. Bowden and Leben (1939) called these interactions between atoms cold welding junctions. Figure (3-2) shows the types of interactions that are established at atomic and adhesive-subscale scales.

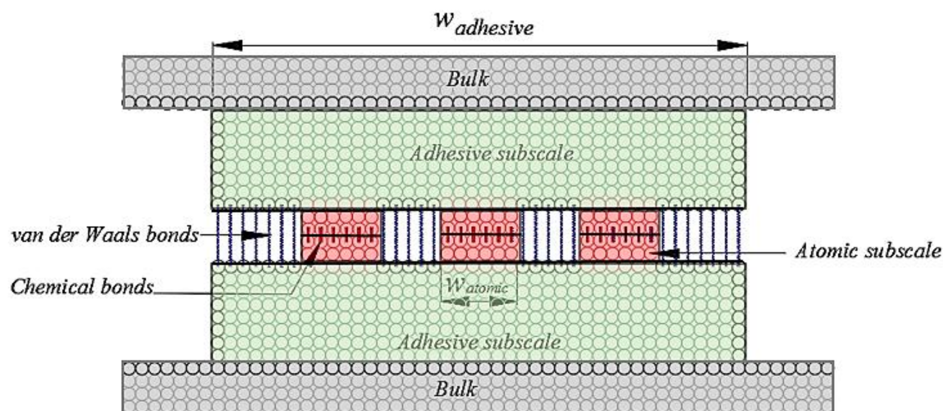

Figure 3-2 Types of interactions established at atomic and adhesive subscales. The fully overlapping moment is shown

During the sliding motion between the surfaces of the teeth, which are in intimate contact, these chemical bonds will break and a significant amount of energy will be dissipated because of this dissociation of bonds. It is proposed that only the atomic set of asperities would engage in a chemical bond while the second nano-subscale of asperities will participate in vdW interactions. Figure (3-3) shows a magnified section of the chemical interactions and vdW bonds.

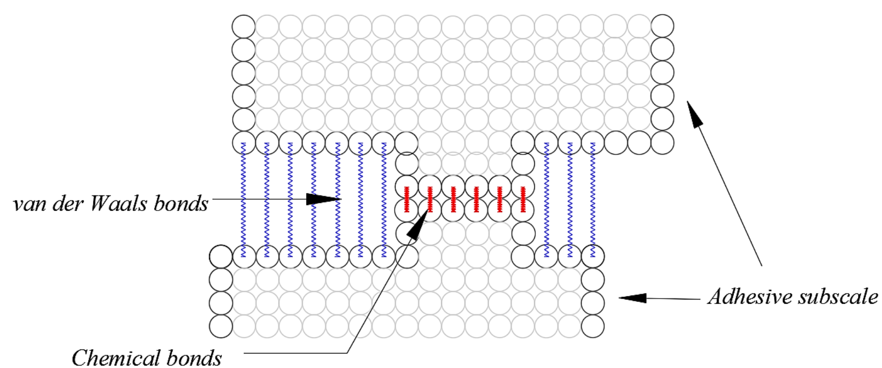

Figure 3-3 Magnified section of sketch of chemical and vdW bonds at the moment of fully overlapping chemical subscale is shown

Figures (3-2) and (3-3) show that there are two subscales of asperities on the first subscale, which is the smallest scale used to represent the atomic subscale. which corresponds to the chemical bonds. The second is the adhesive subscale and is represented by the nanoasperity, where the vdW interactions are likely to ocurr, although they are much weaker than the chemical interactions. In addition, the model contains the bulk of the material on the tooth surface.

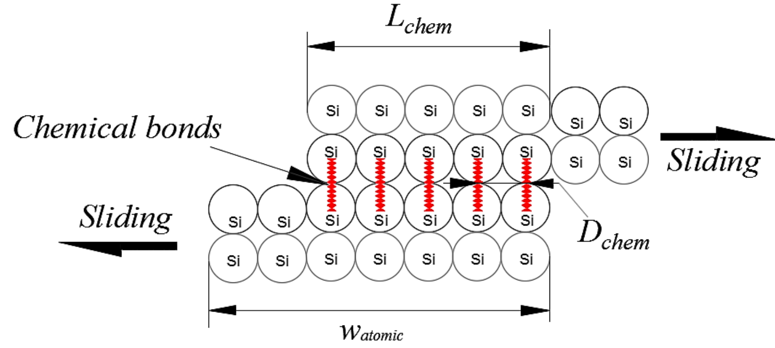

Figure 3-4 The chemical bonds between silicon atoms of non-fully overlapping atomic subscales

It is assumed that cross-section of atomic subscale block is a square ($w_{atomic} \times\ w_{atomic}$). The number of atoms N_{chem} in one atomic block that is involved in chemical bonds with other atoms on the facing surface can be determined as in the following equation:

$$N_{chem} = \frac{w_{atomic} \times L_{chem}}{D_{chem}{}^{2}} \quad (3\text{-}10)$$

where L_{chem} is the current length of the chemically interacting part between the meshing micro teeth surfaces, w_{atomic} *is* the width of the atomic subscale asperity and D_{chem} is the distance between silicon atoms in the crystal. The dissociated energy by breaking through one atomic subscale block will be gradually calculated until all the chemical interactions in the atomic block are broken, as in the following:

$$U_{Totalchem} = N_{chem}\, U_{chem} \quad (3\text{-}11)$$

where U_{chem} is the energy of dissociation of one chemical bond.

3.3.2 Simulations of Energy Dissociation in the VdW Bonds

In this section, the dissipated energy by the dissociation of vdW interactions will be discussed in detail. VdW interaction has attracted the attention of a significant number of researchers during the previous decades. The current model aims to study the effects in

both, the normal and tangential directions of the sliding surface; normally to the surface, which is trying to increase the actual contact area and tangentially to shear the bonds that are generated between the microgear teeth surfaces (see Figure 3-5).

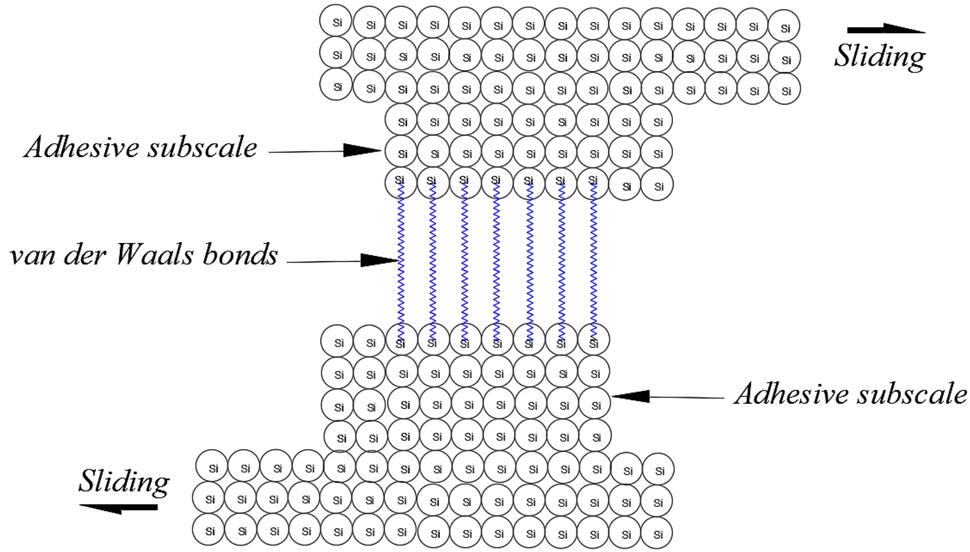

Figure 3-5 The vdW bonds between silicon atoms of slightly shifted adhesive of the nanoblock

However, Maugis approximation (1992) has been used to define the adhesive layer, as shown in the Figure (3-6). As soon as the asperity in the adhesive subscale reaches the adhesive layer, it will jump into the contact. The atoms in this subscale will establish vdW bonds with the atoms of the counterpart surface as illustrated in Figure (3-5). In this case, the N_{vdW} atoms that are engaged in vdW interactions will be as given in Equation (3-12) and the total dissipated energy $U_{TotalvdW}$ by one adhesive subscale asperity will be found as in Equation (3-13):

$$N_{vdW} = \frac{w_{vdW} \times L_{vdW}}{{D_{chem}}^2} \tag{3-12}$$

Where w_{vdW} is the width of the square of the nanoblock, L_{vdW} is the current length of the overlapping nanoblocks.

$$U_{TotalvdW} = N_{vdW} U_{vdW} \tag{3-13}$$

where $U_{TotalvdW}$ is the total dissipated energy in one block in the adhesive subscale by the dissociation of the energy of van de Waals bond breaks.

3.3.3 Simulation of Adhesion Layer on the MEMS Tooth Surface

The Lennard-Jones potential defines the possible energy of interaction of two atoms or molecules based on the distance of separation between them.

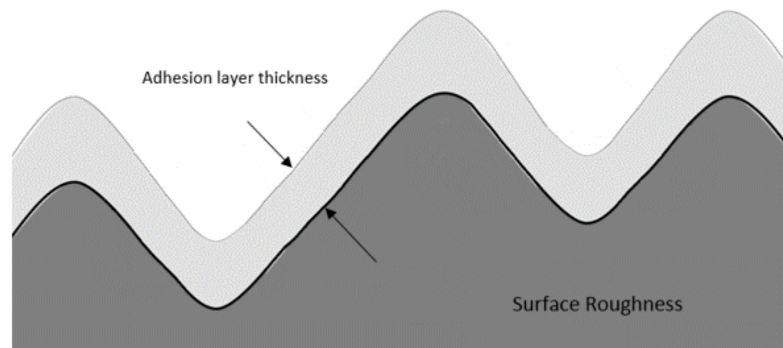

Figure 3-6 The adhesive layer thickness

The potential equation takes into the account the difference between attractive forces and repulsive forces between these two particles. The Lennard-Jones potential is a widely used method to model the vdW interaction between two uncharged molecules or atoms. The expression of the [12-6] Lennard-Jones potential can be seen in Equation (3-14) and a graphical representation is shown in Figure (3-7). This potential is applicable to describe interactions between two molecules.

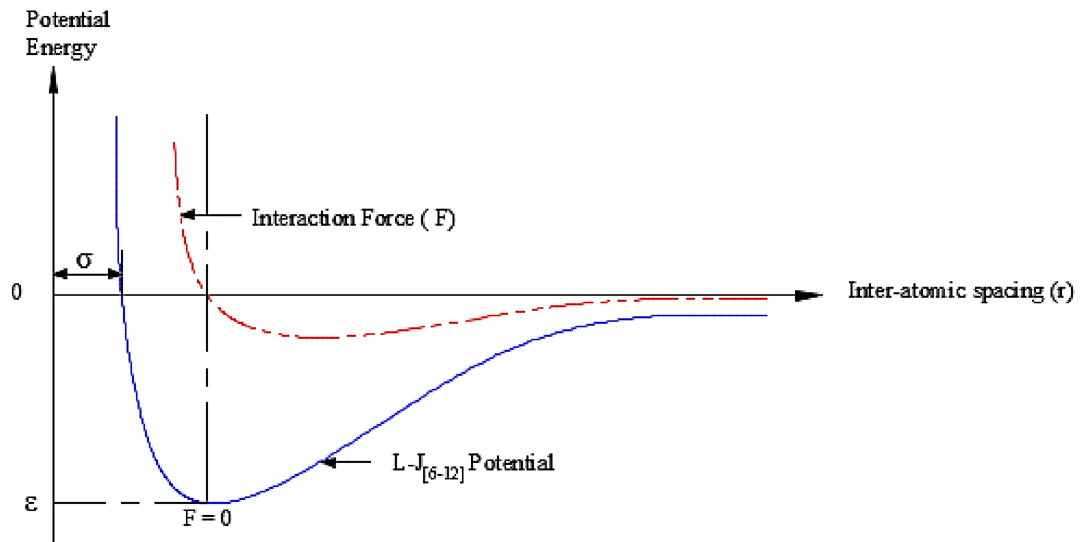

Figure 3-7 The potential and the force for Lennard-Jones

The Lennard-Jones formulae have particular parameters. These parameters are different depending on the type of the material and the particles which have chosen to fit the characteristics of this material. The parameter ε is the depth of the potential curve and it shows how strong is the interaction between molecules. At the distance that corresponds to minimum potential is the equilibrium separation ρ. The second important parameter is σ and it has been defined as the finite distance between particles at which the inter-particle potential equal to zero. The performance of the interaction between two particles as described by the [6-12] Lennard-Jones potential can be summarised as two particles that are attracted to one another until they reach an equilibrium separation. If they are brought even closer, then the particles will experience repulsion:

$$U_{LJ}(r) = 4\varepsilon\left[\left(\frac{\sigma}{r}\right)^{12} - \left(\frac{\sigma}{r}\right)^{6}\right] \quad (3\text{-}14)$$

The Lennard-Jones interaction force can be calculated by differentiation of the potential Equation (3-14) with respect to the separation distance *r*:

$$F_{L-J}(r) = 24\varepsilon\left(\frac{2\sigma^{12}}{r^{13}} - \frac{\sigma^6}{r^7}\right) \tag{3-15}$$

To obtain the stress-strain curve for the adhesive subscale asperities, the [12-6] Lennard-Jones potential will be used to model the interaction between two silicon atoms.

Let us take two silicon atoms as an example. It is know that the radius of one silicon bond is 1.175 Angstrom. Thus, the diameter of one chemical bond is D_{chem} = 2.35Å, which has been considered at the equilibrium distance ρ, where the force is zero. Then, we can find the separation where the potential is zero from the following relation:

$$F_{LJ}(D_{chem}) = 24\varepsilon\left[\frac{2\sigma^{12}}{D_{chem}^{13}} - \frac{\sigma^6}{D_{chem}^{7}}\right] = 0 \tag{3-16}$$

From Equation (3-16), we can obtain $\sigma = D_{chem}\sqrt[6]{\frac{1}{2}} = 2.093\text{Å}$.

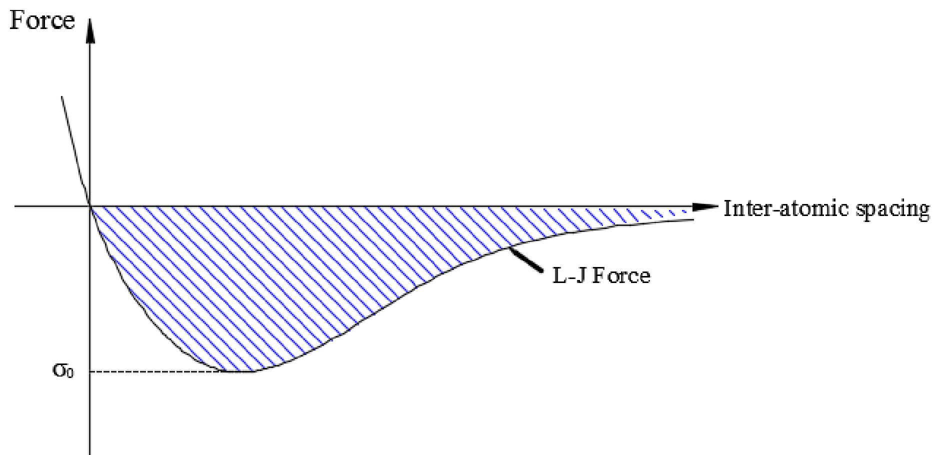

Figure 3-8 Interaction force according to Lennard-Jones

According to the Maugis approximation, the attraction force is constant until the separation between particles reaches a threshold distance. If the separation distance increases further, then the interaction force is null. Figures (3-8) and (3-9) have shown a comparison between Maugis' approximation and the force obtained by differentiating of the Lennard-Jones potential.

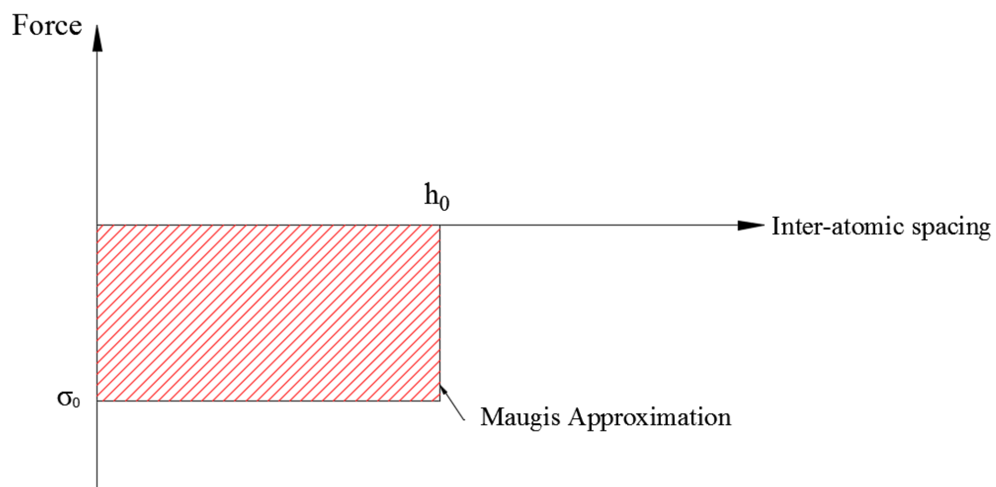

Figure 3-9 The interaction force according to Maugis' approximation

In the Maugis' approximation, the work of adhesion could be expressed related to the illustration in Figure (3-9) and described in Equation (3-17):

$$w = \sigma_0 h_0 \qquad (3\text{-}17)$$

In Maugis's approximation, the maximum attractive force and the work of adhesion match those of Lennard-Jones. Thus, the hatched areas under the curves must be equal. The separation distance h_0 can then be found by Equation (3-17).

3.3.4 Molecular Mechanics Approach to Model Chemical Interactions using Lennard-Jones Potentials

Let us consider a Lennard-Jones potential describing interactions between two molecules or silicon atoms separated by distance z:

$$U_{LJ12-6}(r) = 4\varepsilon\left[\left(\frac{\sigma}{z}\right)^{12} - \left(\frac{\sigma}{z}\right)^{6}\right] \quad (3\text{-}18)$$

It can be assumed that the potential describes a chemical bond. In this case, one only needs to consider interactions between a pair of molecules (atoms).

Therefore, the stress Σ resulting from the total force of interactions between two half-spaces may be obtained by multiplying the force obtained for a single pair by the number of atoms per a unit area N_1 (square meter). The average area A_1 per a surface molecule (an atom) is$A_1 = 1/N_1$.

Young's modulus is equal to the slope of stress-strain curve:

$$E = \frac{d\sum U_{LJ12-6}}{de} = \frac{d\sum_{U_{LJ12-6}}/dz}{de/dz} \quad (3\text{-}19)$$

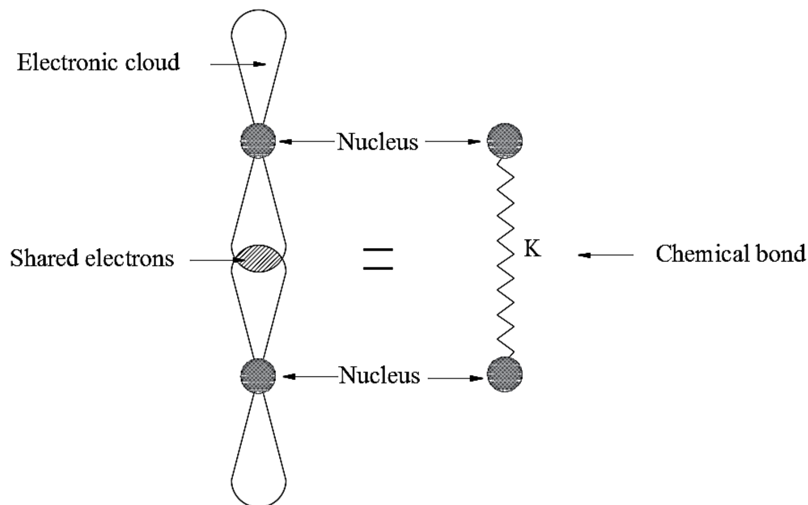

Figure 3-10 Formation of chemical bond by sharing electrons

When the separation distance equals the equilibrium distance ρ , and because of the effect of the strain, e is

$$e = \frac{(z - \rho)}{\rho} \tag{3-20}$$

Therefore, we can obtain

$$\frac{de}{dz} = 1/\rho \tag{3-21}$$

From Hooks law $stress\ \Sigma = Ee,$ where Σ is negative because it is compressive.

$$\Sigma = -\frac{|F_{Total}|}{A} \tag{3-22}$$

$$\frac{dU}{dz}N_1 = K\rho N_1 = \frac{72\varepsilon}{\rho}N_1 \tag{3-23}$$

Where K is the stiffness of the chemical bond which is represented as a spring (see Figure 3-10). Let us apply the above approach to estimate the potential parameters of silicon (Si) crystal, which is made up of individual atoms bonded together in a regular, periodic structure. The silicon atoms may be visualised as having 10 electrons in the inner closed-shell and four electrons in the outer valence shell, as shown in Figure (3-11). The closed-shell electrons do not participate in bonding. Hence, with four outer electrons, each Si atom forms four covalent bonds (a covalent bond consists of two atoms 'sharing' a single electron) with the four surrounding atoms.

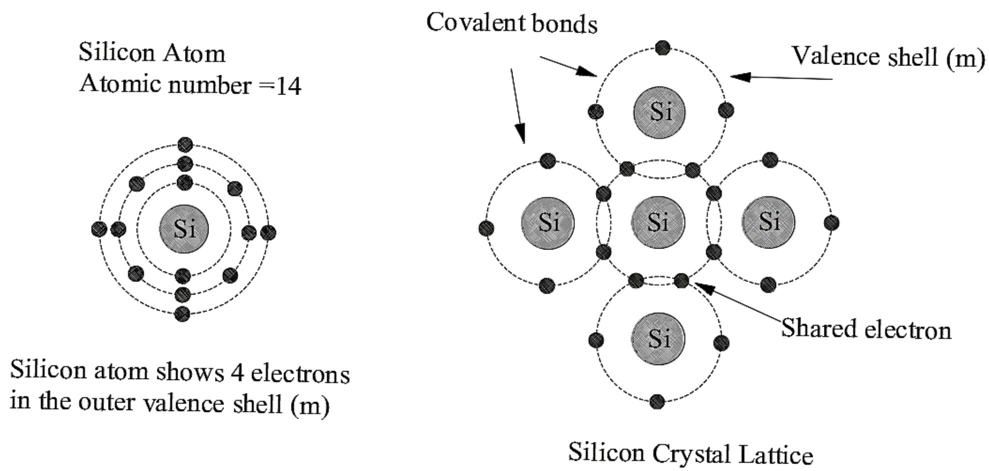

Figure 3-11 Silicon atomic and inter-atomic structure

It is known from the literature that the maximum E value in silicon is 188 Gpa, which occurs in the {111} direction, and the minimum value is 130 Gpa, in the {100} direction (see Hopcroft, 2010). Hence, the estimations in the current model are acceptable if the value of $\varepsilon = 2.902 \times 10^{-20} J$ we then obtain the following estimations (these values are closer to the values described in the literature):

$$N_1 = \frac{1}{(2.35 \times 10^{-10})^2} = 1.8108 \times 10^{19} \text{ atom/m}^2$$

$$\varepsilon = \frac{2.35 \times 10^{-10} * 161 \times 10^9}{72 * 1.8108 \times 10^{19}} = 2.9020 \times 10^{-20}$$

$$E = \frac{72\varepsilon}{\rho} N_1 = \frac{72 \cdot 2.9020 \times 10^{-20}}{2.35 \times 10^{-10}} 1.8108 \times 10^{19} = 161 \times 10^9 \text{ Pa}$$

It could be plotted the potential curve modelling the interaction between two silicon atoms as shown in Figure (3-12).

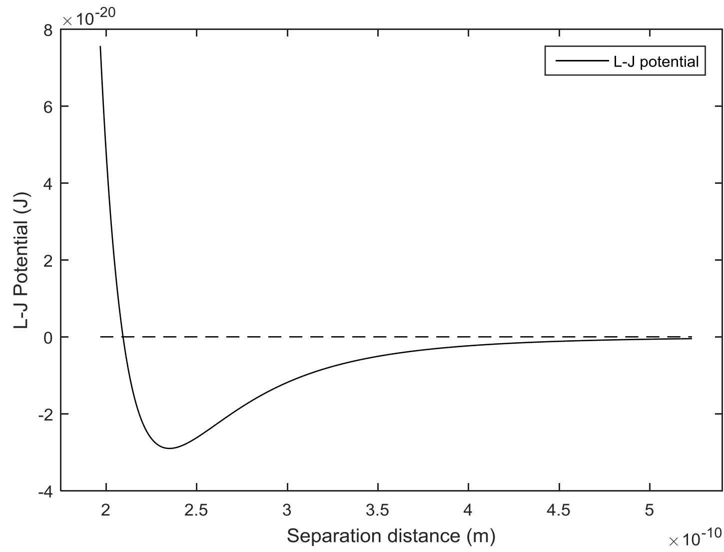

Figure 3-12 Lennard-Jones potential modelling the interaction between two silicon atoms

It was suggested by Savencu (2016) and Borodich and Savencu (2017) to approximate the resulting stress-strain curve plotted in Figure (3-13) by a bilinear elastic-perfectly rigid curve

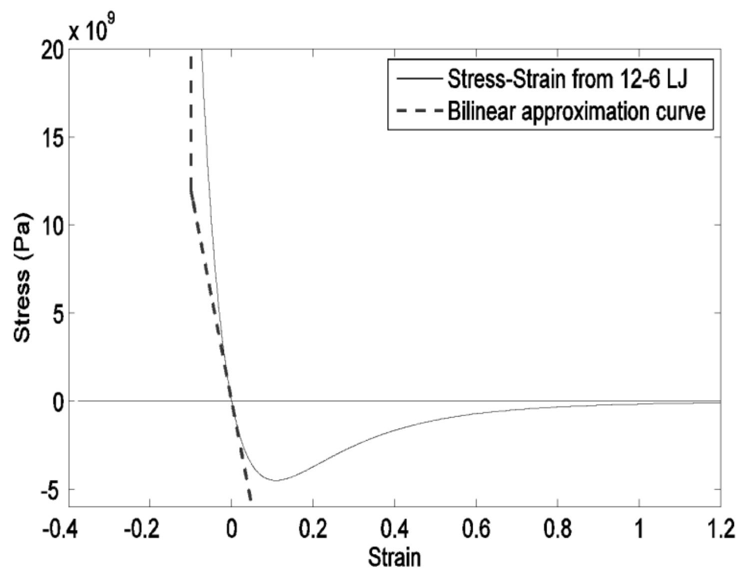

Figure 3-13 The stress-strain curve for nano-asperities (Savencu, 2016)

It can be seen that when compression starts, the nano-asperity deforms according to Hook's law. When it reaches a certain strain threshold, the linear approximation of stress-strain relation becomes meaningless and the load is transferred from the nano-asperity to the micro-asperity. It has been accepted the same assumptions as Savencu (2016) did, i.e. for the considered case of silicon nano-asperities, the threshold strain is 30%, as illustrated in Figure (3-13).

3.3.5 Modelling vdW Interactions using Lennard-Jones Potentials

Now let us consider the vdW interactions between a monomolecular layer surface and a molecule located at distance z_o from the surface (see Figure 3-14).

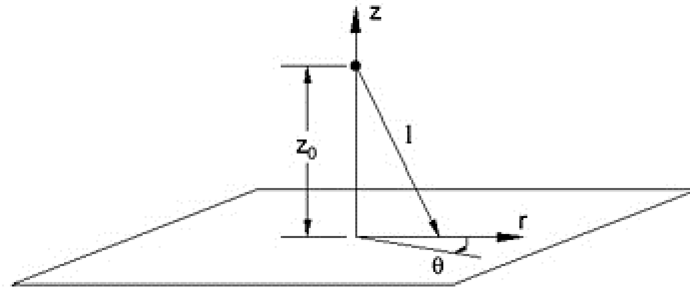

Figure 3-14 Interaction between a particle and a surface (modified from Savencu, 2016)

Because the interactions in the long vdW field depend not only on the near atoms, but also other atoms, we need to use integration. By using Bradley (1932) and Hamaker's (1937) approach, we can substitute the discrete potential by continuously distributed elementary areas:

$$\int_0^{2\pi}\int_0^{\infty} U_{LJ_{12-6}}(l)\, N_1 r\, dr\, d\theta = 2\pi N_1 \int_0^{\infty} 4\varepsilon\left[\left(\frac{\sigma}{l}\right)^{12} - \left(\frac{\sigma}{l}\right)^{6}\right] r\, dr$$

Note that $l = \sqrt{r^2 + z_0^2}$. The integral can then be written as:

$$2\pi N_1 \int_0^{\infty} 4\varepsilon \left[\left(\frac{\sigma}{\sqrt{r^2 + z_0^2}} \right)^{12} - \left(\frac{\sigma}{\sqrt{r^2 + z_0^2}} \right)^{6} \right] \frac{dr^2}{2}$$

$$= 4\pi\varepsilon N_1 \int_0^{\infty} \left[\frac{\sigma^{12}}{(r^2 + z_0^2)^6} - \frac{\sigma^6}{(r^2 + z_0^2)^3} \right] d(r^2 + z_0^2)$$

By substituting $r^2 + z_0^2 = \xi$ and changing the appropriate integration limits, the following integral can be obtained:

$$4\pi\varepsilon N_1 \int_{z_0^2}^{\infty} \left[\frac{\sigma^{12}}{\xi^6} - \frac{\sigma^6}{\xi^3} \right] d\xi = 4\pi\varepsilon N_1 \left[\frac{\sigma^{12}}{-5\xi^5} + \frac{\sigma^6}{2\xi^2} \right]_{z_0^2}^{\infty} = 4\pi\varepsilon N_1 \left(\frac{\sigma^{12}}{5z_0^{10}} - \frac{\sigma^6}{2z_0^4} \right)$$

Thus, the vdW interaction potential for a particle (molecule) and a monomolecular layer surface separated by distance z_0 is:

$$U_{LJ10-4}(z) = 4\pi\varepsilon N_1 \left(\frac{\sigma^{12}}{5z_0^{10}} - \frac{\sigma^6}{2z_0^4} \right)$$

To include the interactions between the particle (molecule) and a half-space of the material (i.e. the interactions between the particle and the sub-surface particles located at $z < 0$), the high potential needs to be integrated along the z-axis. We have to take into account that if l_z is the interlayer distance, then any interval AB along the vertical *z-axis* contains AB/l_z layers. Hence, we have to divide the integral along *z-axis* by l_z. We have:

$$\int_{z_0}^{-\infty} \frac{4\pi\varepsilon}{l_z} N_1 \left(\frac{\sigma^{12}}{5z^{10}} - \frac{\sigma^6}{2z^4} \right) dz = \frac{4\pi\varepsilon}{l_z} N_1 \left[-\frac{\sigma^{12}}{45z^9} + \frac{\sigma^6}{6z^3} \right]_{z_0}^{-\infty} = \frac{4\pi\varepsilon}{l_z} N_1 \left(\frac{\sigma^{12}}{45z_0^9} - \frac{\sigma^6}{6z_0^3} \right)$$

Thus, the interaction potential for a particle (molecule) and a half-space separated by distance z_0 is:

$$U_{LJ_{9-3}} = \frac{4\pi\varepsilon}{l_z} N_1 \sigma^3 \left(\frac{1}{45} \frac{\sigma^9}{z_0^9} - \frac{1}{6} \frac{\sigma^3}{z_0^3} \right)$$

If one needs to consider interactions between a solid (for example, a sphere) and a half-space, then the interactions can be calculated in a two-step manner: (i) calculate the interaction potential between a vertical chain of molecules situated along z-axis; and (ii) calculate the integrated influence of this vertical chains of molecules per unit area of the solid.

To obtain the interaction potential between a chain of particles and a half-space, we integrate $U_{LJ_{9-3}}$ along z-axis to infinity, divide it by l_z and get U_{LJ8-2}:

$$U_{LJ_{8-2}} = \frac{1}{l_z} \int_{z_0}^{\infty} U_{LJ_{9-3}} \, dz$$

$$U_{LJ_{8-2}} = \frac{4\pi\varepsilon}{{l_z}^2} N_1 \sigma^3 \int_{z_0}^{\infty} \left(\frac{1}{45} \frac{\sigma^9}{z^9} - \frac{1}{6} \frac{\sigma^3}{z^3} \right) dz = \frac{4\pi\varepsilon}{{l_z}^2} N_1 \sigma^3 \left(\frac{1}{360} \frac{\sigma^9}{z^8} - \frac{1}{12} \frac{\sigma^3}{z^2} \right)$$

Thus, the interaction potential for a vertical chain of molecules situated along z-axis and a half-space separated by distance z_0 from the chain end is:

$$U_{LJ_{8-2}}(z_0) = \frac{\pi\varepsilon}{3{l_z}^2} N_1 \sigma^4 \left(\frac{1}{30} \frac{\sigma^8}{z_0^8} - \frac{\sigma^2}{z_0^2} \right)$$

To obtain the force of interactions between the chain and a half-space, one needs to differentiate U_{LJ8-2} with respect to z:

$$F_{U_{LJ8-2}} = -\frac{dU_{LJ_{8-2}}(z)}{dz}$$

$$F_{U_{LJ8-2}} = \frac{2\pi\varepsilon}{3{l_z}^2} N_1 \sigma^3 \left(\frac{2}{15} \frac{\sigma^9}{z^9} - \frac{\sigma^3}{z^3} \right)$$

The equilibrium distance can be found by solving the equation:

$$F_{U_{LJ8-2}}(\rho) = 0$$

or

$$\left(\frac{2}{15}\frac{\sigma^9}{\rho^9} - \frac{\sigma^3}{\rho^3}\right) = 0 \;\Rightarrow\; \frac{2}{15}\frac{\sigma^6}{\rho^6} = 1$$

$$\rho = \sqrt[6]{\frac{2}{15}}\sigma$$

To calculate the elastic modulus between layers connected by vdW forces, we have to calculate the slope of the stress-strain curve at the equilibrium distance:

$$\frac{d\sum U_{LJ8-2}}{dz}(\rho) = N_1 F_{U_{LJ8-2}}(\rho)$$

$$\frac{d\sum U_{LJ8-2}}{dz}(\rho) = N_1^2 \frac{2\pi\varepsilon}{{l_z}^2}\sigma^2\left(\frac{2}{5}\frac{\sigma^{10}}{\rho^{10}} - \frac{\sigma^4}{\rho^4}\right) = N_1^2 \frac{2\pi\varepsilon}{{l_z}^2}\left(\frac{15}{2}\right)^{\frac{1}{3}}\rho^2\left[\frac{2}{5}\left(\frac{15}{2}\right)^{\frac{5}{3}} - \left(\frac{15}{2}\right)^{\frac{2}{3}}\right]$$

$$\frac{d\sum U_{LJ8-2}}{dz}(\rho) = N_1^2 \frac{2\pi\varepsilon}{{l_z}^2}\rho^2\frac{15}{2}2 = 30N_1^2\frac{\pi\varepsilon}{{l_z}^2}\rho^2$$

$$\frac{de}{dz} = 1/\rho$$

$$E = \frac{d\sum U_{LJ8-2}}{de} = 30N_1^2\frac{\pi\varepsilon}{{l_z}^2}\rho^3 = 30N_1^2\pi\varepsilon\rho$$

By substituting ε and $\rho = 1.122462\,\sigma = 2.6378 \times 10^{-10}$ m as $\sigma = 2.09 \times 10^{-10}$ m, therefore, the elastic modulus will be equal to $E = 157.26 \times 10^9$ Pa. This value for E is very close to the value that used in this study.

3.3.6 Energy Dissipation by Mechanical Interlocking of Asperities

The energy dissipation by mechanical interlocking of asperities has been calculated by finding the value of the elastic deformation of the nano asperities during the meshing sliding distance. Due to the Polonsky-Keer effect, that has been taken into account in this current model, the deformations of the nanoblock (this includes the adhesive subscale of an asperity and all parts of the atomic subscale of the asperity) is only elastic. The nanoblock has been simulated as a square rod, which is subjected to the compression force, and the block deformes only elastically according to the formula:

$$\delta = \frac{PH}{EA} \quad (3\text{-}24)$$

where δ is the elastic deformation of the contacting asperities in the meshing microgear MEMS teeth, P is the compression force subjected to the nanoblock, H is the length of asperity, A is the area of its cross section, and E is the elastic modulus of the material. The elastic interlocking of the asperities with the counterpart surface might be shown as in Figure (3-15).

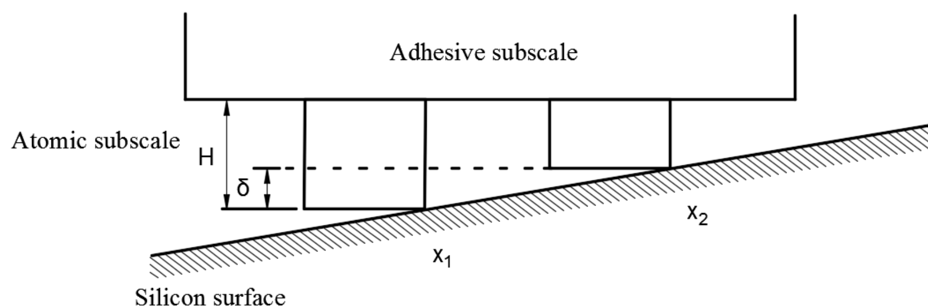

Figure 3-15 Compression in the asperity during the sliding distance

When the hierarchical structure moves from point x_1 to the point x_2, the height of the atomic subscale element will compress by the value of δ and the elastic energy in the element can be calculated according to the equation:

$$\Delta U_{elastic} = \frac{1}{2}\frac{EA}{H}\delta_e^2 \tag{3-25}$$

where δ_e is the deformation or the difference in the height of the element, when the part moves from point x_1 to the point x_2. Summation of the energies spent to deform all parts of the atomic subscale, the energy spent to deform the adhesive subscale of the nanoblock may be treated as elastic interlocking energy of a nanoblock that represents a real surface asperity.

3.4 Simulations of Friction between Two Nominally Flat Surfaces

Here two approaches are used in application to a multiscale structure consisting of two nanoblocks located on an elastic silicon substrate. The former approach (the fixed gap model) assumes that there is a fixed gap between two nominally flat parallel rigid surfaces; the former surface is covered by rigid roughness having the same heights are the roughness of silicon surface measured, while the later surface is covered by the multiscale structure (silicon substrate and hierarchical multiscale nanoblocks). The later approach (the vertical degree of freedom model) assumes that the gap between two nominally flat parallel rigid surfaces (it is assumed again that the former surface is covered by rigid roughness having the same heights are the roughness of silicon surface measured, while the later surface is covered by the multiscale structure) is not fixed, there is the vertical degree of freedom a nanoblock, however the compressing load acting on

the multiscale structure is constant. The models are not multilevel because all elements of the same scale have the same height.

3.4.1 The Fixed Gap Model

The simulation of this model depends on the assumption of a constant distance between the mean line in the silicon roughness profile and the top point in the multiscale structure. In other words, the multiscale hierarchical model has been fixed from the upper side and compression has only been allowed from the bottom side of the structure (see Figure 3-16 and Figure 3-17).

In addition to the bulk volume of the silicon, the model consists of two subscales: the atomic subscale and the adhesive subscale.

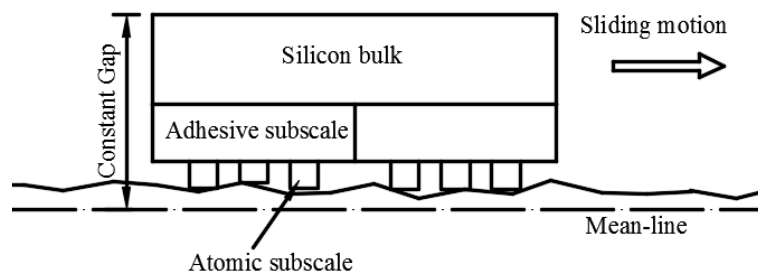

Figure 3-16 The multiscale structure in the fixed gap model (*G* =const.).

The subscales depend on the calculation of Abbot-Firestone curve, as shown in Figure (3-18). Depending on the roughness parameters, the dimensions of the atomic and adhesive subscale asperities in the multiscale structure have been calculated on the root mean square R_q and the arithmetic height of asperities R_a.

The roughness parameters have been defined as a two dimensional profile and not as a three dimensional rough surface. Maugis (2000) has illustrated that it is quite hard in measurement to pass from the statistical characteristics of a profile, which is represented

as a series of peaks and valleys, to the statistical features of a surface, which is represented as contour lines. Earlier studies neglected this difference until Nayak (1971) explained it in his study of the correlation of the properties of roughness profile and surface area. Nayak theory was originally named ‘random processes theory’. In this theory, Nayak expressed a comparison between the number of peaks per unit length to the density of summits per unit area, the mean height of peaks to the mean height of summits, and the mean curvature of peaks to the mean curvature of summits (see Nayak, 1971, Maugis, 2000, p. 321).

Figure (3-17) illustrates the specific dimensions of the fixed gap multiscale hierarchical model. These dimensions have been calculated using the experimental data obtained for a silicon surface roughness. Figure (3-18) shows the experimental data of the silicon roughness profile that has been obtained from AFM and the corresponding Abbot-Firestone curve.

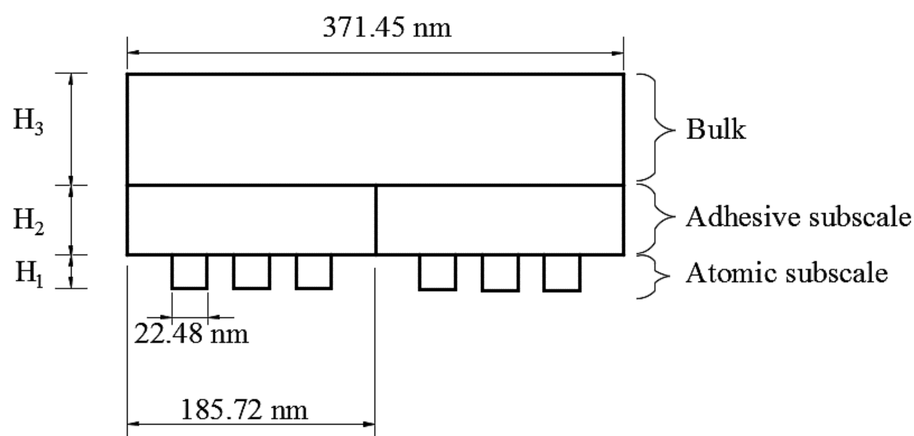

Figure 3-17 The dimensions of the fixed gap hierarchical model

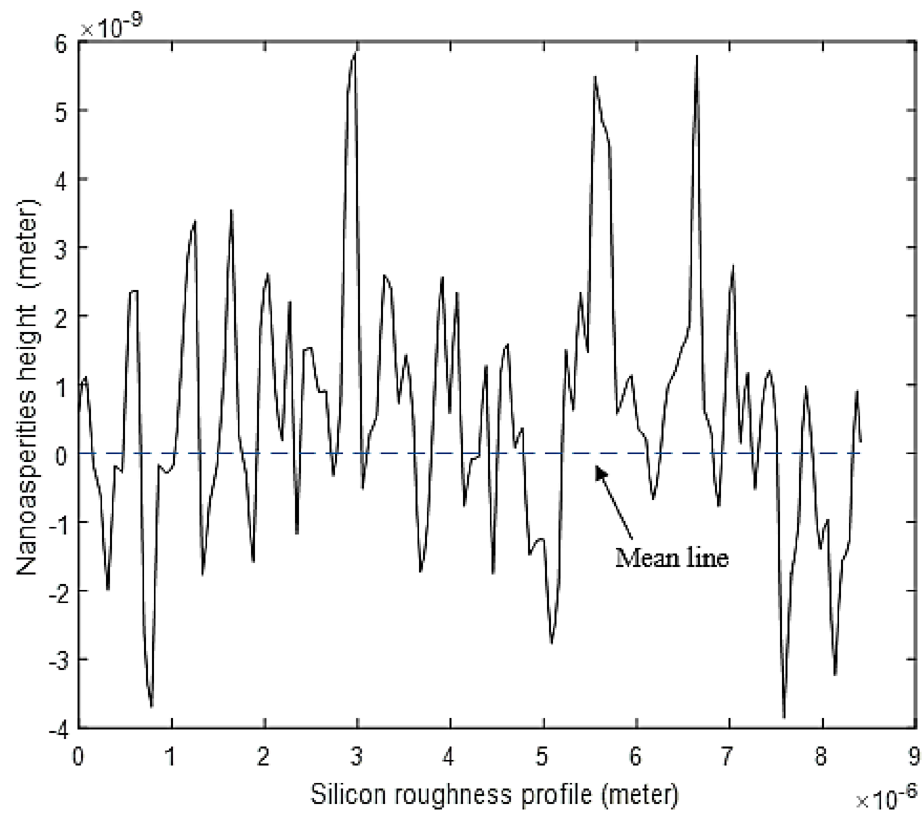

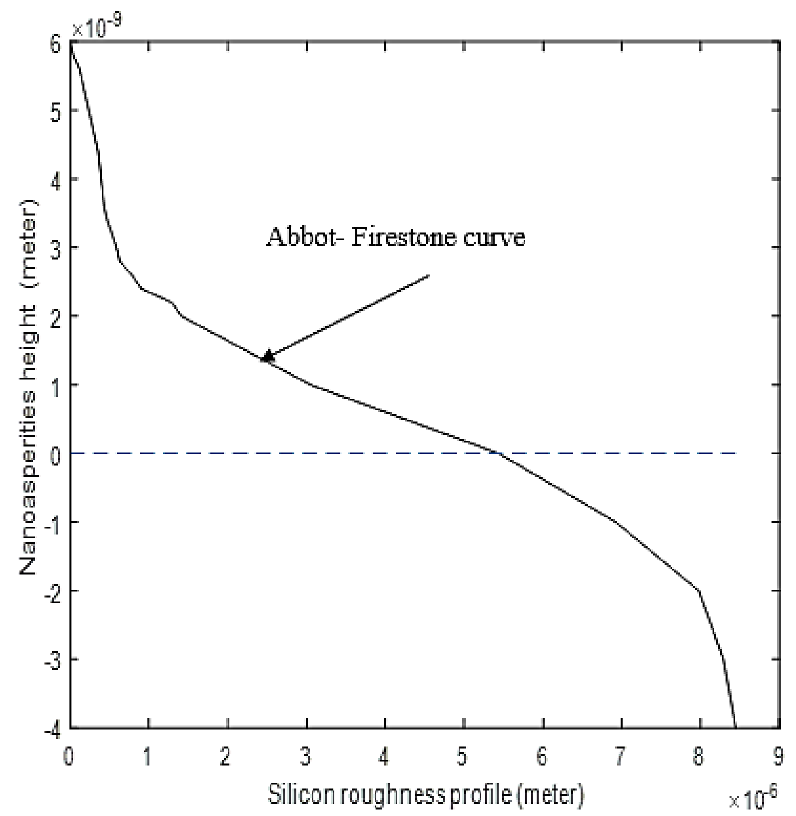

Figure 3-18 Abbott- Firestone curve for silicon profile

Using AFM data, it was obtained the arithmetic height of asperities $R_a = 1.2612$ nm and for the root mean square $R_q = 1.6433$ nm. The R_q was considered to be a reference point to calculate the dimensions of the multiscale structure. The atomic subscale set of the asperities has been assumed to be located at 50 percent of the root mean square (R_q). Therefore, the height of first set of the atomic subscale asperities has been calculated to be equal to $H_{atomic} = 0.82164$ nm. The adhesive subscale set of the nano asperities have been taken to be located at (1.2 R_q). Therefore, the height of these subscale asperities was found to be equal to $H_{adh} = 2.11$nm (see Savencu, 2016). The fixed gap multiscale structure used in the numerical simulations is shown in Figure (3-19).

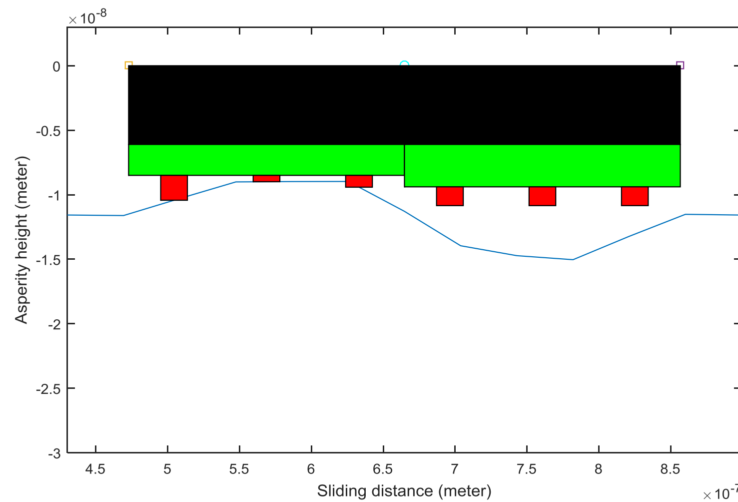

Figure 3-19 Fixed gap multiscale structure used in the numerical simulations.

The adhesive subscale blocks have been taken without any space between them. Meanwhile, the width of the atomic subscale block has been calculated according to the equation of the average width for asperities, as follows:

$$d = \frac{1}{n}\sum_{i=1}^{n} d_i \quad (3\text{-}26)$$

The average width for the atomic block in the atomic subscale was (22.48nm) and for the adhesive subscale has been found to be equal to (185.72nm).

To calculate the distance between atomic blocks, the root mean square of the distance between asperities λ_q equations was used, where Δ_q is the root mean square average slope of the profile and is found as follows:

$$\lambda_q = 2\pi \frac{R_q}{\Delta_q}, \quad \text{where } \Delta_q = \sqrt{\frac{1}{n-1}\sum_{i=1}^{n} Si^2} \quad (3\text{-}27)$$

where S_i is the slope of the profile at each point along the profile. Δ_q was found (0.0245) and according to this root mean square average slope, the root mean square of the distance between asperities λ_q for the atomic subscale has been calculated to be (64.35nm).

The multiscale hierarchical fixed-gap model has been implemented in the specific feature to reflect the contact between the microgear MEMS teeth when they are in the meshing state. The results of the implementation are illustrated as follow, from Equation (3-7) we can get Figure (3-20) that shows the friction force along the sliding distance. Figure (3-21) shows the force of adhesion in the fixed-gap model. The adhesive force is constant because the multiscale structure is fully contact within adhesive layer of the surface, i.e. $G < h_0$ (see Figure (3-6) and Figure (3-9)). The total coefficient of friction during the sliding distance can be obtained from Equation (3-8) and illustrated in Figure (3-22) which consists of the energy lost due to dissociations of both chemical and vdW bonds and also the energy loss by the elastic interlocking component.

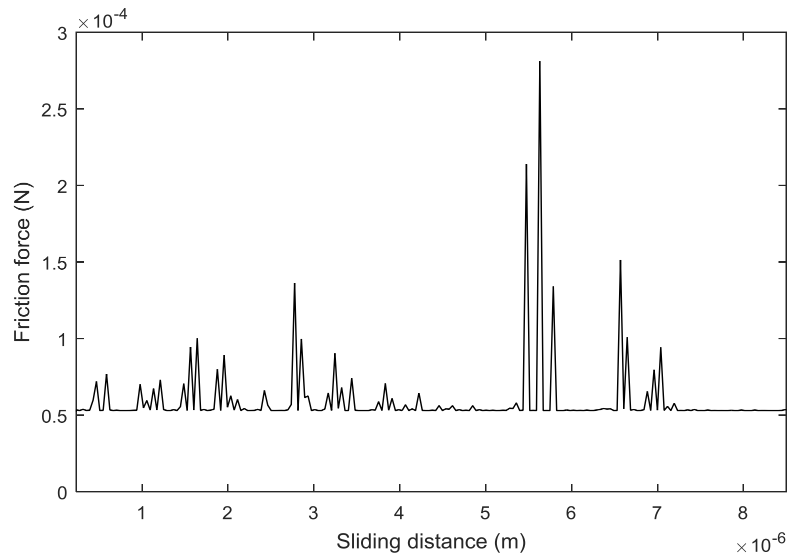

Figure 3-20 Friction force over sliding distance in the fixed-gap model

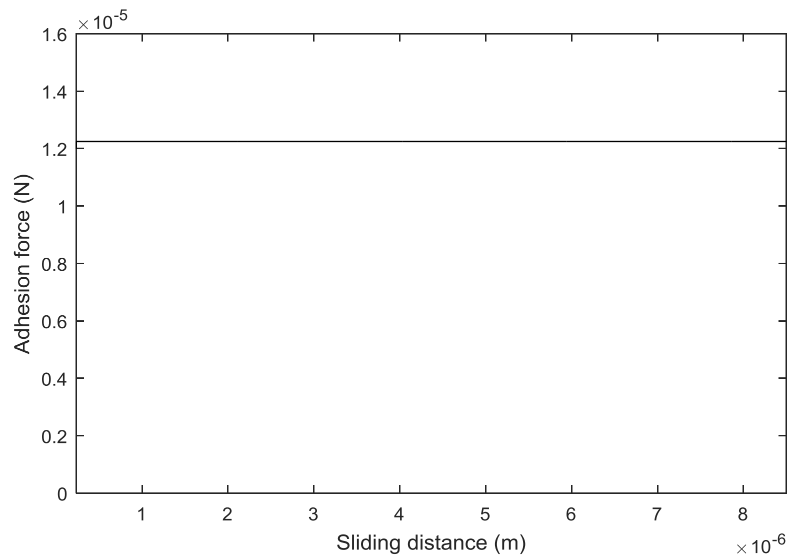

Figure 3-21 Adhesion force over sliding distance in the fixed-gap model

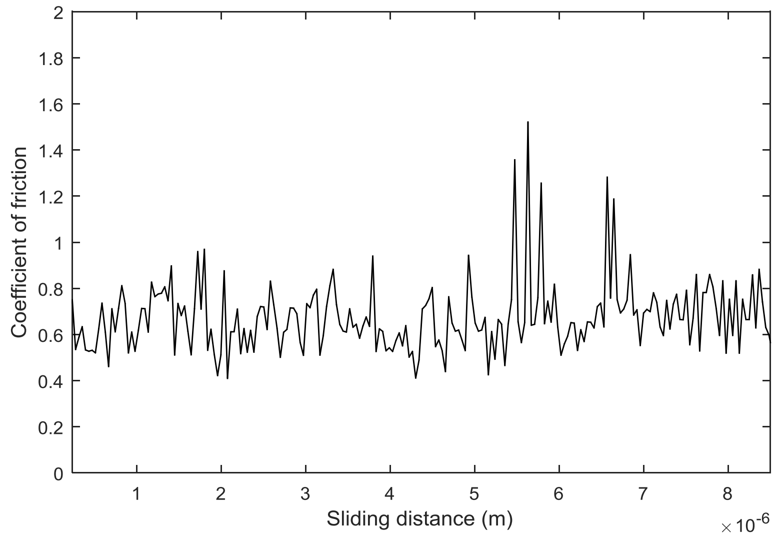

Figure 3-22 Coefficient of friction over sliding distance in the fixed-gap model

The compression force acting on the nanostructure representing a surface asperity is shown in Figure (3-23). The force is calculated over the contact sliding distance in the fixed-gap model

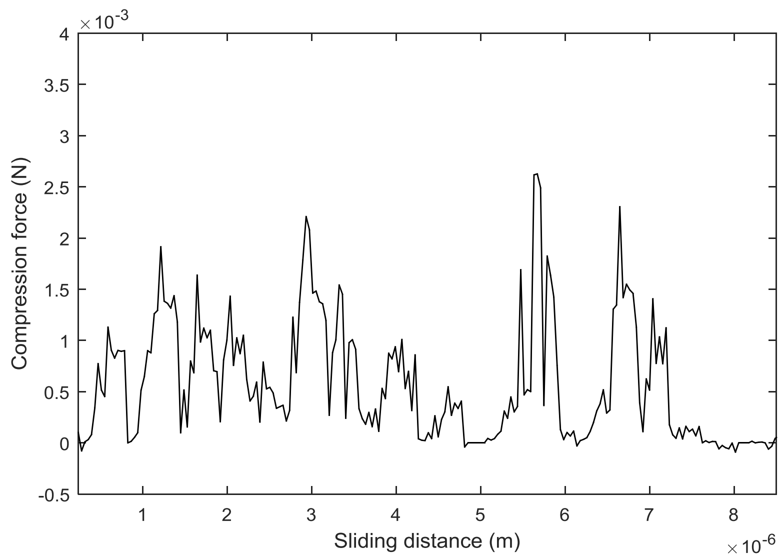

Figure 3-23 Compression force acting on the nanostructure over sliding distance in the fixed-gap model

The normal stress on the atomic scale elements is shown in Figure (3-24). The normal stress is calculated over the sliding distance in the fixed-gap model.

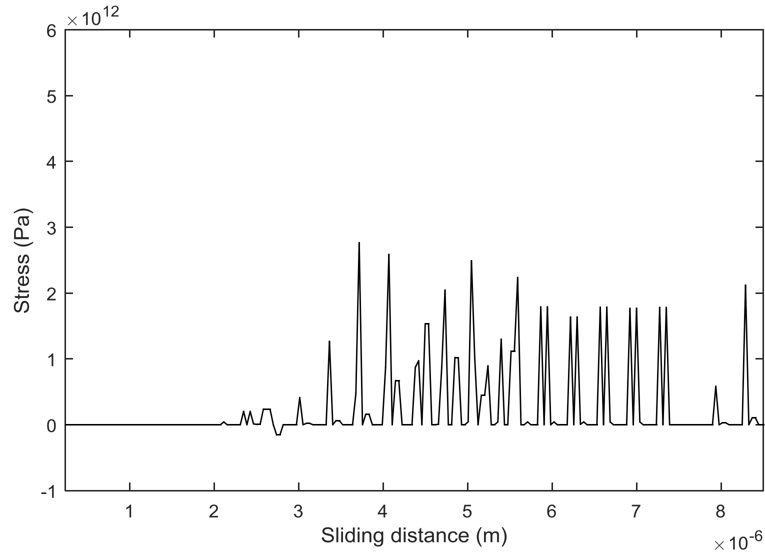

Figure 3-24 Normal stress on the atomic scale element over sliding distance in the fixed-gap model

However, the total shrinking over the nanostructure is shown in Figure (3-25). This value was calculated over the sliding distance in the fixed-gap model.

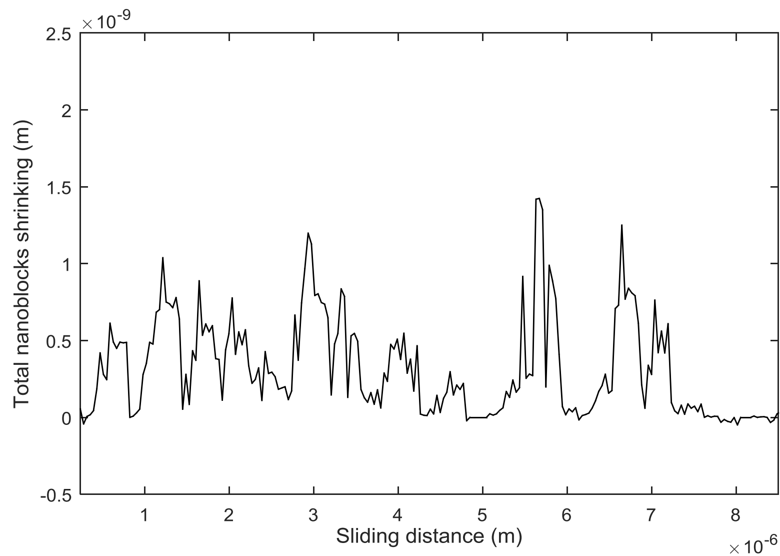

Figure 3-25 Shrink value in nanostructure calculated over sliding distance in the fixed-gap model

3.4.2 Simulations for the Multi-scale Hierarchical Structure with a Vertical Degree of Freedom

In this model, the main structure of the multiscale frame has been characterised depending on the amount of area, which has been calculated in the specific subscales (see Figure (3-26). The model has been designed to consist of a hierarchical multiscale asperity structure and the supported rigid surface meshed, in addition to the sliding relative motion. Silicon roughness profile has been obtained by using the Park Systems XE-100 (AFM device) in the laboratory of the High Value Manufacturing group, Cardiff University, as shown in Figure (3-18). The hierarchical multiscale asperity nanoblock is characterised to reflect all of the physical and mechanical properties for the actual surface of the microgear MEMS tooth.

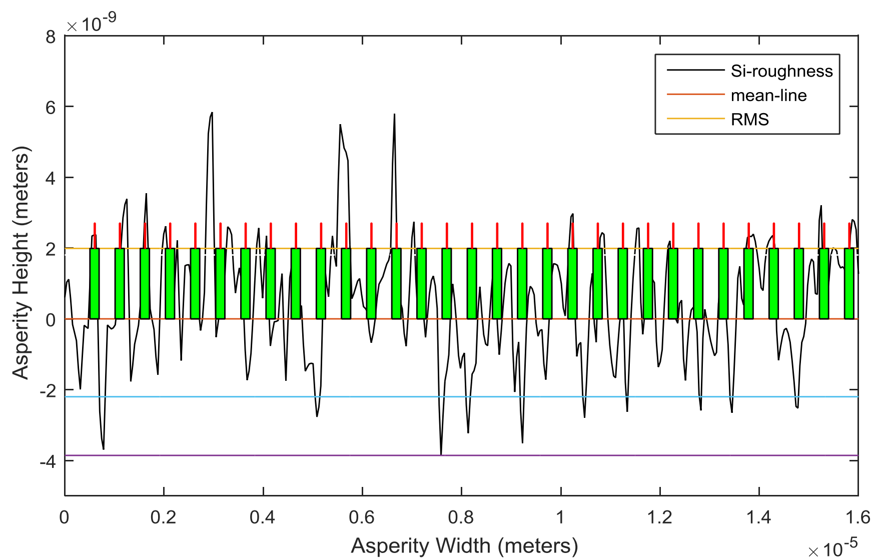

Figure 3-26 Computation of the width of the chemical and van der Waals interaction domain for silicon roughness profile

The height and width of the adhesive subscale asperities have been calculated by determining the area of the surface, which is limited between the mean line and the root

mean square for the silicon roughness profile. This amount of surface area is then equally redistributed, as shown in Figure (3-27).

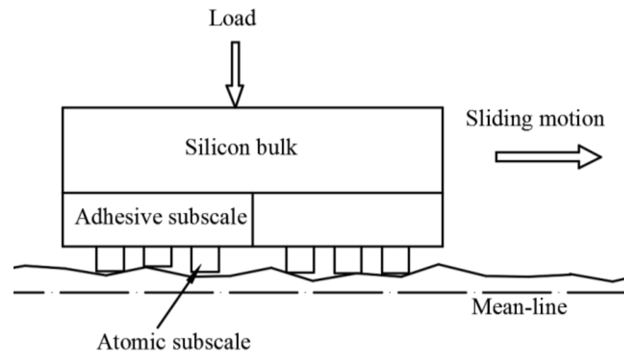

Figure 3-27 A multi-scale hierarchical structure with a vertical degree of freedom

Similarly, the height and width of the atomic subscale asperities, as well as the distance between them, were determined by analysing the measurement of the silicon surface roughness at atomic subscale by using an AFM device (see for example Savencu, 2016, Almuramady and Borodich, 2016 and 2017).

3.5 Estimation of the COF Taking into Account the Dissociation of the Chemical and vdW Bonds for Silicon

In the current model with a vertical free degree of freedom, we can calculate the estimated coefficient of friction for one sub-adhesive asperity, assuming that all of the atomic subscale asperities on its surface have established chemical and vdW interactions. As described previously, the microgear silicon MEMS surface is measured by AFM to obtain the nanoscale roughness.

The geometry of the atomic subscale and adhesive subscale asperities has then been calculated as shown in Figures (3-27) and (3-28) depending on the area distribution concept as shown in Figure (3-26). In this geometry, the width of the adhesive subscale

asperity has been calculated to be equal to195 nm, the atomic subscale asperity width equal to 19.5 nm.

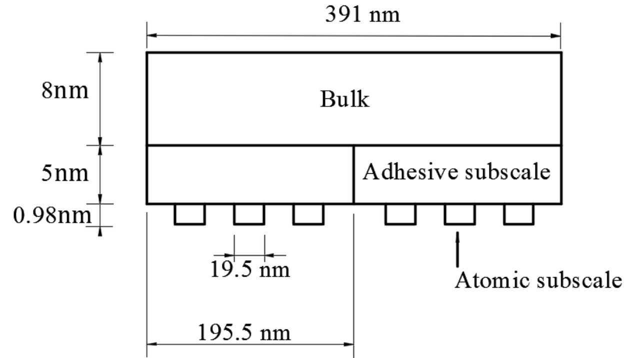

Figure 3-28 Multiscale hierarchical structure with vertical free degree of freedom

For a pure silicon surface, the dissociation energy due to breaking the chemical bonds between two silicon atoms is equal to 327 kJ/mol (Dean 1992 and 1999), hence the energy of one chemical bond is 5.42×10^{-19} J.

It is not mentioned clearly in the literature what energy is required to break one vdW bond. It is known that this energy has to be much lower than the chemical energy, so it can be assumed that this energy is 100 times less than the chemical energy (see Savencu, 2016). Therefore, the dissociation energy, which is released by breaking one vdW bond, U_{vdW}, can be calculated as equal to (5.42×10^{-21} J).

The silicon atom radius has been calculated from the cubic structure of the silicon particle to be equal to 1.175 Å (see Figure 3-29). Thus, the diameter of one chemical bond is D_{chem} = 2.35 Å:

$$r_{Si} = \frac{\sqrt{3}}{8} a = \frac{\sqrt{3}}{8} \times 5.43 = 1.175 \text{ Å}$$

where a is the silicon lattice constant.

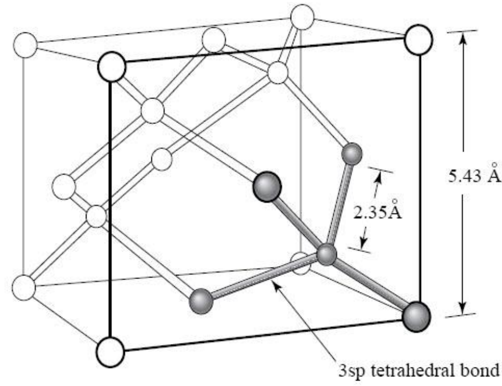

Figure 3-29 Silicon crystal structure

The width of the atomic subscale asperity is $w_{atomic} = 19.5$ nm. Therefore, the number of chemical interactions for fully overlapping atomic subscale block is:

$$N_{chem} = \left(\frac{w_{atomic} \times L_{chem}}{D_{chem}{}^{2}}\right)^{2} = 7388.6$$

Similarly, the number of vdW bonds per one adhesive subscale-asperity can be calculated from the width of the vdW contact to the diameter of the bond. The density of the atoms that create vdW bonds is the same as the density of the atoms involved in chemical bonds. From this, we can find the average number of vdW interactions per one adhesive subscale-asperity to be as follows in N_{vdW}:

$$N_{vdW} = \left(\frac{w_{vdW} \times L_{vdW}}{D_{chem}{}^{2}}\right)^{2} = 688546.8$$

When the adhesive subscale-asperity moves along the distance length *x* on the microgear silicon MEMS tooth surface, the energy lost via the dissociation of chemical and vdW bonds can be calculated from the equation of U_{diss}:

$$U_{diss} = n\,(N_{chem}U_{chem} + N_{vdW}U_{vdW})\frac{x}{D_{chem}}$$

Where n is the number of nanoblocks in contact.

$$N_{chem}\,U_{chem} = 4 \times 10^{-15}\text{J}$$

$$N_{vdW}U_{vdW} = 3.73 \times 10^{-15}\text{ J}$$

This can be represented as the energy dissipated by the force of friction when moving over the sliding distance length x on the microgear silicon MEMS tooth surface. Therefore, this energy equation can be written in another way with respect to friction force:

$$U_{diss} = F_f\,x \rightarrow F_f = \frac{U_{diss}}{x} \tag{3-28}$$

where F_f is the force of friction along the distance x. However, the friction force can also be written with respect to the coefficient of friction:

$$F_f = \mu_{aparr}(F_{ext} + F_{adh}) \tag{3-29}$$

where F_{ext} is the external force applied to compress the adhesive subscale and atomic asperities and F_{adh} is the force of adhesion. The apparent coefficient of friction over the sliding distance x can then be expressed as:

$$\mu_{appar} = \frac{U_{diss}}{(F_{ext} + F_{adh})\,x} \tag{3-30}$$

The adhesive subscale and atomic asperities are compressed only in their elastic limit and the mechanical behaviour of these asperities will be perfectly elastic due to Polonsky-Keer effect (see section 2-2). The external force has been assumed to be the same as that used in most of the literature related to MEMS devices, which is $F_{ext} = 25$ μN (see Patton and Zabinski, 2005 and Rezvanian et al., 2007).

Adhesion force, or the molecular attraction between surfaces, has been taken into account in both the fixed gap and the vertical degree of freedom models, which also means that adhesion force arises between asperities when they approach each other and then finally come into contact. Adhesion force has been calculated depending on the Maugis approximation to the adhesion zone between the contacting surfaces. This approach assumes that the surface profile has been covered by an adhesive layer with a thickness that is equal to the specific height. In the current work, the thickness is assumed to be equal to the height of the adhesive subscale asperity. The particle in the atomic subscale asperity will jump in contact as soon as it reaches this adhesive layer and it creates a junction between the surfaces. The force needed to pull-off this junction, or adhesion to detach the asperities from each other and leave the adhesion zone, has been calculated here as the force of adhesion, as in the equation below:

$$F_{adh} = n\, F_{adh1} \tag{3-31}$$

where F_{adh} represents the force of adhesion between the counterparts of the microgear MEMS tooth surfaces, n is the number of nanoblocks within contact and F_{adh1} is the pull-off force needed to detach one atomic block, which can be found by:

$$F_{adh1} = (8\pi w E^{*} C_{NS} a^{3})^{1/2} \tag{3-32}$$

where w is the work of adhesion according to Tas et al., (1996) and Kendall (2007), E^* is the contact modulus, C_{NS} is the coefficient of no-slip (Borodich and Keer, 2004, Borodich, 2014) and a is the half distance of contact according to the hertz line contact theory.

$$C_{NS} = (1 - \upsilon)\, ln(3 - 4\upsilon)/(1 - 2\upsilon) \tag{3-33}$$

According to Lomboy (2011) the work of adhesion can found by:

$$w_{12} = \frac{A_{12}}{12\pi D_o^2} \tag{3-34}$$

The force of adhesion for one atomic subscale asperity has been assumed to be equal to the pull-off force according to non-slip Boussinesq-Kendall theory (see Almuramady and Borodich, 2017):

$$F_{adh1} = \sqrt{8\,\pi\,w_{12}\,E^{*}C_{NS}\,a_1^3} = 3.75\times\,10^{-5}\mathrm{N}$$

The work of adhesion (w_{12}) is equal to the vdW energy between two silicon surfaces, which is calculated as (Tas et al.,1996):

$$w_{12} = \frac{A_{12}}{12\,\pi\,D_0^2} = \;1.31\;\mathrm{J/m^2}$$

where A_{12} is the silicon Hamaker constant $A_{12} = 1.1\;\times\;10^{-18}$ J and D_0 is the separation distance for silicon equal to $D_0 = 2.56$ Å (Tas et al., 1996). Hamaker constant also can be defined as (Hamaker, 1937):

$$A_{12} = \pi^2\rho_1\rho_2 C$$

where ρ_1 and ρ_2 are the number of atoms per unit volume, and *C* is the London-vdW constant. Hamaker's approach to calculate the vdW energy between bodies was based on pairwise integration, which is the same as Bradley's (1932) approach to spherical particles. Hamaker (1937) presents the results in a manner suitable for numerical calculations and extends the method for other surfaces. Hamaker's approach assumes that the forces are additive and non-retarded.

Young's modulus for silicon has been taken to be E = 161 GPa, and Poisson's ratio ν = 0.23 (Teodorescu et al, 2009); thus, the reduced contact modulus is:

$$E^{*} = \frac{E}{2\,(1-\nu^{2})} = 85 \text{ GPa}$$

The no-slip coefficient (Borodich, 2014) is:

$$C_{NS} = \frac{(1-\nu)\ln(3-4\,\nu)}{1-2\,\nu} = 1.044$$

The radius of contact a_1 is approximated as half the width of the vdW interaction step of the nano-asperity:

$$a_1 = \frac{w_{adhesive}}{2} = 97.5 \text{ nm}$$

Therefore, the force of adhesion for one atomic subscale asperity F_{adh1} will be known, so the total force of adhesion can be calculated because it is assumed that all atomic subscale asperities on the edge of the adhesive subscale asperities are in contact with the counter microgear tooth surface:

$$F_{adh} = n\,F_{adh1} = 3.386 \times 10^{-4}\text{N}$$

The apparent coefficient of friction can now be calculated:

$$\mu_{appar} = \frac{U_{diss}}{(F_{ext} + F_{adh})\,x}$$

$$\mu_{appar} = \frac{n(N_{chem}U_{chem} + N_{vdW}U_{vdW})\dfrac{x}{D_{chem}}}{(F_{ext} + F_{adh})x}$$

$$\mu_{appar} = \frac{n(N_{chem}U_{chem} + N_{vdW}U_{vdW})}{(F_{ext} + F_{adh})D_{chem}} = 0.82$$

3.6 Results of Numerical Simulations Using Various Parameters of Contact

3.6.1 Non-functionalised Silicon Microgear MEMS Tooth

When the silicon microgear MEMS teeth work in a high vacuum environment, the possibility of stiction and high friction between microgear MEMS teeth surfaces will increase rapidly because the source of surface contamination is progressively removed; in other words, there is no contamination between the surfaces. Therefore, because of the high stiction between the contacting microgear MEMS silicon teeth surfaces, the chemical interactions that are established between the particles in the counterpart's surfaces will be significant. These interactions will create a permanent junction point by so-called cold welding (see Bowden and Leben, 1938, Bowden and Tabor, 1943 and Lu et al., 2010). These welded zones will restrict the work of the microgear MEMS teeth and sometimes will not even allow them to work. To keep the continuity of the sliding motion between the teeth surfaces, the tangential force applied should overcome the stiction; in other words, the chemical interactions that have been established between the surfaces.

The results in this section have been obtained from the simulations of the multiscale hierarchical structure with a vertical degree of freedom (see section 3.4.2). Figure (3-30) shows the total energy dissipated through the different mechanisms between the counterpart's surfaces. The majority of dissipated energy comes through the dissociation of chemical bonds (more than 60%) and less that 1% through the elastic interlocking between the counterpart's surfaces and the rest of energy dissipated comes through the dissociation of van der Waals interactions.

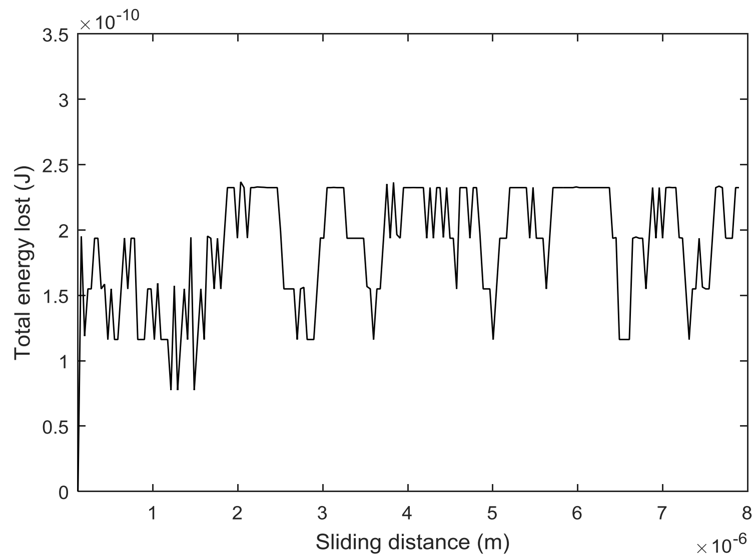

Figure 3-30 Total energy dissipated through different mechanisms between counterparts surfaces

The coefficient of friction of the silicon microgear MEMS tooth surface against another silicon microgear MEMS tooth surface as a function of instantaneous time was calculated through a numerical simulation of dry adhesive frictional model.

Figure (3-31) illustrates the coefficient of friction for non-functionalised silicon microgear MEMS teeth surface during the sliding distance.

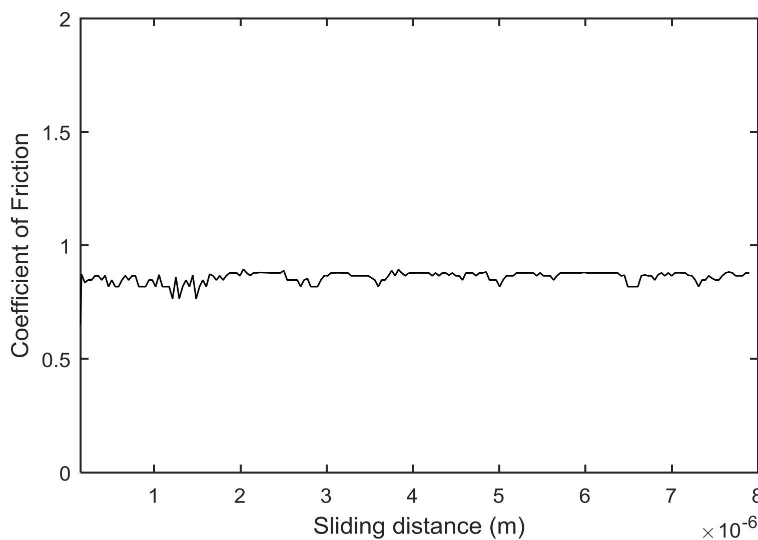

Figure 3-31 Coefficient of friction for non-functionalised coating teeth surface

The friction force was determined by measuring the total energy dissipated in the contact area between the surfaces and during the whole sliding distance through different mechanisms, such as dissociation of chemical and vdW bonds or via the elastic interlocking between surfaces.

In Figure (3-32) shows the friction force, which has been calculated for non-functionalised silicon microgear MEMS teeth surface.

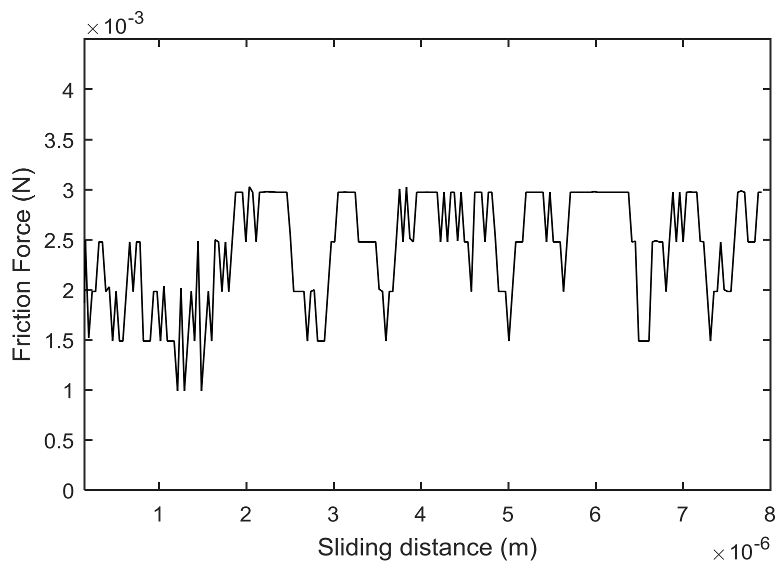

Figure 3-32 Friction force for non-functionalised microgear MEMS teeth surface

For further clarification, a magnified section of the friction force for a non-functionalised tooth surface is illustrated in Figure (3-33).

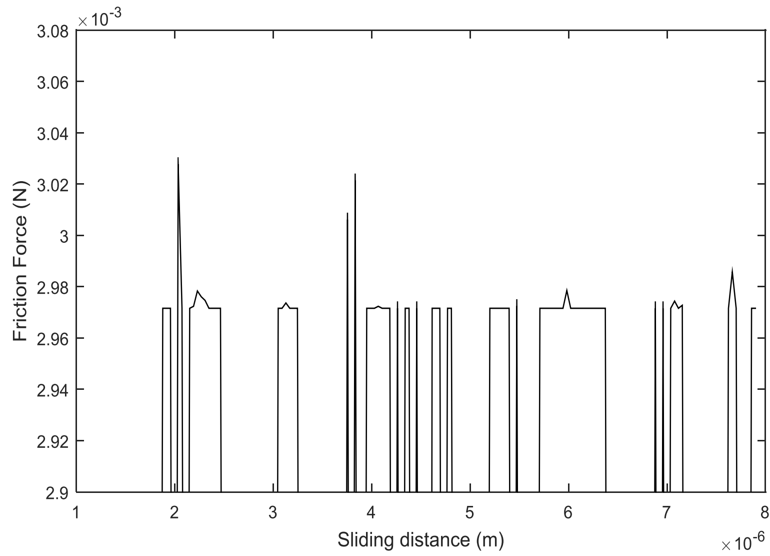

Figure 3-33 Magnified section of friction force for non-functionalised coating teeth surface (notice the scale of friction force in the section)

Figure (3-34) illustrates the distribution of the adhesion force along the silicon microgear MEMS teeth during the sliding distance. The maximum value of the adhesion force is 3.2×10^{-4} N, this value is closed to the value that has been obtained from Equation (3-31).

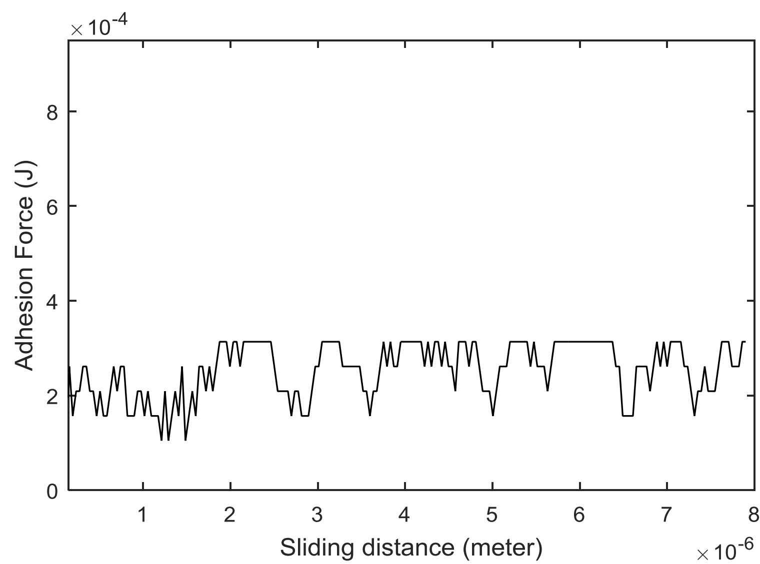

Figure 3-34 Adhesion force for non-functionalised coating teeth surface

The dissipated energy due to the elastic interlocking of the asperities is the energy lost when the asperities of the contacting counter-parts microgear MEMS tooth surfaces are elastically deformed. Figure (3-35) shows the elastic behaviour of the adhesive subscale and atomic subscale asperities.

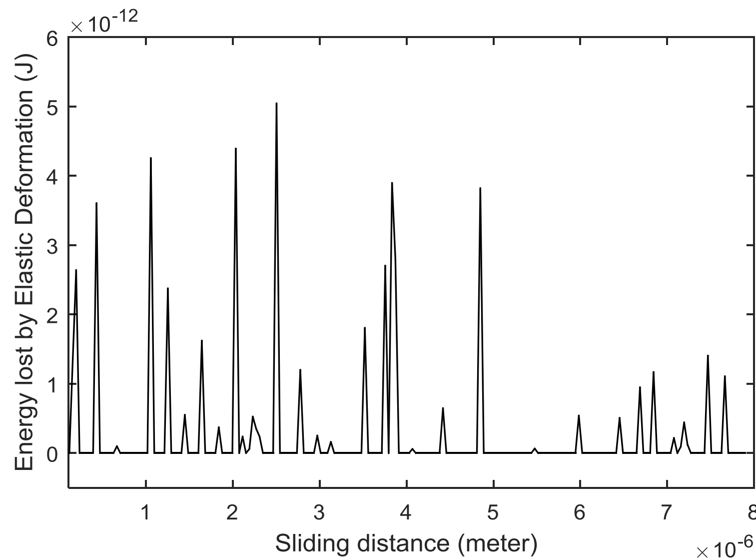

Figure 3-35 Energy dissipated via the elastic interlocking between the counterpart's surfaces

3.7 Discussion of the Influence of Environmental Conditions on Dry Friction and Extensions of Models to Non-crystalline Coatings

Classical microscopic tribological systems can be described as a science that deals with the phenomena of contact of an object's surface and it relative motion, friction, adhesion and so on. At the nanoscale, the effects of phenomena such as friction, adhesion and also the interactions may be very effective or it may significantly restrict the reliability of MEMS devices, or it may not allow them to work at all (see Maboudian et al., 2002). Some of MEMS devices suffer from contact problems, especially at the nanoscale. Therefore, contact models need to be developed to study nanoscale structures.

Researchers who wish to get a full understanding of the nonlinear contact problems in MEMS devices at different scales face many obstacles. For example, the interaction between physical bodies at the nanoscale is one of the most important features in the structures of nanomechanics. These disciplines have to use equations that are adjusted to the specific character of the nanometre length scale, which is in addition to the application of the mechanical system and solving these problems at the nanoscale (Borodich et al., 2016). These physical and chemical interactions, which work in small distances such as molecular adhesion caused by vdW forces, chemical interactions, and other various surface forces, are among the objectives of the current work.

3.8 Conclusions to Chapter 3

The simulation of the multiscale, multi-blocks hierarchical model has been developed to work with silicon MEMS surfaces. The current simulations have been based on the modification of single block model, which has been developed early by Savencu and Borodich (2015). The model takes into the account the chemical and physical interactions that may occur between surfaces in a vacuum environment. The surface roughness analysis have showed that MEMS surface does not have any microscale roughness and, hence, there is no plastic deformation. The model has been used to simulate various tribological phenomena, including friction and adhesion of surfaces. The results of the numerical simulations show that high stiction occurred between pure and clean silicon MEMS surfaces when they work in a vacuum environment.

Chapter 4 Modelling of the Frictional Work of a MEMS Gear

4.1 Introduction

In the previous chapter, a new model was developed to compute the friction force between the silicon surfaces by using the energy dissipated through different physical and chemical mechanisms between two parallel nominally flat surfaces over a given sliding distance. While in this chapter, the model was used to cover the surface of the microgear MEMS tooth surface. More specifically, the model was applied to the curved teeth surfaces using nanoblocks consisting of atomic and adhesive subscales located at varying levels. The microgear roughness analysis, geometry and theories that are used in the calculations will be discussed. Simulations for the experimental study of MEMS teeth roughness and modelling have been conducted for silicon MEMS real topography.

4.2 Microgear MEMS Surface Topography

In the current models, silicon topography is the essential and important base to test and configure the main structure of the model. The roughness parameters have been calculated and implemented in the hierarchical model, such as the root mean square of the asperities RMS or R_q, arithmetic height of asperities R_a, and the average width of the asperities is used to prepare and build the frame of nanoasperity blocks (more details in section 4.2.3).

4.2.1 Experimental Study of MEMS Teeth Roughness Modelling

The geometry of silicon asperities (height and width of the atomic and adhesive subscale asperities), as well as the distance between them, were determined by analysing the measurement of the silicon surface roughness at nano and atomic scale by using an AFM device. The silicon roughness was measured using the XE-100 AFM from Park Systems. Brousseau et al. (2015) has described this AFM device in detail. The height distribution of the roughness data was defined as series of point along the surface of the sample. Figure (4-1) shows the measurement data of the silicon sample after removing the overall profile slope from AFM data.

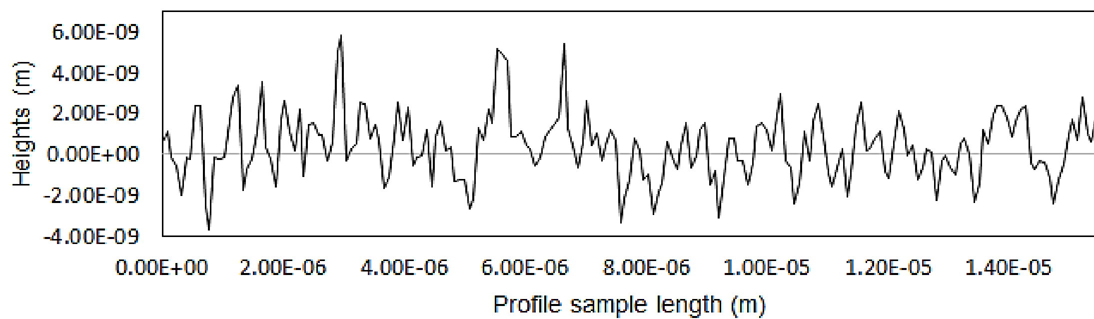

Figure 4-1 Section of silicon AFM roughness profile

From Figure (4-1) it can be seen that the silicon roughness profile data can be assumed to be a series of heights y_n, which were measured at each x where x_n=7.8×10^{-8}m, where n= 0, 1, 2, 3,…...n. Therefore, as illustrated in Figure (4-2) the interval Δx between two sequent roughness points was (7.8×10^{-8}m).

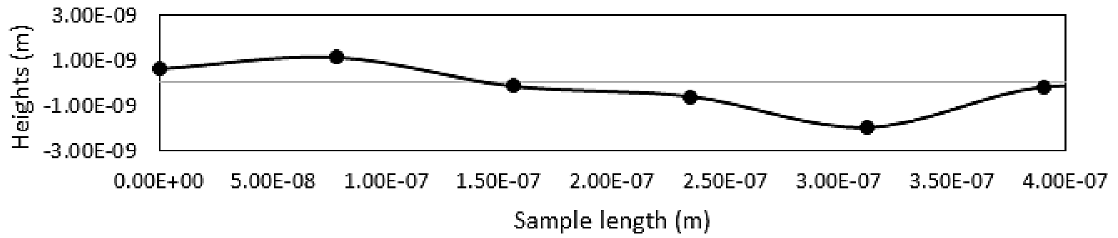

Figure 4-2 A small segment of silicon AFM roughness

For a programming requirement, an interpolation for the roughness data has been done by using the shape-preserving interpolant function in MatLab software. After this interpolation, as shown in Figure (4-3), the new interval Δx between two sequent silicon roughness points became 3.9×10^{-8}m.

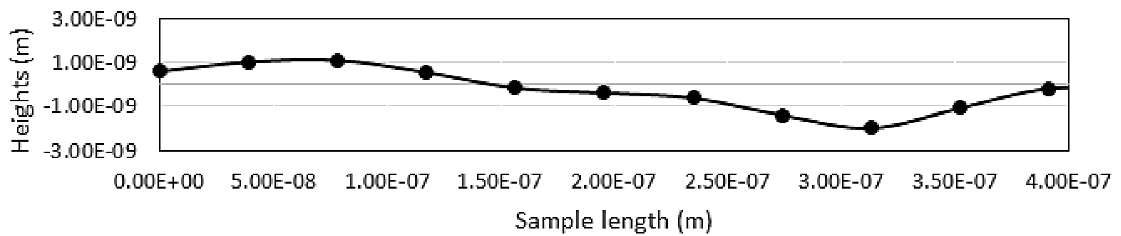

Figure 4-3 Resulting profile using the shape-preserving interpolant function to interpolate silicon roughness

4.2.2 Modifications and Manufacturing Techniques of MEMS Microgears

The rough surfaces that have been used in modelling the microgear silicon MEMS tooth structure are prepared and modified in the following steps. First, the real silicon topography has been measured by an AFM device, as shown in Figure (4-1). The distance between the measured roughness spots Δx was 7.8×10^{8}m, and this is the key parameter in the multiscale hierarchical model. Therefore, the shape preserving function and MatLab software are used to decrease the distance between the point to become $3.9 \times$

10^8m, as shown in Figures (4-2) and (4-3). The obtained silicon roughness profile has then been superimposed on the smooth surface of the microgear, which has been calculated by the classical Hertz line contact theory with respect to the dimension of the meshing microgear MEMS tooth that was considered in this study. The preparation process of the silicon microgear profile will be presented graphically in the next sections.

The whole preparation steps were done for both the micropinion and the microgear in the meshing gear system. Finally, the micropinion and the microgear are assumed to be in a sliding contact motion to simulate the influence of adhesive dry friction between the microgear MEMS teeth surfaces.

4.2.3 Statistical Analysis of the MEMS Gear Surface

A real silicon profile, which was tested by an AFM, has been used in the calculation to characterise the hierarchical multiscale structure that is shown in Figure (4-1). The silicon profile that has been determined represents a series of points along the peaks and valleys of the surface topography. A large number of roughness parameters are needed to describe the characteristics of the surface, especially at nano or micro scale. For example, Whitehouse (1982) and Borodich et al. (2015) have pointed that there are more than 30 parameters and functions related to roughness property descriptions. However, they found that it is difficult to predict which of these parameters can cover the specific surface characteristics of different materials.

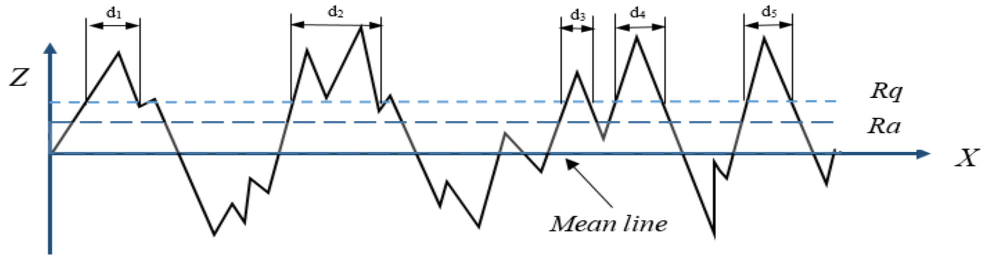

Figure 4-4 The roughness parameter with respect to mean line (adapted from Dagnall, 1980)

The roughness parameters that have been considered in the current study to analyse the silicon surface profile were related to the height, width and shape of the asperities on the surface. Therefore, the features of the hierarchical multiscale model can be found from the surface roughness parameters, such as the root mean square of the asperities RMS or R_q, arithmetic height of asperities R_a, and the average width of the asperities and so on. The mathematical expressions of the parameters that were considered in the calculation are illustrated in the following equations:

$$R_a = 1/n \int_{i=1}^{n} hi \tag{4-1}$$

$$R_q = \sqrt{1/n \int_{i=1}^{n} hi^2} \tag{4-2}$$

where hi is the height of the silicon profile. The R_a and R_q have been considered as key parameters to calculate the dimensions of the multiscale hierarchical structure, $R_a =$ 1.3616 nm and $R_q = 1.6235$ nm. The first set of asperities is found in the multiscale structure, which is called the atomic subscale, where the chemical interactions are significant and there is a high possibility to occur. The next scale is the adhesive subscale, which lies between the bulk material of silicon surface from inner side and the atomic

subscale from outer side. In this scale of the structure, the vdW interactions are dominant. First subscale has been taken as atomic blocks; hence, the height of this subscale was less than (1nm). The second subscale of the nanoblock has been taken as a slab with height of (5nm).

The width of the subscale of the block was calculated according to the formula below for the first and second subscales:

$$d = \frac{1}{n}\sum_{i=1}^{n} d_i \tag{4-3}$$

The average width for the atomic subscale has been found to be equal to (19.5 nm) while the width of adhesive subscale has been calculated to be equal to (195.5 nm) without any space between the nanoblocks.

To calculate the distance between atomic subscale blocks in the first subscale, a surface roughness parameter named the root mean square of the distance between asperities (λ_q) has been used as in the following (see Dagnall, 1980):

$$\lambda_q = 2\pi \frac{R_q}{\Delta_q} \tag{4-5}$$

where Δ_q represents the root mean square average slope of the asperities on the silicon roughness profile and can be found as in the following equation:

$$\Delta_q = \sqrt{\frac{1}{n-1}\sum_{i=1}^{n} {S_i}^2} \tag{4-6}$$

Where S_i is the slope of the asperities of silicon profile at each point along the surface. Δ_q was found to be equal to (0.0241) and according to this root mean square average

slope, the root mean square of the distance λ_q between atomic blocks of asperities at the atomic subscale in the hierarchical multiscale structure has been found to be equal to $(58.4nm)$.

The main assumptions of the current multiscale hierarchical model is that it works in the elastic range of deflection and the nanoblocks are modelled as elastic square rods, so there is no plastic effect. Therefore, the force can be found by using the following equation:

$$F = \frac{EA}{H}\,\delta \qquad (4\text{-}7)$$

where F is the force to which an atomic or nanoblock is subjected, H is the height of the block, E is the elastic modulus of silicon and A is the area of the cross-section of the block, which is under the influence of the subjected force. The total deflection at each subscale in the hierarchical structure was calculated and then the resultant force was found, which is represented by the normal nominal force at each spot along the length of silicon profile of the microgear MEMS tooth.

4.2.4 Specific Features of MEMS Surface Scales

Multiscale hierarchical nanoblocks are superimposed on the silicon gear tooth surface within gaps to simulate the real tooth roughness and they have been used as a new specific approach. This approach has been applied for the first time in the modelling of the microgear silicon MEMS tooth surfaces by implementation of the Polonsky and Keer effect in the simulation of adhesion and friction of dry contact. The surfaces of the microgear MEMS were assumed to be clean and they are contacting in vacuum environment. It is shown that the MEMS tooth surface does not have any microscale roughness. Therefore, there is no plastic deformation of nanoasperity due to the

Polonsky-Keer effect. The adhesion layer is defined similarly to the Maugis approximation. The force of adhesion for each nanoasperity is assumed to be equal to a pull-off force as in the Boussinesq-Kendall model.

4.3 Contact Geometry of Microgears in MEMS.

The geometry and tribological behaviour of rough surfaces have played a major role in the reliability of the structure and operation of MEMS and other micromachined devices, especially for the microgears that have been used in different types of MEMS devices. Microgears must have a high resistance to wear to ensure high mechanical reliability as well as low friction to ensure transmission efficiency (Takeuchi et al., 2000). The failures of the mechanisms in microgears are mostly caused by stiction and wear between the contacting surfaces. Recent studies of the contact problem in microgears have shown that friction is a process in which very complicated adhesion is involved. The mechanisms responsible for adhesion during friction are difficult to investigate (Krim, 2002). In MEMS and micromachined devices, for example, the failures mechanisms are often caused by friction, stiction and wear of the contact surfaces (Tanner, 2000).

Figure (4-5) shows an overview of the microgear system that has been considered in this study. This system consists of a pair of spur microgears that are meshed with each other, which is often used in MEMS and other different micro-machines. Involute gear geometry is chosen for use in this study. MEMS gears are usually very small and relatively thin, with thickness of the order of $2\mu m$. The dimensions of the microgear MEMS system that is used in this thesis are as follows: the diameter of the micropinion is $81\mu m$ and the number of teeth is 19. While the diameter of the microgear is $303\mu m$ and the number of teeth is 76, as in Teodorescu et al. (2007, 2008 and 2009).

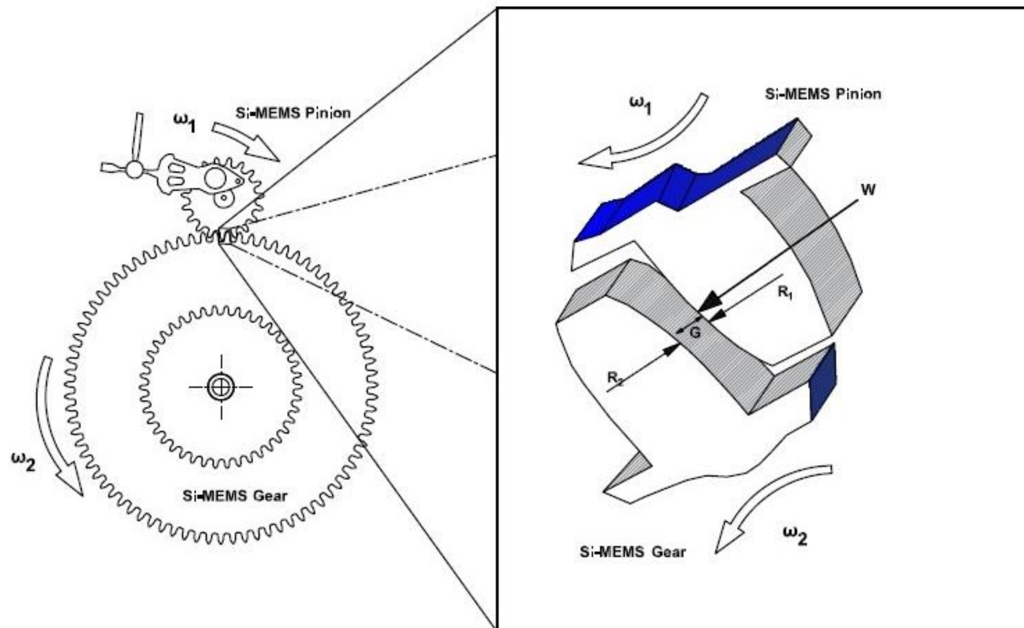

Figure 4-5 Scheme for the MEMS gears and two meshing gear teeth (modified from Teodorescu et al. 2009)

Sliding contact between two microgear teeth in the meshing process as they transmit load and torque is an example of a dry contact phase and this is the main objective of the current study.

For spur microgears, this can be modelled as a contact line problem. A detailed analysis of these contacts presents a significant challenge because the contact geometry and operating conditions are constantly changing throughout the meshing cycle. The contact between two meshing involute gear teeth progresses along a straight line that is tangential to the base circles of both gears, as shown in Figures (4-6) and (4-7). The angle of inclination of this line, which is termed the line of action, to the line perpendicular to the line of centres A_1A_2 is the pressure angle ψ (which is constant for teeth of involute form).

In addition, c is the distance between the current point of contact and the pitch location, and is a value of how far along the line of action the contact occurs. It is zero at the pitch

point and positive in the direction of motion of the gear teeth. It starts at the first point of contact and finishes at the last point of contact or, in the other words, along the length of the path of contact, as shown in Figure (4-6). In this sketch, the numbers 1 and 2 have been used as a subscript to refer to the micropinion and microgear, respectively. Subscripts (*b)* and (*a*) are used to distinguish the base and the addendum circles, respectively.

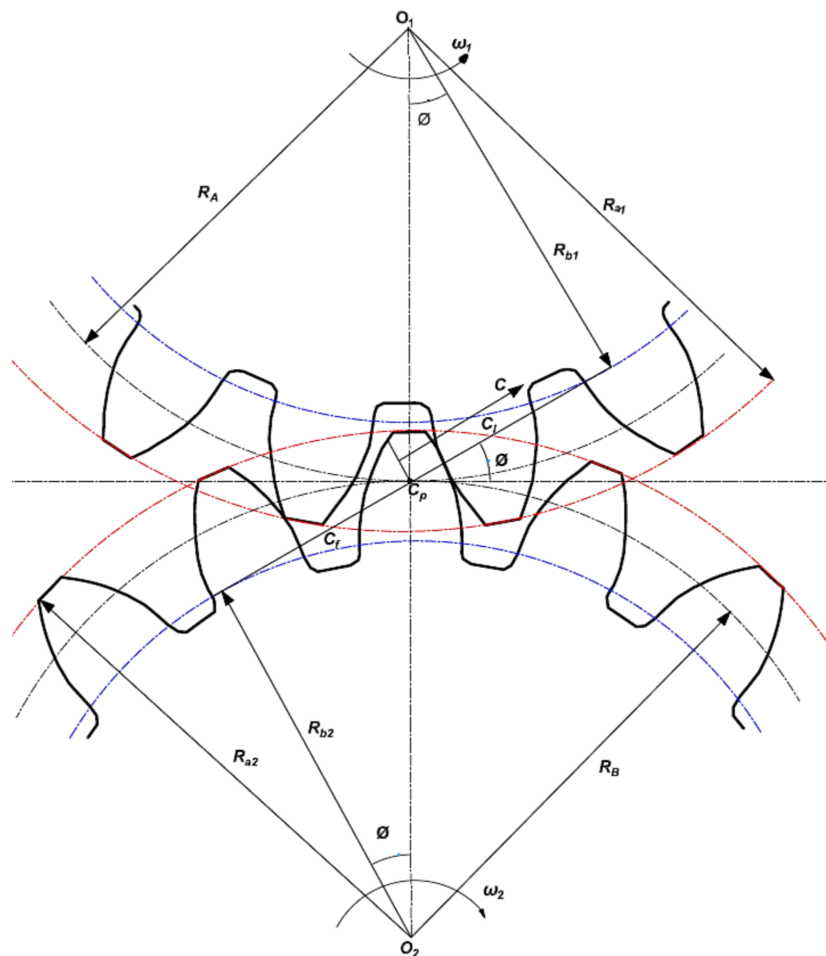

Figure 4-6 Contact path of meshing microgears MEMS

Davies (2005) has discussed the contact problem between two meshing teeth using classical linear contact model (Timoshenko and Goodier, 1970 and Johnson, 1985). The

contact between two meshing teeth can be simplified as a contact between two parallel cylindrical rollers and the curvature of both surfaces can be calculated for this line contact problem. Figure (4-7) shows the simplified contact geometry of involute teeth.

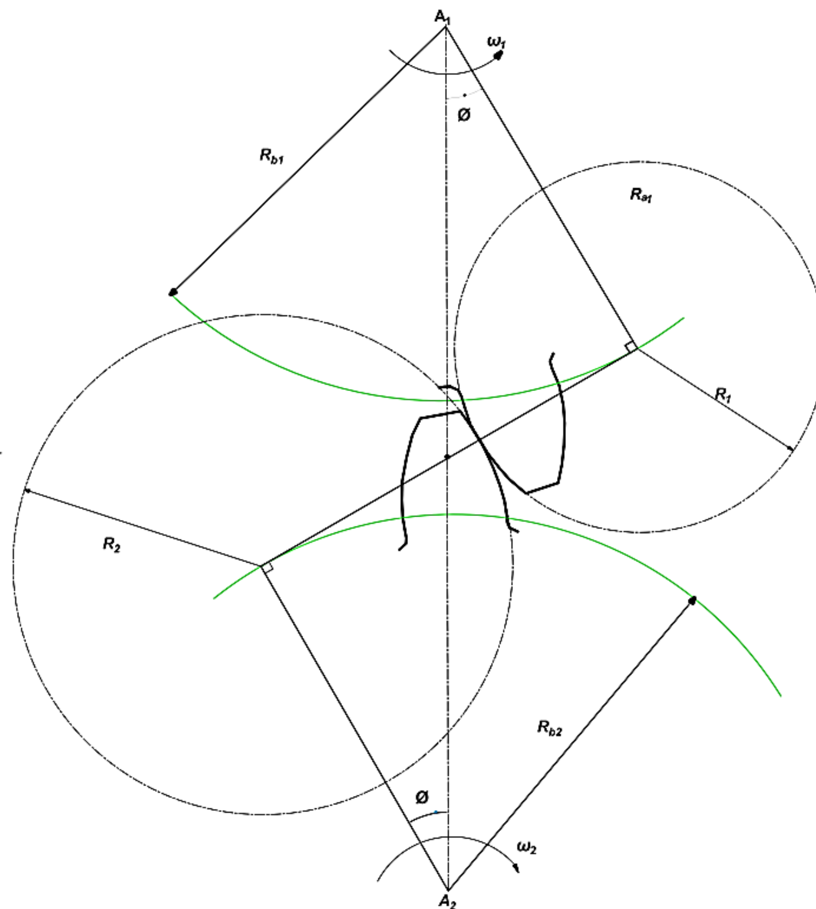

Figure 4-7 Simplified contact geometry of involute teeth (modified from Davies, 2005)

Figure (4-8) shows the next step of the procedure. Contact will be assumed to be a contact between two cylindrical rollers. Before and after the contact, the shape of the cylinder is similar to a parabola due to elastic deformation. Classic Hertz line contact theory has been used to calculate the separation distance of each point on the surface from the contact plane in the contact geometry. However, R_1 and R_2 depend on the time moment

of their contact process, while $R_{ef}(t)$ is the radius of relative curvature and it is time dependent.

$$z_1 = \frac{x^2}{2R_1} \tag{4-8}$$

$$z_2 = \frac{x^2}{2R_2} \tag{4-9}$$

Total separation distance zone of the geometry $z(x)$ can be calculated as in following:

$$z(x) = z_1 + z_2 = \frac{1}{2}\left(\frac{1}{R_1} + \frac{1}{R_2}\right)x^2 \tag{4-10}$$

$$\frac{1}{R_{ef}} = \frac{1}{R_1} + \frac{1}{R_2} \tag{4-11}$$

where R_{ef} is the radius of relative curvature.

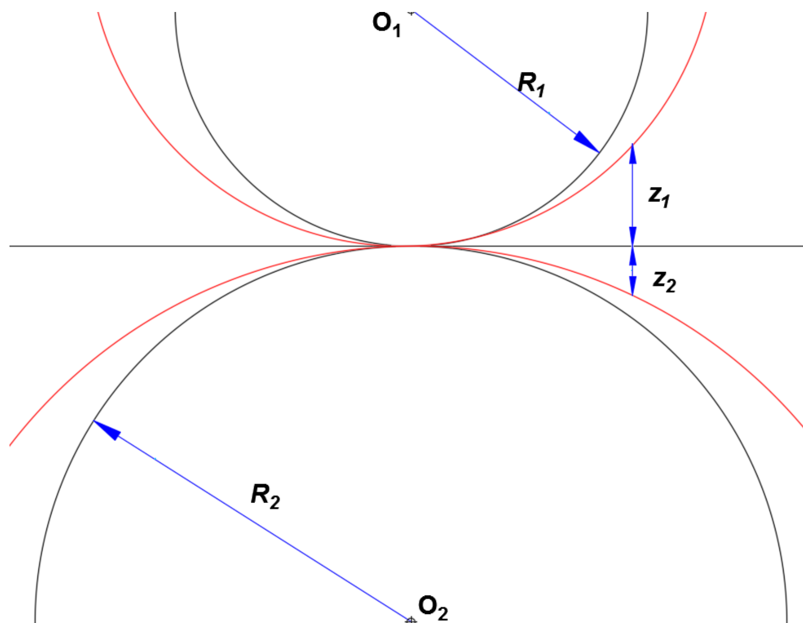

Figure 4-8 Two cylindrical shapes before and after contact (modified from Davies, 2005)

The contact geometry of microgears is hard to determine for two reasons:

1- The microgear teeth have been generated as an involute profile and the radius of curvature, surface speeds, and load throughout the mesh are constantly changing and need to be accounted for.
2- The contact point is constantly moving along the face of the micro-tooth; therefore, before the geometry can be determined, we should understand how the microgears are in contact.

The next part describes the contact between gear teeth and how it can be modelled, in addition to introducing an approach that allows the actual measured roughness of the gear teeth to be incorporated. Results are then presented for the smooth surfaces problem as well as the rough-surface cases for different meshes.

The operating conditions to solve these issues can be explained as follows: when the sliding contact point moves on each face, they move at the same angular velocity as the microgear itself and the angular motion of the contact is centred at the point of tangency of the line of action of the base circle, as illustrated in Figure (4-7). This allows the velocity tangential to the surfaces at the contacting point between the two surfaces to be calculated from:

$$u_i = (r_{bi} tan\emptyset + c)\omega_i \tag{4-12}$$

Where $i = 1$ and 2 for the micropinion and the microgear respectively. Then, the first and last points of contact, c_f and c_l, have determined respectively. The first point of contact c_f and last contact points c_l can be determined depending on the base radius, tip radius, and pressure angle. These individual parts have been defined in Figure (4-6),

along with the line of action. The lengths CB and TB are distances along the line of action in the positive c direction is outlined by:

$$CB = r_{b2} tan\emptyset \quad \text{and} \quad TB = \sqrt{r_{t2}^2 - r_{b2}^2} \tag{4-13}$$

The first contact point c_f is determined from these lengths as:

$$c_f = CB - TB \tag{4-14}$$

$$c_f = r_{b2} tan\emptyset - \sqrt{r_{t2}^2 - r_{b2}^2} \tag{4-15}$$

Similarly, the last contact point c_l could be determined by using Equation (4-16):

$$c_l = \sqrt{r_{t1}^2 - r_{b1}^2} - r_{b1} tan\emptyset \tag{4-16}$$

These allow the length of contact Δc to be determined as:

$$\Delta c = c_l - c_f \tag{4-17}$$

Using the velocity at which the contact point moves, the time taken t for the contact to progress from first to last point is given from:

$$t = \frac{\Delta c}{v_{contact}} \tag{4-18}$$

The time increment δt between each point that makes up the meshing cycle can be calculated as:

$$\delta t = \frac{t}{number\ of\ steps} \tag{4-19}$$

The radius of curvature of any point on the involute is the distance from that point to a tangential point on the base circle.

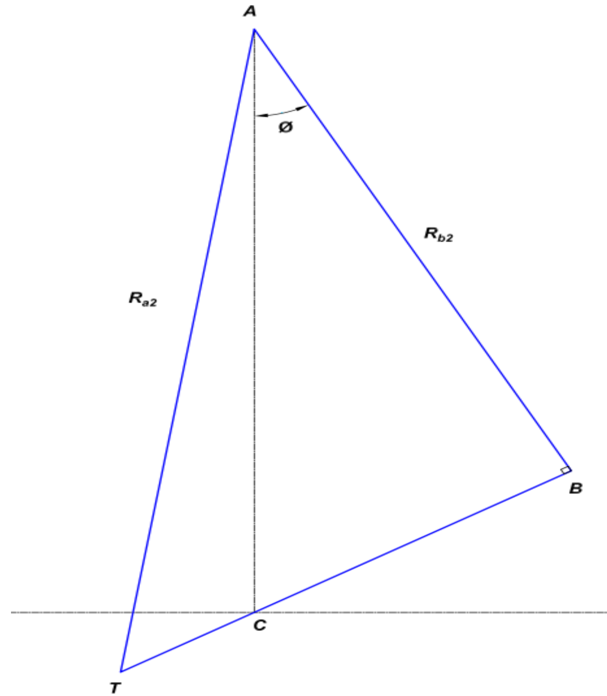

Figure 4-9 The path of contact between two meshing microgear teeth

The contact area between microgears teeth is small; the curvature change within the contact due to the tooth involute should be also small. Therefore, a realistic assumption is to use the radius of curvature of the point at the centre of the contact allowing the radius of two equivalent micro teeth R_{1i} and R_{2i} will be determined as in Equations (4-20) and (4-21), respectively:

$$R_{1i} = r_{b1} tan\emptyset + c \tag{4-20}$$

$$R_{2i} = r_{b2} tan\emptyset - c \tag{4-21}$$

4.3.1 Load Distribution over the Meshing Gear Contact Cycle

The difference in the distributed load over the contact distance can be calculated statically and dynamically, and it depends on the microgear face surface. The effects of the different types of profiles adjustment on the static and dynamic loading conditions have been illustrated in various studies (see, for example, Lin et al., 1989). The static contact load function is easy to find because of its dependence only on the geometry and the meshing cycle of the contact. This function has been widely used in a variety of styles of spur gear analysis and calculations. Figure (4-10) shows a schematic distribution of the load sharing function across the gear flank profile, where A and B stand for the first and last point of single tooth contact, respectively.

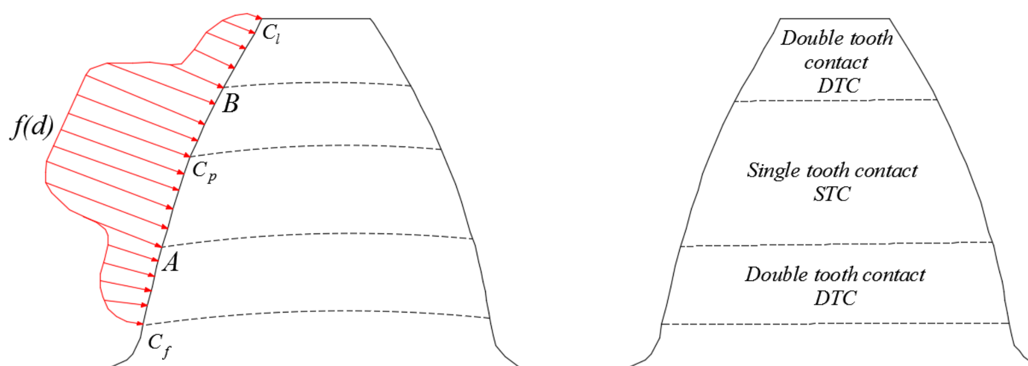

Figure 4-10 Load distribution in Single and Double tooth contact regions (adapted from Imrek, 2009)

Both load sharing functions are plotted across the coordinate on the line of action c in Figure (4-11). The load function that has been shown in Figure (4-11a) does not take into account lubricant behaviour and tooth deflection at the root. Therefore, at the double tooth contact (DTC) zones, the load has a constant magnitude of the half of the constant maximum load at the single tooth contact (STC) area. The second load function is affected

by the tooth deflection and presence of any type of the lubricant. Therefore, the starting, at c_f, and ending, at c_f, the values of the meshing contact distance are three times less than the constant maximum load at the STC zone, they then gradually increase until A. At the A, the load instantaneously rises from two-thirds to the unity of the maximum load, and there is an instant drop of the load at B and then gradually decrease until c_f.

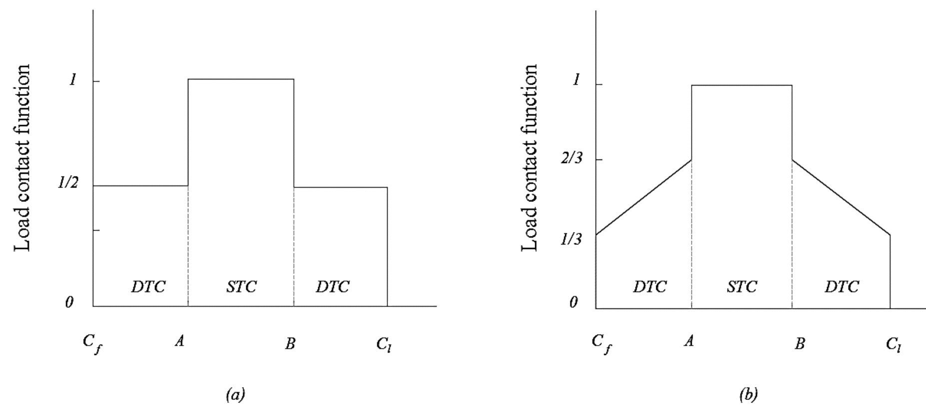

Figure 4-11 Load distribution with STC and DTC zones in (a) dry contact and (b) lubricated contact (adapted from ASM, 1992)

The static load function gives an explicit approximation of the load difference over the sliding distance; therefore, the dynamic load function shall be used whenever the measured values are available.

Thus, in this thesis we intend to consider the case of the highest loads acting on a MEMS tooth, therefore, only the single tooth contact *STC* case is considered further. As it has been mentioned above, the maximum external force acting on the MEMS tooth is $F_{ext} = 25\ \mu\text{N}$ (see Patton and Zabinski, 2005 and Rezvanian et al., 2007).

4.4 Hertz Line Contact of MEMS Microgears

The pressure distribution has been calculated according to the classical line contact Hertz theory and is represented in Figure (4-12), where $p(x)$ is the pressure. It has been determined at each single point along the contact region between the meshing microgear MEMS tooth surfaces, this study will focus on the STC only. In addition, p_o has been referred to the maximum pressure during contact; L, in this specific case, is the thickness of the microgear MEMS tooth; and, R_1 and R_2 are the radii of the curvature of the micropinion and microgear teeth, respectively.

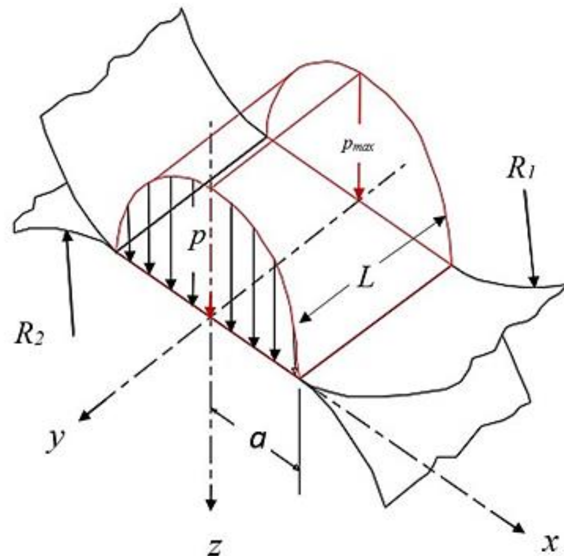

Figure 4-12 Pressure distribution P(x) developed when two cylinders pressed together

As a simplification of the contact problem between the microgears MEMS and by using the Hertz line contact approach, as shown in Figure (4-13), the pressure distribution $p(x)$ along the silicon MEMS micro-tooth profile can be calculated (see Timoshenko and Goodier, 1970 and Johnson, 1985):

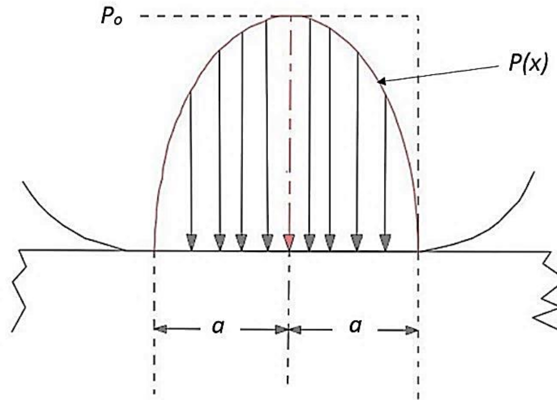

Figure 4-13 2D pressure distribution *p(x)* and the maximum pressure (*pₒ*)

$$p(x) = p_o \sqrt{1 - \frac{x^2}{a^2}} \quad (4\text{-}22)$$

The area of contact at each position of contact can be found by calculating the half-length of contact (a) multiplying the width of the tooth by (L), as shown in Figure (4-12):

$$A = 2aL \quad (4\text{-}23)$$

$$a = \sqrt{\frac{4pR_{ef}}{\pi E^*}} \quad (4\text{-}24)$$

where the load applied is p, and R_{ef} is the radius of relative curvature while E^* is the modulus of contact and can found by:

$$\frac{1}{E^*} = \frac{1 - \upsilon_1^2}{E_1} + \frac{1 - \upsilon_2^2}{E_2} \quad (4\text{-}25)$$

In addition, the maximum pressure can be calculated at each point of contact according to the formula of p_o:

$$p_o = \frac{2p}{\pi a} \quad (4\text{-}26)$$

4.5 Modelling of a Frictionless Gear MEMS Contact

The first step was to assume that the contact between the microgear teeth is a frictionless contact and then calculate the pressure distribution by applying the assumptions of Hertz line contact problem, which has been discussed in the previous section. By using the function of pressure distribution that has been suggested by Hertz in Equation (4-22), the results will be as in the Figure (4-14):

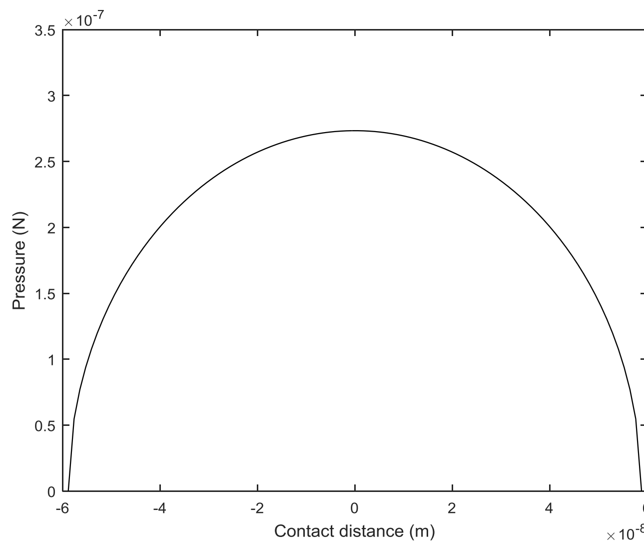

Figure 4-14 Pressure distribution for the frictionless contact between two microgear MEMS teeth

Where a is the half contact length in contact area and is equal to (5.8869×10^{-8}m); therefore, the total contact length is ($1.1774e \times 10^{-7}$m). The maximum pressure in the contact zone has also been calculated to be (2.7332×10^{-7}N) according to Equation (4-26). The effects of the sliding and traction motion have then been added to the calculation during the simulation of the contact between microgear MEMS teeth.

Figure (4-15) shows the contact between the smooth and frictionless microgear MEMS teeth surfaces. This step has been done to calculate the initial gaps between teeth surfaces.

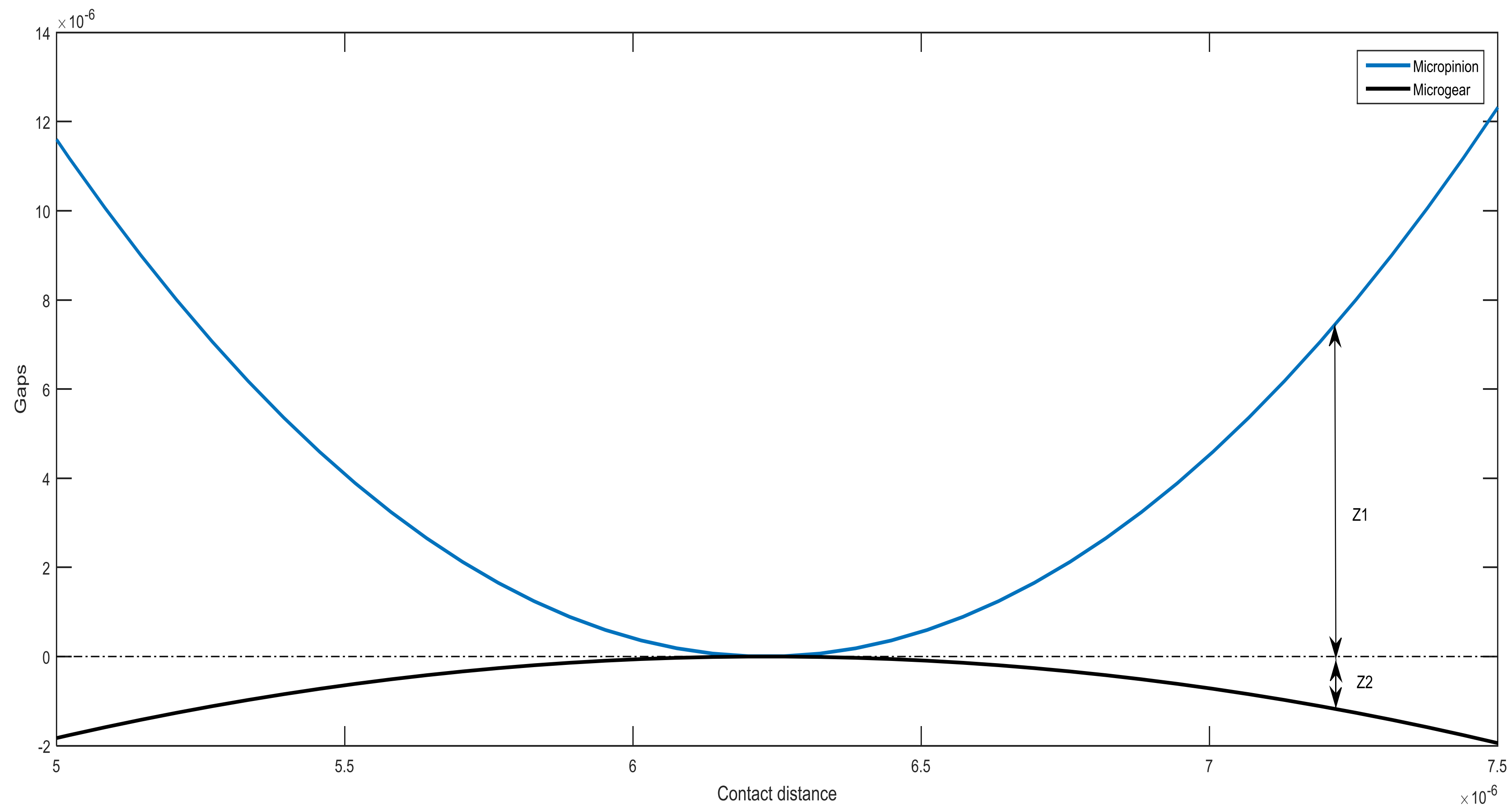

Figure 4-15 Contact between smooth microgear teeth surface

The obtained silicon roughness profile, which is shown in Figure (4-1), has then been superimposed on the smooth surface of the microgear. The gaps between microgear MEMS teeth surface has been calculated by using the classical Hertz line contact theory. A description of the meshing microgear MEMS has been illustrated in the Figure (4-5) and the dimensions was calculated depending on the information that has been illustrated in Teodorescu (2009). The preparation steps of the silicon microgear profile has been presented graphically in Figures (4-16) and (4-17).

These preparation processes were done for both the micropinion and the microgear in the meshing microgear system. Finally, the micropinion and the microgear are assumed to be in a sliding contact motion to simulate the effect of adhesion and dry friction between the microgear MEMS teeth surfaces.

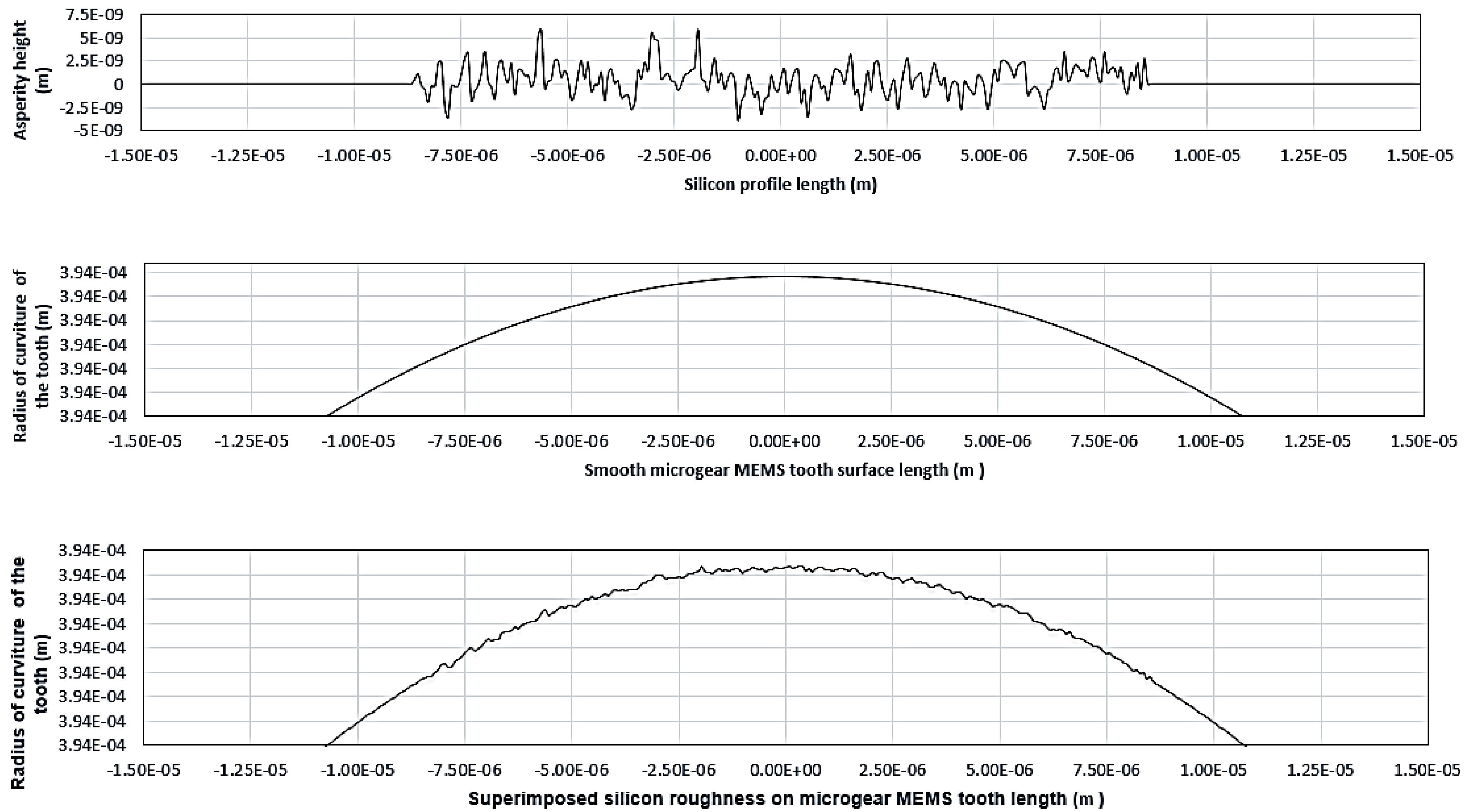

Figure 4-16 Silicon roughness profile superimposed on the microgear MEMS tooth surface

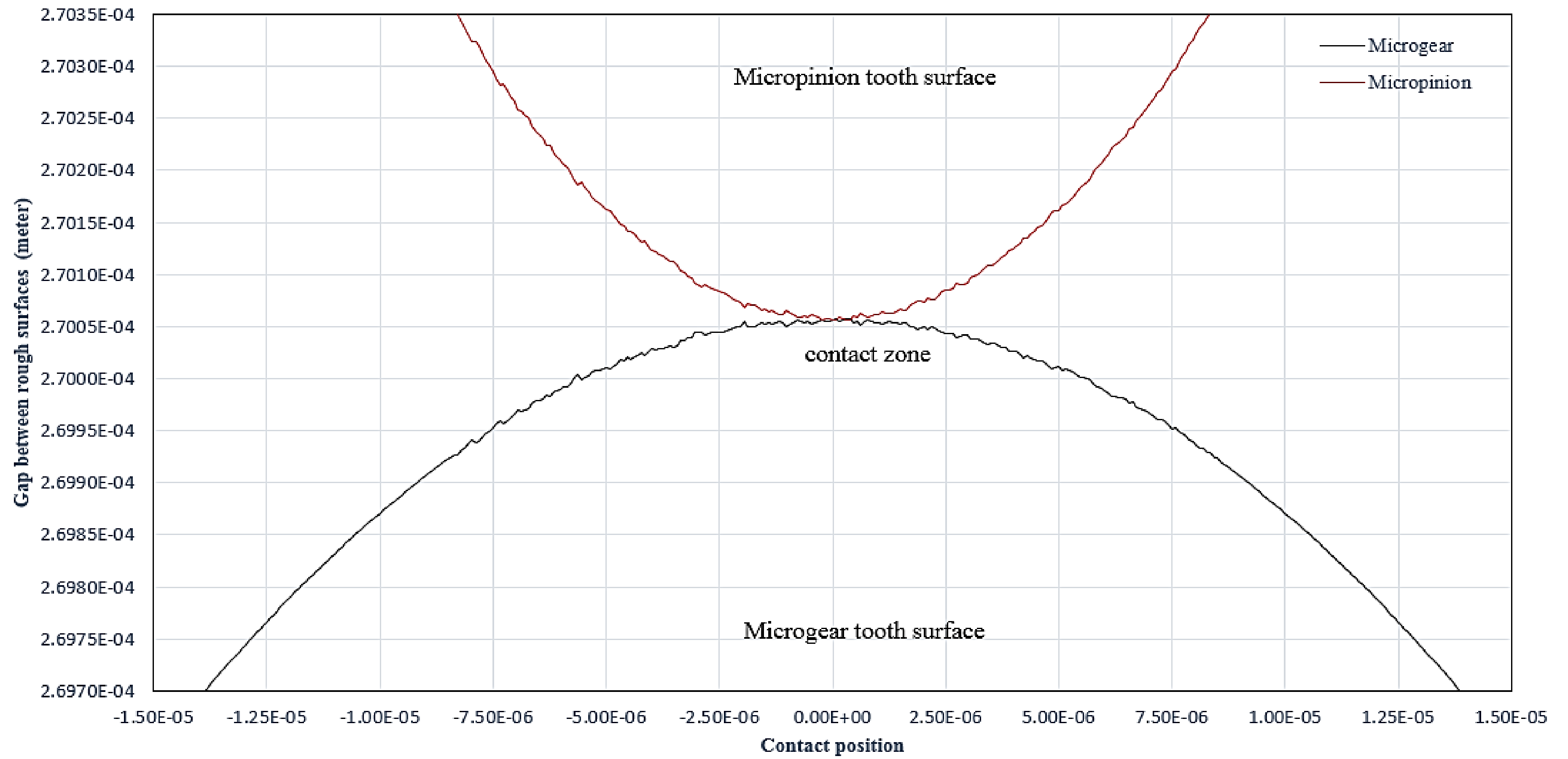

Figure 4-17 Rough contact between the micropinion and the microgear in the meshing microgear MEMS system

4.6 The Algorithm for Searching of True Gaps

Contact problems have been considered to have associated with frictionless Hertz line contact theory. In this contact, when the two curved bodies of different radii of curvature are brought into the contact they will initially touch each other along a line. The most classic line contact problems are teeth gear meshing and rollers bearing contacts (see e.g. Johnson, 1985, Davies, 2005). The problem has been extracted to frictional line contact theory by developing Cardiff numerical solver (see Evans et al., 2013 and Khaustov, 2016). The 2D Cardiff contact solver has been modified because the original solver was developed for EHL contact (Al-Mayali and Evans, 2016, Khaustov 2016), while we consider the case when there is no lubricant.

An approach has been applied to allow the meshing microgear MEMS teeth to be modelled in this study. The simulation combines the changes in the geometry of the microgear teeth, the change in the sliding motion and allows a constant load to be applied over the sliding distance. The load has defined using a constant load in the fixed-load model and variable load when there is fixed gap model.

The numerical simulation has applied in the beginning by using smooth microgear teeth surfaces and then it has run with real silicon roughness profiles applied to each microgear tooth. The contact of smooth surfaces has applied in the beginning to calculate the initial separation distance between the two microgears surfaces as so-called here '*gaps*' during the sliding distance. Then, with the real silicon, counterpart's surface gaps have been calculated in all locations over the sliding distance. The difference separation distance

gives information on how the gap changes over the sliding motion, thus giving the normal and friction forces prescribed through the contact.

In the simulations of the real silicon surface, a software code has developed that allowed the roughness data taken from the silicon roughness profile to be related back to the points on the gear tooth from which it came. As soon as the simulation is running, the contact has centred upon a known part of the microgear tooth surface, which allows the point in the roughness file that corresponds to the contact to be determined. The remainder of the points can be determined using trigonometry (for more details see section 4-3).

To describe the procedure of our simulations, we need to explain the following points:

1- Start the modified 2D Cardiff contact solver by inputting the external nominal normal pressure distribution p and tangential F_t stresses (these distributions are found according to the Hertz line contact theory).

2- Find the actual gaps between contacting MEMS teeth for each of the nanoblocks in the condition of a dry contact (the gaps obtained from 2D Cardiff contact solver vary over the tooth, therefore, the gap for each nanoblock depends on its location).

3- Calculate the actual height of the nanoblocks that are compressed (the nanoblock may be compressed by another nanoblock (asperity) located on the counterpart).

4- Calculate the compressive force acting on the nanoblock according to its actual height.

5- Apply the model with vertical degree of freedom model (the fixed load model described in Chapter 3) for each of the nanoblocks and calculate frictional force acting on a specified asperity.

6- Calculate the total friction force $(F_f)_{Total}$ and the COF depending on the $(F_f)_{Total}$.

7- Use an iterative procedure if the initial F_t and the obtained $(F_f)_{Total}$ differ more than a prescribed value and stop the procedure if F_t and $(F_f)_{Total}$ are close to each other.

The whole steps of the process are described in the flowchart in Figure (4-18).

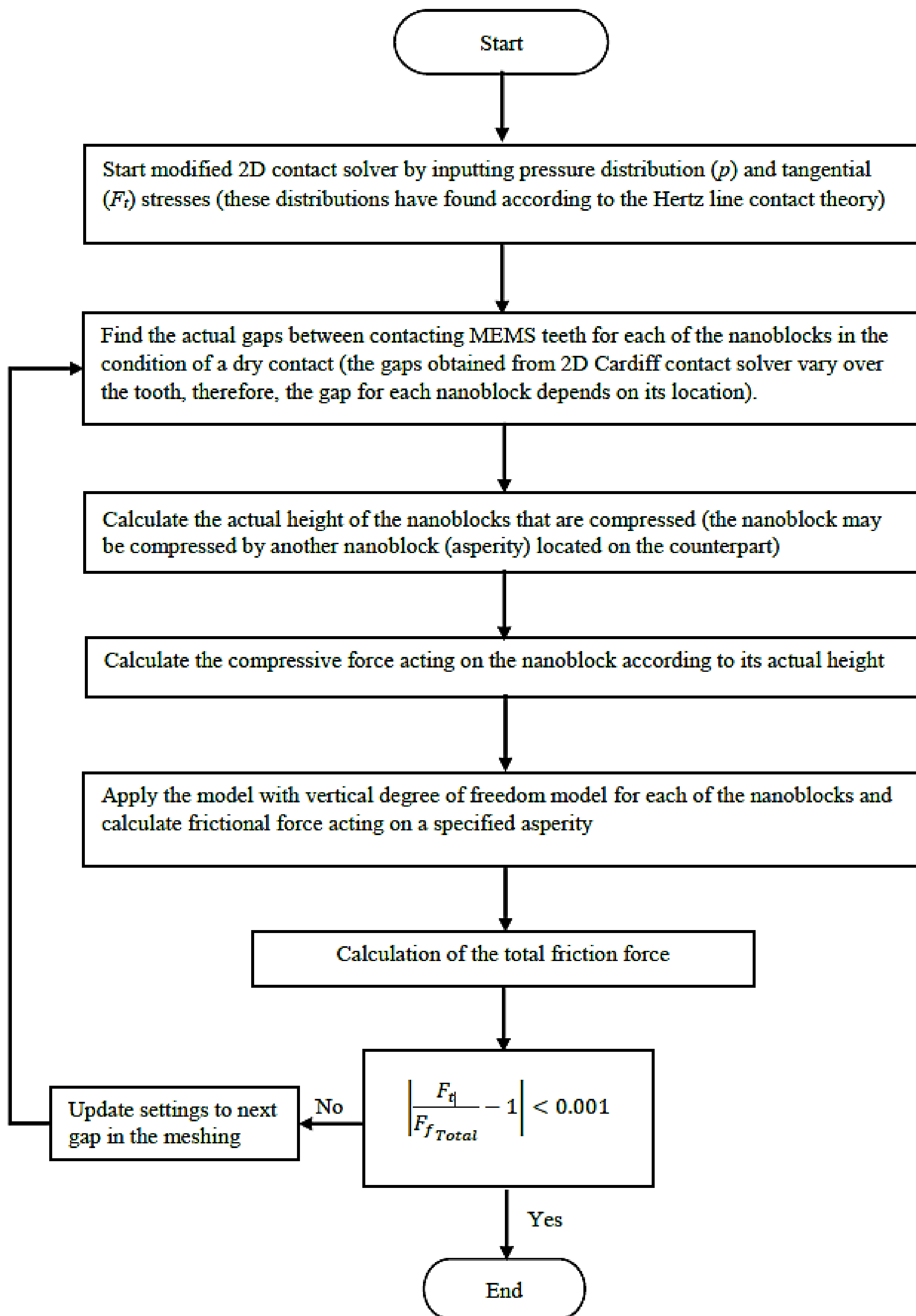

Figure 4-18 Flow chart of the process of searching true gaps

4.7 Effect of Normal and Tangential Force on the Interaction between Particles in Microgears

During sliding contact interactions between the silicon molecules on the outer layers of the microgear MEMS tooth surfaces will be established. To keep the system working, these interactions should not exceed the value of tangential force, which is responsible for the sliding motion between the contact-meshing surfaces of the microgear MEMS teeth.

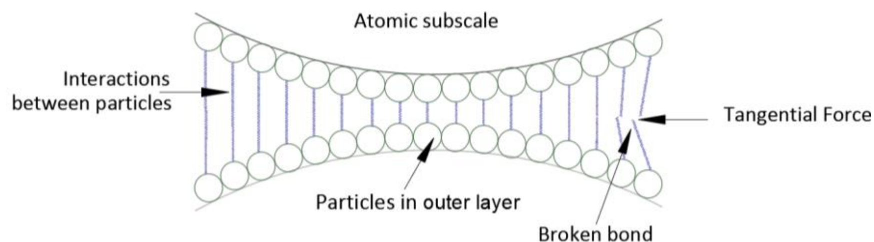

Figure 4-19 Effects of tangential force on the interaction between particles

This tangential force will work to shear the chemical junction generated between the silicon particles of the tooth surfaces (see Figure 4-19).

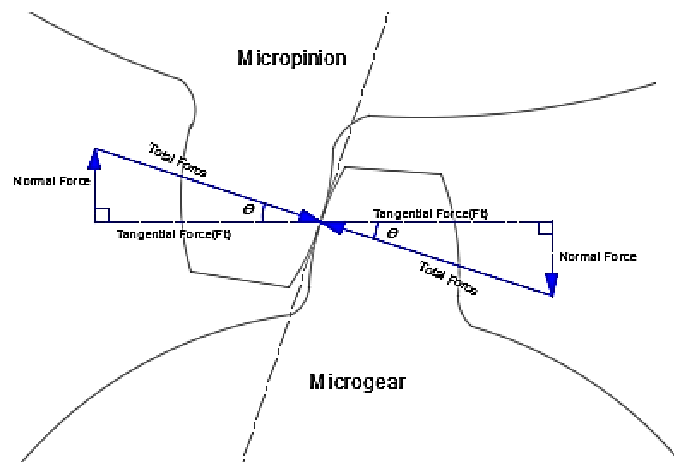

Figure 4-20 Illustrations of the tangential force of meshing microgear MEMS teeth

The micropinion is the driving gear and the microgear is the driven gear. The tooth on the micropinion pushes the tooth on the microgear with a tangential force F_t. The torque on the gear MEMS is T_r and can be found by $T_r = F\ d$, where F is the total force applied from micropinion on microgear and d is the distance. Therefore, we know that

$$F_t = T_{r_{micropinion}} / R_{micropinion} \quad (4\text{-}27)$$

Where $T_{r_{micropinion}}$ is the torque on the micropinion and $R_{micropinion}$ is the radius of the micropinion in MEMS. However, this force does not convert directly into a tangential force on the micro pinion. Forces through the micro pinion teeth can only be transmitted to the point where the teeth surface are in contact. Since the surfaces are designed to have nano and atomic subscales asperities, the force could be passed on to the surface through these asperities when they are in contact. This force is denoted by the *total force* in Figure (4-20). These forces could be represented as two perpendicular components: a tangential component, which equals to the F_t and a radial component that is referring to the normal force F_n. The normal component F_n pushes the microgear teeth to separate from each other. The microgears MEMS will contact each other at the same angles whatever the amount of force has been applied to them, so an increase in the tangential force will also increase the normal force.

In the current model and based on Equation (4-27) it was found that the tangential force F_t that will make the microgear MEMS system continue working without any interrupting due to stiction is equal to 2.82×10^{-3} N.

4.8 Friction, Adhesion, Stiction and Wear in Silicon Microgears MEMS

In the contact between the microgear teeth surfaces in MEMS and micromachined devices, there are different types of forces associated with the MEMS that scale down with the size. When the size of MEMS and the micromachined devices has reduced from millimetres to micrometres, the surface area will decrease by a million times and the volume will decrease by a billion times. Therefore, the resistive forces such as friction and surface tension, which are proportional to the area, will be increased a thousand times more than the forces proportional to the volume, such as inertial and electromagnetic forces (see Rymuza and Pytko, 2010).

The resistive forces between the contacting surfaces will cause tribological challenges because friction, stiction, wear and the surface contamination, which will effect on the MEMS performance and even, can prevent the MEMS from working. For example, in micro motors, the intermittent contact at the rotor-stator interface and physical contact at the rotor-hub interface result in wear issues and necessitates low friction/stiction between the contacting surfaces. Consequently, there is a need to develop materials for the bearing bushing that are both compatible with processes of the MEMS fabrication, and which provide superior friction and wear performance. Many have tried to understand the mechanisms of friction between contacting surfaces, for example, Yu-Chong and Muller (1990) have measured the friction and stiction in micro-motors, Gabriel et al. (1990) have studied turbines and gear structures, while Lim et al. (1990) have investigated polysilicon microstructures. However, stiction and adhesion phenomena, as well as their mechanisms require further study (Mastrangelo, 1997). Furthermore, in surface micromachining, the

suspended microstructures of these devices can sometimes collapse and permanently adhere to the underlying substrate (Guckel and Burns, 1989).

4.9 Numerical Simulations of the Frictional Work of Gear MEMS

The tooth roughness of microgear MEMS is described as superposition of two hierarchical atomic and adhesive subscales that are specified by the character of interactions at the subscale. It is assumed that the microgear MEMS tooth works in vacuum environment, in addition to the bulk volume of the silicon. The subscale asperities have been indicted depending on the calculation of the Abbot- Firestone curve. The amount of energy dissipated by different physical and chemical mechanisms in additional to the sliding contact motion between the counterparts has been calculated and used to evaluate the frictional force.

4.9.1 Simulations for the Multi-scale Hierarchical Structure with a Vertical Degree of Freedom

It is assumed that the microgear MEMS tooth works in vacuum environment. Therefore, the amount of energy dissipated by different physical and chemical mechanisms in additional to the sliding contact motion between the counterparts has been calculated and used to evaluate the frictional force. Tooth surface has been modelled by multiscale hierarchical structures (see Figure 4-22) of multiple blocks, which have covered the whole surface of the tooth and are located on different scales. The width of the adhesive subscale where the vdW interactions are likely to occur denotes as $w_{adhesive}$ and atomic subscale, where the chemical interactions are significant.

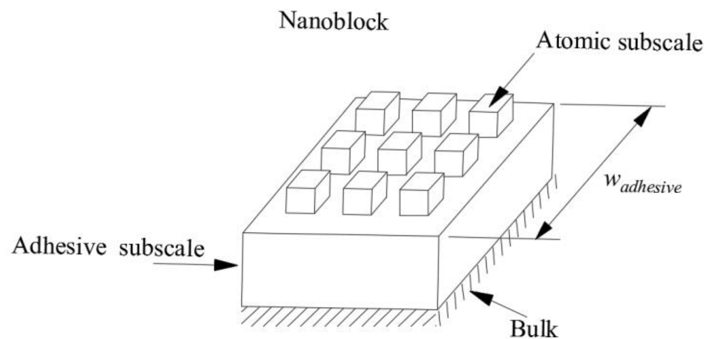

Figure 4-21 Nanoblock of the surface roughness consisting of adhesive subscale and atomic blocks

The position of each block is specified by the gaps between the meshing microgear teeth surfaces at each particular instance, as shown in Figure (4-15).

The dimension of the meshing microgear is the same as used in Teodorescu et al. (2009). Figure (4-17) showed the micro-pinion that is meshing with a microgear by using the real silicon surface roughness. The gap between the surfaces of the meshing teeth, which is different at each time step, is calculated using Hertz line contact theory.

In this study, a modified multiscale hierarchical model of an asperity is employed in order to simulate the work of multi-asperity rough surfaces of MEMS microgear teeth, as shown in Figure (4-22). Micro-tooth surface is modelled, as a bulk silicon-based MEMS surface covered by multiscale hierarchical structure roughness having two subscales specified by the character of interactions: atomic subscale, where the chemical interactions are significant, and adhesive subscale, where the vdW interactions are likely occur (see also Figure 4-23).

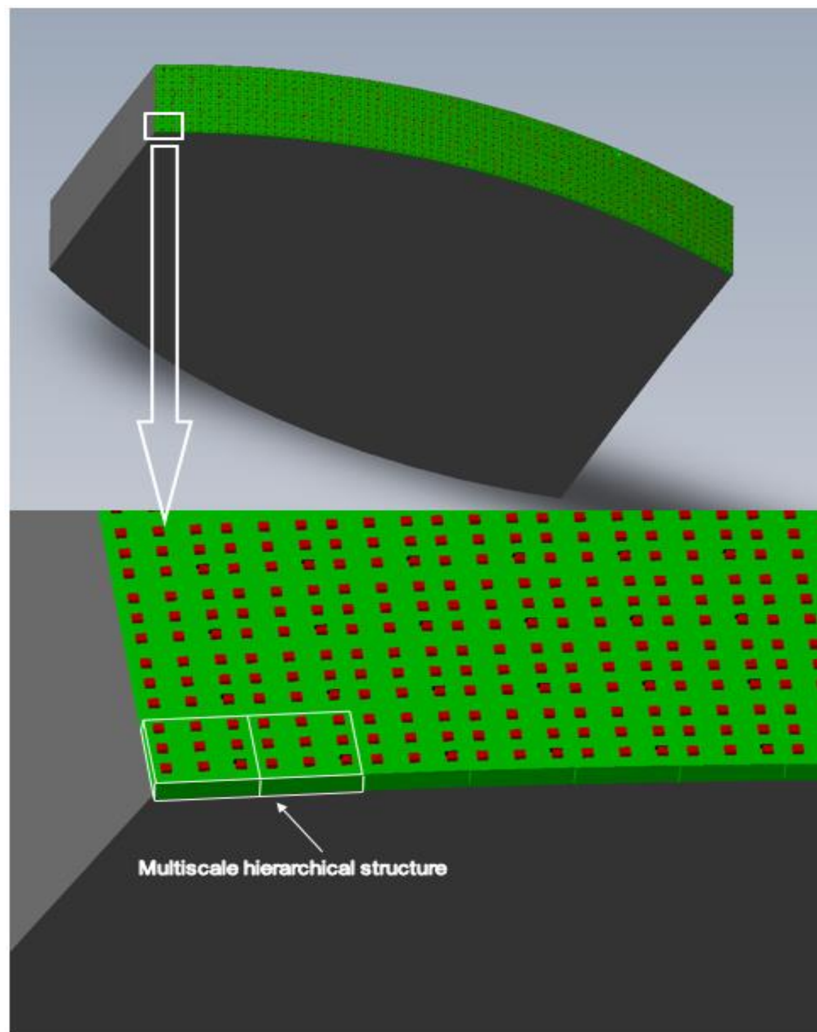

Figure 4-22 (a) Modelling of the hierarchical structure on the microgear surface. (b) Magnified section of modelling of the hierarchical structure on the microgear surface

Friction force has been determined by using the energy loss over the entire surface of microgear MEMS tooth, which can be obtained by different mechanisms, over the sliding distance along the microgear tooth according to Equation (3-5). The difference here is that all of the blocks or multiscale hierarchical structures will lose energy, the friction force and the coefficient of friction (COF) will be calculated while taking the different physical and chemical mechanisms into account.

4.9.2 Numerical Simulation Results Using Various Parameters of Contact

The silicon roughness profile that has been used for this section and for all the models presented in the previous sections and in the multiscale hierarchical model are given in Figure (3-26). Both microgear MEMS teeth are made from silicon. The sample of the real silicon roughness profile was illustrated in Figure (4-16). Numerical simulations will start with the multiscale hierarchical blocks structure, which is shown in Figure (4-23). There are two adhesive subscale blocks each of which has nine atomic subscale blocks, each being 19.5nm wide. The width of the adhesive block is 195.5 nm. Therefore, the support surface has been extruded to the depth of the adhesive subscale block width (which is in this case equal to 195.5nm). The adhesive block has a square cross-section. The atomic subscale blocks have a square cross-section and they are distributed uniformly on the end of the adhesive block to correspond with the silicon MEMS tooth surface roughness asperities. The technique that was used to characterise the roughness has been described in section 3.5.

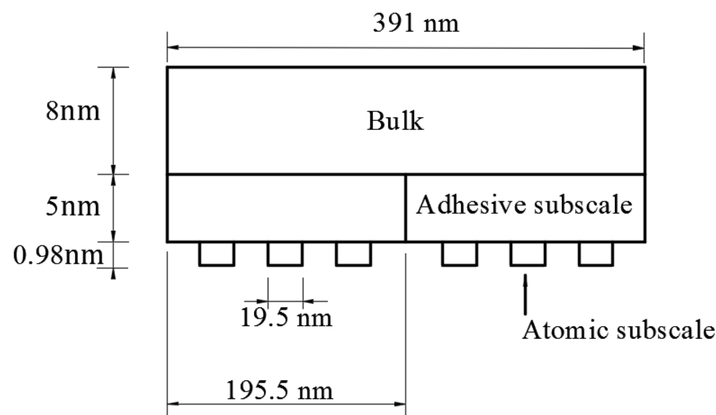

Figure 4-23 The multiscale hierarchical structure vertically scaled up by a considerable factor to make the geometry distinguishable

4.9.3 Dependence of COF on External Load

This section will illustrate the results of the numerical simulation of the multiscale hierarchical blocks structure that shows how the external load (and consequently, elasticity) influences the COF. We assume that when the nanoblocks are deformed elastically, the atomic blocks on their ends will establish contact with the counter-surface. The dissociation of these interactions will lead to dissipation of energy, which results in a friction force and the value of the COF. The graphs presented in next Figures will show the dependence the COF and of the dissipated energy on the external load.

Figure (4-24) shows results obtained for sliding distance x , under a constant load of 25μN. The numerical simulation shows that the COF of the structure that has been described above is about 0.9. This magnitude of COF coincides with the value estimated in section 3.5 and with the values of the COF for the two silicon surfaces sliding over each other as given in the literature, which is approximately between 0.55 and 1.2.

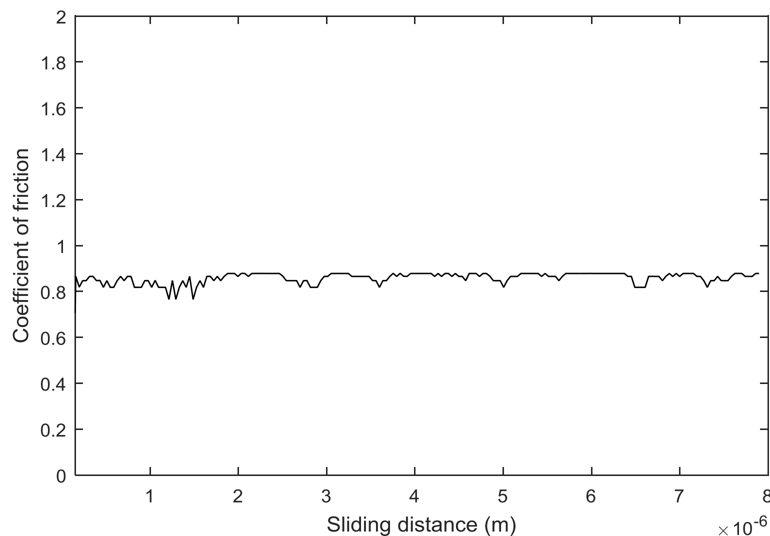

Figure 4-24 COF when the load w=25μN

Figure (4-25) shows the total dissipated energy due to dissociation of the chemical and vdW interactions also the energy loss due to the elastic interlocking between nanoblocks on the counterpart surfaces when the external load is 25μN.

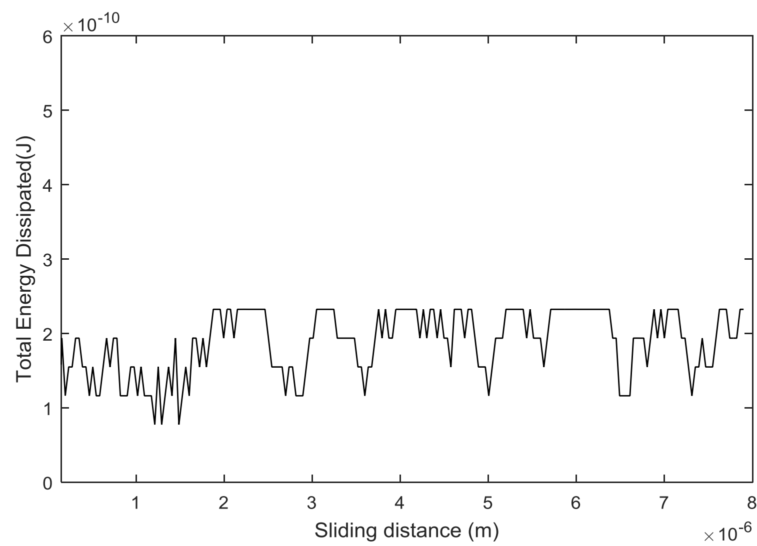

Figure 4-25 Total dissipated energy when the load w=25μN

Figure (4-26) shows the coefficient of friction when applied an external load equal to 50 μN.

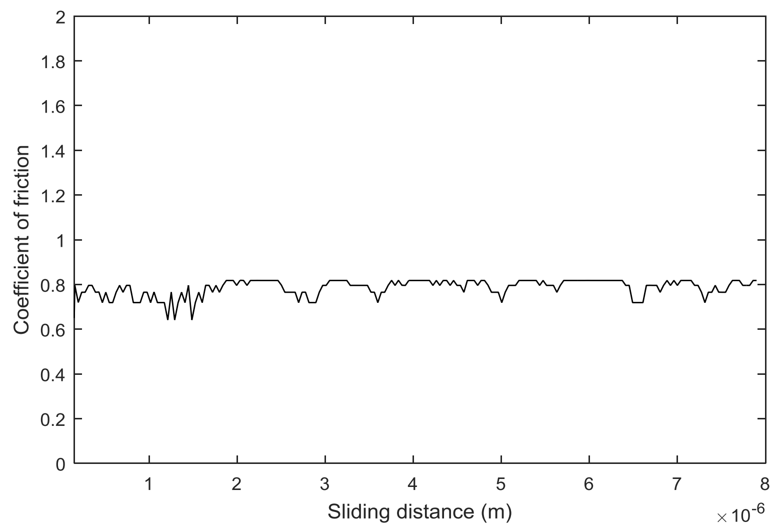

Figure 4-26 COF when the load w=50μN

While Figure (4-27) shows the total dissipated energy due to dissociation of interactions when the external load becomes 50 μN.

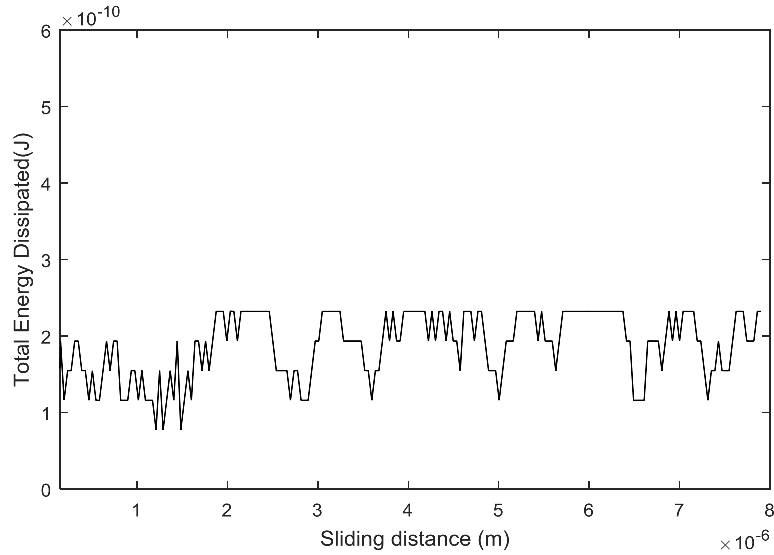

Figure 4-27 Total dissipated energy when the load w=50μN

If the external load has increased to 75μN, the COF will reach to approximately 0.7 as shown in Figure (4-28)

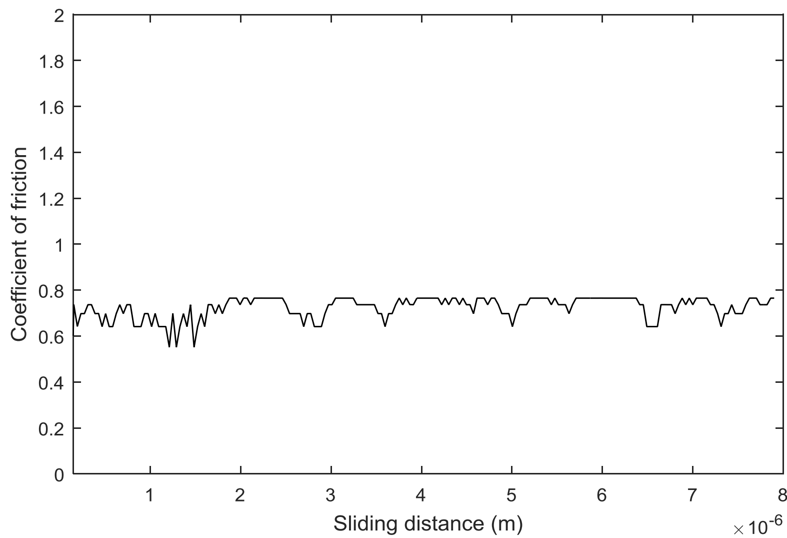

Figure 4-28 COF when the load w=75μN

The total dissipated energy, which has been caused by breaking bonds, will be slightly varied when load at 75µN as it has presented in Figure (4-29)

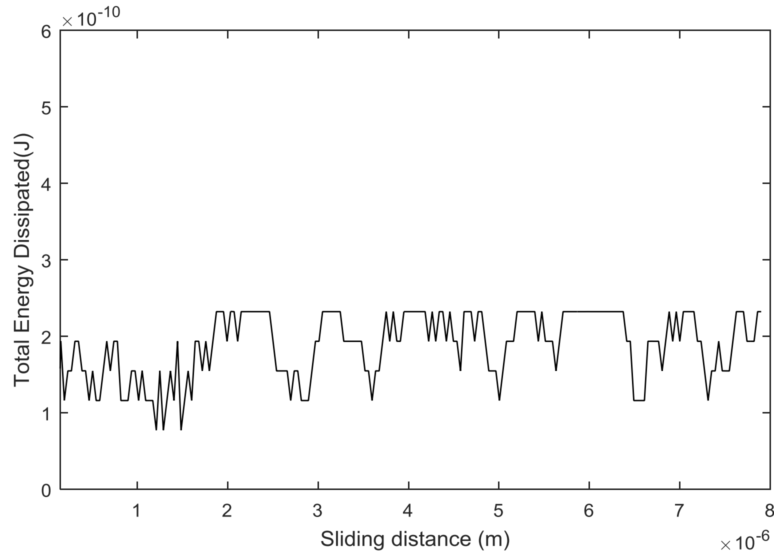

Figure 4-29 Total dissipated energy when the load w=75µN

Figures (4-30) to (4-31) show the dependence of the friction coefficient and of the dissipated energy on the external load equal to 100µN.

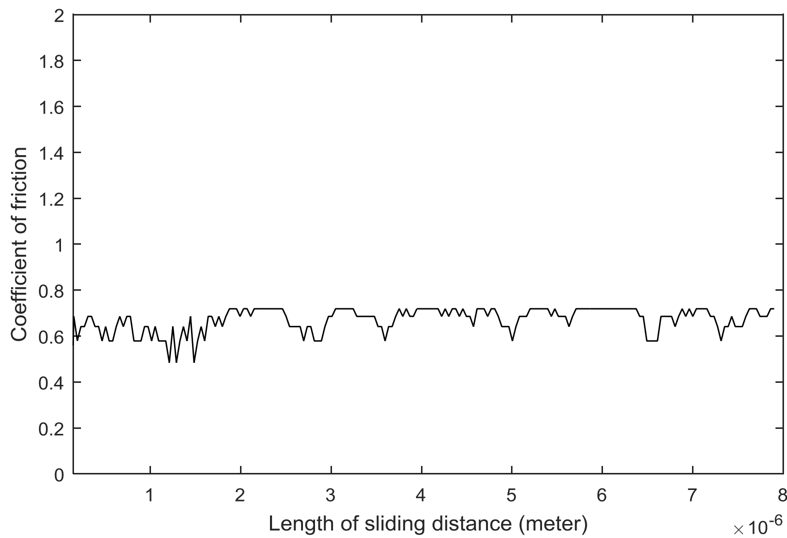

Figure 4-30 COF when the load w=100µN

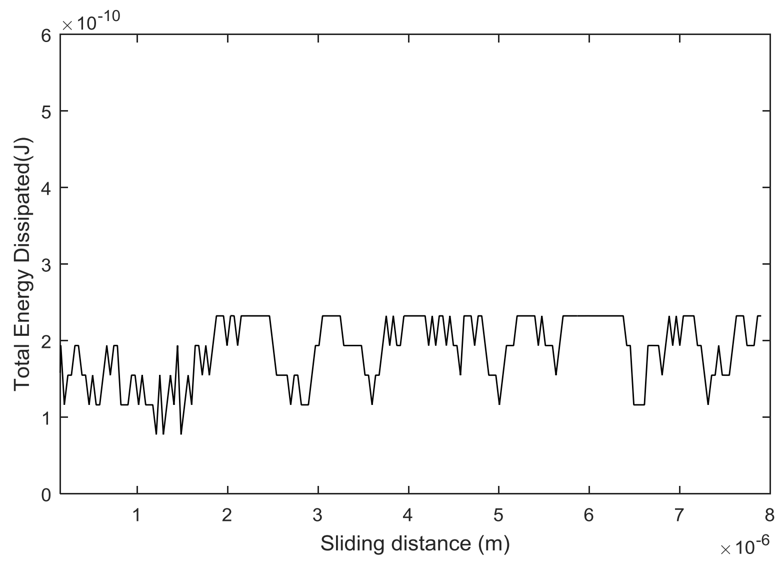

Figure 4-31 Total dissipated energy when the load w=100µN

When the external load reaches to 125µN, the coefficient of friction will become nearly about 0.65 as shown in Figure (4-32)

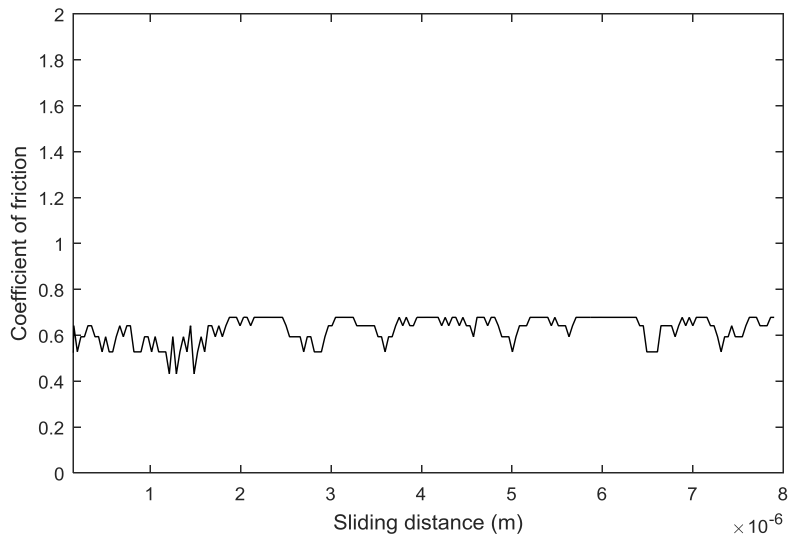

Figure 4-32 COF when the load w=125µN

However, the total energy loss will be as shown in Figure (4-33), when the external load reaches to 125μN.

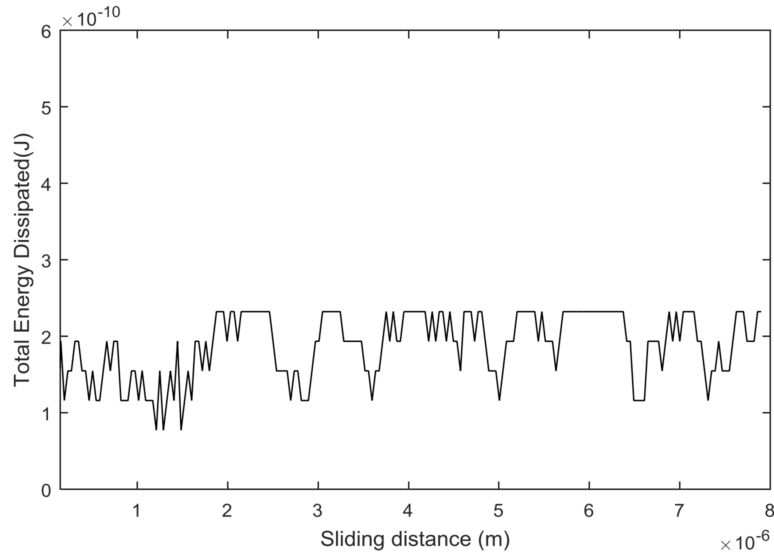

Figure 4-33 Total dissipated energy when the load w=125μN

If the load w=150μN, then the results are presented in the Figures (4-34) and (4-35) for COF and total dissipated energy, respectively.

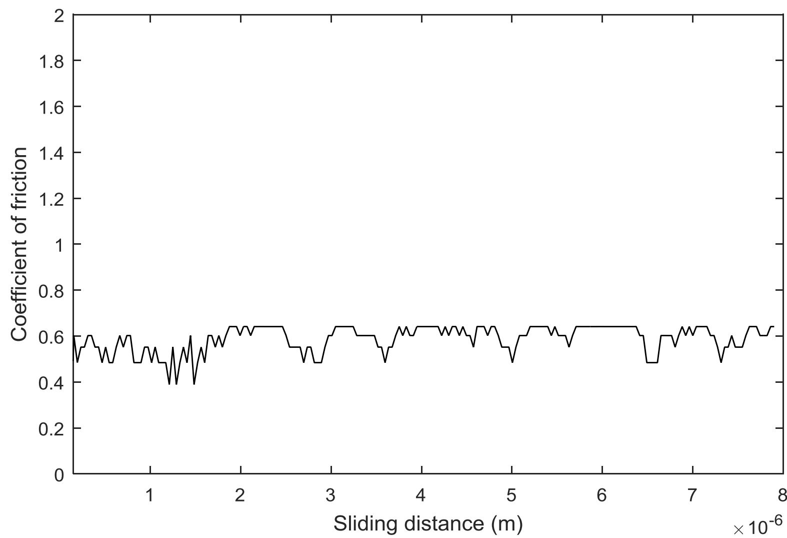

Figure 4-34 COF when the load w=150μN

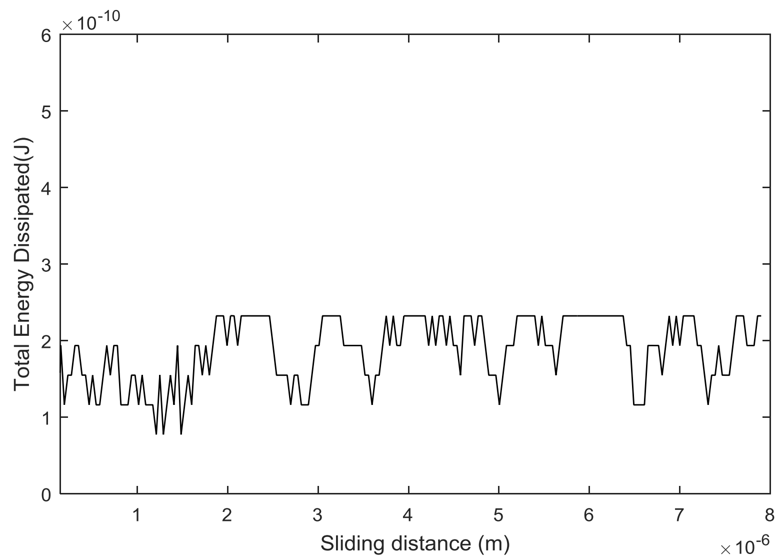

Figure 4-35 Total dissipated energy when the load w=150µN

The external load that applied will increased gradually at each step to show its effects on the COF (see Figure 4-36) and total energy loss (see in Figure 4-37), when the external load is 175µN.

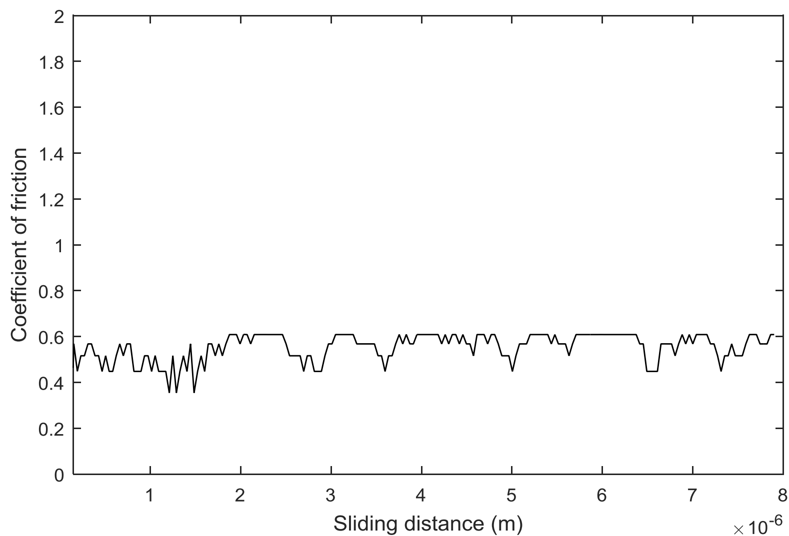

Figure 4-36 COF when the load w=175µN

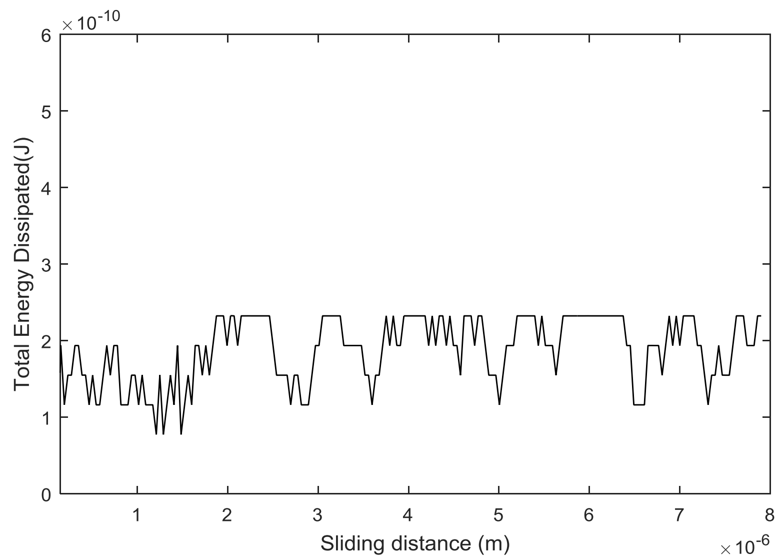

Figure 4-37 Total dissipated energy when the load w=175μN

The COF reaches to more than 0.6 when the external load equal to 200μN as it presented in the Figure (4-38)

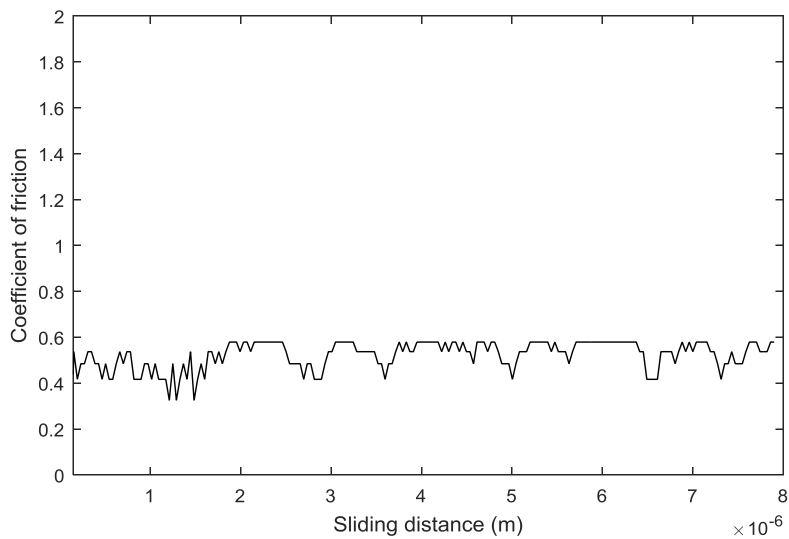

Figure 4-38 COF when the load w=200μN

Figure (4-39) shows results of the total dissipated energy for the external load w=200µN.

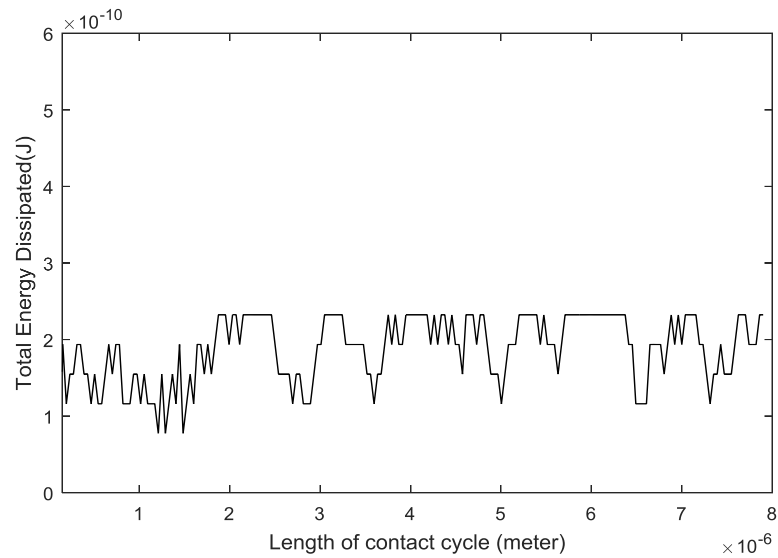

Figure 4-39 Total dissipated energy when the load w=200µN

Figure (4-40) shows that the COF is slightly decreased when the external load equal to 225µN.

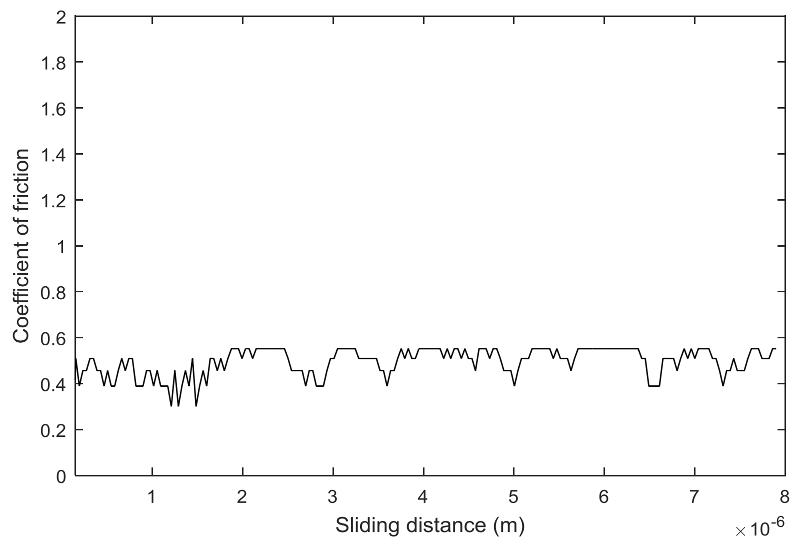

Figure 4-40 COF when the load w=225µN

The total energy loss will be as shown in Figure (4-41), when the external load reaches to 225μN.

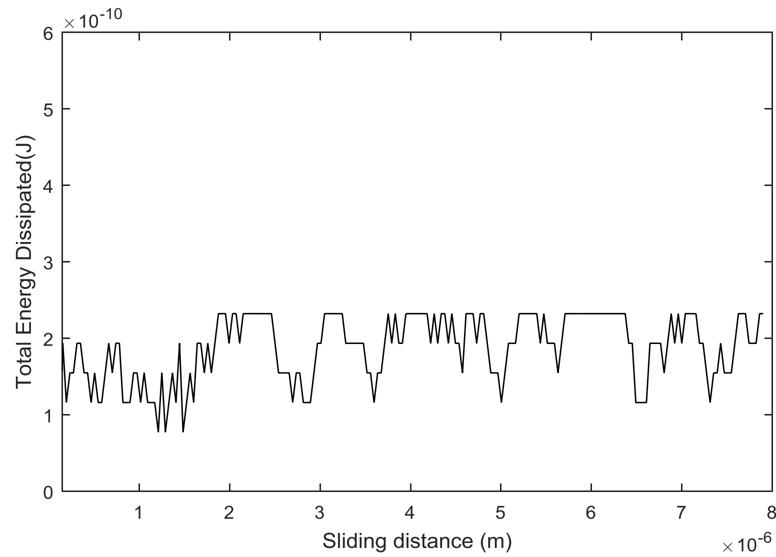

Figure 4-41 Total dissipated energy when the load w=225μN

While in the Figure (4-42) of COF and Figure (4-43) of the total energy loss show the effect of increase the value of external load to 250μN.

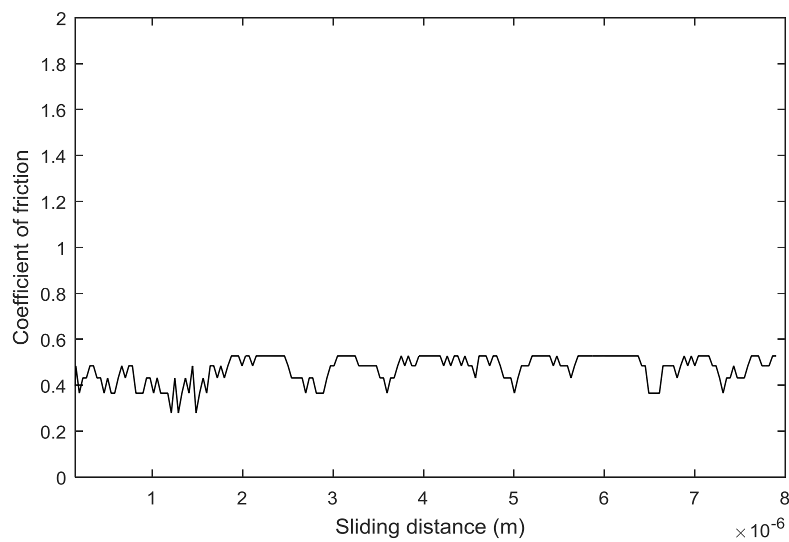

Figure 4-42 COF when the load w=250μN

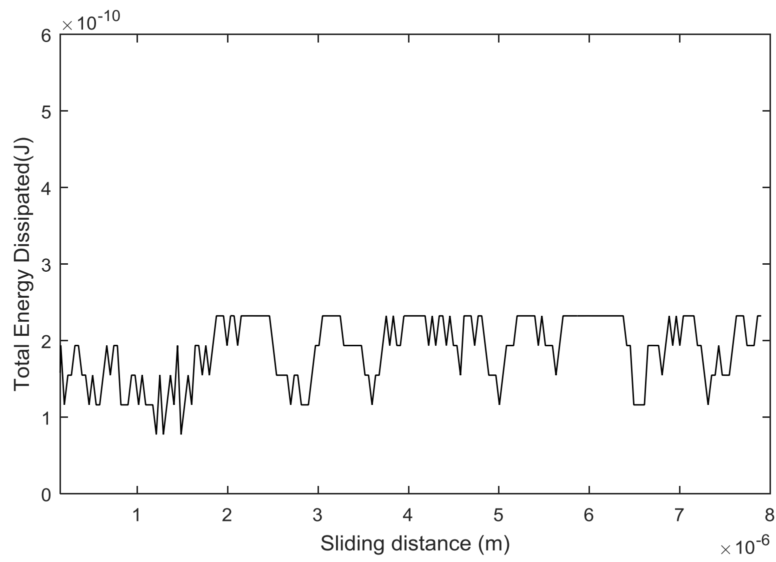

Figure 4-43 Total dissipated energy when the load w=250µN

Figure (4-44) presented the values of COF when the load w=275µN, the value of COF has slightly decreased.

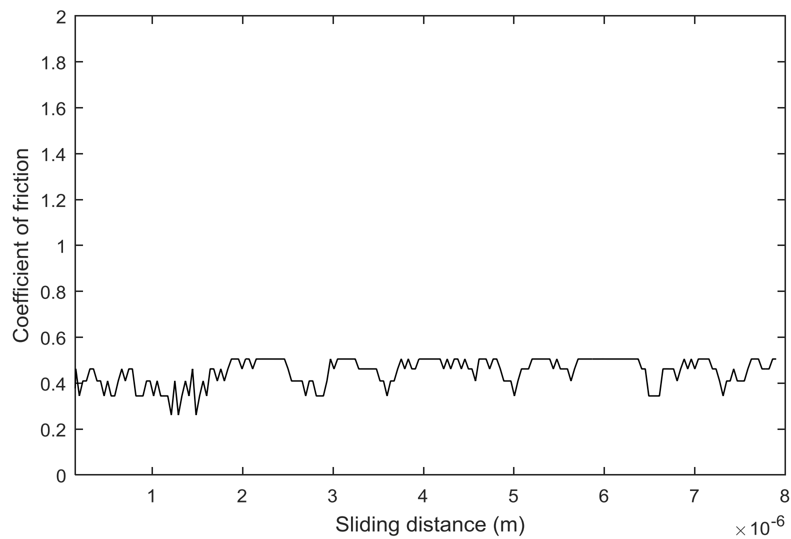

Figure 4-44 COF when the load w=275µN

However, the total energy lost, when the external load reaches to 275μN, is illustrated in Figure (4-45).

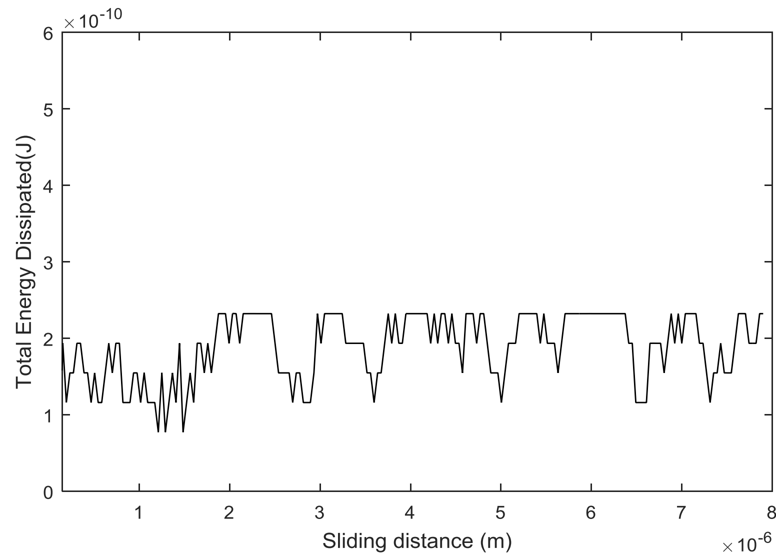

Figure 4-45 Total dissipated energy when the load w=275μN

Finally, when the external load reaches to 300μN, the coefficient of friction will be decreased to about 0.45 as shown in Figure (4-46).

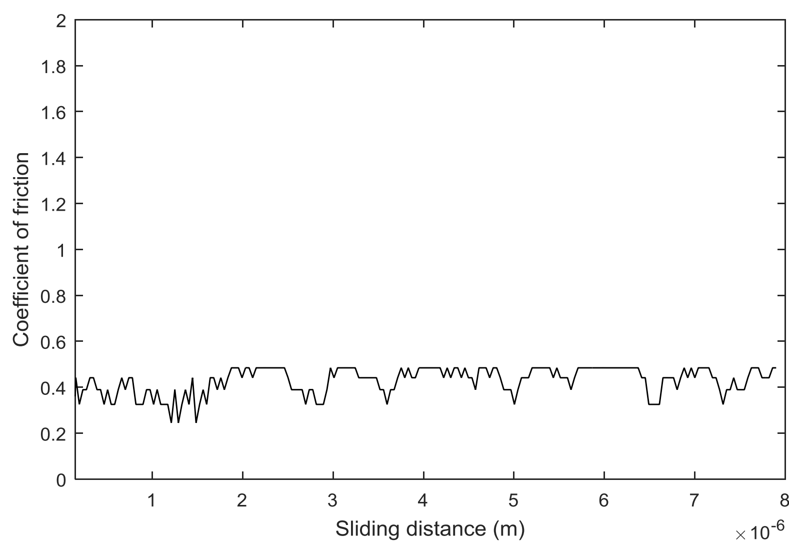

Figure 4-46 COF when the load w=300μN

While, the total energy dissipated due to breaking bonds and elastic interlocking of nanoblocks, when the external load reaches to 300μN is shown in Figure (4-47).

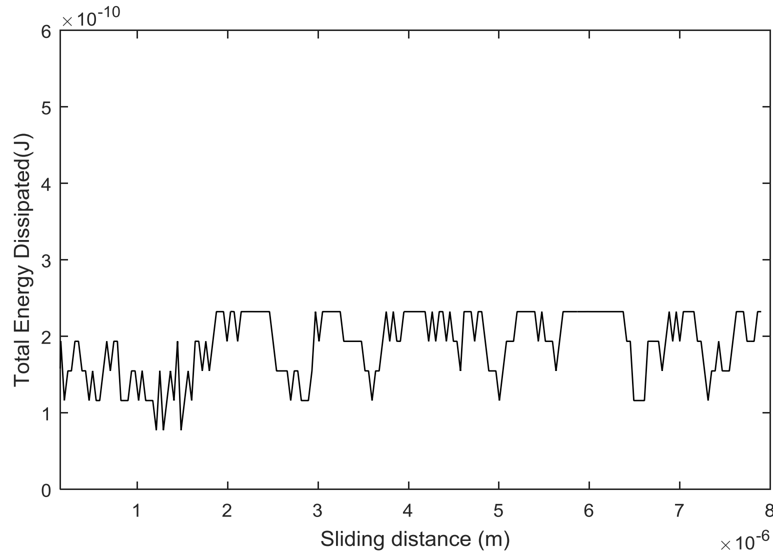

Figure 4-47 Total dissipated energy when the load w=300μN

The magnitudes of the external load have been taken to show the effect of the change of the load on the value of the COF. Force was expressed in terms of the elastic limit of the bulk of the multiscale hierarchical blocks structure. Considering that we have two adhesive subscale asperities, the values for the load in the above graphs were obtained as follows:

$$w_1 = 25\mu N \qquad w_2 = 50\mu N$$
$$w_3 = 75\mu N \qquad w_4 = 100\mu N$$
$$w_5 = 125\mu N \qquad w_6 = 150\mu N$$
$$w_7 = 175\mu N \qquad w_8 = 200\mu N$$
$$w_9 = 225\mu N \qquad w_{10} = 205\mu N$$
$$w_{11} = 275\mu N \qquad w_{12} = 300\mu N$$

Figure (4-48) has been presented to show the effect of change the load on the value of the coefficient of friction, it shows that when external load is increased, the COF decreased due to increase in the normal forces applied during the contact.

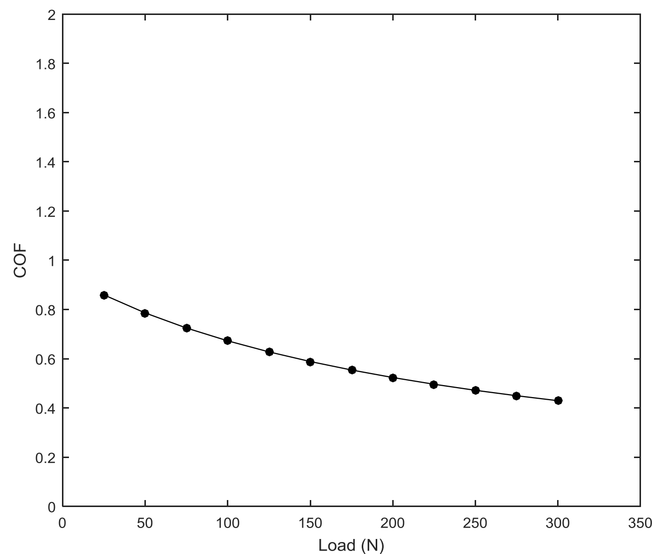

Figure 4-48 Effect of change of the load on the value of the friction coefficient

While Figure (4-49) shows the effect of changing of load on the value of the total dissipated energy. The results, which are obtained in this figure, show increase in the total energy loss and this is logical due to the increase in the area of contact and this will lead to increase the number of broken chemical and vdW bonds. These results are identical with the results that have been obtained by Savencu (2016).

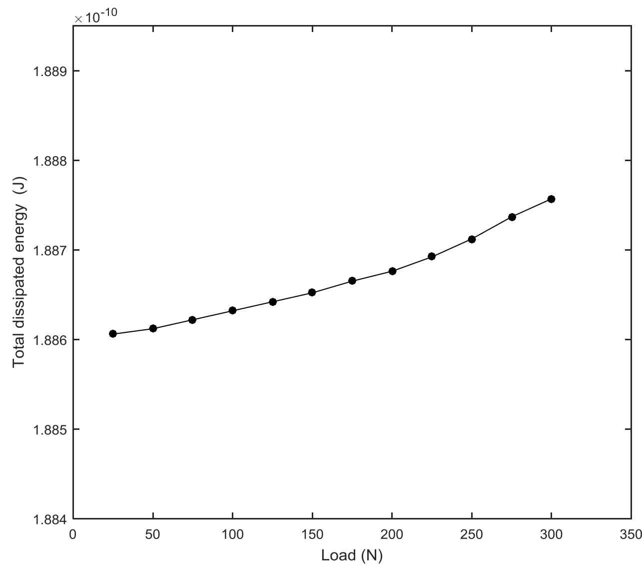

Figure 4-49 Effect of the change of the load on the value of the total dissipated energy

4.9.4 Dependence of the COF on nominal contact area

This section will focus on the effect of the increase of the nominal contact area on the COF. The values of the nominal area for which the simulation has been performed are expressed in terms of the cross-sectional area of a single adhesive subscale asperity $A_{adhesive}$. The normal force has been taken to be $w = 25$µN.

Figure (4-50) shows the effect of changing the nominal area under action on the COF, the result has showed that the current result are matching with the trend of the results that have been obtained by Savencu (2016).

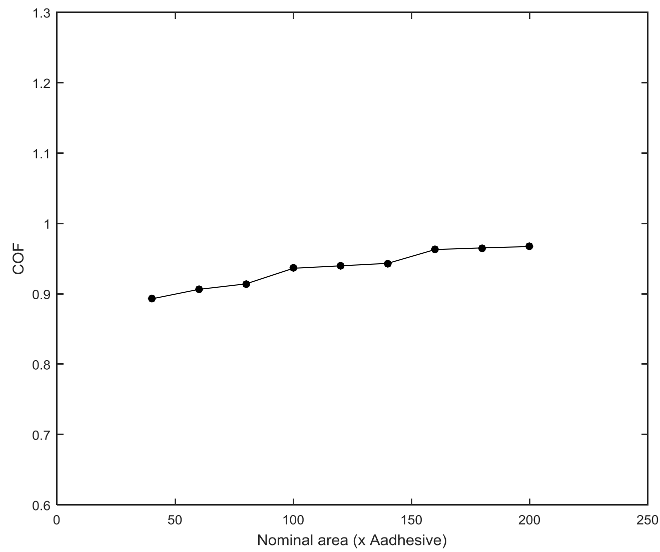

Figure 4-49 Effect of nominal area on the COF

Figure (4-51) shows the effect of increasing the nominal area on the total energy dissipated also the result has showed that there is the same trend of the results that have been obtained by Savencu (2016).

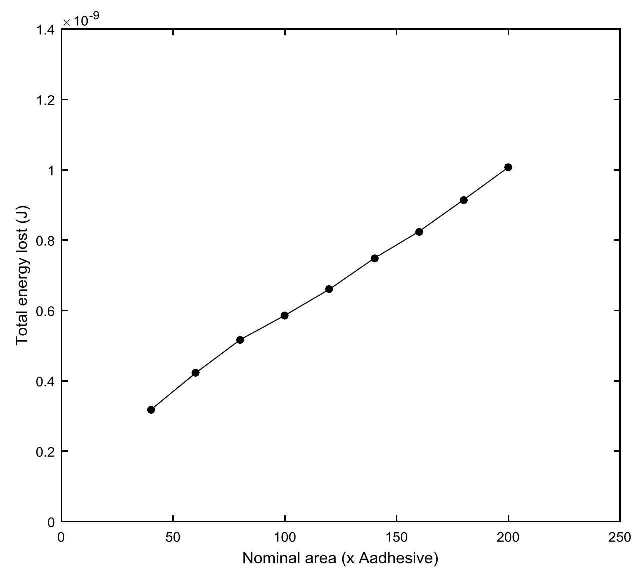

Figure 4-50 Effect of nominal area on the total dissipated energy

4.10 Conclusion to Chapter 4

In this chapter, multiscale, multi-blocks hierarchical models have been implemented in the simulation of a sliding contact between two curved silicon-based MEMS teeth surfaces. The numerical simulations have been used to show the results of the friction force F_f and the coefficient of friction μ over the sliding distance between the microgear teeth surfaces. It has been noticed that F_f is very high compared to the tangential force F_t that was obtained from Equation (4-27), which is needed to keep the sliding motion between the teeth surfaces. Therefore, high stiction occurs between the pure and clean silicon MEMS teeth when they are working in a vacuum environment. The magnitude of tangential force F_t required to start the motion should be larger than the friction force F_f to keep the motion between the teeth surfaces.

The numerical simulations for the non-functionalised silicon-based MEMS surfaces have been illustrated and discussed in the previous sections. They have shown that the possibility of stiction between the clean silicon MEMS surfaces is very high. To find a solution for stiction problem between the microgear MEMS teeth surfaces, the teeth surfaces will be modified and functionalised by the carbon-based coating layers to reduce the friction as well as the possibility of stiction, which will be discussed in the next chapter.

Chapter 5 Functionalised Silicon MEMS Microgear Tooth Surfaces, Damage Accumulation and Wear of the Functionalised Layer

5.1 Introduction

Wear considerably decreases the lifetime and reliability of small-scale micromachined devices. Maboudian et al. (1997, 1998, and 2002) have explained that adhesion and stiction could be significant at the nanoscale, which might rapidly reduce MEMS reliability or even not allow the micromachined elements to work at all. Therefore, many techniques have been employed to reduce effects of adhesion and stiction. Because the interactions between teeth occur due to bonding of surfaces to each other (see, for example, Mastrangelo and Hsu, 1993), one of the most useful techniques is the chemical modification of the surfaces by functionalising these surfaces by ultra-thin coatings. The functionalised coatings are applied to the MEMS microgear tooth surfaces to reduce friction and avoid the chemical bonding (the cold welding) between surfaces, and, in turn, to avoid stiction. In this chapter, the surface chemical modification process will be applied based on the Octadecyltrichlorosilane (OTS) self-assembly monomolecular (SAM) layers. The results of our numerical simulations related to contact between MEMS gear teeth covered by monomolecular functionalised coatings will be presented.

5.2 Functionalised Surfaces

The chemical surface modifications in the MEMS fields are used to enhance the behaviour of the surface with respect to the wear, friction, adhesion and stiction. There

are several different procedures for applying these surface chemical modifications. Figure (5-1) illustrates some of these types such as one-step, two-steps and multiple-steps functionalisation process. The substrate is the original surface and it is cleaned before surface treatment. The chemical surface enhancements contain the desired terminal groups of chemical compounds, which are coated onto the external layer of the original surface material, which is silicon in this study, the material of the microgear MEMS tooth, and so the substrate here is silicon.

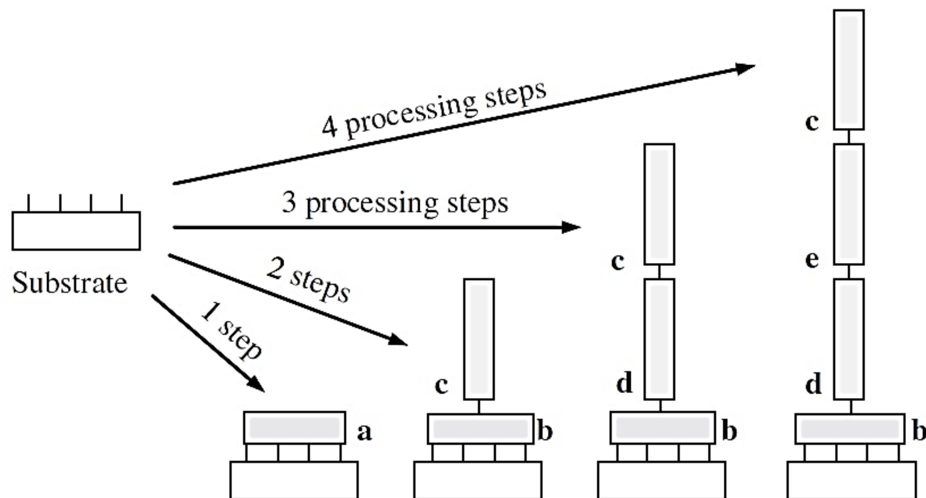

Figure 5-1 A single step and multistep surface chemical modification procedure (Ghodssi and Lin, 2011)

Ghodssi and Lin (2011) have explained that the substrate material can effect the reliability, robustness and durability of the functionalised coating layer. In case of multi-step functionalising process, the properties of the layer underneath external layer may be also effected, therefore substrate surface should be treated carefully before the process.

5.3 Materials for Functionalised Layers

The production reliability of silicon microgear MEMS may be reduced by irreversible stiction between the surfaces of the microgear teeth. According to the results of the numerical simulation for the non-functionalised coating microgear silicon MEMS teeth surfaces that has been shown in chapter 4, there is a high possibility for stiction between these surfaces due to the high chemical interactions between contacting surfaces. Because of the micro/nanoscales of MEMS elements, the traditional types of lubricants are not applicable (Srinivasan et al., 1998). In this case, adhesion and friction will be a serious matter (Rymuza, 1999), especially those with sliding interfaces such as MEMS. During contact between clean surfaces occurring in a vacuum environment, cold welding (cohesion) could be established within the area of the contact (see Derjaguin 1934a, Bowden and Leben, 1938; Bowden and Tabor, 1943). The best solution to avoid stiction is a chemical surface functionalisation coating applied on the silicon microgear MEMS teeth. The surface functionalisation coatings have been applied on the MEMS microgear teeth surfaces is an ultra-thin OTS-SAM layer.

A wide range of surface coatings materials have been produced especially those based on carbon and other coating materials (Dong et al., 2006, Flater et al., 2007). These coatings materials have the ability to work as solid lubricants and as anti-wear coatings in different industrial and research applications. Besides they provide relatively low friction, these materials provide a very high resistance to wear and fracture. These types of monomolecular functionalised layer consist of head, terminal and spacer groups. However, the molecular spacer group or simply a spacer is any flexible part of a molecule that is providing a good linking between two other parts of a molecule. A typical example of SAM layers is the functionalised silane compounds self-assembled on silicon surfaces

(see Figure 5-2), which will be investigated in this study. These layer are containing a head, terminal and spacer groups, where the flexible spacer groups can provide an essential links for the stability of molecule structure.

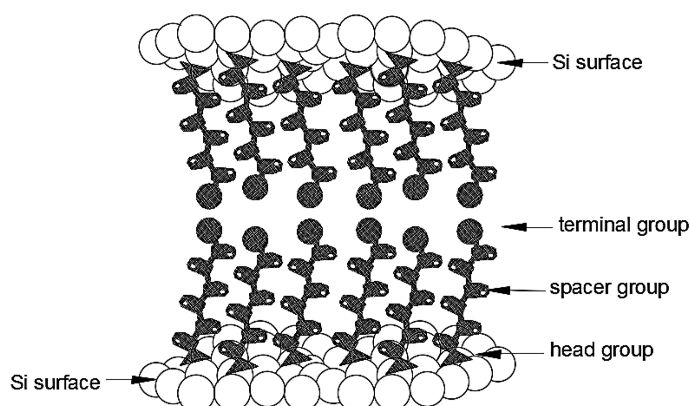

Figure 5-2 OTS self-assembled monomolecular layers on silicon

Recently, the self-assembled monomolecular have received much more attention due to their steady chemical and physical properties. In addition, their easy preparation, small thickness and good covalent bonding with the substrate (Mastrangelo, 1999). Moreover, the properties of the SAM layers such as simple alkane chains octyltrichlorosilane (OTS), which can be easy controlled by changing the chain length or the terminal group that makes these functionalised coating monomolecular layers more attractive than the other. SAM layers are two-dimensional molecular ultra-thin layers organized by one layer of molecules assembled on silicon substrate by a special feature of union as shown in Figure (5-3).

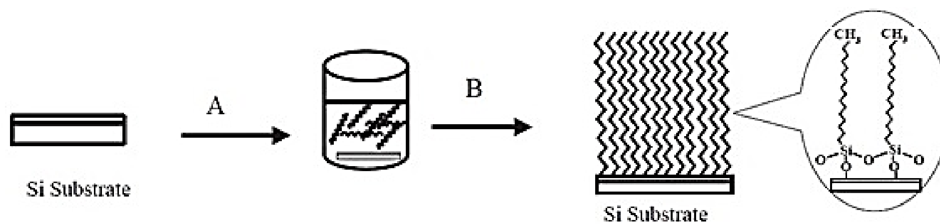

Figure 5-3 Octadecyltrichlorosilane (OTS) self-assembled monomolecular layer (see Kulkarni, et al., 2006)

SAM layer thickness typically starts from a few angstroms up to several nanometers and depends on the molecular structure and the orientation angle of the molecule chain with respect to the substrate surface. Generally, they are formed simply by exposing silicon substrate to the vapour phase of the desired molecule and incubation for a period. During these processes, the head groups are absorbed onto the silicon substrate from the vapour phase followed by a slow, two-dimensional organization of tail groups.

At the beginning, amphiphilic molecules form either a disordered mass of molecules or a lying down phase (see Figure (5-4)).

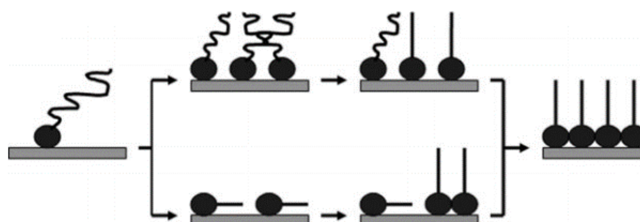

Figure 5-4 The processes and orientation of SAM layer (Ulman, 2013).

Then after a few hours, crystalline or semi crystalline structures gradually begin to form on the substrate surface. Rather than a technique such as chemical vapour deposition or molecular beam epitaxy to add molecules to a surface (often with poor control over the thickness of the molecular layer), the self-assembled procedure is convenient and the SAM layers are bonded in an orderly and compact manner with the substrate.

5.4 Simulations of the Frictional Work of a Functionalised Gear MEMS

It is assumed that an OTS-SAM layer is uniformly distributed on the entire microgear tooth contacting surface, as will be illustrated later in this section. When the surface is fully functionalised, the chemical bond between silicon-to-silicon atoms on the contacting surfaces will be approximately dismissed and there are only the vdW interactions that are created between the coating OTS SAM molecules.

5.4.1 Frictional Force between Interacting Functionalised Surfaces

The friction force $F_{f(OTS+Si)}$ for the functionalised surfaces can then be calculated from the dissipated energy $U_{diss(OTS+Si)}$, which is obtained by the dissociation of the vdW bonds in addition to the energy of the elastic interlocking between the asperities on the counterpart surfaces.

$$F_{f(OTS+Si)} = \frac{U_{diss(OTS+Si)}}{x} \tag{5-1}$$

When the monomolecular layer starts to wear away the energy loss due to dissociation of chemical interactions between silicon atoms is taken into account and it is denoted as $U_{Totalchem(OTS+Si)}$. While, the energy loss due to dissociation of vdW interaction over

the coated surface is $U_{TotalvdW(OTS+Si)}$ and the elastic energy is $U_{elastic(OTS+Si)}$. Therefore, the equation describing the friction force could now be written as:

$$F_{f(OTS+Si)} = \frac{U_{Totalchem(OTS+Si)} + U_{TotalvdW(OTS+Si)} + U_{elastic(OTS+Si)}}{x} \quad (5\text{-}2)$$

The COF ($\mu_{(OTS+Si)}$) for the functionalised surface will be calculated in the same way by using the total dissipated energy. This energy has been found through the mechanisms of contact as the dissociation of chemical, vdW interactions and the elastic interlocking energy asperities on the counterpart's surfaces, which are covered by the functionalised coating OTS layer in addition to the uncovered silicon surface.

$$\mu_{(OTS+Si)} = \frac{U_{Totalchem(OTS+Si)}}{(\boldsymbol{F_N} + \boldsymbol{F_{adh}})\ x} + \frac{U_{TotalvdW(OTS+Si)}}{(\boldsymbol{F_N} + \boldsymbol{F_{adh}})\ x} + \frac{U_{elastic(OTS+Si)}}{(\boldsymbol{F_N} + \boldsymbol{F_{adh}})\ x} \quad (5\text{-}3)$$

Then, the COF could be expressed as in the following:

$$\mu_{(OTS+Si)} = \mu_{chem} + \mu_{vdW} + \mu_{elastic} \quad (5\text{-}4)$$

Compared with equation (3-9), the possibility of stiction between the microgear MEMS teeth surfaces due to the different physical and chemical interactions, which typically cause cold welding junctions, will be rapidly reduced in this case. The characteristics (OTS-SAM) layer can be managed by changing the length of its chain or the terminal group.

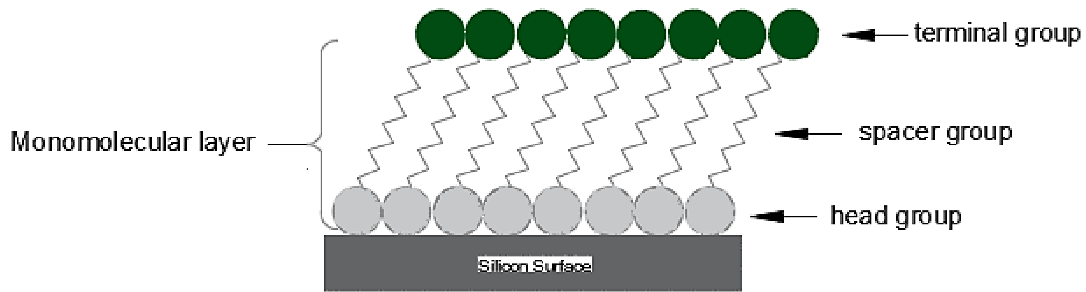

Figure 5-5 OTS-SAM layer distributed uniformly on the tooth surface

The higher reduction in the possibility of stiction when applying the OTS-SAM layer is due to their higher hydrophobicity, non-reactive terminal group, uniformity and higher packing density of the monomolecular layer. Therefore, the vdW interactions between the particles has been generated and affected during the sliding distance. After wear starts to occur over the functionalised monomolecular coating layer, the chemical interaction between the silicon particles will begin again and will gradually increase as the number of contact cycles increases. In other words, stiction will start to occur again when functionalised coating starts to wear away.

5.4.2 Tangential Force between Interacting Molecules

In the sliding of functionalised microgear MEMS tooth surfaces on each other, the chemical interactions between them will be small compared with the value of the tangential force $(F_t > F_f)$ due to the stability and non-reactive of the terminal group. Tangential force is necessary to keep the microgear system working without any interruption. It is typically responsible for the sliding motion of the microgear MEMS tooth surfaces over each other.

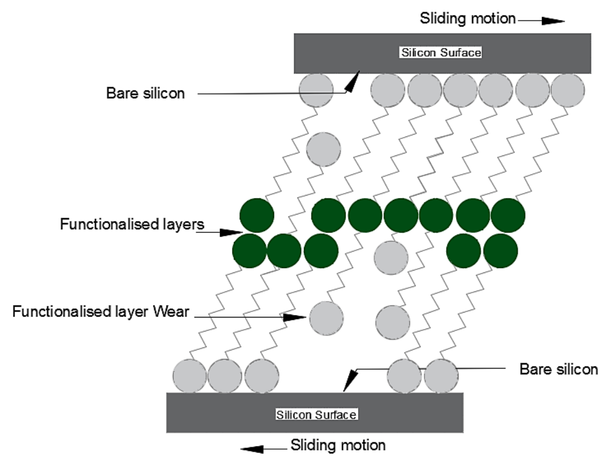

Figure 5-6 Effects of the tangential force on the interaction between particles

This force works to break the chemical bonds between the contacting surfaces, these bonds are generated between the counterpart particles of the coating monomolecular layer. In other words, if $F_t > F_f$, then the possibility of stiction between particles on the contacting surfaces is rapidly decreased due to the high tangential force that exceeds the friction force at the junction's areas.

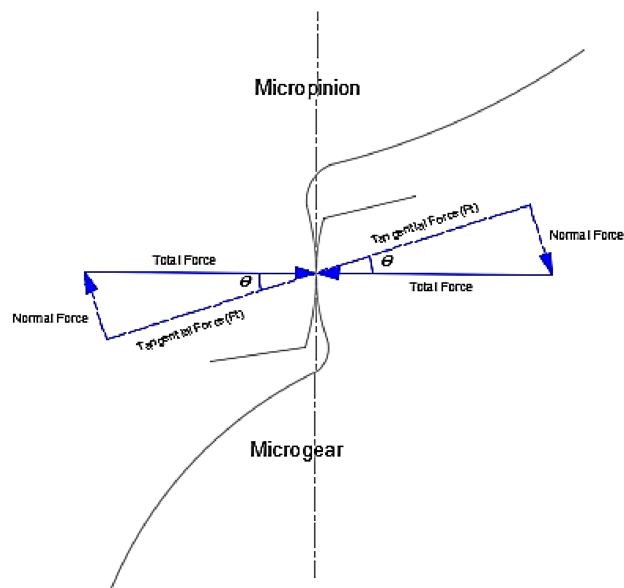

Figure 5-7 The tangential force of meshing microgear MEMS teeth

The tooth on the micropinion pushes the tooth on the microgear with a tangential force F_t . As it follows from (4-27):

$$F_t \ = T_{r\ micropinion} \ / \ R_{micropinion} \ = \ 2.82 \times 10^{-3} \text{ N} \qquad (5\text{-}5)$$

This force is not directly transmitted as a tangential force on the micropinion but these forces through the micropinion teeth can only be transmitted to the point where the teeth surface are in contact (see notation in section 4-7). Given that these surfaces are designed to have a nano adhesive subscale and atomic asperities, force can be passed on to the surface through these asperities when they are in contact.

Figure (5-7) has denoted the total force acting on the micropinion tooth toward the microgear tooth, and vice versa. These forces can be represented as two perpendicular components: normal and tangential forces. The normal component F_n pushes the microgear teeth to separate them from each other, while the tangential F_t tries to make them slide over each other. The microgear surfaces will contact at the same angles whatever the amount of force is applied on them and, therefore, any increase in the tangential force will increase the normal force.

As soon as the functionalised coating monolayer is worn away, stiction again occurs between the particles on the meshing surfaces. When the OTS particles start to leave the surface, chemical bonds will begin to be generated between the uncovered spaces. Therefore, the possibility of stiction also starts to increase as each particle of the coating is worn away (see Figure 5-8).

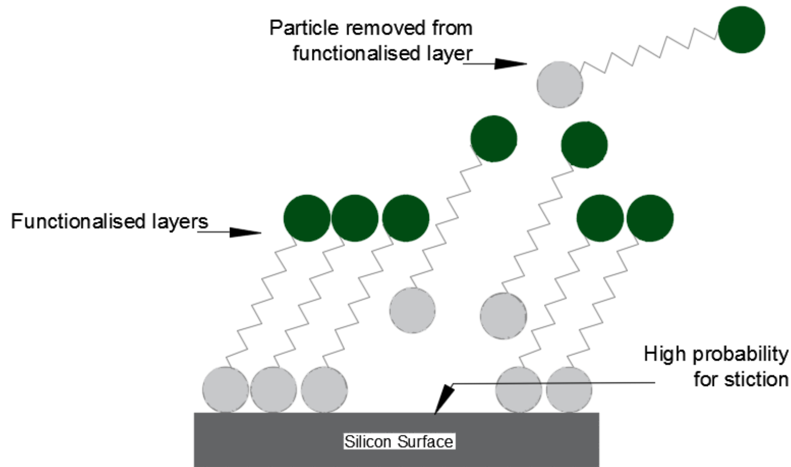

Figure 5-8 Functionalised coating OTS layer worn away

The wear of OTS-SAM layer has been assumed to be increased with respect to the number of contact cycles.

We have to clarify the meaning of the term 'cycle' to avoid any confusion further. Let us consider the microgear, i.e. the gear having larger radius R_B, and micropinion, i.e. the gear having smaller radius R_A (see Figure 4-6). As it has been described in Chapter 4, when two meshing gears transmit rotational motion, the gears are designed so that the velocity at the point of contact of the two pitch circles is the same for each gear.

During one full turn of the microgear, each its tooth has only one meshing contact, while each tooth of the micropinion will have several meshing contacts (actually a micropinion tooth will have four meshing contacts in the case described in Figure 4-6). The number of meshing contacts of a tooth will be called as the meshing cycle number.

During one meshing contact, the pressure acting on each nanoblock is not constant. In fact, we will observe increasing and decreasing of the load acting on the nanoblock within one meshing cycle. The number of increasing and decreasing of the load will be called the

cycle and it will be denoted as k. Note that the amplitude of the load will vary from one cycle to another one. When we are speaking about the MEMS durability we can replace the time variable by the number of meshing cycles N.

5.4.3 Microgear MEMS Stiction, Formulation and Solutions

In this section, Goryacheva and Torskaya model of damage was modified and applied on the microgear MEMS teeth surfaces. Sliding microgear MEMS teeth can be hierarchically organized as multiscale asperities over a microgear MEMS tooth. A monomolecular functionalised coating layer has covered the surface of the microgear MEMS tooth (see Figure 5-9).

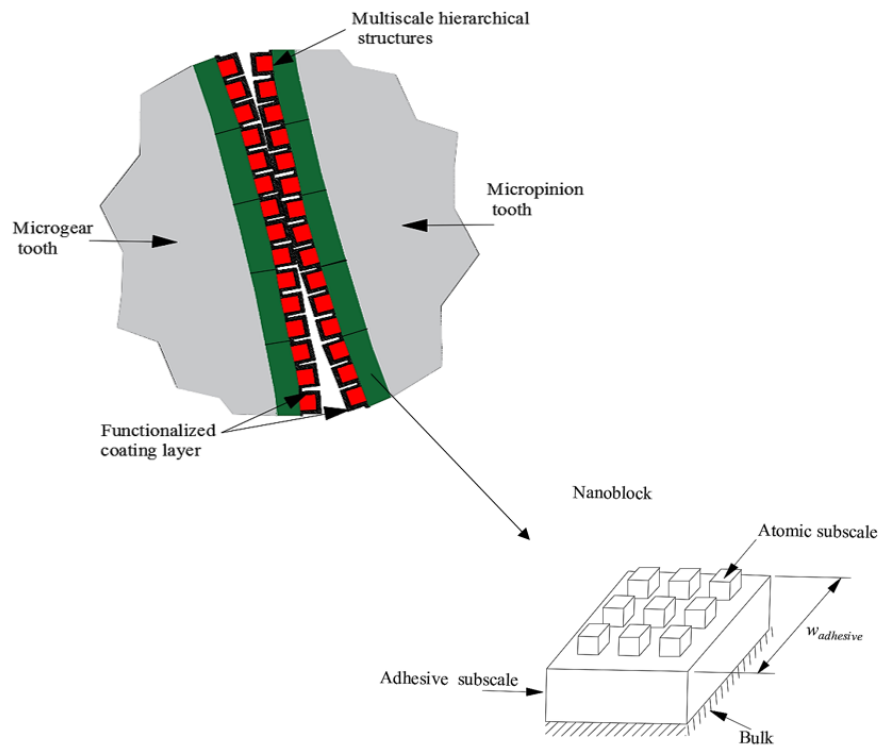

Figure 5-9 Hierarchically organised multiscale nanoblocks (red and green) covering the surface of microgear tooth (grey). The functionalised SAM layer coating is shown in black.

The nanoblocks asperities are located over the microtooth surface and the nanoblocks are distributed at the nodes of a square lattice with period $w_{adhesive}$, as shown in Figure (5-9). The microgear MEMS meshing teeth system was under the effects of nominal pressure, p_t adhesion force and friction force. The total friction force is determined depending on the total energy dissipated through the sliding distance due to the dissociation of the chemical and vdW interactions (see Equation 5-1)

Due to the stiction between the meshing microgear MEMS teeth, a specific ultra-thin functionalised coating layer has been applied to prevent stiction between counterpart teeth surfaces (see Figure 5-11). Friction force has been found by calculating the total energy loss through different physical-chemical mechanisms. This energy lost is due to dissociation of chemical and vdW bonds, and the energy lost through elastic deformation of nanoasperity during the sliding contact distance. The height and width of the adhesive subscale asperities have been calculated by determining the area of the surface, which is limited between the mean line and the root mean square for the silicon roughness profile. This amount of surface area is then equally redistributed, as shown in Figure (5-10).

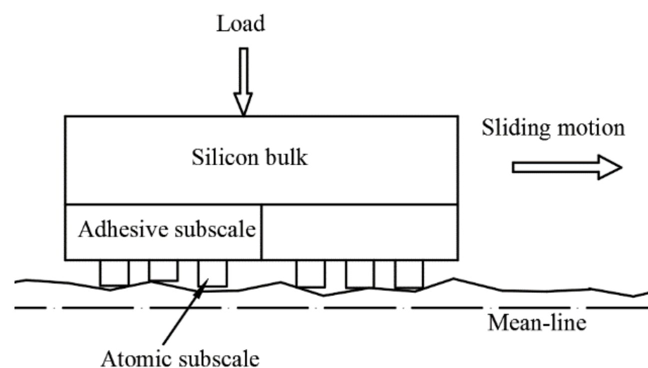

Figure 5-10 Multi-scale hierarchical structure with a vertical degree of freedom

Similarly, the height and width of the atomic subscale asperities, as well as the distance between them, were determined by analysing the measurement of the silicon surface roughness at atomic subscale by using an AFM device (see for example Savencu, 2016 and Almuramady and Borodich, 2017). A carbon-based functionalised coating monomolecular layer has been used in this model, which is molecular ultra-thin layer organized by one layer of molecules assembled on silicon substrate as shown in Figure (5-11).

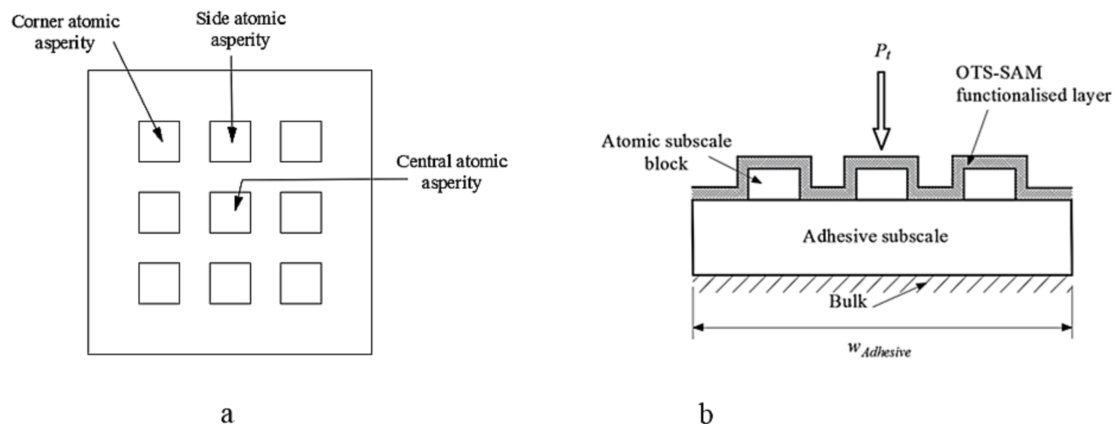

Figure 5-11 (a) Top view of the nanoblock and (b) monomolecular carbon-based functionalised coating layer on the microgear MEMS tooth nanoblock

Where $w_{adhasive}$ is the width of the adhesive subscale asperity. The nanoblock is coated by monomolecular functionalised coating layer. The properties of the substrate have assumed not effect by coating layer because it is just a monomolecular layer thickness. During the sliding of the microgear MEMS tooth surfaces on each other, the nanoblocks generate a high friction force with respect to the number of contact mesh cycles. This will cause a destruction of the surface functionalised layer over the microgear MEMS tooth surface.

5.5 Damage Accumulation Models

It is clear that the functionalised layer accumulate some damage when two teeth contact each other. The damage mechanics (Krajcinovic, 1996, Rabotnov 1963) have been well developed for bulk materials. Rabotnov has introduced an internal damage variable ω ($0 \leq \omega \leq 1$), while Kachanov worked with continuity variable ψ ($\psi = 1 - \omega$). If $\omega = 0$ then the material is undamaged, if $\omega = 1$ then the material is completely damaged. The damage variable ω is very important to study damage evolution of materials. It has been shown that often the use of the parameter is physically justified and it provides a measure of the influence that randomly distributed micro defects exert on the macro parameters of a structure and its macro response (Krajcinovic, 1983). The concept of damage has various applications (Rabotnov 1963, Goryacheva and Torskaya 2003, Manoylov et al., 2013).

Models of discrete contact developed by Goryacheva (1998), Goryacheva and Torskaya (2003, 2010) were introduced to calculate the damage accumulation in a relatively thick coating layer. The calculations were performed by applying a periodic system of indenters. It was assumed that the system works at high friction rate. The damage accumulation was calculated taking into account the effects of the surface geometry parameters at the microscale and the sub-stresses in the coating layer joined to an elastic surface.

5.5.1 The Extension of Goryacheva-Torskaya Model

It has been suggested in Chapter 3 to model a rough silicon micro-tooth MEMS surface as a bulk silicon material covered by asperities that are represented as nanoblocks having two subscales specified by the character of interactions: atomic subscale, where the

chemical interactions are significant, and adhesive subscale, where the vdW interactions are likely occur (Almuramady and Borodich, 2016). As it has been shown in Chapter 4, there is a high possibility that silicon microgear MEMS cannot work due to stiction between clean silicon surfaces. Hence, it has been suggested here to cover the surfaces by OTS-SAM layers. Because the layers are monomolecular, the Goryacheva and Torskaya (2010) model of damage accumulation has to be modified in order to reflect the specific of SAM layers. These monomolecular layers do not affect the subsurface stress fields in the tooth under a specific external load, however, they may significantly affect the frictional force. Indeed, they prevent the creation of the chemical bonds between atomic subscale asperities. Hence, even if one of the contacting surfaces has no functionalised coating monomolecular layer (it can be worn away in meshing cycles), no chemical interactions may happen. The full chemical interaction occur only when both functionalised layers are worn away and only in this case stiction will occur.

In the original Goryacheva and Torskaya (2010) model, the damage function is dependent on the coordinates, y and z along with the time variable t , i.e. $\omega(x, y, z, t)$. However, in the case microgear MEMS we assume the validity of the classic linear contact theory. Hence, nothing depends on the y coordinate.

In addition, we will study damage accumulation in the OTS SAM layers. If $\omega = 0$ then all chemical bonds between the SAM layer and the asperity exist, i.e. there is no damage, if $\omega = 1$ then the chemical bonds between the layer and the asperity are completely damaged and the functionalised layer has been worn away. Hence, nothing depends on the z coordinate in a monomolecular layer. Thus, we can characterize the damage by $\omega(x, t)$ variable.

5.5.2 The Contact Problem Solution

The modified Goryacheva-Torskaya model of the coating's damage accumulation consisted of the following steps of calculations:

(i) Calculate the contact pressure and friction forces taken into account adhesion effects.

(ii) Calculate and analyse of the damage accumulation on the surface coating layer.

(iii) Find the sub-surface directional stresses along the contact sliding distance within the discrete contact points.

In order to make the model more realistic and remove the artificial stresses singularity at the edge of atomic blocks, the geometry of the atomic subscale block has been approximated as shown in Figure (5-12).

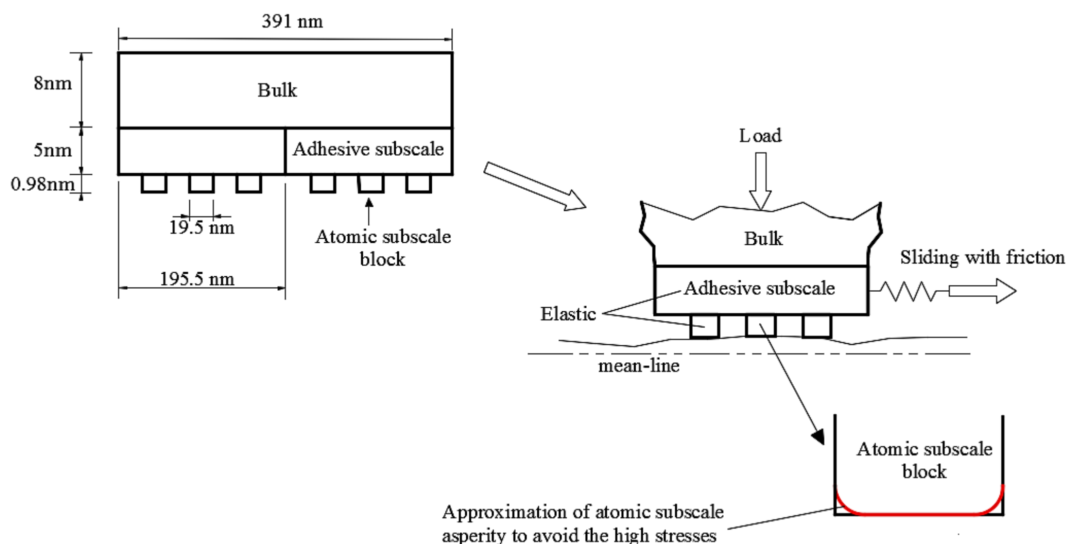

Figure 5-12 Approximation of geometry shape for the atomic subscale asperities

As a solution to the problem of an elastic contact the shape of the atomic block is given by a power-law function (a monomial) of degree d (see Borodich, 2014 and Borodich et al., 2014) According to the following shape function

$$f(r) = B_d r^d \quad (5\text{-}6)$$

where d is the power of the approximation (see Figure 5-13).

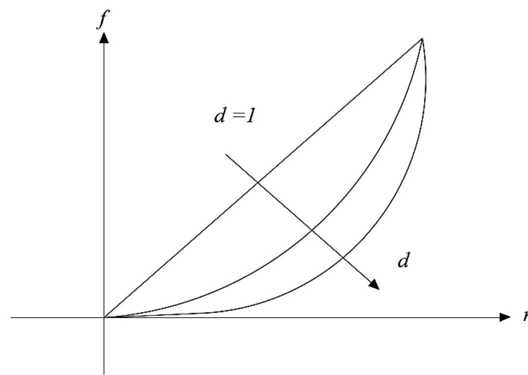

Figure 5-13 Effect of degree of the shape approximation

If $d = 4$ then it looks similar to an indenter with flat base and semicircular edges. The geometrical parameter B_4 was calculated to be equal to $4 \times 10^{22}\ \mathrm{m}^{-3}$ for the geometry of atomic asperities.

To show the effect of approximation especially close to the edge, the shift distance could be calculated from power law as follows:

$$z = f(r) = B_4\ r^4 \quad (5\text{-}7)$$

Then by using the half width of one atomic subscale asperity as $(r) = 9.75 \times 10^{-9}\mathrm{m}$, and $B_4 = 4 \times 10^{22}\mathrm{m}^{-3}$, then $z = 4 \times 10^{22} \times (9.75 \times 10^{-9})^4$, that means $z = 3.62 \times 10^{-10} = 3.62$ Å. Therefore, the atomic subscale asperity edge will be shifted by z ,

which is approximately distance of two atoms, that is relatively small distance but in the same time rapidly reduce the stresses on the edges of the asperity (see Figure 5-14).

Moreover, by using Equation (4-8) for the same value of the depth z we find the equivalent radius of approximated atomic asperity $R = 131.3$ nm, then the effective radius according to Hertz theory R_{ef} can be obtained by using Equation (4-11). To find the radius of contact (a) in this case depending on hertz contact theory

$$a = \left(\frac{3\,p\,R_{ef}}{4\,E^*}\right)^{\frac{1}{3}}$$

The effective radius according to Hertz theory is $R_{ef} = 131.3 \times 10^{-9}$m. The pressure applied on the corner atomic asperity is $p = 0.8275 \times 10^{-6}$ N and the contact modulus is $E^* = 8.4996 \times 10^{10}$ Pa. By substituting these values in the above equation, the radius of contact will be obtained as $a = 8.95 \times 10^{-9}$ m

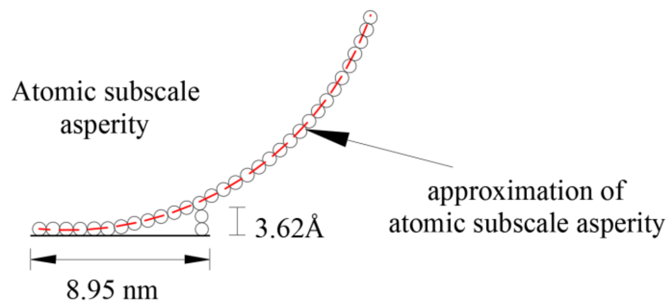

Figure 5-14 Change in the edge of atomic subscale asperity due to approximation

Pressure and surface stresses have been calculated taken into account the mutual effect. The coefficient of the friction for the self-assembly monolayer OTS-SAM functionalised coating layer over the silicon microgear MEMS tooth surface has been calculated for

fully functionalised tooth surface, as shown in Figure (5-15) and second when the wear started to occur by stiction or due to the operation process. The coefficient of friction was found to decrease from 0.85 for bare silicon to 0.2 for self-assembled monomolecular layer microgear MEMS teeth surfaces. The higher reduction in the coefficient of friction when applying the OTS-SAM layer is due to their higher hydrophobicity, non-reactive the terminal group, uniformity and higher packing density of the monomolecular layer. For bare silicon, stick-slip maybe occurs due to stiction (cohesion) or so-called cold welding between silicon contact surfaces, but this phenomenon has been completely eliminated for OTS-SAM functionalised coated layer. SAM layers have been widely proposed and characterised as the lubricants for MEMS (see for example, Ghodssi and Lin, 2011, Maboudian and Howe, 1997). These monomolecular films can decrease the COF, stiction and wear if they have deposited on the silicon substrate (Komvopoulos, 1996, Spearing, 2000, Srinivasan et al., 1998).

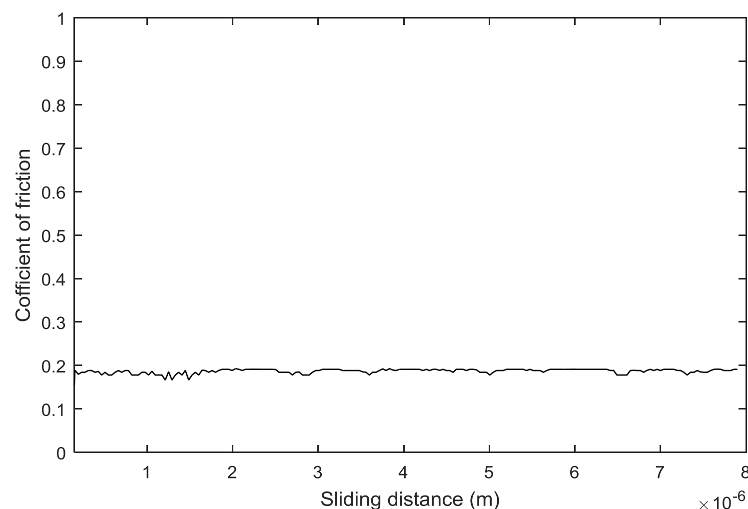

Figure 5-15 COF for functionalised coating teeth surface by OTS– SAM layer

When the microgear MEMS tooth surface is fully protected with OTS-SAM coating layer, the value of the COF is approximately 0.2. This value is quite suitable to continue the operating system without any problems occurring due to stiction or friction.

Hence, $U_{Totalchem} = 0$ our calculations have taken into account just termination of the chemically active tips of bare silicon asperities by self-assembled monomolecular layer of Octadecyltrichlorosilane ($CH_3(CH_2)_{17}SiCl_3, OTS$). Due to lack of reliable experimental results, we have not taken into account the possibility of formation of the double layers between the coated surfaces. However, if we look out the structure of the SAM layer where the head group is attached (chemical sorption) to the silicon surface while the tails (spacer and terminals groups) are organised into regular arrangement (orientation) molecular structure. Then, we can see that it is very likely that the functionalised coating layers form charged double layers. Due to similar charged tails, the double layer interactions between the self-assembled monomolecular layers are repulsive; this will lead to decrease the value of the compressing force,

$$F_N + F_{adh} < F_N$$

Therefore, for the same normal force F_N the approach of the surface will decrease and hence, both values of $U_{TotalvdW}$ and $U_{elastic}$ will decrease. This will lead to general decrease of the COF. This can be the reason that the COF for OTS-SAM layer that was calculated from our model is 0.2, while it was measured to be about 0.075 for 50gm and sliding velocity 0.1mm/sec by Satyanarayana et al., (2005). However, for velocity equal to 2 cm/sec and load equal to 5gm, our estimations are quite close to their experimental observations (see Figure 5-16).

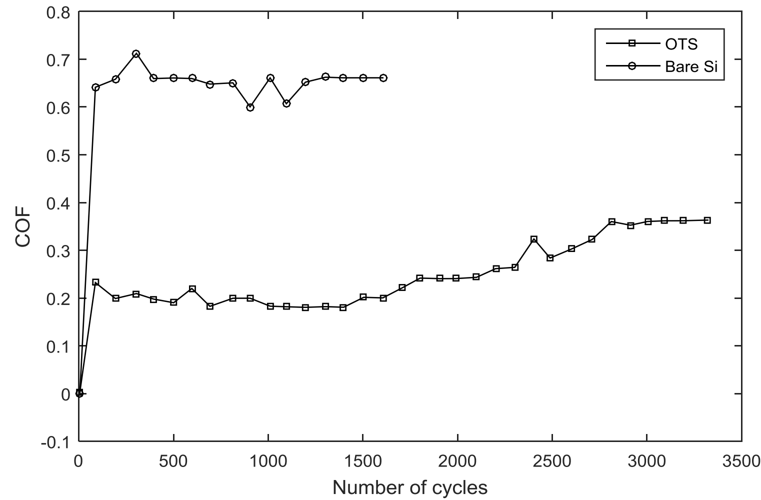

Figure 5-16 Variation of COF with sliding cycles for bare Si and OTS at a sliding velocity of 2cm/sec and normal load of 5gm (Satyanarayana et al., 2005)

Figure (5-16) shows that the COF in the case of OTS coating starts to increase when the damage occurs in the coating layer after 1000 cycles. The number of cycles are the pin on disc cycles, which do not have the same meaning as the meshing cycles. Indeed, radius of curvature is the same during the cycle and this is 3D problem, while, we are interested in 2D linear contact problems.

The load values have been used to determine the contact pressures as well as the principal shear stress at the sliding contact surfaces. The results are obtained for six different values of loading (see Table 1) that have been chosen for single adhesive subscale asperity. The results for load distributions between atomic asperities are presented in the following table:

Table 5-1 Nominal and distributed load over the atomic subscale asperities

Load for adhesive asperity, $\times 10^{-6}$ N	Corner asperity, $\times 10^{-6}$ N	Side asperity, $\times 10^{-6}$ N	Central asperity $\times 10^{-6}$ N
0.8166	0.0963	0.0884	0.0782
0.99	0.1167	0.1071	0.0947
1.7944	0.2115	0.1941	0.1717
3.4279	0.4041	0.3709	0.3281
4.4055	0.5193	0.4766	0.4216
7.0165	0.8275	0.7595	0.6719

For the corner atomic subscale block at maximum load 0.8275×10^{-6} N the results of contact pressure and principal shear stress τ are presented in Figure (5-17a) and Figure (5-17b) respectively. The radius of contact is 8.95 nm as it shown in Figure (5-14).

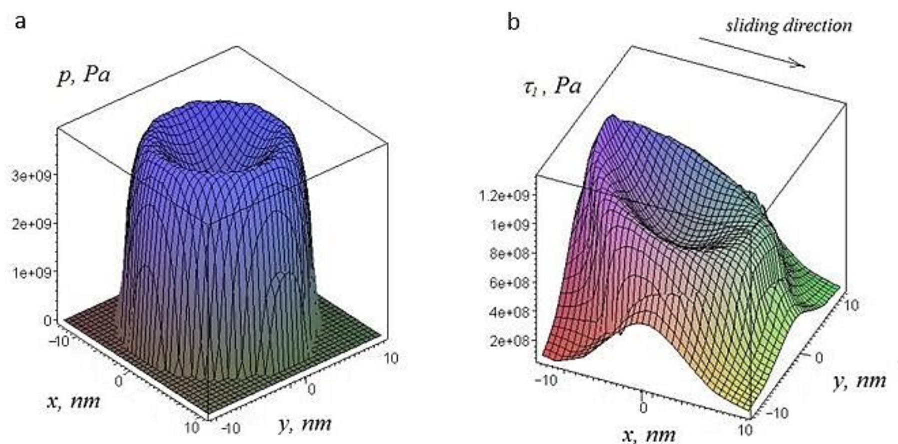

Figure 5-17 Corner atomic subscale block at maximum load 0.8275×10^{-6} N (a) Contact pressure; (b) Principal shear stress τ_1

Simulations have showed that the atomic subscale asperity, which is located at the corner of the adhesive subscale asperity, will be under stresses higher than other asperities. Because of that, the cracks or damage in the functionalised coating layer will begin in the edge of the asperity. Figure (5-18b) shows clearly that there is high principle shear stress on the edge of the adhesive subscale asperity (at the corner atomic subscale asperity),

which gives damage a high chance to start there. It can be explained why the coatings fracture occurs not simultaneously. The results of calculations for contact area are in the following table:

Table 5-2 Nominal load and the radius of contact area over the atomic subscale asperities

Load for adhesive asperity, $\times 10^{-6}$ N	Corner asperity, nm	Side asperity, nm	Central asperity, nm
0.817	5.82	5.72	5.59
0.991	6.05	5.94	5.80
1.794	6.82	6.70	6.52
3.428	7.76	7.62	7.44
4.405	8.16	8.02	7.82
7.016	8.95	8.80	8.59

To model the accumulation damage in the surface functionalised monomolecular layer, the function characterizes the material damage at the point $M(x, y, z)$, and depends on the stress amplitude values at this point. The model of the damage linear summation is used (the damage increment at each moment does not depend on the value of the already accumulated damage). Stiction occurs at the time instant t^* at which this function reaches a threshold level at some point.

The damage accumulation rate $\partial\omega(x,t)/\partial t$ has been considered as a function of shear stress at the specified point along the tooth sliding direction. The other parameters are depending on the material of the functionalised coating layer and substrate. The relation between the damage accumulation rate and the amplitude value $\Delta\tau_1$ of the principal shear stress at the point can be presented as the following modification of the Rabotnov equation (see Rabotnov, 1963):

$$\dot{\omega}(x,t) = \frac{\partial\omega(x,t)}{\partial t} = c \cdot (\Delta\tau_1(x,t))^m \qquad (5\text{-}8)$$

Where c and m are phenomenological parameters and $\Delta\tau_1(x,t)$ is the amplitude value of the principal shear stress at the point x for one period of sliding loading. The parameter c is

used to normalise the equation. Indeed, the physical dimensions of the components are the following:

$$[\dot{\omega}] = T^{-1};\ [\Delta\tau_1] = FL^{-2};\ [(\Delta\tau_1)^m] = (FL^{-2})^m;\ [c] = (FL^{-2})^{-m}T^{-1}$$

where F, L and T are the dimensions of force, length, and time respectively. Here we have used the Maxwell notation $[\cdot]$ for physical dimension of the variable in the square brackets. If the problem is periodic, then we can replace the time variable by the number of cycles N.

Now we have to estimate the number of subcycles k that is how many times we can observe increasing and decreasing of the load acting on the nanoblock within one cycle for MEMS teeth.

$$\dot{\omega}(x,k) = c \cdot (\Delta\tau_1(x,k))^m \tag{5-9}$$

The equation (5-9) can be transformed to an equation for damage $\omega(x,k)$, which is accumulated at fixed point x during k subcycles of a mesh cycle in a nanoblock

$$\omega(x,k) = \sum_{i=1}^{k} c_1 \cdot (\Delta\tau_{1i}(x,k))^m \tag{5-10}$$

Where c_1 is a normalization parameter such that the damage $\omega(x,k)$ calculated according to (5-10) satisfies the restrictions ($0 \le \omega \le 1$). The physical dimension of c_1 is

$$[c_1] = (FL^{-2})^{-m} \tag{5-11}$$

Using the numerical simulations, we obtained the graph of the distribution of pressure acting on a tooth along x (sliding distance). According to the pressure distribution over sliding distance, there are $k = 48$ fluctuation cycles of pressures (see Figure 5-18).

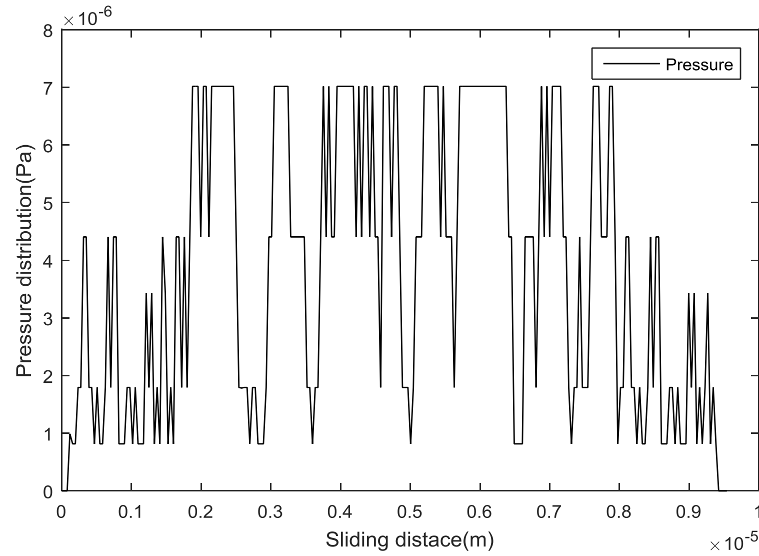

Figure 5-18 Distribution of pressure acting on a tooth along x (sliding distance). There are $k = 48$ picks of the pressure fluctuations.

Because each nanoblock at the atomic subscale has 9 asperities and 9 different values of the principal shear stress $\Delta\tau_1$ acting on each atomic asperity will be calculated using the distribution of pressure obtained. Taking cross-sections in sliding direction through the center of contact zone for each of the atomic asperity of a nanoblock to show the principal shear stress distributions, which are presented below for corner atomic subscale asperity (red line), side atomic subscale asperity (green line) and central atomic subscale asperity (blue line) in two different loads (minimum and maximum) applied on the adhesive nanoblock:

Figure (5-19) shows principal shear stress distributions when the minimum load is applied on the adhesive subscale block, which equal to 0.816×10^{-6}N, while Figure (5-20) shows these distributions when load at its maximum value 7.016×10^{-6}N .

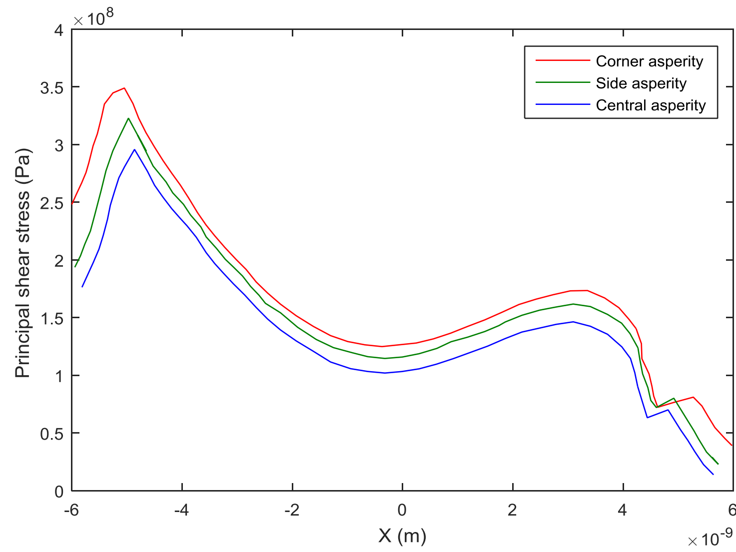

Figure 5-19 Principal shear stress distributions when load is minimum 0.816×10^{-6}N.

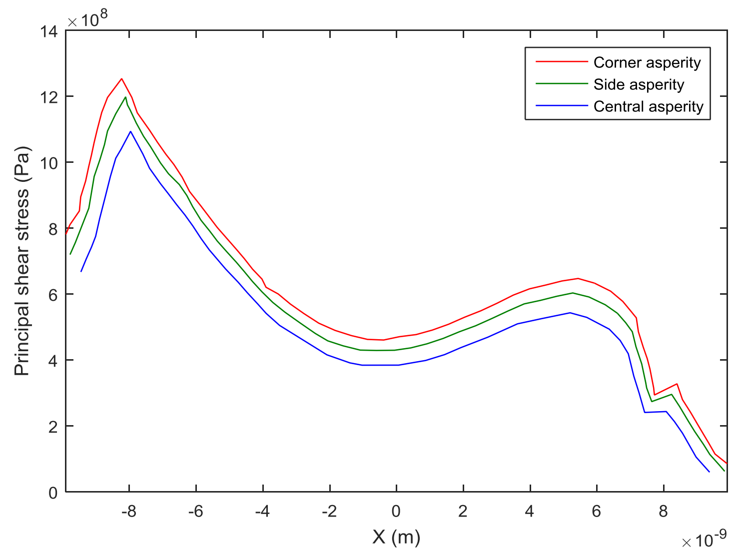

Figure 5-20 Principal shear stress distributions when load is maximum 7.016×10^{-6}N.

Figure (5-21) shows principal shear stress distributions for the corner atomic subscale asperity, when it under the effect of different values of loads applied for example (0.816×10^{-6}N, 3.428×10^{-6}N and 7.016×10^{-6}N for red, green, blue lines respectively).

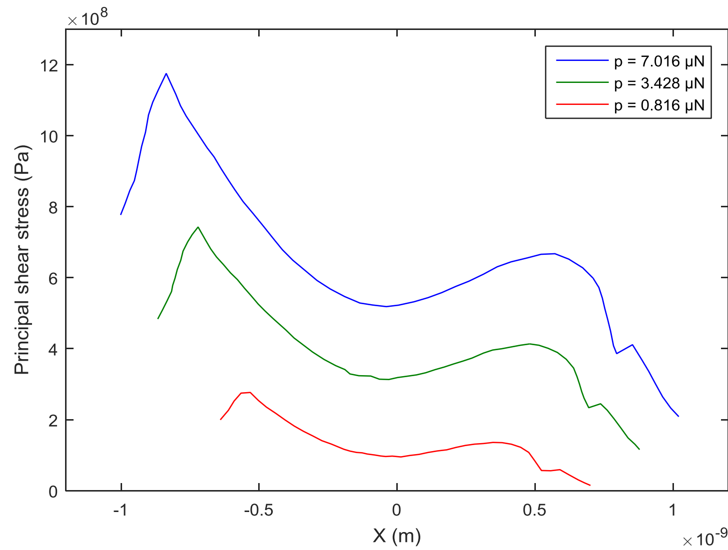

Figure 5-21 Principal shear stress distributions for the corner atomic block with different values of load (0.816×10^{-6}N, 3.428×10^{-6}N and 7.016×10^{-6}N for red, green, blue lines respectively.

The numerical results for damage function ω has been calculated with two different value for the phenomenological parameter m obtained for $m = 1$ and $m = 2$ (the summation of 48 meshing cycles for the corner atomic block (red line) , side block (green line) and central atomic block (yellow line)). One can see that there is significant difference when this parameter m changes. Figure (5-22) shows that the maximum value for damage function equal (2.4×10^{10}) when $m = 1$. While, Figure (5-23) shows it is equal to (1.6×10^{19}) when the parameter $m = 2$.

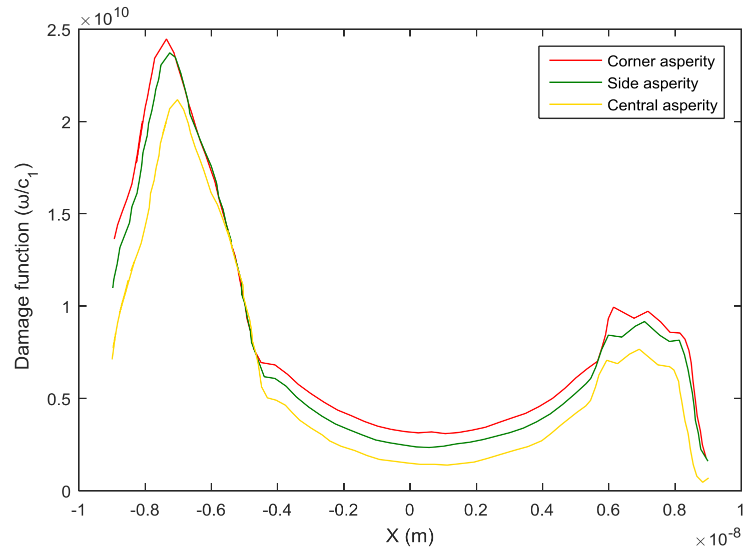

Figure 5-22 Damage function (ω/c_1) when m=1, for one nanoblock

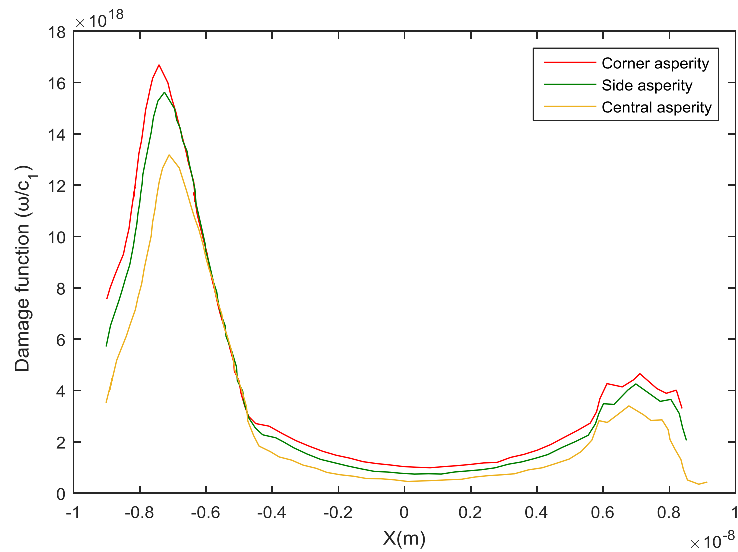

Figure 5-23 Damage function (ω/c_1) when m=2, for one nanoblock

Comment. The Figures 5-17, 5-19 – 5-23 have been obtained in collaboration with Professors I.G. Goryacheva and E.V. Torskaya and presented here with their permission.

The maximum values for the damage function (ω/c_1) have been calculated with respect to their location on the nanoblock and presented in Table (5-3) when the parameter $m =$

1 and in Table (5-4) when $m = 2$. These calculations are reported for the corner, side and central atomic block respectively to show the variation of damage with respect to their location on the nanoblock asperity.

Table 5-3 Maximum values for ω/c_1 when $m = 1$ and their location:

Asperity position	x, m	ω/c_1 , Pa
Corner asperity	-0.823×10^{-8}	0.248×10^{11}
Side asperity	-0.801×10^{-8}	0.243×10^{11}
Central asperity	-0.7791×10^{-8}	0.226×10^{11}

Table 5-4 Maximum values for $\omega/c_1$when $m = 2$ and their location:

Asperity position	x, m	ω/c_1 , Pa^2
Corner asperity	-0.81801×10^{-8}	0.1706082×10^{20}
Side asperity	-0.79900×10^{-8}	0.1607712×10^{20}
Central asperity	-0.77999×10^{-8}	0.1387791×10^{20}

That means the lifetime of the corner atomic block, which is located at the corner of the adhesive subscale asperity where the shear stress at maximum value, will be less than the lifetime of central atomic subscale block by 9% when $m = 1$ and by 18.65% when $m = 2$. In other words, the start of coating damage at the point of maximum shear stress concentration.

At first sight the values of shear stresses of the order of GPa looks unrealistic. However, as it was discussed in Chapter 3, (see Figure 3-13), the interactions are non-linear, and they do not have plastic deformations due to the Polonsky-Keer effect, and the total load per very small area of atomic scale asperities may be very high.

The stiction between the MEMS gear tooth surfaces may occur when the functionalised SAM layer is removed from almost all atomic scale (for both contacting surfaces) within the single tooth contact zone *STC* for more details see section (4.3.1). This may happen during the same cycle.

It has been noticed that the lifetime of microgear MEMS tooth that has a functionalised surface with OTS monomolecular layer and subjected to the constant loads has increased. According to the evolutions and the amount of damage in the monomolecular layer, there is an initiation step which occurs before the establishment of damage, and then the growth of this damage.

When the functionalised coating layer has totally covered the tooth surface, the effect of stiction is significantly limited over the microgear MEMS tooth surface. When the damage starts growing in the functionalised OTS SAM layer, the possibility of stiction between the counterpart surfaces of the teeth will increase. The accumulation damage in OTS-SAM layer has started and gradually increased until it reaches an active level when 40% or more of this layer has been worn away (see Figure 5-24). The cumulative damage has grown enough to change the distribution of chemical and vdW interactions on the tooth surface significantly.

When the functionalised layer is totally removed from the microgear MEMS tooth surface, stiction occurs between the elements and it will not allow the system to work.

5.5.3 Coefficient of Friction for OTS-SAM layer

This section will describe the COF for the silicon microgear MEMS tooth surfaces that are functionalised with the OTS-SAM layer and when the wear occurs in the coating layer.

The dissipated energy due to the dissociation of the chemical and the vdW bonds between the particles of the functionalised coating monolayer on the counterpart's microgear teeth surfaces and the elastic deformation of the asperities were calculated assuming different values of the functionalised layer are worn away.

The friction force and the COF have been calculated as a percentage of the functionalised coating monomolecular layer wears, as it has shown in the results of this chapter. Figure (5-24) shows the percentages of wear in the monomolecular layer that have been chosen between 0%, when the tooth surface is totally coated and 100% when the functionalised coating OTS monomolecular layer is totally worn away.

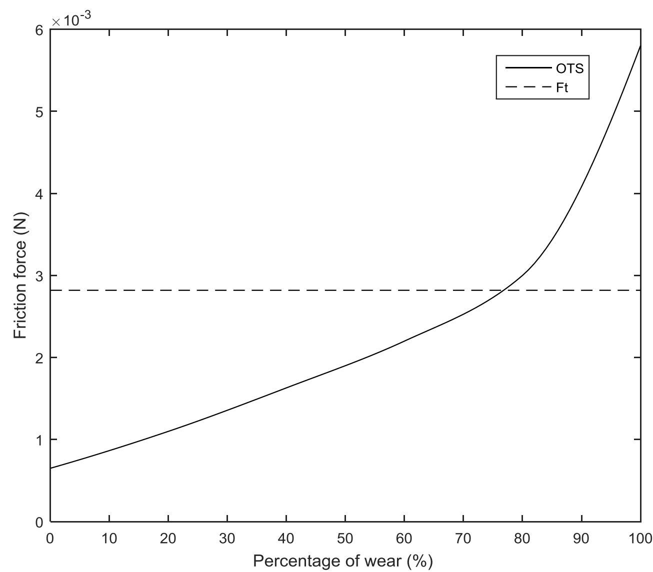

Figure 5-24 Friction force (the solid line) in the OTS-SAM layer and the tangential force (F_t) value (the dash line) required to keep the system in motion

In fact, it is assumed that the OTS-SAM layer has been removed completely from the contacting surface of the micropinion tooth, while only Ω percent of the functionalised layer has been removed from the contacting surface of the microgear tooth. In the numerical simulations Ω was taken as 0, 20, 40, 60, 80, 100. Evidently, the values $\Omega = 0$ and $\Omega = 100$ correspond to functionalised and non-functionalised cases respectively.

An example of these results is presented in Figure (5-25). It shows that for $\Omega = 20$, the COF increases from 0.185 to 0.32. At this stage of sliding contact, some of the OTS-

SAM molecules start to move away from the microgear MEMS tooth surface due to shear force, which is formed on the surface by the sliding motion and friction. However, with the COF value, the microgears meshing system is working normally and safely without any stiction.

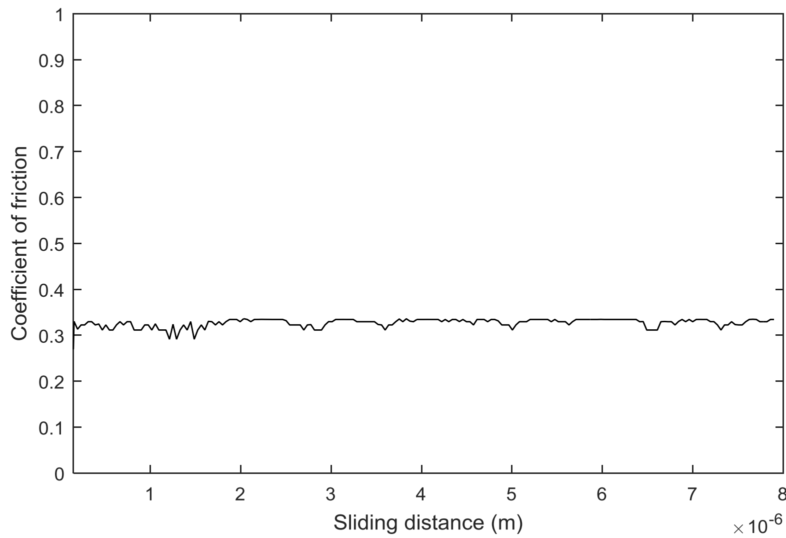

Figure 5-25 The COF for $\Omega = 20$ in the functionalised coating teeth surface

Another example of these results is presented in Figure (5-26). It shows that for $\Omega = 80$, the COF increases to approximately 0.75. At this stage of sliding contact, the sliding motion in this situation will start struggling to continue and the interaction becomes stronger and stronger. The silicon microgear MEMS structure works but it is not efficient due to the high possibility of stiction between teeth, which may lead to the failure of the structure of the microsystem.

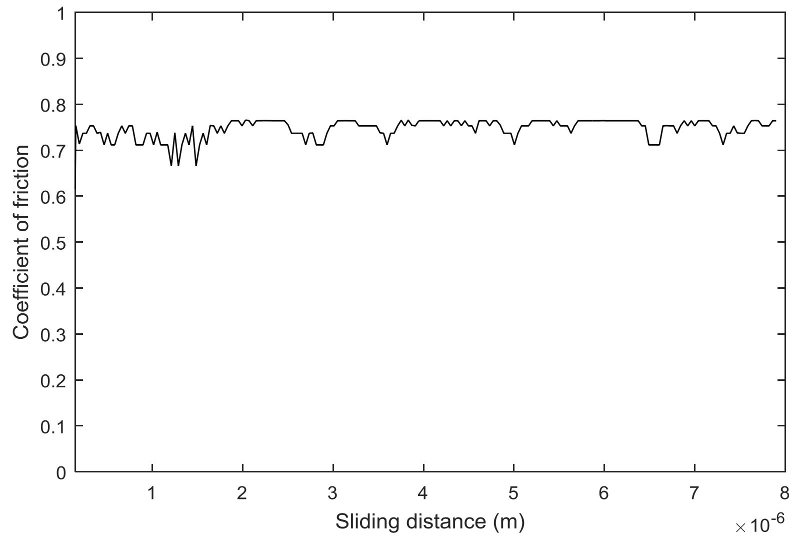

Figure 5-26 The COF for $\Omega = 80$ in the functionalised coating teeth surface

However, the friction, which is represented in the Figure (5-27), is clearly near the tangential force magnitude $\left(F_f \cong F_t \right)$, which means that the microgear MEMS mechanism is in a critical state (reached to the threshold point). Therefore, the possibility of MEMS structure collapse starts to be significant and if the damage in the functionalised coating OTS monolayer jumps by more than 80%, then failure can occur at any time during the operation process.

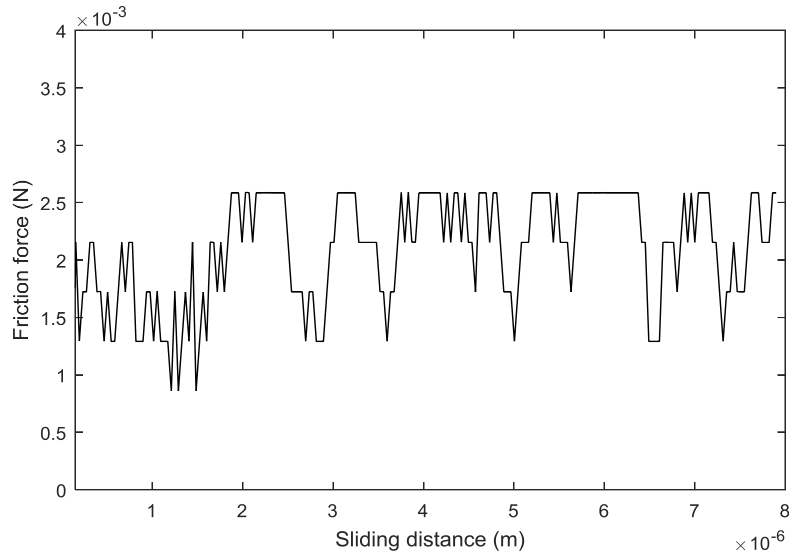

Figure 5-27 Friction force for $\Omega = 80$ in the functionalised teeth surface

The results of all numerical simulations are combined in Figure (5-28). It shows the COF when the microgear MEMS tooth surfaces are totally functionalised, the value of the COF has been indicated at 0.185. This value is quite suitable to continue the operating system without any problems occurring due to stiction or friction.

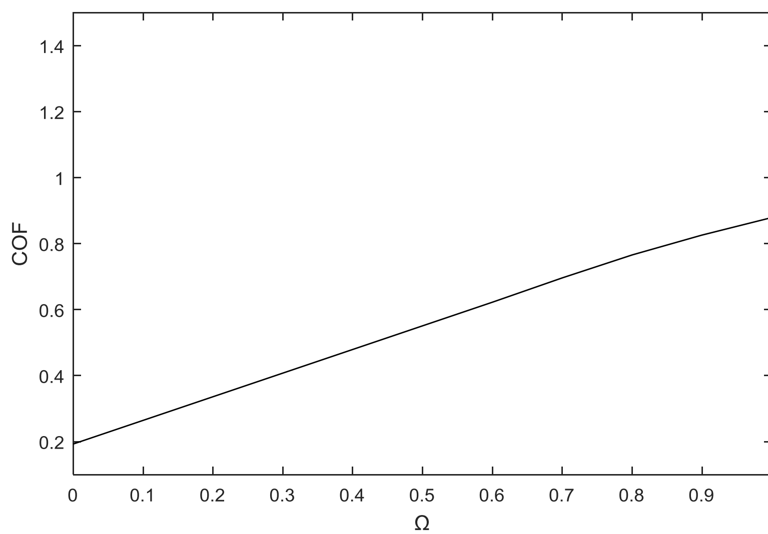

Figure 5-28 The value of COF with respect to Ω

One can see clearly in Figure (5-28) the difference in the value of the COF between the functionalised surfaces by OTS-SAM layer, which is than 0.185 and the value of COF when the monomolecular layer is completely removed from the meshing surfaces, which is equal to 0.84. These values are quite close to the experimental observations that obtained by Satyanarayana et al., 2005 (see more detail in Figure 5-16).

5.6 Conclusion to Chapter 5

Damage accumulation model has been developed to show the damage in the OTS SAM functionalised layers based on the Goryacheva-Torskaya damage model. Numerical simulations for the functionalised MEMS microgear tooth surfaces by SAM layers show that initially there is no stiction between each other. Stiction occurs after some number of meshing cycles because the functionalised monomolecular is gradually worn away due to damage accumulation in this layer.

It has taken into account just termination of the chemically active tips of bare silicon asperities by OTS SAM layers. Due to lack of reliable experimental results, the possibility of formation of the double layers between the coated surfaces was not taken into account. However, the head group is attached (chemical sorption) to the silicon surface while the tails (spacer and terminals groups) are organised into regular arrangement (orientation) molecular structure. Then, it is very likely that the functionalised coating layers form charged double layers. Due to similar charged tails, the double layer interactions between the SAM layers are repulsive; this will lead to decrease the value of the compressing force. This will lead to general decrease of the COF. The calculated COF are quite close to the experimental observations found in literature.

The damage variable ω for SAM layer reflects the amount of chemical bonds broken. These include the vertical bonds between the layer and the substrate (silicon asperity at atomic subscale) and the horizontal bonds between the molecules of SAM layers. The quantitative expressions for these numbers and their relations to the percentage Ω of the functionalised layer that was removed from the contacting surface of the microgear tooth may be obtained by additional experimental studies that are out the scope of this thesis.

Chapter 6 Conclusions and Future Work

6.1 Conclusion

1- It has been shown experimentally that roughness of silicon microgear MEMS tooth surfaces is only within the nanometre scale, hence there are no microscale asperities. It is argued that there is no plastic deformations of the nanoscale asperities due to the Polonsky-Keer effect.

2- It has been developed a multiscale, multi-blocks hierarchical model of nanoscale asperities (the nanoblock model) for numerical simulations of the work of silicon microgear MEMS teeth having rough surfaces. This is an extension of the single block model that was developed by Savencu and Borodich (2015). The model takes into account the different chemical and physical mechanisms of interactions that may occur between surfaces in a vacuum environment. The Lennard- Jones potential has been used to estimate the interaction potential between the particles (molecules) on the counterpart contacting surfaces.

   The dimensions of the nanoblock model have been taken using the statistical analysis of AFM experimental data on the roughness of a silicon surface.

3- The nanoblock model has been used to simulate various tribological phenomena, including friction and wear of MEMS microgear surfaces. To simulate real geometry of the curved microgear rough surfaces, nano-blocks have been superimposed along the surface of a microgear tooth. The distances (the gap) between the contacting surfaces of microgears meshing teeth, that are different at each time step, have been calculated using an iterative approach using the 2D Cardiff solver.

4- The numerical simulation of friction interactions between teeth surfaces has been implemented to calculate the friction force and the COF by using the total energy dissipated during sliding contact between the MEMS conjunction surfaces.

5- Numerical simulations have been used to study the frictional contact process between the pure and clean silicon MEMS microgear tooth surfaces working in a vacuum environment. It has been found that there is high possibility that stiction occurs between the tooth surfaces.

6- It has been shown that the possibility for stiction reduce significantly if the tooth surfaces are covered by functionalised self-assembled monomolecular layers (carbon-based coatings).

7- Damage accumulation model has been developed to study the damage in carbon-based functionalised coating monomolecular based on the Goryacheva-Torskaya model for damage accumulation in fatigue elements. Numerical simulations for silicon-based MEMS microgear tooth surfaces functionalised by monomolecular layer show that initially there is no stiction between each other. However, the stiction occur after some number of cycles because the functionalised monomolecular is gradually worn away due to damage accumulation in this layer.

6.2 Future Work

1- Apply the same dry adhesive frictional model in a natural environment, not a vacuum one and show the effect of oxidation of silicon surfaces on the performance of silicon MEMS.

2- The effect of an increase of temperature in the contact zone between the silicon microgear MEMS tooth surfaces should also be examined.

3- Future work should examine the influence of fatigue and cracks in a silicon microgear MEMS tooth.
4- To take into account the double layer interaction between the self-assembled monolayer-modified substrates and to calculate the double layer force.
5- Using additional experimental studies, to evaluate the damage variable ω for SAM layers and its relation to the percentage of the functionalised layer worn away.

References

Adams, G.G. and Nosonovsky, M., 2000. Contact modelling-forces. *Tribology International*, *33*, 5, pp.431-442.

Adams, G.G., 2014. Adhesion and pull-off force of an elastic indenter from an elastic half-space. In *the Royal Society,* 470, No. 2169, p. 20140317.

Akhmatov, A.S., 1963. *Molecular physics of boundary friction*. Moscow.

Akhmatov, A.S., 1966. *Molecular physics of boundary friction*, 2108. Israel program for scientific translations.

Al-Mayali, M.F., Evans, H.P. and Sharif, K.J., 2016. Assessment of the effects of residual stresses on fatigue life of real rough surfaces in lubricated contact. In *Students on Applied Engineering (ISCAE), International Conference for IEEE*. (pp. 123-128).

Almuramady N. and Borodich F. M. 2016. Adhesive Contact between Silicon-Based Mems Tooth Surfaces Modelled by the Multiscale Multi-Block Model. *Proceedings of the 1th International Conference on Advances in Automotive Technologies 2016, 11-14 October 2016, Yildiz Technical University, Istanbul, Turkey*, ISBN: 978-605-9546-01-0, pp 129–135.

Almuramady N., Borodich F. M. and Savencu O. 2016. Studies of stiction between MEMS microgear teeth by multilevel hierarchical models. *Proceedings of the 9th Nano Congress for Next Generation. August 01-02, 2016 Manchester, UK*, doi: 10.4172/2157-7439.C1.040.

Almuramady N. and Borodich F. M. 2017. Adhesive Contact between Silicon-Based Mems Tooth Surfaces Modelled by the Multiscale Multi-Block Model. International Journal of Advances on Automotive and Technology, 1, No. 2, pp. 59-66. doi: 10.15659/ijaat.17.04.523

Al-Musawi, R.S.J., Brousseau, E.B., Geng, Y. and Borodich, F.M., 2016. Insight into mechanics of AFM tip-based nanomachining: bending of cantilevers and machined grooves. *Nanotechnology*, *27*, 38, p.385302.

Anis, Y.H., Mills, J.K. and Cleghorn, W.L., 2006, May. Active microgripper interface used in microassembly of MEMS. In *Electrical and Computer Engineering, 2006. CCECE'06. Canadian Conference*, *IEEE,* pp. 352-354.

Archard, J.F., 1957. Elastic deformation and the laws of friction. In *Proceedings of the Royal Society of London A: Mathematical, Physical and Engineering Sciences,* 243, No. 1233, pp. 190-205.

Ashurst, W.R., Carraro, C. and Maboudian, R., 2003. Vapor phase anti-stiction coatings for MEMS. *IEEE Transactions on Device and Materials Reliability*, *3*, 4, pp.173-178.

Banks, D., 2006. *Microengineering, MEMS, and Interfacing: a Practical Guide*. CRC press.

Beach, E.R., Tormoen, G.W., Drelich, J. and Han, R., 2002. Pull-off force measurements between rough surfaces by atomic force microscopy. *Journal of Colloid and Interface Science*, *247*, 1, pp.84-99.

Beeby, S., 2004. *MEMS Mechanical Sensors*. Artech House.

Berger, E.J., 2002. Friction modeling for dynamic system simulation. *Applied Mechanics Reviews*, *55*, 6, pp.535-577.

Bernstein, J., Cho, S., King, A.T., Kourepenis, A., Maciel, P. and Weinberg, M., 1993. A micromachined comb-drive tuning fork rate gyroscope. In *Micro Electro Mechanical Systems, 1993, MEMS'93, Proceedings An Investigation of Micro Structures, Sensors, Actuators, Machines and Systems. IEEE.* pp. 143-148.

Bhushan, B. ed., 2008. *Nanotribology and nanomechanics: an introduction*. Springer Science and Business Media. Berlin, Germany.

Binnig, G., Quate, C.F. and Gerber, C., 1986. Atomic force microscope. *Physical review letters*, *56*, 9, p.930.

Borodich, F.M., 1993. Similarity properties of discrete contact between a fractal punch and an elastic medium. *Comptes Rendus de l'Acad. des Sciences, Paris, Ser. 2*, 316,2, 281-286.

Borodich, F.M., 1998a. Parametric homogeneity and non-classical self-similarity. I. Mathematical background. *Acta mechanica*, 131, pp. 27-45.

Borodich, F.M., 1998b. Parametric homogeneity and non-classical self-similarity. II. Some applications. *Acta mechanica*, 131, pp. 47-67.

Borodich, F.M., 2002. Comment on "Elastoplastic contact between randomly rough surfaces". *Physical review letters*, *88*, 6, p.069601.

Borodich, F.M. 2005 Analytical studies of contact problems for fractal surfaces. In: *Life Cycle Tribology, Proc. 31st Leeds-Lyon Symposium on Tribology, Leeds 2004, Tribology and Interface Engineering Series*, Elsevier, Amsterdam, 537-545. ISBN 0 444 51687 5.

Borodich F.M., 2007. Translation of Historical Paper. Introduction to V A Zhuravlev's historical paper: 'On the question of theoretical justification of the Amontons-Coulomb law for friction of unlubricated surfaces'. *Proc. Instn Mech Engrs, Part J: J. Engineering Tribology*, **221**, J8, pp.893-898.

Borodich, F.M., 2013. Fractal contact mechanics. In *Encyclopedia of Tribology*, pp. 1249-1258. Springer US.

Borodich, F.M., 2014. The Hertz-type and adhesive contact problems for depth-sensing indentation. *Adv. Appl. Mech*, *47*, pp.225-366.

Borodich, F.M. and Galanov, B.A., 2002. Self-similar problems of elastic contact for non-convex punches. *Journal of the Mechanics and Physics of Solids*, *50*, 11, pp.2441-2461.

Borodich, F.M., Galanov, B.A. and Suarez-Alvarez, M.M., 2014. The JKR-type adhesive contact problems for power-law shaped axisymmetric punches. *Journal of the Mechanics and Physics of Solids*, *68*, pp.14-32.

Borodich, F.M. and Keer, L.M., 2004. Evaluation of elastic modulus of materials by adhesive (no–slip) nano–indentation. In *Proceedings of the Royal Society of London A: Mathematical, Physical and Engineering Sciences*, 460, No. 2042, pp. 507-514.

Borodich F.M. and Mosolov, A.B. 1991. Fractal contact of solids. *Zh. Tekh. Fiz.*, 61(9), 50-54. English transl. in *Sov. Phys.-Tech. Phys.*, 36, 9, 995-997.

Borodich, F.M. and Mosolov, A.B., 1992. Fractal roughness in contact problems. *Journal of Applied Mathematics and Mechanics*, *56*, 5, pp.681-690.

Borodich, F.M. and Onishchenko, D.A., 1993. Fractal roughness in contact and friction problems (the simplest models). *Journal of Friction and Wear, 14, 3, pp.14-19.*

Borodich, F.M. and Onishchenko, D.A., 1999. Similarity and fractality in the modelling of roughness by a multilevel profile with hierarchical structure. *International Journal of Solids and Structures*, 36, pp. 2585-2612

Borodich, F.M., Pepelyshev, A. and Savencu, O., 2015. Micro and nano scale statistical properties of rough surfaces of significance in their friction. *Proceedings of the 6th Vienna International Conference on Nano-Technology - Viennano '15, Wiener Neustadt, Austria, 23-25 November 2015.*

Borodich, F.M., Pepelyshev, A. and Savencu, O., 2016. Statistical approaches to description of rough engineering surfaces at nano and microscales. *Tribology International*, *103*, pp.197-207.

Borodich F.M. and Savencu O. 2017. Hierarchical models of engineering rough surfaces and bio-inspired adhesives. In: Bio-Inspired Structured Adhesives: Biological Prototypes, Fabrication, Tribological Properties, Contact Mechanics, and Novel Concepts. Eds. L. Heepe, L. Xue and S. Gorb, Springer.

Bowden, F. P., Tabor, D. 1956. *Friction and Lubrication*, London, Methuen.UK.

Bowden, F.P. and Leben, L., 1938. Nature of sliding and the analysis of friction. *Nature*, *141*, p.691.

Bowden, F.P. and Leben, L., 1939. The nature of sliding and the analysis of friction. *Proceedings of the Royal Society of London. Series A, Mathematical and Physical Sciences*, pp.371-391.

Bowden, F.P. and Tabor, D., 1943. The lubrication by thin metallic films and the action of bearing metals. *Journal of Applied Physics*, *14*, 3, pp.141-151.

Bowden, F.P. and Tabor, D., 1973. *Friction: An Introduction to Tribology*. RE Krieger Publishing Company.

Bradley, R. S. 1932. The cohesive force between solid surfaces and the surface energy of solids. *Philosophical Magazine,* 13**,** 853-862

Brousseau, E., Al-Musawi, R.S. and Lebiez, D., 2015. A hybrid roll-to-roll AFM set-up for high throughput tip-based nano-machining. *Manufacturing Letters*, *6*, pp.10-13.

Bush, A.W., Gibson, R.D. and Keogh, G.P., 1979. Strongly anisotropic rough surfaces. *Journal of Lubrication Technology*, *101*, 1, pp.15-20.

Butt, H.J., Cappella, B. and Kappl, M., 2005. Force measurements with the atomic force microscope: Technique, interpretation and applications. *Surface science reports*, *59*, 1, pp.1-152.

Cai, S. and Bhushan, B., 2007. Three-dimensional sliding contact analysis of multilayered solids with rough surfaces. *Journal of Tribology*, *129*, 1, pp.40-59.

Cao, L., Mantell, S. and Polla, D., 2001. Design and simulation of an implantable medical drug delivery system using microelectromechanical systems technology. *Sensors and Actuators A: Physical*, *94*, 1, pp.117-125.

Carpick, R.W. and Salmeron, M., 1997. Scratching the surface: fundamental investigations of tribology with atomic force microscopy. *Chemical Reviews*, *97*, 4, pp.1163-1194.

Carpick, R.W., Flater, E.E., VanLangendon, J.R. and de Boer, M.P., 2002. Friction in MEMS: from single to multiple asperity contact. In *Int. Congr. Exposition Exp. Appl. Mech*, pp. 282-287.

Chau, K.H.L. and Sulouff, R.E., 1998. Technology for the high-volume manufacturing of integrated surface-micromachined accelerometer products. *Microelectronics Journal*, *29*, 9, pp.579-586.

Dagnall, H., 1980. *Exploring surface texture*. Rank Taylor Hobson.

Davies, C.N., 2005. *Effects of non-Newtonian rheology on the line contact elastohydrodynamic lubrication problem* (PhD dissertation, Cardiff University).

Dean, J. A., 1999. *Lange's Handbook of Chemistry*. New York, McGraw-Hill.

Dean, J.A., 1992. *Lange's Handbook of Chemistry, Section 4–Properties of Atoms, Radicals, and Bonds*. Mcgraw-Hill, New York.

Dejeu, J., Bechelany, M., Rougeot, P., Philippe, L. and Gauthier, M., 2011. Adhesion control for micro-and nanomanipulation. *ACS nano*, *5*, 6, pp.4648-4657.

Derjaguin, B. 1934a. Molekulartheorie der äußeren Reibung. *Zeitschrift für Physik*, 88, 661-675

Derjaguin, B. 1934b. Untersuchungen über die Reibung und Adhäsion, IV. Theorie des Anhaftens kleiner Teilchen. *Kolloid Zeitschrift*, 69, pp. 155–164

Derjaguin, B.V., 1934c. Molecular theory of friction and sliding. *Zhurn. Phis. Khim (in Russian)*, 5, pp.1165-1172.

Deryagin, B.V., Krotova, N.A. and Smilga, V.P., 1978. Adhesion of Solids. Engl Ed Translated by RK Johnson.

Deshpande, V. S., Needleman, A. and Van der Giessen, E., 2003. Scaling of discrete dislocation predictions for near-threshold fatigue crack growth. *Acta Materialia*, *51*, 15, pp.4637-4651.

Dong, J., Wang, A., Ng, K.S. and Mao, G., 2006. Self-assembly of octadecyltrichlorosilane monolayers on silicon-based substrates by chemical vapor deposition. *Thin Solid Films*, *515*, 4, pp.2116-2122.

Dong, L. and Nelson, B.J., 2007. Tutorial-Robotics in the small part II: nanorobotics. *IEEE Robotics and Automation Magazine*, *14*, 3, pp.111-121.

Dowson, D., 1979. *History of tribology*. Addison-Wesley Longman Limited.

Evans, H.P., Snidle, R.W., Sharif, K.J., Shaw, B.A. and Zhang, J., 2013. Analysis of micro-elastohydrodynamic lubrication and prediction of surface fatigue damage in micropitting tests on helical gears. *Journal of Tribology*, *135*, 1, p.011501.

Fischer, A.C., Forsberg, F., Lapisa, M., Bleiker, S. J., Stemme, G., Roxhed, N. and Niklaus, F., 2015. Integrating MEMS and ICs. *Microsystems and Nanoengineering*, 1, p. 15005. doi:10.1038/micronano.2015.5

Flater, E.E., Ashurst, W.R. and Carpick, R.W., 2007. Nanotribology of octadecyltrichlorosilane monolayers and silicon: self-mated versus unmated interfaces and local packing density effects. *Langmuir*, *23*, 18, pp.9242-9252.

Frankfort, H., 1943. *More sculpture from the Diyala region*, 60. University of Chicago Press.

Gabriel, K. J., Behi, F., Mahadevan, R. and Mehregany, M., 1990. In situ friction and wear measurements in integrated polysilicon mechanisms. *Sensors and Actuators A: Physical*, *21*, 1-3, pp.184-188.

Gad-el-Hak, M. ed., 2002. *The MEMS Handbook*. CRC press.

Gad-el-Hak, M. ed., 2006. *The MEMS Handbook*, 2, Florida: CRC/Taylor and Francis.

Galin, L.A., 2008. *Contact Problems: The Legacy of LA Galin*, 155, Springer Science and Business Media.

Gent, A.N. and Kaang, S., 1986. Pull-off forces for adhesive tapes. *Journal of applied polymer science*, *32*, 4, pp.4689-4700.

Ghodssi, R. and Lin, P. eds., 2011. *MEMS materials and processes handbook*. Springer Science and Business Media.

Goryacheva, I. (1998). *Contact Mechanics in Tribology*. Dordrecht, Kluwer.

Goryacheva, I. and Makhovskaya, Y., 2008. Adhesion effects in contact interaction of solids. *Comptes Rendus Mécanique*, *336*, 1-2, pp.118-125.

Goryacheva, I.G. and Makhovskaya, Y.Y., 2001. Adhesive interaction of elastic bodies. *Journal of Applied Mathematics and Mechanics*, *65*, 2, pp.273-282.

Goryacheva, I.G. and Torskaya, E.V., 2003. Stress and fracture analysis in periodic contact problem for coated bodies. *Fatigue and Fracture of Engineering Materials and Structures*, *26*, 4, pp.343-348.

Goryacheva, I.G. and Torskaya, E.V., 2010. Modeling of fatigue wear of a two-layered elastic half-space in contact with periodic system of indenters. *Wear*, *268*, 11, pp.1417-1422.

Greenwood, J. A., 1990. Surface modelling in tribology. *In Applied surface modelling* (Eds C. F. M. Creasy and C. Craggs), pp. 61–75 (Ellis Horwood, New York).

Greenwood, J.A. and Williamson, J.B.P., 1966, December. Contact of nominally flat surfaces. In *Proceedings of the Royal Society of London A: Mathematical, Physical and Engineering Sciences*, 295, No. 1442, pp. 300-319.

Greenwood, J.A. and Wu, J.J., 2001. Surface roughness and contact: an apology. *Meccanica*, *36*, 6, pp.617-630.

Guckel, H., Sniegowski, J.J., Christenson, T.R., Mohney, S. and Kelly, T.F., 1989. Fabrication of micromechanical devices from polysilicon films with smooth surfaces. *Sensors and Actuators*, *20*, 1-2, pp.117-122.

Hamaker, H. C., 1937. The London-van der Waals attraction between spherical particles. *physica, 4*, 10, pp.1058-1072.

Hardy, W.B., 1936. *Collected Scientific Papers of Sir William Bate Hardy*. Cambridge Uni. Press.

Hertz, H., 1882. Ueber die Beruehrung elastischer Koerper (On Contact Between Elastic Bodies). *Gesammelte Werke (Collected Works)*, 1

Hopcroft, M.A., Nix, W.D. and Kenny, T.W., 2010. What is the Young's Modulus of Silicon? *Journal of microelectromechanical systems*, *19*, 2, pp.229-238.

Hull, D. and Bacon, D.J., Fifth Edition, 2011. *Introduction to Dislocations*. Butterworth-Heinemann.

Hutchings, I.M., 2016. Leonardo da Vinci′ s studies of friction. *Wear*, *360*, pp.51-66.

Jackson, R.L. and Streator, J.L., 2006. A multi-scale model for contact between rough surfaces. *Wear*, *261*(11), pp.1337-1347.

Jackson, R.L., 2011, March. A model for the adhesion of multiscale rough surfaces in MEMS. In *System Theory (SSST), 2011 IEEE 43rd Southeastern Symposium on*, pp. 257-262.

Johnson, K.L., 1975. Non-Hertzian contact of elastic spheres. *The Mechanics of Contact Between Deformable Solids, edited by AD de Pater and JJ Kalker (Delft University Press, Delft, The Netherlands, 1975)*, pp.26-40.

Johnson, K.L., 1985. *Contact Mechanics*. Cambridge university press.

Kachanov, L., 1986. *Introduction to Continuum Damage Mechanics.* Dordrecht, Springer Netherlands.

Kallman, J.S., Hoover, W.G., Hoover, C.G., De Groot, A.J., Lee, S.M. and Wooten, F., 1993. Molecular dynamics of silicon indentation. Physical Review B, 47, 13, p.7705-7709.

Karpenko, Y.A. and Akay, A., 2001. A numerical model of friction between rough surfaces. *Tribology International*, *34*, 8, pp.531-545.

Kendall, K., 2007. *Molecular Adhesion and Its Applications: The Sticky Universe*. Springer Science and Business Media.

Khaustov, S., 2016. *Elastohydrodynamic lubrication and surface fatigue modelling of spur gears over the meshing cycle* (PhD dissertation, Cardiff University).

Kim, S. H., Dugger, M. T., and Mittal, K. L. 2010. *Adhesion aspects in MEMS/NEMS*. Leiden, Brill.pp.240.

Komvopoulos, K. and Gong, Z.Q., 2007. Stress analysis of a layered elastic solid in contact with a rough surface exhibiting fractal behavior. *International Journal of Solids and Structures*, *44*, 7, pp.2109-2129.

Komvopoulos, K., 1996. Surface engineering and microtribology for microelectromechanical systems. *Wear*, *200*, 1-2, pp.305-327.

Kragelsky, I. V., Dobychin, M. M. and Kombalov, V. S. 1982. *Friction and Wear: calculation methods*. Oxford, Pergamon Press.

Krajcinovic, D., 1983. Constitutive equations for damaging materials. *Journal of applied Mechanics*, *50*, 2, pp.355-360.

Krajcinovic, D., 1996. *Damage Mechanics*. Elsevier.

Krim, J., 2002. Surface science and the atomic-scale origins of friction: what once was old is new again. *Surface Science*, *500*, 1, pp.741-758.

Kuhlmann-Wilsdorf, D., 1996. What role for contact spots and dislocations in friction and wear? *Wear*, 200, 1, pp.8-29.

Kulkarni, S.A., Mirji, S.A., Mandale, A.B. and Vijayamohanan, K.P., 2006. Thermal stability of self-assembled octadecyltrichlorosilane monolayers on planar and curved silica surfaces. *Thin Solid Films*, *496*, 2, pp.420-425.

Leang K. and Taylor C. 2008. Design and Fabrication of A Multifunctional Scanning Probe with Integrated Tip Changer for Fully Automated Nanofabrication. *23rd ASPE Anual Meeting and 12th ICPE: 19-24*.

Leondes, C. T. 2006. *MEMS/NEMS: Handbook Techniques and Applications*. New York, Springer.

Li, L., 2010. Applications of MEMS actuators in micro/nano robotic manipulators. In *Computer Engineering and Technology (ICCET), 2010 2nd International Conference, IEEE,* pp. V2-649.

Lim, M.G., Chang, J.C., Schultz, D.P., Howe, R.T. and White, R.M., 1990. Polysilicon microstructures to characterize static friction. In *Micro Electro Mechanical Systems, 1990. Proceedings, An Investigation of Micro Structures, Sensors, Actuators, Machines and Robots. IEEE*, pp. 82-88.

Liu, X., Tong, J. and Sun, Y., 2007. A millimeter-sized nanomanipulator with sub-nanometer positioning resolution and large force output. *Smart Materials and Structures*, *16*, 5, pp.1742-1750.

Lomboy, G., Sundararajan, S., Wang, K. and Subramaniam, S., 2011. A test method for determining adhesion forces and Hamaker constants of cementitious materials using atomic force microscopy. *Cement and Concrete Research*, 41, 11, pp.1157-1166.

Lu, Y., Huang, J.Y., Wang, C., Sun, S. and Lou, J., 2010. Cold welding of ultrathin gold nanowires. *Nature nanotechnology*, 5, 3, pp.218-224.

Maboudian, R. and Howe, R.T., 1997. Critical review: Adhesion in surface micromechanical structures. *Journal of Vacuum Science and Technology B:*

Microelectronics and Nanometer Structures Processing, Measurement, and Phenomena, *15*, 1, pp.1-20.

Maboudian, R., 1998. Surface processes in MEMS technology. *Surface Science Reports*, *30*, 6-8, pp.207-269.

Maboudian, R., Ashurst, W.R. and Carraro, C., 2002. Tribological challenges in micromechanical systems. *Tribology letters*, *12*, 2, pp.95-100.

Madou, M.J., 2002. *Fundamentals of Microfabrication: The Science of Miniaturization*. CRC press.

Majumdar, A. and Bhushan, B., 1990. Role of fractal geometry in roughness characterization and contact mechanics of surfaces. *ASME J. Tribol*, *112*, 2, pp.205-216.

Majumdar, A. and Bhushan, B., 1991. Fractal model of elastic-plastic contact between rough surfaces. *ASME J. Tribol*, *113*, 1, pp.1-11.

Manoylov, A.V., Bryant, M.J. and Evans, H.P., 2013. Dry elasto-plastic contact of nominally flat surfaces. *Tribology International*, *65*, pp.248-258.

Mastrangelo, C.H. and Hsu, C.H., 1993. Mechanical stability and adhesion of microstructures under capillary forces. I. Basic theory. *Journal of Microelectromechanical systems*, *2*, 1, pp.33-43.

Mastrangelo, C.H., 1997. Adhesion-related failure mechanisms in micromechanical devices. *Tribology Letters*, *3*, 3, pp.223-238.

Mastrangelo, C.H., 1999. Suppression of stiction in MEMS. In *MRS Proceedings,* 605, p. 105, Cambridge University Press.

Mate, C.M., 2008. *Tribology on the small scale: a bottom up approach to friction, lubrication, and wear*, 6. Oxford University Press.

Maugis, D., 1992. Adhesion of spheres: the JKR-DMT transition using a Dugdale model. *Journal of colloid and interface science*, *150*, 1, pp.243-269.

Maugis, D., 2000. *Contact, Adhesion and Rupture of Elastic Solids*, Berlin, Springer-Verlag Berlin Heidelberg.

McCool, J.I., 1986. Comparison of models for the contact of rough surfaces. *Wear*, *107*, 1, pp.37-60.

Mesarovic, S.D. and Fleck, N.A., 1999, July. Spherical indentation of elastic–plastic solids. In *Proceedings of the Royal Society of London A: Mathematical, Physical and Engineering Sciences*, 455, No. 1987, pp. 2707-2728.

Meyers, M.A., Mishra, A. and Benson, D.J., 2006. Mechanical properties of nanocrystalline materials. *Progress in materials science*, *51*, 4, pp.427-556.

Moore, D. F., 1975. *Principles and Applications of Tribology*. Oxford, Pergamon Press.

Moore, N.W. and Houston, J.E., 2010. The pull-off force and the work of adhesion: new challenges at the nanoscale. *Journal of Adhesion Science and Technology*, *24*, 15-16, pp.2531-2544.

Mordehai, D., Rabkin, E. and Srolovitz, D.J., 2011. Pseudoelastic deformation during nanoscale adhesive contact formation. *Physical review letters*, *107*, 9, p.096101.

Myshkin, N.K., Petrokovets, M.I. and Chizhik, S.A., 1998. Simulation of real contact in tribology. *Tribology International*, *31*(1), pp.79-86.

Nayak, P.R., 1971. Random process model of rough surfaces. ASME. New York

Papadimitriou, G.I., Papazoglou, C. and Pomportsis, A.S., 2003. Optical switching: switch fabrics, techniques, and architectures. *Journal of lightwave technology*, *21*, 2, pp.384-405.

Patton, S.T. and Zabinski, J.S., 2005. Failure mechanisms of capacitive MEMS RF switch contacts. *Tribology Letters*, *19*, 4, pp.265-272.

Plesha, M.E. and Ni, D., 2001. Scaling of geological discontinuity normal load–deformation response using fractal geometry. *International journal for numerical and analytical methods in geomechanics*, *25*, 8, pp.741-756.

Polonsky, I.A. and Keer, L.M., 1996a. Scale effects of elastic-plastic behavior of microscopic asperity contacts. *Journal of Tribology*, *118*, pp.335-340.

Polonsky, I.A. and Keer, L.M., 1996b. Simulation of microscopic elastic-plastic contacts by using discrete dislocations. In *Proceedings of the Royal Society of London A: Mathematical, Physical and Engineering Sciences*, 452, No. 1953, pp. 2173-2194.

Poon, C.Y. and Bhushan, B., 1995. Comparison of surface roughness measurements by stylus profiler, AFM and non-contact optical profiler. *Wear*, *190*, 1, pp.76-88.

Popov, V., 2010. *Contact mechanics and friction: physical principles and applications*. Springer Science and Business Media.

Prandtl, L. 1928. A conceptual model of the kinetic theory of solid bodies. *Zeitschrift Fur Angewandte Mathematik Und Mechanik,* 8**,** pp.85-106.(Translated from German original by Popov, V. L., Gray, J. 2012. Prandtl-Tomlinson model: History and applications in friction, plasticity, and nanotechnologies. *Z. Angew. Math. Mech.* **92**, 9, pp.683-708.

PRIME Faraday Partnership 2002. An Introduction to MEMS (Micro-electromechanical Systems). *Wolfson School of Mechanical and Manufacturing Engineering*- Loughborough University, Loughborough.

Rabinovich, Y.I., Adler, J.J., Ata, A., Singh, R.K. and Moudgil, B.M., 2000a. Adhesion between nanoscale rough surfaces: I. Role of asperity geometry. *Journal of Colloid and Interface Science*, *232*, 1, pp.10-16.

Rabinovich, Y.I., Adler, J.J., Ata, A., Singh, R.K. and Moudgil, B.M., 2000b. Adhesion between nanoscale rough surfaces: II. Measurement and comparison with theory. *Journal of Colloid and Interface Science*, *232*, 1, pp.17-24.

Rabotnov, Y.N., 1963. Creep problems in structural members. [Translated from Russian original to English by Transcripta service LTD, London, 1969].

Raja, J., Muralikrishnan, B. and Fu, S., 2002. Recent advances in separation of roughness, waviness and form. *Precision Engineering*, *26*, 2, pp.222-235.

Ramakrishna, S.N., Nalam, P.C., Clasohm, L.Y. and Spencer, N.D., 2013. Study of adhesion and friction properties on a nanoparticle gradient surface: transition from JKR to DMT contact mechanics. *Langmuir*, *29*, 1, pp.175-182.

Rezvanian, O., Zikry, M.A., Brown, C. and Krim, J., 2007. Surface roughness, asperity contact and gold RF MEMS switch behavior. *Journal of Micromechanics and Microengineering*, *17*, 10, p.2006.

Rosen, Y. ed., 2012. *Biomaterials Science: An Integrated Clinical and Engineering Approach*. CRC Press.

Rumpf, H., and Bull, F. A. 1990. *Particle technology*. London, Chapman and Hall.

Rymuza, Z. and Pytko, S., 2010. Scaling in friction experiments. *Scientific Problems of Machines Operation and Maintenance*, *45*, 3, pp.7-18.

Rymuza, Z., 1999. Control tribological and mechanical properties of MEMS surfaces. Part 1: critical review. *Microsystem Technologies*, *5*, 4, pp.173-180.

Sainsot, P., Leroy, J.M. and Villechaise, B., 1990. Effect of surface coatings in a rough normally loaded contact. *Tribology Series*, *17*, pp.151-156.

Savencu, O. and Borodich, F.M., 2014. Modelling of friction using a structural multilevel hierarchical model of rough surfaces. In *Proc. NSCM-27: the 27th Nordic Seminar on Computational Mechanics, KTH, Stockholm, ISSN0348-467X*, pp. 136-139.

Savencu, O., 2016. *Simulations of dry friction between rough surfaces and corresponding nonlinear problems at nano and microscales* (PhD dissertation, Cardiff University).

Satyanarayana, N., Sinha, S.K. and Srinivasan, M.P., 2005. Friction and wear life evaluation of silane based self-assembled monolayers on silicon surface. *Tribology and Interface Engineering Series*, *48*, pp.821-826.

Scherge, M., Gorb, S. and Gorb, S.N., 2001. *Biological micro-and nanotribology*. Springer Science and Business Media.

Serry, F.M., Walliser, D. and Maclay, G.J., 1998. The role of the Casimir effect in the static deflection and stiction of membrane strips in microelectromechanical systems (MEMS). *Journal of Applied Physics*, *84*, 5, pp.2501-2506.

Setter, N. 2005. *Electroceramic-Based MEMS: fabrication-technology and applications*. New York, Springer.

Shukla, N., Gellman, A.J., Ma, X. and Gui, J., 2002. Effect of humidity on lubricated carbon overcoats. *Tribology Letters*, *12*, 2, pp.105-109.

Shi, X. and Zhao, Y.P., 2004. Comparison of various adhesion contact theories and the influence of dimensionless load parameter. *Journal of Adhesion Science and Technology*, 18(1), pp.55-68.

Sinha, S.K. ed., 2013. *Nano-tribology and Materials in MEMS*. Springer Berlin Heidelberg.

Sitte, R., 2016. MEMS design simplification with virtual prototyping. *Facta Universitatis, Series: Electronics and Energetics*, *29*, 1, pp.11-34.

Spearing, S.M., 2000. Materials issues in microelectromechanical systems (MEMS). *Acta materialia*, *48*, 1, pp.179-196.

Srinivasan, U., Houston, M.R., Howe, R.T. and Maboudian, R., 1998. Alkyltrichlorosilane-based self-assembled monolayer films for stiction reduction in silicon micromachines. *Journal of Microelectromechanical Systems*, *7*, 2, pp.252-260.

Stephens, L.S., Siripuram, R., Hayden, M. and McCartt, B., 2004. Deterministic micro asperities on bearings and seals using a modified LIGA process. In *ASME Journal of Engineering for Gas Turbines and Power. pp.126, 147.*

Suh, A.Y., Polycarpou, A.A. and Conry, T.F., 2003. Detailed surface roughness characterization of engineering surfaces undergoing tribological testing leading to scuffing. *Wear*, *255*, 1, pp.556-568.

Takeuchi, H., Nakamura, K., Shimizu, N. and Shibaike, N., 2000. Optimization of mechanical interface for a practical micro-reducer. In *Micro Electro Mechanical Systems, 2000. MEMS 2000. The Thirteenth Annual International Conference*, *IEEE*, pp. 170-175.

Tanner, D.M., 2000. Reliability of surface micromachined microelectromechanical actuators. In *Microelectronics, 2000. Proceedings in 22nd International Conference, IEEE*, 1, pp. 97-104.

Tanner, D.M., 2009. MEMS reliability: Where are we now? *Microelectronics reliability*, *49*, 9, pp.937-940.

Tas, N., Sonnenberg, T., Jansen, H., Legtenberg, R. and Elwenspoek, M., 1996. Stiction in surface micromachining. *Journal of Micromechanics and Microengineering*, *6*, 4, p.385.

Tas, N.R., Gui, C. and Elwenspoek, M., 2000. Static friction in elastic adhesive MEMS contacts, models and experiment. In *Micro Electro Mechanical Systems, 2000. MEMS 2000. The Thirteenth Annual International Conference*, *IEEE*, pp. 193-198.

Teodorescu, M. and Rahnejat, H., 2007. Dry and wet nano-scale impact dynamics of rough surfaces with or without a self-assembled monolayer. *Proceedings of the Institution of Mechanical Engineers, Part N: Journal of Nanoengineering and Nanosystems*, *221*, 2, pp.49-58.

Teodorescu, M., Theodossiades, S. and Rahnejat, H., 2008. Influence of SAM degradation on MEMS gear dynamics. In *5th European Congress on Computational Methods in Applied Sciences and Engineering, ECCOMAS. Venice, Italy.*

Teodorescu, M., Theodossiades, S. and Rahnejat, H., 2009. Impact dynamics of rough and surface protected MEMS gears. *Tribology international*, *42*, 2, pp.197-205.

Timoshenko, S.P. and Goodier, J.N., 1970. Theory of elasticity. *McGraw-Hill Book Co., Inc., USA.*

Tiwari, A. and Raj, B. eds., 2015. *Materials and Failures in MEMS and NEMS*. John Wiley and Sons. USA.

Tomlinson, G.A., 1929. CVI. A molecular theory of friction. *The London, Edinburgh, and Dublin philosophical magazine and journal of science*, *7*, 46, pp.905-939.

Torskaya, E.B., 2002. Analysis of friction effect on stress state of coated bodies. *Journal of Friction and Wear*, *23*, 2, pp.16-23.

Torskaya, E.V. and Goryacheva, I.G., 2003. The effect of interface imperfection and external loading on the axisymmetric contact with a coated solid. *Wear*, *254*, 5, pp.538-545.

Ulman, A., 2013. *An Introduction to Ultrathin Organic Films: From Langmuir-Blodgett to Self-Assembly*. Academic press.

Vorburger, T.V. and Raja, J., 1990. *Surface finish metrology tutorial*. National Inst. of Standards and Technology.

Warren, T.L. and Krajcinovic, D., 1995. Fractal models of elastic-perfectly plastic contact of rough surfaces based on the Cantor set. *International Journal of Solids and Structures*, *32*, 19, pp.2907-2922.

Warren, T.L. and Krajcinovic, D., 1996. Random cantor set models for the elastic-perfectly plastic contact of rough surfaces. *Wear*, *196*, 1-2, pp.1-15.

Whitehouse, D.J. and Archard, J.F., 1970. The properties of random surfaces of significance in their contact. In *Proceedings of the Royal Society of London A: Mathematical, Physical and Engineering Sciences,* 316, No. 1524, pp. 97-121.

Whitehouse, D.J., 1974. Stylus techniques. In *Characterization of Solid Surfaces*, pp. 49-74. Springer US.

Whitehouse, D.J., 1982. The parameter rash—is there a cure? *Wear*, *83*, 1, pp.75-78.

Yang, P. and Liao, N., 2007. Surface sliding simulation in micro-gear train for adhesion problem and tribology design by using molecular dynamics model. *Computational materials science*, *38*, 4, pp.678-684.

Yeow, T.W., Law, K.E. and Goldenberg, A., 2001. MEMS optical switches. *IEEE Communications magazine*, *39*, 11, pp.158-163.

Yu-Chong, T. and Muller, R.S., 1990. Frictional study of IC-processed micromotors. *Sensors and Actuators A: Physical*, *21*, 1-3, pp.180-183.

Zesch, W., Brunner, M. and Weber, A., 1997. Vacuum tool for handling microobjects with a nanorobot. In *Robotics and Automation, 1997. Proceeding 1997 IEEE International Conference,* 2, pp. 1761-1766.

Zhang, Y., Chen, B.K., Liu, X. and Sun, Y., 2010. Autonomous robotic pick-and-place of microobjects. *IEEE Transactions on Robotics*, *26*, 1, pp.200-207.

Zhao, Y.P., Wang, L.S. and Yu, T.X., 2003. Mechanics of adhesion in MEMS—a review. *Journal of Adhesion Science and Technology*, *17*, 4, pp.519-546.

Zhou, Z., Wang, Z. and Lin, L., 2012. *Microsystems and Nanotechnology*. Tsinghua University Press.

Zhuravlev, V. A., 1940. On the question of theoretical justification of the Amontons – Coulomb law for friction of unlubricated surfaces. *Journal of Technical Physics*, 10, 17: 1447–52.

Zhuravlev, V.P., 2013. On the history of the dry friction law. *Mechanics of Solids*, *48*, 4, pp.364-369.